===================== **TOKAMAKS** =====================

Accuracy of Reconstruction of the Transport Coefficients and ECRH Power Profile in Tokamaks from Solutions to Inverse Problems

V. F. Andreev* and N. V. Kas'yanova**

Russian Research Centre Kurchatov Institute, pl. Kurchatova 1, Moscow, 123182 Russia
**Moscow Institute of Physics and Technology, Institutskiĭ pr. 9, Dolgoprudnyĭ, Moscow oblast, 141700 Russia*
Received April 28, 2004; in final form, December 14, 2004

Abstract—Experiments on ECR plasma heating provide a powerful method for studying electron transport in tokamak plasmas and reconstructing the transport coefficients. An analysis of such experiments requires, however, reliable knowledge of the profile of the ECRH power and the region where it is deposited. In the present paper, the transport coefficients and ECRH power profile are reconstructed from the solutions to inverse problems by analyzing the transient process after ECR heating is switched on or off. In order to calculate the plasma parameters with this approach, it is necessary to know how the accuracy of the solutions to inverse problems depends on the errors in the input parameters. The accuracy of reconstruction of the ECRH power profile and transport coefficients in model problems is investigated as a function of errors in measuring the electron temperature. The results of this investigation are used to analyze experiments with ECR plasma heating in the T-10 tokamak and to estimate the accuracy of the results obtained. © 2005 Pleiades Publishing, Inc.

1. INTRODUCTION

Investigation of the electron transport in tokamaks is important for understanding the physical processes in tokamak plasmas. Electron transport can be studied experimentally in the steady-state phase of a discharge on the basis of power-balance calculations, in the transient phase after switching on or off the heating source, or during modulated ECR heating [1] (from the analysis of the heat pulse propagation) [2–5]. The method of modulating the input power is usually applied in ECRH experiments.

ECR heating provides a convenient tool for investigating the propagation of temperature perturbations in a plasma. Its advantages over other heating methods are as follows: first, the input power is almost completely deposited in the plasma electrons, and second, the heating region is narrow and its position can be changed by varying the toroidal magnetic field; the latter circumstance makes it possible to carry out experiments with on-axis and off-axis ECR heating.

The analysis of ECRH experiments, however, has its own difficulties, arising from the need to determine the profile of the ECRH power and the region where it is deposited. The ECRH power profile can be found, e.g., from the jump in the derivative of the electron temperature after ECR heating is switched on or off. In this way, the maximum time interval under analysis, Δt, is determined by the inequality $\Delta t < \tau$, where $\tau = 3 w_0^2 / 8 \chi_e$ is the characteristic time, w_0 is the half-width of the ECRH power profile, and χ_e is the local electron heat diffusivity. Consequently, calculating the ECRH power

profile needs special experiments with plasmas at very low level of heat diffusion [2, 6] and also measurements of the electron temperature with high spatial and temporal resolutions. However, because of noises from the plasma and measuring equipment, the derivative of the electron temperature in a short time interval cannot be calculated with sufficient accuracy. As a result, the calculated ECRH power profile is wider than the actual one, which is explained by the spreading of the electron temperature profile due to heat conduction [7].

The ECRH power profile can also be calculated by the ray-tracing method, e.g., using the TORAY computer code [8]. This approach, however, requires a good knowledge of the ECRH power injection geometry and yields an ECRH power profile that corresponds to the ideal case of complete absorption of the input power. Of course, actual experimental conditions may differ from this ideal case in many respects.

Hence, in order for the ECR heating to be extensively used to investigate electron transport in tokamak plasmas, an accurate and thorough analysis of the existing experimental data is necessary. In this context, a promising method is to reconstruct the transport coefficients and ECRH power profile by solving inverse problems [9–13]. Under the assumption that the electron temperature is known at several radial positions and at several instants of time, the transport coefficients and the profile of the heating source power are found from the condition for the discrepancy functional (the normalized difference between the measured and calculated temperature values) to be at minimum. In this approach, the heat transport equations are formulated

for the transient process after ECR heating is switched on or off. The transport coefficients and the profile of the heating source power are reconstructed from the solutions to inverse problems. This method was implemented in the COBRA computer code [9]. Since inverse problems are ill-posed, processing real experiments by the reconstruction method in question implies a special analysis of how the accuracy of the solutions to inverse problems depends on the errors in the input experimental data.

The objective of the present paper is to investigate how the accuracy of reconstruction of the transport coefficients and ECRH power profile by solving inverse problems depends on the errors in measuring the electron temperature.

2. MATHEMATICAL MODEL

We will describe the transient process after switching on ECR heating as follows (the transient process after ECR heating is switched off can be described in a similar way) [12, 13]: We write the heat conduction equations, as well as the boundary and initial conditions, for the electron temperature $T^S(r)$ (with superscript S) corresponding to the steady-state plasma before switching on ECR heating and for the electron temperature $T(r, t)$ (without superscript) corresponding to the transient process after ECR heating is switched on:

$$\frac{3}{2}\frac{\partial}{\partial t}(n^S T^S) = \frac{1}{r}\frac{\partial}{\partial r}\left(rn^S \chi_e^S \frac{\partial T^S}{\partial r}\right)$$
$$-\frac{1}{r}\frac{\partial}{\partial r}(rn^S u_e^S T^S) + P_{OH}^S + Q^S, \quad (1)$$

$$\partial T^s/\partial r(r = 0, t) = 0, \quad T^S(r = 1, t) = T_0,$$

$$\frac{3}{2}\frac{\partial}{\partial t}(nT) = \frac{1}{r}\frac{\partial}{\partial r}\left(rn\chi_e \frac{\partial T}{\partial r}\right) - \frac{1}{r}\frac{\partial}{\partial r}(rnu_e T)$$
$$+ P_{OH} + Q + P_{EC}, \quad (2)$$

$$\partial T/\partial r(r = 0, t) = 0, \quad T(r = 1, t) = T_0, \quad t > t_S,$$

$$T(r, t = t_S) = T^S(r), \quad 0 < r < 1,$$

where r is the dimensionless radius, t_S is the time at which ECR heating is switched on, and T_0 is the electron temperature at the plasma boundary. For the steady-state plasma, the notation is as follows: $n^S(r)$ is the electron density, $T^S(r)$ is the electron temperature, P_{OH}^S is the ohmic heating power, and Q^S is the heat sink term. For the transient process after ECR heating is switched on, the notation is as follows: $n(r, t)$ is the electron density, $T(r, t)$ is the electron temperature, P_{EC} is the ECRH power, P_{OH} is the ohmic heating power, and Q is the heat sink term.

In heat conduction equations (1) and (2), the total heat flux W is assumed to be the sum of the diffusive and convective components:

$$W = -n\chi_e\frac{\partial T}{\partial r} + nu_e T, \quad (3)$$

where χ_e is the electron heat diffusivity and u_e is the heat convection velocity. Hence, Eqs. (1) and (2) can incorporate the convective heat flux $5/2\Gamma_n T_e$, where Γ_n is the particle flux.

In Eqs. (1) and (2), the unknowns are the transport coefficients χ_e^S, u_e^S, χ_e, and u_e and the ECRH power profile P_{EC}. It is possible to formulate an inverse problem of reconstructing all of the four unknowns at once. Such a problem is not easy to solve, however, and the most difficult point is that its solution requires experimental data with very small measurement errors. This is why, in order to formulate and solve the inverse problem of reconstructing the transport coefficients, it is necessary to choose a particular model for each of them and to simplify the basic equations. Note that, for a steady-state plasma, the problem of determining the coefficients χ_e and u_e simultaneously is degenerate: it is possible to find only total flux (3) rather than its diffusive and convective components. It is for this reason that the transport coefficients χ_e and u_e can be determined separately only by analyzing the transient process.

We represent the density $n(r, t)$ and temperature $T(r, t)$ for the transient process as the sums of the steady-state values $n^S(r, t)$ and $T^S(r, t)$ and the variations $\tilde{n}(r, t)$ and $\tilde{T}(r, t)$:

$$n(r, t) = n^S(r) + \tilde{n}(r, t),$$
$$T(r, t) = T^S(r) + \tilde{T}(r, t). \quad (4)$$

After ECR heating is switched on, the power is mainly deposited in the electron plasma component; consequently, the electron temperature changes at a much faster rate than does the electron density. As a consequence, the relative density variation $\tilde{n}$ is much smaller than the relative temperature variation $\tilde{T}$. Here, we are considering the transient process that occur on time scales of 10–20 ms; this allows us to ignore the electron density variations, i.e., to assume that the following relationships are satisfied:

$$\tilde{n}/n^S \ll \tilde{T}/T^S, \quad \tilde{n}/n^S \ll 1, \quad n(r, t) = n^S(r). \quad (5)$$

The transport coefficients χ_e and u_e in Eq. (2) can depend on many local plasma parameters. In our analysis, we restrict ourselves to considering the problem in a simplified formulation [1]. We assume that the electron heat diffusivity χ_e and heat convection velocity u_e

are functions of the local values of the electron density, the electron temperature, and their gradients:

$$\chi_e = \chi_e(n, T, \nabla n, \nabla T), \quad u_e = u_e(n, T, \nabla n, \nabla T). \quad (6)$$

In order to describe transient process, we expand the transport coefficients χ_e and u_e in the increments in the independent variables T and ∇T in the vicinities of the steady-state values of the density n^S and temperature T^S. We also ignore the terms of the second order in the temperature variations $\tilde{T}$ and $\nabla \tilde{T}$:

$$\begin{aligned}
\chi_e &\approx \chi_e^S + (\partial \chi_e / \partial T)^S \tilde{T} + (\partial \chi_e / \partial \nabla T)^S \nabla \tilde{T}, \\
u_e &\approx u_e^S + (\partial u_e / \partial T)^S \tilde{T} + (\partial u_e / \partial \nabla T)^S \nabla \tilde{T}.
\end{aligned} \quad (7)$$

Analogously, we expand the ohmic heating power P_{OH} and heat sinks Q in the vicinity of their steady state values P_{OH}^S and Q^S and ignore the corresponding second-order terms. In Eqs. (1) and (2), the ohmic heating terms, P_{OH}^S and P_{OH}, and the heat sink terms, Q^S and Q, are given by the standard formulas [13]

$$\begin{aligned}
P_{OH} - P_{OH}^S &\approx (\partial P_{OH} / \partial T)^S \tilde{T}, \\
Q - Q^S &\approx (\partial Q / \partial T)^S \tilde{T}.
\end{aligned} \quad (8)$$

Subtracting Eq. (1) from Eq. (2) and using formulas (7) and (8), we arrive at the following linearized equation for the electron temperature variation $\tilde{T}(r, t)$:

$$\frac{3}{2}\frac{\partial}{\partial t}(n^S \tilde{T}) = \frac{1}{r}\frac{\partial}{\partial r}\left(rK\frac{\partial \tilde{T}}{\partial r}\right) - \frac{1}{r}\frac{\partial}{\partial r}(rV\tilde{T}) + P_{EC}$$

$$+ [(\partial P_{OH}/\partial T)^S + (\partial Q/\partial T)^S]\tilde{T}, \quad (9)$$

$$\partial \tilde{T}/\partial r(r = 0, r) = 0, \quad \tilde{T}(r = 1, t) = 0, \quad t > t_S,$$

$$\tilde{T}(r, t_S) = 0, \quad 0 < r < 1.$$

Here, the following notation is introduced:

$$\begin{aligned}
K &= n^S[\chi_e^S + (\partial \chi_e/\partial \nabla T)^S \nabla T^S + (\partial u_e/\partial \nabla T)^S T^S], \\
V &= n^S[u_e^S + (\partial u_e/\partial T)^S T^S + (\partial \chi_e/\partial T)^S \nabla T^S].
\end{aligned} \quad (10)$$

Equation (9) and relationships (10) have the following properties [1]:

(i) Transport coefficients (10) in the transient process differ from the coefficients χ_e^S and u_e^S in the steady state.

(ii) If the coefficient χ_e is a function of the electron temperature T only, then linearized equation (9) always contains the convective term, even when the convective heat flux does not enter ($u_e^S \equiv 0$) into basic equations (1) and (2).

(iii) The coefficients K and V in linearized equation (9) are time-independent and are functions only of the steady-state plasma parameters; i.e., they are determined only by the density and temperature distributions.

3. FORMULATION OF THE INVERSE PROBLEM AND NUMERICAL ALGORITHM FOR SOLVING IT

Here, we formulate the inverse problems of reconstructing the transport coefficients and ECRH power profile for the problem given by Eqs. (9) with transport coefficients (10). Let the transient process after ECR heating is switched on or off be described by Eqs. (9) with time-independent coefficients K and V. The known parameters are assumed to be the electron temperature variations f_i^k measured experimentally at N radial positions $r_i (i = 1, \dots, N)$ at M times $t_k (k = 1, \dots, M)$ and some of the global plasma parameters, namely, the major and minor plasma radii, the total plasma current, the ohmic heating power, and the ECRH power.

We begin by writing the discrepancy functional

$$J = \frac{1}{2}\sum_{k=1}^{M}\sum_{i=1}^{N}\gamma_i[\tilde{T}(r_i, t_k) - f_i^k]^2 / \sum_{k=1}^{M}\sum_{i=1}^{N}\gamma_i[f_i^k]^2, \quad (11)$$

where the weighting factors γ_i are to be chosen in accordance with the reliability of information from each of the measurement channels.

The inverse problem (problem I) is formulated as follows. It is necessary to determine such profiles of the ECRH power $P_{EC}(r)$, heat diffusivity $K(r)$, and heat convection velocity $V(r)$ with which the solution $\tilde{T}(r, t)$ to heat conduction equation (9) minimizes discrepancy functional (11).

The method for solving problem I assumes a parametric representation of the sought functions. We expand the unknown functions $K(r)$, $V(r)$, and $P_{EC}(r)$ in certain basis polynomial functions [13, 14]:

$$K(r) = \sum_{j=1}^{M_K} k_j \varphi_j(r), \quad V(r) = \sum_{j=1}^{M_V} v_j \psi_j(r), \quad (12)$$

$$P_{EC}(r) = A\exp[-((r - r_0)/w)^\alpha].$$

Here, $\varphi_j, \psi_j = \{1, r, r^2, r^3, \dots\}$ are polynomials; r_0 is the position of the center of the ECRH power profile; w is its half-width; and the constants A and α determine the magnitude and profile of the ECRH power.

Hence, the solution of problem I reduces to the determination of the vector of the unknown parameters

$$\mathbf{P} \quad (13)$$
$$= \{k_j(j = 1, \dots, M_K), v_j(j = 1, \dots, M_V), A, r_0, w, \alpha\}$$

from the condition that discrepancy functional (11) be at minimum.

Problem I is solved by the method of iterative regularization [14], which consists of the following steps:

(i) the initial vector $\mathbf{P}^s$ ($s = 1$) of the sought parameters is specified and Eq. (9) is solved,

(ii) the gradient ∇J^s of discrepancy functional (11) and the descent depth vector $\mathbf{h}^s$ are calculated, and

(iii) a new approximation for the sought parameters is determined from the relationship $P_i^{s+1} = P_i^s + h_i^s \partial J^s / \partial P_i$.

Iteration procedure (i)–(iii) minimizes discrepancy functional (11), thereby giving the desired solution to problem I.

One of the difficulties in solving inverse problem I is that of choosing the basis polynomial functions and parameters M_K and M_V in expansion (12). To overcome this difficulty, it is necessary to refer to additional experimental information. For instance, the ECRH power profile is chosen by taking into account the fact that independent computations with the TORAY code [8] yield a nearly Gaussian profile of the deposited ECRH power. In such circumstances, it remains to find the profile parameters $\{r_0, w, \alpha\}$.

The choice of the values of the parameters M_K and M_V is motivated by the following considerations: From experiments and from numerical simulations of the transient process after switching off ECR heating, it is known that the heat flux W (see Eq. (3)) is a smooth function of both radius and time. Consequently, in order to describe the evolution of the heat flux by means of expansion (12), it is sufficient to set $M_K = 3$–4 (the basis polynomials being $\{1, r, r^2, r^3\}$) and $M_V = 2$–3 (the basis polynomials being $\{r, r^2, r^3\}$). Accounting for a larger number of terms in expression (12) only slightly increases the accuracy of reconstruction of the heat flux but make the solution of the inverse problem less stable because of the errors in the input experimental data.

Note that one of the aims of our numerical analysis of model experiments is just the proper choice of the values of the parameters M_K and M_V with which to process real experimental data.

4. NUMERICAL INVESTIGATION OF THE ACCURACY OF RECONSTRUCTION OF THE TRANSPORT COEFFICIENTS AND ECRH POWER PROFILE

Since inverse problem I is ill-posed, its solution depends on the errors in the input parameters. Consequently, it is necessary to investigate how the accuracy of reconstruction of the transport coefficients and ECRH power profile depends on the errors in measuring the electron temperature. This will be done by analyzing the numerical results of a "quasi-real" experiment.

The quasi-real experiment consists in the following steps:

(i) The problem given by Eqs. (9) with transport coefficients (10) is solved within the time interval $\Delta t = 10$ ms for given profiles of the transport coefficients $K(r)$ and $V(r)$ and for a given ECRH power profile $P_{EC}(r)$. The result is the temperature distribution $\tilde{T}(r, t)$.

(ii) The solution $\tilde{T}(r, t)$ for each of the measurement channels ($i = \overline{1, N}$) is randomly perturbed in the absolute value, the perturbation amplitude δ at M time points being distributed according to a normal law. The result is the perturbed data $\tilde{T}^p(r_i, t_j)$, ($i = \overline{1, N}$, $j = \overline{1, M}$).

(iii) Inverse problem I is solved with the perturbed data $\tilde{T}^p(r_i, t_j)$ as the input parameters. The result is the profiles of the transport coefficients, $\chi_e^p(r) = K^p(r)/n^S(r)$ and $u_e^p(r) = V^p(r)/n^S(r)$, and the ECRH power profile $P_{EC}^p(r)$.

(iv) Steps (ii) and (iii) are repeated 10–20 times. From the resulting sequences of parameter values $\{\chi_{e,n}^p\}$, $\{u_{e,n}^p\}$, $\{P_{EC,n}^p\}$ the following statistical quantities are calculated:

(a) the mathematical expectation

$$\bar{\xi} = M(\xi) = 1/N \sum_{n=1}^{N} \xi_n; \tag{14}$$

(b) the relative deviation

$$\Delta = (P - M)/P, \tag{15}$$

where P is the exact value;

(c) the dispersion

$$\bar{\sigma} = \sqrt{M((\xi - \bar{\xi})^2)}; \tag{16}$$

and

(d) the relative dispersion

$$\sigma = \bar{\sigma}/|M|. \tag{17}$$

Hence, for a series of N calculations, the mathematical expectation $\bar{\xi}$ characterizes the mean value of the quantity being reconstructed, the relative deviation Δ characterizes the accuracy with which the quantity $\bar{\xi}$ is calculated, the dispersion $\bar{\sigma}$ gives the mean error in one particular calculation, and the relative dispersion σ characterizes this error in percentage.

In model problem II, the transient process after switching on ECR heating is described by Eqs. (9) with transport coefficients (10). The perturbed heat flux $\tilde{W}$
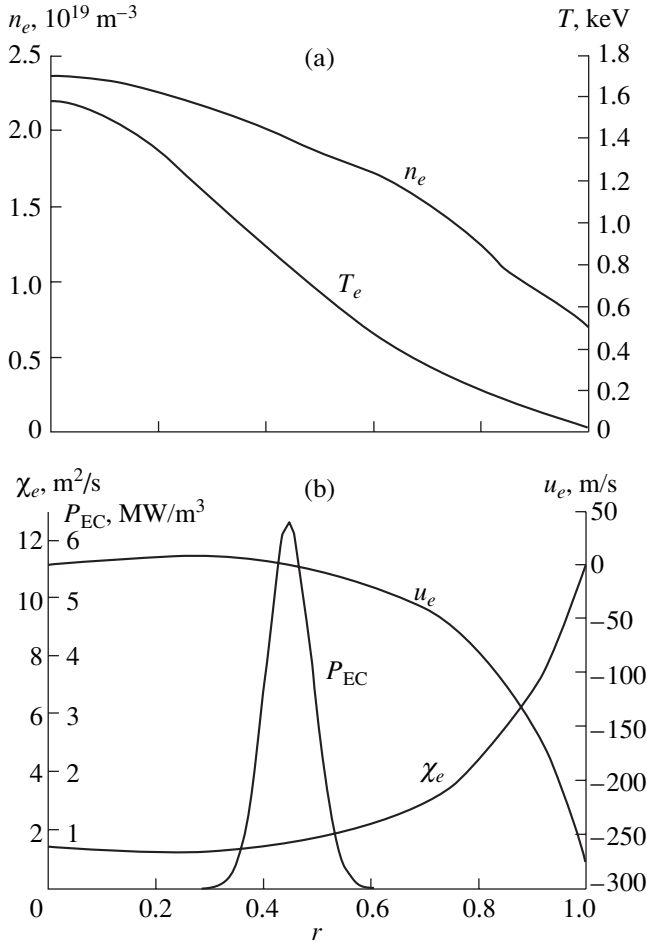
Fig. 1. (a) Steady-state profiles of the electron temperature $T^S(r)$ and electron density $n^S(r)$ before switching on ECR heating and (b) the corresponding electron heat diffusivity $\chi_e(r)$, heat convection velocity $u_e(r)$, and ECRH power profile $P_{EC}(r)$ for model problem II.
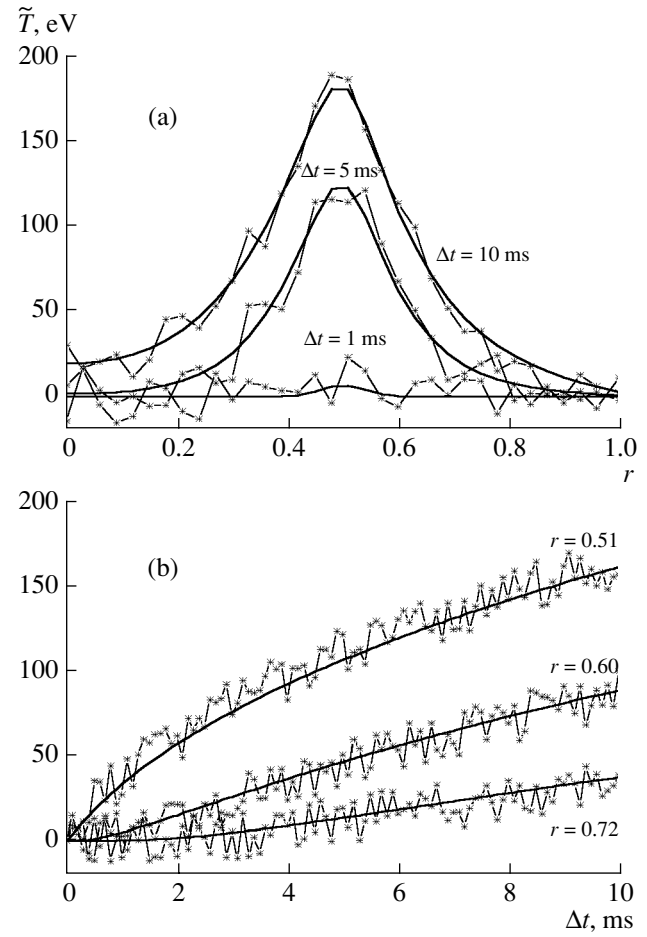

Fig. 2. (a) Radial profiles of the electron temperature at three different times and (b) time evolution of the electron temperature at three different radial positions after switching on ECR heating: the solid curves are the solutions to model problem II and the symbols are the perturbed input parameters for inverse problem I, the absolute error from each measurement channel being $\delta = 30$ eV.

is represented as a sum of the diffusive and convective components:

$$\tilde{W} = -K\frac{\partial \tilde{T}}{\partial r} + V\tilde{T}, \qquad (18)$$

where the profiles of the transport coefficients $K(r)$ and $V(r)$ and the ECRH power profile $P_{EC}(r)$ are specified as

$$K(r) = a_1 + a_2 r + a_3 r^2,$$

$$a_1 = 2.433 \ [\text{m}^{-1} \ \text{s}^{-1}], \quad a_2 = -5.273 \ [\text{m}^{-1} \ \text{s}^{-1}],$$

$$a_3 = 5.608 \ [\text{m}^{-1} \ \text{s}^{-1}], \quad V(r) = b_1 r + b_2 r^2, \qquad (19)$$

$$b_1 = 157.5 \ [\text{m}^{-1} \ \text{s}^{-1}], \quad b_2 = -350 \ [\text{m}^{-2} \ \text{s}^{-1}],$$

$$P_{EC}(r) = A\exp[-((r - r_0)/w)^2],$$

$r_0 = 0.45$, $w = 0.04$ m, the total ECRH power being $P_{EC} = 0.4$ MW.

For model problem II, the transport coefficients and ECRH power profile were chosen to fit the real experimental data.

Figure 1a shows the steady-state profiles of the electron temperature $T^S(r)$ and electron density $n^S(r)$ before switching on ECR heating for model problem II.

Figure 1b shows the profiles of the electron heat diffusivity $\chi_e(r)$, heat convection velocity $u_e(r)$, and ECRH power $P_{EC}(r)$ for model problem II.

Figure 2a shows the radial electron temperature profiles $\tilde{T}(r, t)$ calculated for several different times after switching on ECR heating.

Figure 2b shows the time evolution of the electron temperature obtained from several measurement channels after switching on ECR heating.

The solid curves in Figs. 2a and 2b show the solution to model problem II, and the symbols correspond

Table 1

Δ/δ	20 eV	30 eV	40 eV	σ/δ	20 eV	30 eV	40 eV
$(\Delta\chi_e)_{min}$	−1%	−2.5%	−3.5%	$(\sigma\chi_e)_{min}$	2%	2%	3%
$(\Delta\chi_e)_{max}$	4%	5.5%	12%	$(\sigma\chi_e)_{max}$	17%	18%	23%
Δw	0.5%	7%	8.5%	σw	8%	11%	15%
Δr_0	0.1%	0.01%	0.02%	σr_0	0.2%	0.2%	0.3%

to the "experimental" temperature for inverse problem I. The absolute error from each measurement channel is $\delta = 30$ eV. From the figures, we see that variations in the electron temperature in the ECR heating region amount to about 200 eV. This indicates that the relative error from the measurements channels in the ECR heating region is about 10–15%.

Note that the solutions to inverse problem I that will be presented below were obtained by using the data from 34 measurement channels ($N = 34$), i.e., from measurements of the electron temperature at 34 different radial positions and from 100 time points for each of the measurement channels ($M = 100$). In fact, the number of channels for positional measurements over the radius is determined by the half-width w of the ECRH power profile, which is usually equal to 2–4 cm. Accordingly, the required accuracy of reconstruction of the ECRH power profile can be achieved with measurement channels separated by a distance of about 1 cm (i.e., the ECRH power profile is reconstructed from measurements made at five to eight different radial positions). For the T-10 tokamak (with a minor radius of $a = 30$ cm), $N = 34$ measurement channels ensure the required spatial resolution (of about 1 cm).

The accuracy of reconstruction of the transport coefficients and ECRH power profile was investigated in terms of the two main problems.

Problem 1. Investigation of the accuracy of reconstruction of the transport coefficients and ECRH power profile as a function of errors in measuring the electron temperature for the known structure of the heat flux $\tilde{W}$ (18).

Problem 2. Investigation of the accuracy of reconstruction of the structure of the heat flux $\tilde{W}$ (18) as a function of errors in measuring the electron temperature, i.e., the accuracy of reconstruction of the diffusive and convective components of the perturbed heat flux.

5. ANALYSIS OF THE ACCURACY OF RECONSTRUCTION OF THE TRANSPORT COEFFICIENTS AND ECRH POWER PROFILE

5.1. Heat Flux $\tilde{W}$ with the Diffusive Component Only

Let the heat flux $\tilde{W}$ in model problem II have only the diffusive component. The objective of this section is to analyze how the accuracy of reconstruction of the

electron heat diffusivity and ECRH power profiles, $\chi_e(r)$ and $P_{EC}(r)$, depends on the absolute error δ in measuring the electron temperature.

Inverse problem I was solved under the assumption that the heat flux $\tilde{W}$ had the diffusive component only, i.e., $V \equiv 0$. The coefficient K was expanded in the basis polynomials $\{1, r, r^2\}$.

Figure 3 shows the relative deviations Δ (15) and relative dispersions σ (17) for the electron heat diffusivity χ_e, the central radial position r_0 of the ECR heating region, and the half-width w of the ECRH power profile for different values of the error in the input data: $\delta = 20$, 30, and 40 eV. The results of the relevant numerical analysis are summarized in Table 1.

Note that the central radial position r_0 of the ECR heating region is reconstructed with high accuracy, which is explained by the use of measurement data from many radial positions.

5.2. Heat Flux $\tilde{W}$ with Both the Diffusive and Convective Components

Let the heat flux $\tilde{W}$ in model problem II have both the diffusive and convective components. The objective of this section is to analyze how the accuracy of reconstruction of the profiles of the transport coefficients $\chi_e(r)$ and $u_e(r)$, as well as of the ECRH power profile $P_{EC}(r)$, depends on the absolute error δ in measuring the electron temperature.

Inverse problem I was solved under the assumption that the heat flux $\tilde{W}$ had both the diffusive and convective components. The coefficients K and V were expanded, respectively, in the basis polynomials $\{1, r, r^2\}$ and $\{r, r^2\}$. The results of the relevant numerical analysis are summarized in Table 2.

As compared to the results of Section 5.1, the accuracy of reconstruction is lower. Accordingly, in order to increase the accuracy of reconstruction of the transport coefficients, it is necessary to use more precise input data. Note that the accuracy of reconstruction of the parameter r_0 remains high ($\Delta r_0 \leq 0.2\%$, $\sigma r_0 \leq 0.4\%$) and is essentially independent of the error δ in the input data.
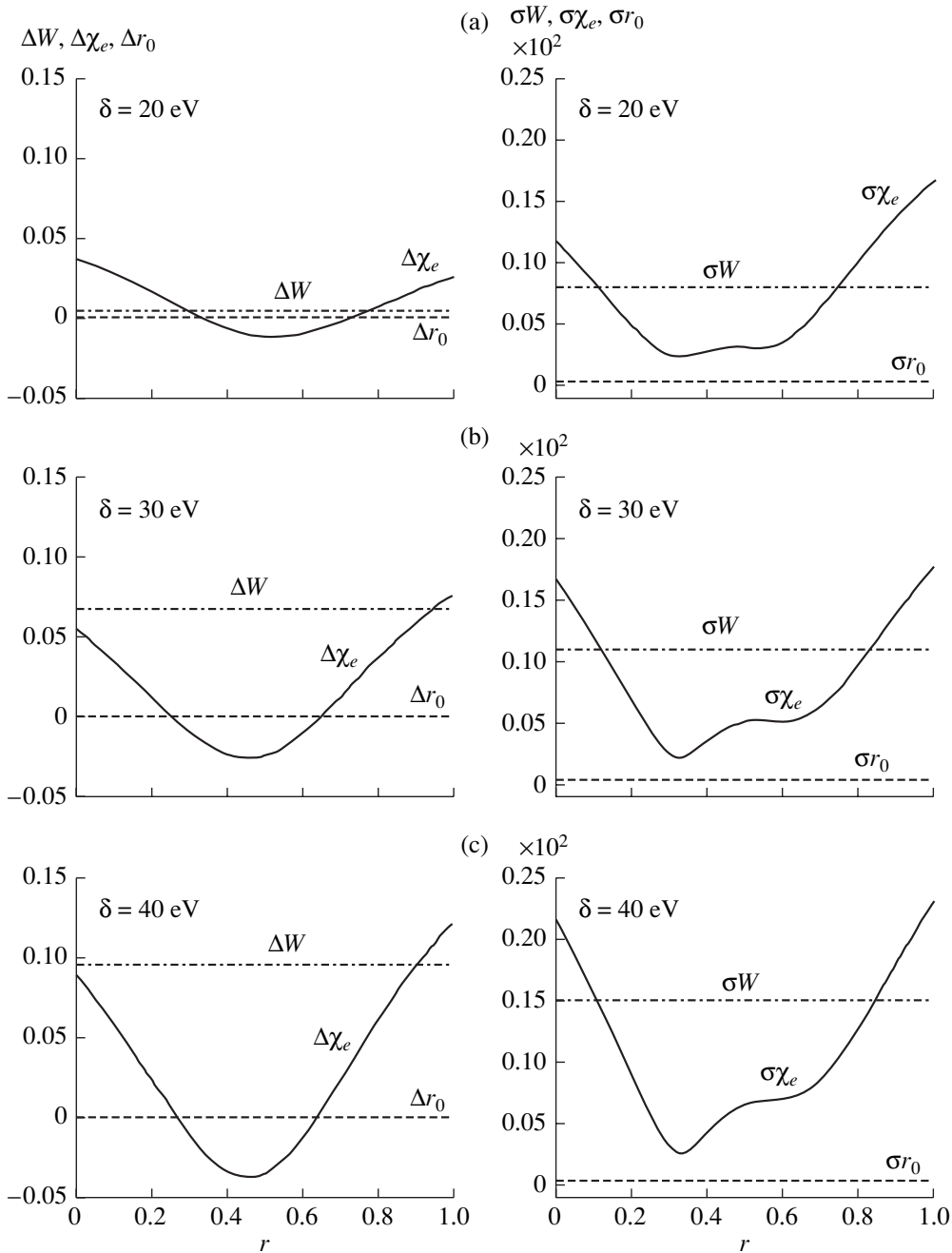
Fig. 3. Relative deviation Δ (15) and relative dispersion σ (17) of the electron heat diffusivity χ_e, the central radial position r_0 of the ECR heating region, and the half-width w of the ECRH power profile for different values of the error in the input data for the problem solved in Section 5.1: δ = (a) 20, (b) 30, and (c) 40 eV.

6. ANALYSIS OF THE ACCURACY OF RECONSTRUCTION OF THE HEAT FLUX STRUCTURE

6.1. Heat Flux $\tilde{W}$ with the Diffusive Component Only

Let the heat flux $\tilde{W}$ in model problem II have only the diffusive component. The objective of this section is to determine the error δ in measuring the electron temperature with which it is still possible to obtain from the

solution to inverse problem I a definite answer to the question of whether the heat flux $\tilde{W}$ has no convective component.

Inverse problem I was solved under the assumption that the heat flux $\tilde{W}$ had both the diffusive and convective components. The coefficients K and V were expanded, respectively, in the basis polynomials $\{1, r, r^2\}$ and $\{r, r^2\}$.

Table 2

Δ/δ	10 eV	20 eV	30 eV	σ/Δ	10 eV	20 eV	30 eV
$(\Delta\chi_e)_{min}$	2%	10%	13%	$(\sigma\chi_e)_{min}$	3%	6%	9%
$(\Delta\chi_e)_{max}$	7%	15%	22%	$(\sigma\chi_e)_{max}$	13%	25%	33%
$(\Delta u_e)_{min}$	2%	8%	11%	$(\sigma u_e)_{min}$	5%	11%	16%
$(\Delta u_e)_{max}$	8%	19%	35%	$(\sigma u_e)_{max}$	14%	31%	42%
Δw	–3%	–9%	–19%	σw	3%	6%	8%
Δr_0	0.01%	0.1%	0.2%	σr_0	0.2%	0.3%	0.4%

Figure 4 shows the diffusive, $\tilde{W}_{diff} = -K\partial\tilde{T}/\partial r$, and convective, $\tilde{W}_{conv} = V\tilde{T}$, components of the heat flux $\tilde{W}$ at the time $\Delta t = 10$ ms (corresponding to the full run time of the code), calculated from the solution to inverse problem I for two different values of the error in the input data.
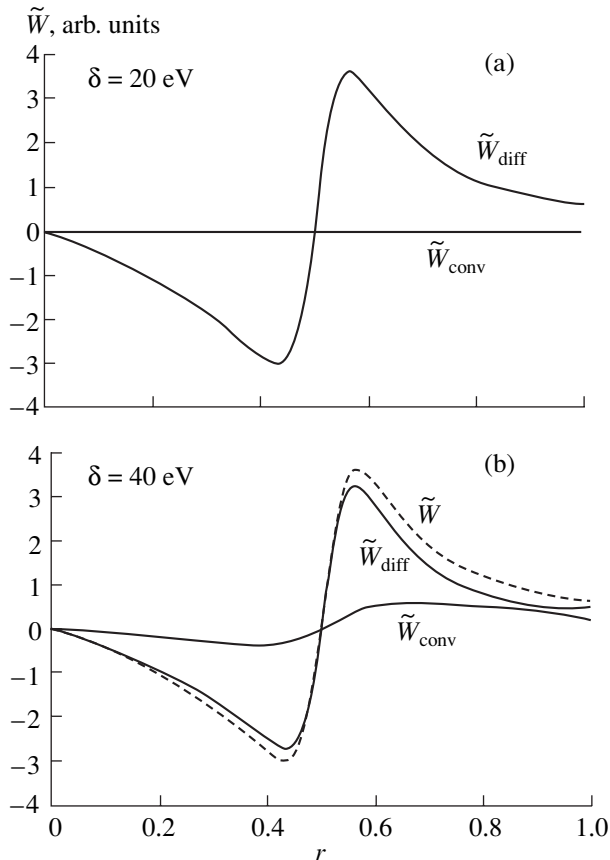

Fig. 4. Diffusive, $\tilde{W}_{diff} = -K\partial\tilde{T}/\partial r$, and convective, $\tilde{W}_{conv} = V\tilde{T}$, components of the heat flux $\tilde{W}$ at the time $\Delta t = 10$ ms (corresponding to the full run time of the code) from the solution to inverse problem I for different values of the error in the input data: δ = (a) 20 and (b) 40 eV. The dashed curve is the exact profile of the heat flux $\tilde{W}$ in model problem II.

When the error in the input data is $\delta = 20$ eV, the heat flux $\tilde{W}$ obtained by solving problem I differs from the exact one by 2% on average; in this case, the convective component of the heat flux $\tilde{W}$ is only about 0.5%. These results make it possible to unambiguously conclude that the heat flux in model problem II is purely diffusive.

The larger the error δ, the larger the fictitious convective component $\tilde{W}_{conv}$ in the heat flux $\tilde{W}$. For $\delta = 40$ eV, the heat flux obtained by solving the inverse problem differs from the exact one by 8% on average; in this case, however, the convective component of the heat flux is as great as 24%. This indicates that the heat flux structure calculated from the solution to inverse problem I differs strongly from the original structure.

Hence, when the error δ in the input data exceeds 30 eV, the solution to inverse problem I does not give a precise answer to the question of whether or not the heat flux in model problem II has the convective component.

6.2. Heat Flux $\tilde{W}$ with Both the Diffusive and Convective Components

Let the heat flux $\tilde{W}$ in model problem II have both the diffusive and convective components. The objective of this section is to determine the error δ in measuring the electron temperature with which it is possible to obtain from the solution to inverse problem I a definite answer to the question of whether the heat flux $\tilde{W}$ has both the diffusive and convective components.

Problem I was solved under the assumption that the heat flux $\tilde{W}$ had the diffusive component only, i.e., $V = 0$. The coefficient K was expanded in the polynomials $\{1, r, r^2\}$. The results of the relevant numerical analysis are summarized in Table 3.

An important point to note is that solving problem I yields small dispersions of the values of χ_e and of w, namely, $\sigma\chi_e < 8\%$ and $\sigma w = 3\%$, which are much less than the exact ones, $29\% < \Delta\chi_e < 71\%$ and $\Delta w = 98\%$. Moreover, the resulting solution depends weakly on the error δ in the input data.

Table 3

Δ/δ	10 eV	20 eV	30 eV	σ/δ	10 eV	20 eV	30 eV
$(\Delta\chi_e)_{min}$	28%	29%	30%	$(\sigma\chi_e)_{min}$	0.3%	0.5%	1%
$(\Delta\chi_e)_{max}$	71%	71%	71%	$(\sigma\chi_e)_{max}$	3%	6%	8%
Δw	98%	98%	99%	σw	1%	2%	3%
Δr_0	0.01%	0.02%	0.05%	σr_0	0.01%	0.06%	0.1%

Hence, in Sections 5.2 and 6.2, we have obtained two different solutions for the same input data. This is a consequence of the fact that inverse problem I is ill-posed: because of the errors in experimental data, it admits two solutions having different physical properties. One of the solutions contains the convective heat flux, and the other does not. In order to decide which of the solutions is physically reasonable, we compare discrepancy functionals (11) for the cases studied in Sections 5.2 and 6.2.

When the error in the input data is $\delta = 10$ eV, the averaged values of the discrepancy functionals differ by 54% ($\bar{J} = 8.95 \times 10^{-4}$ for the case of Section 5.2 and $\bar{J} = 1.38 \times 10^{-3}$ for the case of Section 6.2). With these results, a comparison between the discrepancy functionals enables us to unambiguously conclude that the correct solution is that obtained in Section 5.2; i.e., the heat flux $\tilde{W}$ has the convective component.

When the error in the input data is $\delta = 30$ eV, the averaged values of the discrepancy functionals differ by 5.4% ($\bar{J} = 8.18 \times 10^{-3}$ for the case of Section 6.2 and $\bar{J} = 7.80 \times 10^{-3}$ for the case of Section 5.2).

This indicates that discrepancy functional (11) has two maxima, corresponding to two different solutions. In order to choose the correct solution, it is necessary to refer to additional experimental information, e.g., to specify the parameters of the ECRH power profile.

Since, in Sections 5.2 and 6.2, the parameter r_0 is reconstructed with high accuracy while the error in reconstructing the parameter w is large, additional information should to be involved in such a way as to specify the half-width of the ECRH power profile. When the parameter w is fixed ($w = 4$ cm), the average values of the discrepancy functionals for the measurement error $\delta = 30$ eV differ by 21% ($\bar{J} = 9.49 \times 10^{-3}$ for the case of Section 6.2 and $\bar{J} = 7.80 \times 10^{-3}$ for the case of Section 5.2). Hence, if the half-width of the ECRH power profile is known (is determined from, e.g., the TORAY code [8]), then, for measurement errors of $\delta < 30$ eV, the solution to inverse problem I leads to an unambiguous conclusion that the heat flux $\tilde{W}$ has both the diffusive and convective components.

7. DEPENDENCE OF THE ACCURACY OF RECONSTRUCTION OF THE TRANSPORT COEFFICIENTS AND ECRH POWER PROFILE ON THE ERROR IN THE INITIAL CONDITIONS

The ECRH power profile can be reconstructed from the jump in the time derivative of the electron temperature at the time at which ECR heating is switched on or off [7]. The results of calculating this derivative, however, are sensitive to errors in specifying the steady-state electron temperature before switching on or off ECR heating. The objective of this section is to investigate how the accuracy of reconstruction of the transport coefficients and ECRH power profile depends on the error in specifying the steady-state electron temperature.

Numerical investigations were carried out by using the following algorithm: For given profiles of the electron heat diffusivity $\chi_e(r)$ and ECRH power $P_{EC}(r)$, model problem II was solved and the distribution $\tilde{T}(r, t)$ was determined. The total temperature $T(r, t)$ before switching on ECR heating (at $t < t_S$) was then equal to $T(r, t) = T^S(r)$; after switching on ECR heating (at $t > t_S$), it was equal to $T(r, t) = T^S(r) + \tilde{T}(r, t)$. For both $t < t_S$ and $t > t_S$, the temperature $T(r, t)$ for each measurement channel was perturbed with the error $\delta = 20$ eV. The steady-state temperature profile $T_p^S(r)$ for each measurement channel was smoothed over the time intervals $\delta t = 1, 2,$ and 4 ms (which corresponded to 11, 21, and 41 time points) to obtain the profiles $\bar{T}_p^S(r)$. For each of the smoothed temperature profiles $\bar{T}_p^S(r)$, the temperature variations $\tilde{T}^p(r, t) = T^p(r, t) - \bar{T}_p^S(r)$ were calculated and were then used as input experimental data. Inverse problem I was solved under the assumption that the heat flux $\tilde{W}$ had the diffusive component only, i.e., that $V = 0$. The coefficient K was expanded in the $\{1, r, r^2\}$ polynomials. The results of the relevant numerical analysis are summarized in Table 4.

Hence, with the steady-state temperature profile $T^S(r)$ being smoothed beforehand, it is possible to substantially increase the accuracy of reconstruction of the electron heat diffusivity χ_e and ECRH power profile $P_{EC}(r)$ for the fixed error $\delta = 20$ eV in the input data.

Table 4

Smoothing	0	1 ms	4 ms	Smoothing	0	1 ms	4 ms
$(\Delta\chi_e)_{min}$	–8%	–1%	–1%	$(\sigma\chi_e)_{min}$	7%	2%	1%
$(\Delta\chi_e)_{max}$	29%	3%	0.5%	$(\sigma\chi_e)_{max}$	76%	17%	10%
Δw	14%	0.2%	0.7%	σw	36%	8%	4%
Δr_0	0.2%	0.07%	0.04%	σr_0	0.4%	0.2%	0.1%

8. ANALYSIS OF T-10 EXPERIMENTS WITH SWITCHING-OFF OF ECR HEATING

In this section, we present the results of analyzing a series of experiments carried out in the T-10 tokamak (with the major radius $R = 150$ cm and the minor radius $a = 30$ cm). In those experiments, off-axis ECR heating was provided by two gyrotrons, each operating with a power of about 300 kW at a frequency of 140 GHz (X-mode, the second harmonic of the electron gyrofrequency).
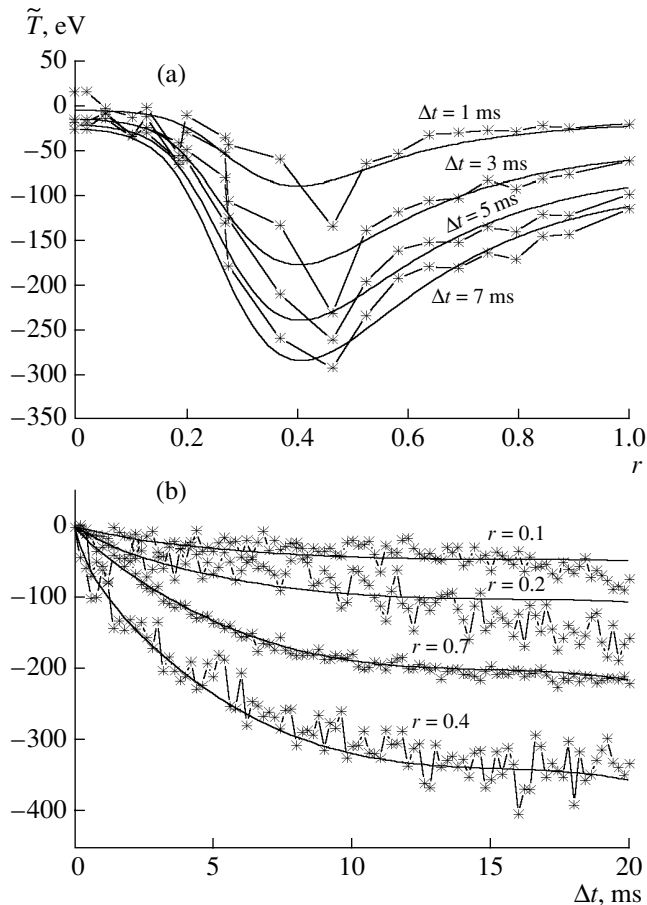
Fig. 5. (a) Radial profiles of the electron temperature at different times and (b) time evolution of the electron temperature at different radial positions after switching off ECR heating in T-10 shot no. 32917: the solid curves are the solutions to inverse problem I and the symbols are the experimental data.

In solving inverse problem I, the electron heat diffusivity $K(r)$ and heat convection velocity $V(r)$ were expanded, respectively, in the polynomials $\{1, r, r^2\}$ and $\{r, r^2, r^3\}$. The task was to reconstruct the parameter r_0 for a fixed total input power, $P_{EC} = 600$ kW, and a fixed half-width of the ECRH power profile, $w = 0.02$ m. That the profile half-width w should be fixed in solving inverse problem I stems from the fact that the electron temperature was determined from only 18 measurement channels, separated over the radius by a distance of about 2.5 cm. This value of w was chosen according to calculations with the TORAY code [8]. The results of examining the transient process after off-axis ECR heating was switched off are illustrated in Figs. 5–7 for a series of 14 T-10 shots.

Figures 5a and 5b show the radial profiles and time evolution of the electron temperature $\tilde{T}(r, t)$ after switching off ECR heating for one of the discharges under analysis (shot no. 32917). The symbols in the figures are the experimental data, and the solid curves are the solutions to inverse problem I.

Figures 6a and 6b show the radial profiles of the electron heat diffusivity $\chi_e(r)$ and heat convection velocity $u_e(r)$ calculated from the solution to inverse problem I for all 14 shots.

Figure 7 shows the averaged values $\bar{\xi}$ (14) (solid curves) and the dispersions $\bar{\sigma}$ (16) (dashed curves) of the electron heat diffusivity $\chi_e(r)$ (Fig. 7a) and heat convection velocity $u_e(r)$ (Fig. 7b) calculated for all 14 shots.

Note that inverse problem I was solved for two types of heat flux structure $\tilde{W}$ (18). In one type, the heat flux $\tilde{W}$ had both the diffusive and convective components; in the second type, the heat flux $\tilde{W}$ had the diffusive component only. Calculations show that, for the first case, the averaged value of the discrepancy functional is 10% less than that for the second case. This enables us to conclude that the heat flux has both the diffusive and convective components.

Let us now compare the results obtained in this section by processing the real experiments with those obtained in Sections 5 and 6 from the model calculations. The experimental errors in measuring the electron temperature at different radial positions (channels) are in the range from $\delta = 20$ eV to $\delta = 50$ eV (see
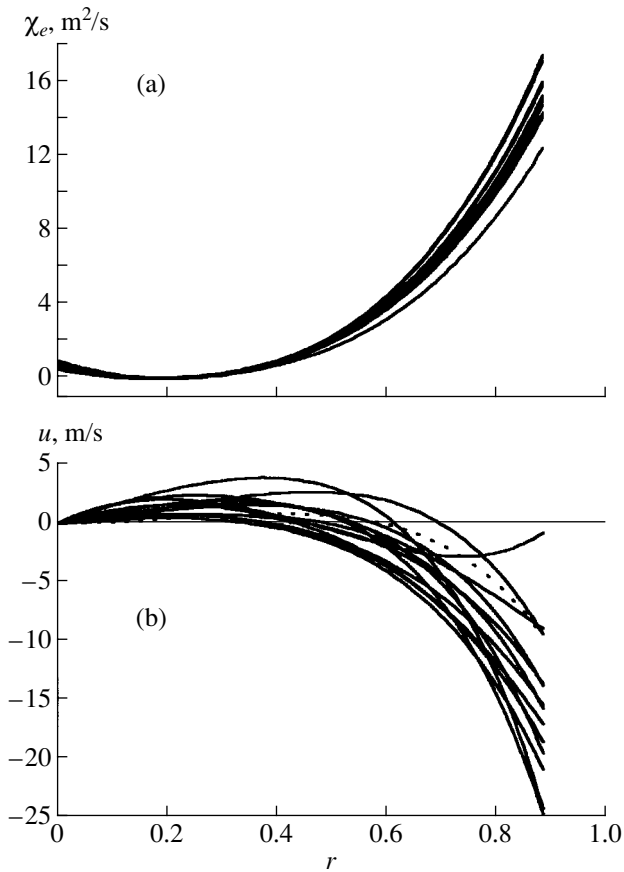
Fig. 6. Radial profiles of (a) the electron heat diffusivity $\chi_e(r)$ and (b) heat convection velocity $u_e(r)$ calculated from the solution to inverse problem I for 14 T-10 shots.
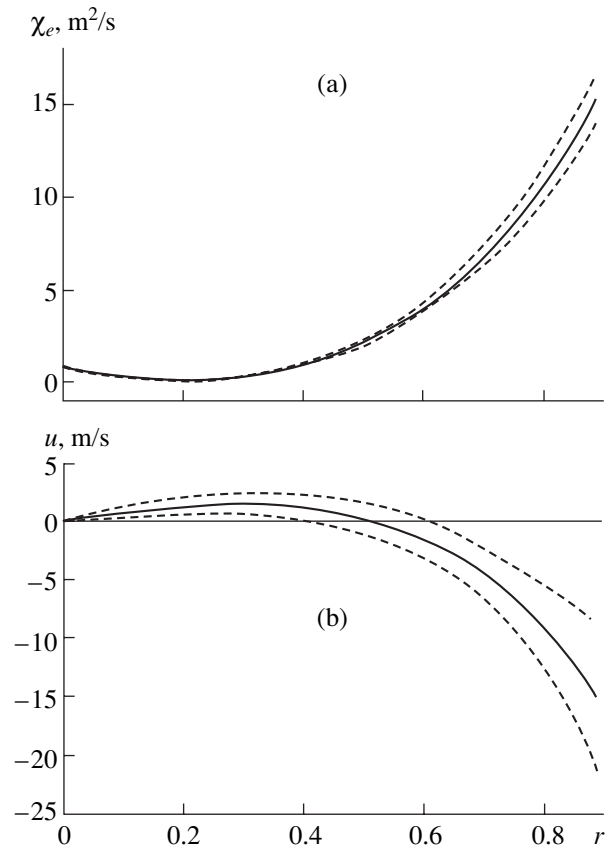

Fig. 7. Average value (solid curves) and dispersion (dashed curves) of (a) the electron heat diffusivity $\chi_e(r)$ and (b) the heat convection velocity $u_e(r)$ calculated for 14 T-10 shots.

Figs. 6a, 6b), which is consistent with the range of measurement errors considered in the model calculations, namely, that from $\delta = 10$ eV to $\delta = 40$ eV for each of the measurement channels. Note that the central radial position r_0 of the ECR heating region is reconstructed with very high accuracy: the relative dispersion is $\sigma r_0 = 1\%$, which correlates well with the results of model calculations (see Table 2). The relative dispersion for the electron heat diffusivity χ_e is in the range $7\% < \sigma\chi_e < 26\%$, which also agrees well with the range $9\% < \sigma\chi_e < 33\%$ obtained in model calculations (see Section 6.1). The relative dispersion for the heat convection velocity u_e is $39\% < \sigma u_e < 80\%$, which is approximately twice as large as the relative dispersion $16\% < \sigma u_e < 42\%$ found in model calculations (see Section 5.2). This discrepancy can be explained as being due to the larger errors in measuring the electron temperature in comparison to those used for the model problem and also due to the smaller number of measurement channels.

Hence, a comparison of the results of processing the real experiments (a series of 14 T-10 shots) to the results of model calculations shows that they are in good agreement. This indicates that the results of our investigations can be used to estimate the accuracy of

reconstruction of transport coefficients in analyzing the real experiments. In this way, we can use the results of model experiments (see Table 2) to arrive at the following estimates. The electron heat diffusivity χ_e (Fig. 7a) is reconstructed with an accuracy of about 13–22%, the accuracy of reconstruction of the heat convection velocity u_e is about 22–55%, and the accuracy of reconstruction of the radial position r_0 of the region where the ECRH power is deposited is about 1%.

9. CONCLUSIONS

Based on the results of our numerical investigations, we can draw the following conclusions about the accuracy of reconstruction of the transport coefficients and ECRH power profile from the solutions to inverse problems.

(i) We have shown that, in order to reconstruct the transport coefficients and ECRH power profile with an accuracy of no worse than 30%, the absolute error δ in determining the electron temperature from each of the measurement channels should be no larger than $\delta \leq 20$ eV (the relative error is about 10%).

(ii) We have found that it is possible to adequately reconstruct the structure of the total heat flux (i.e., to unambiguously determine the diffusive and convective components of the heat flux) if the absolute error in measuring the electron temperature is no larger than $\delta \leq 20$ eV (the relative error is about 10%). With additional information on, e.g., the half-width of the ECRH power profile, the structure of the heat flux can be adequately reconstructed if the absolute error is no larger than $\delta \leq 40$ eV (the relative error is about 20%).

(iii) We have demonstrated that the accuracy of reconstruction of the transport coefficients and ECRH power profile depends sensitively on the error in specifying the steady-state electron temperature before switching on or off ECR heating. By smoothing the steady-state electron temperature over the time interval $\delta t = 4$ ms (over 41 time points), it is possible to substantially reduce the error in reconstructing the plasma parameters that is associated with errors in the initial conditions.

(iv) We have reconstructed the transport coefficients and ECRH power profile for a series of T-10 shots and have investigated the accuracy of this reconstruction. The results obtained by processing the data from ECR heating experiments in the T-10 tokamak agree well with the estimates from our numerical investigations.

ACKNOWLEDGMENTS

REFERENCES

1. N. J. Lopes Cardozo, Plasma Phys. Controlled Fusion **37**, 799 (1995).

2. F. Ryter, F. Leuterer, G. Pereverzev, *et al.*, Phys. Rev. Lett. **86**, 5498 (2001).

3. F. Ryter, F. Leuterer, G. Pereverzev, *et al.*, Plasma Phys. Controlled Fusion **44**, A407 (2002).

4. G. T. Hoang, X. Garbet, X. L. Zhu, *et al.*, Phys. Rev. Lett. **87**, 125001 (2001).

5. F. Ryter, C. Angioni, M. Beurskens, *et al.*, Plasma Phys. Controlled Fusion **43**, A323 (2001).

6. K. Kirov, F. Leuterer, G. Pereverzev, *et al.*, in *Proceedings of the 29th European Conference for Controlled Fusion and Plasma Physics, Montreux, 2002*; ECA **26B**, 3.046 (2002).

7. F. Leuterer, A. G. Peeters, G. Pereverzev, *et al.*, in *Proceedings of the 24th European Conference for Controlled Fusion and Plasma Physics, Berchtesgaden, 1997*; ECA **21A** (IV), 1533 (1997).

8. R. H. Cohen, Phys. Fluids **30**, 2442 (1987).

9. V. F. Andreev, Yu. N. Dnestrovskij, and A. M. Popov, Nucl. Fusion **33**, 499 (1993).

10. V. F. Andreev, Yu. N. Dnestrovskij, K. A. Razumova, and A. V. Sushkov, in *Proceedings of the 24th European Conference for Controlled Fusion and Plasma Physics, Berchtesgaden, 1997*; ECA **21A** (II), 937 (1997).

11. V. F. Andreev, Yu. N. Dnestrovskij, S. E. Lysenko, *et al.*, in *Proceedings of the 26th European Conference for Controlled Fusion and Plasma Physics, Maastricht, 1999*; ECA **23J**, 853 (1999).

12. V. F. Andreev, Yu. N. Dnestrovskij, S. E. Lysenko, *et al.*, Vopr. At. Nauki Tekh., Ser. Termoyadernyĭ Sintez, No. 1, 116 (2000).

13. V. F. Andreev, Yu. N. Dnestrovskij, K. A. Razumova, and A. V. Sushkov, Fiz. Plazmy **28**, 403 (2002) [Plasma Phys. Rep. **28**, 367 (2002)].

14. O. M. Alifanov, E. A. Artyukhov, and S. V. Rumyantsev, *Extremal Methods for Solving Ill-Posed Problems* (Nauka, Moscow, 1988) [in Russian].

Translated by O.E. Khadin

================================ **TOKAMAKS** ================================

Injection of a High-Density Plasma into the Globus-M Spherical Tokamak

K. B. Abramova, A. V. Voronin, V. K. Gusev, E. E. Mukhin, Yu. V. Petrov, N. V. Sakharov, and F. V. Chernyshev

Ioffe Physicotechnical Institute, Russian Academy of Sciences, Politekhnicheskaya ul. 26, St. Petersburg, 194021 Russia
Received July 28, 2004; in final form, October 6, 2004

Abstract—A new type of plasma source with titanium hydride granules used as a hydrogen accumulator was employed to inject a dense, highly ionized plasma jet into the Globus-M spherical tokamak. The experiments have shown that the jet penetrates through the tokamak magnetic field and increases the plasma density, without disturbing the stability of the plasma column. It is found that, when the plasma jet is injected before a discharge, more favorable conditions (as compared to those during gas puffing) are created for the current ramp-up at a lower MHD activity in the plasma column. Plasma injection at the instant of maximum current results in a more rapid growth in the plasma density in comparison to gas puffing. © 2005 Pleiades Publishing, Inc.

1. INTRODUCTION

An important problem of controlled fusion research is the development of new types of high-density plasma sources. One requirement to be met in modern plasma devices (and even more so in future fusion reactors) is that the optimal distribution of the fuel density must be rapidly produced in the region where the plasma is confined and heated. In order for the injected fuel to penetrate through the dense hot plasma layers to the burning region, it must have a sufficiently large directed momentum. The total number of particles in a bunch with a density above 10^{20} m^{-3} and velocity of 10–800 cm/s should be 10^{18}–10^{23}.

Experiments on fuel injection into the tokamak plasma core can provide a better insight into fundamental problems of plasma physics, such as the problem of confinement and stability of a magnetized plasma. A local increase in the tokamak plasma density changes the plasma pressure profile, thereby affecting plasma stability. A local jump in the plasma density also gives rise to a radial electric field, which leads to the generation of a transport barrier and to an improvement of the plasma confinement in this region. This necessitates a thorough study of the mechanisms for trapping, confinement, and thermalization of an injected dense plasma bunch.

Systems for accelerating gas jets, solid pellets, and plasma bunches are well studied and are widely used to fuel plasma devices.

The use of inexpensive and simple gas-puff systems in tokamaks is inefficient. Low-energy neutrals usually slow down at the periphery of the plasma column and poorly penetrate into the plasma core.

The velocities to which pneumatic low-Z gas guns and centrifuges can accelerate cryogenic hydrogen pellets 1–6 mm in diameter are at most 3 km/s [1], whereas with electromagnetic rail guns, velocities as high as 7 km/s can be attained [2]. Experiments have shown that a further increase in the pellet velocity cannot be achieved without ionizing the fuel and transforming it into a plasma state.

The maximal fuel velocities were reached in pulsed plasma accelerators (see, e.g., [3]). Plasma accelerators have long been used as plasma sources in experiments and applications. In such accelerators, plasma is produced and accelerated by an electric discharge excited between coaxial electrodes. A plasma cluster with a density of less than 10^{20} m^{-3} can be accelerated to a velocity above 100 km/s.

In [4], it was proposed to supply a tokamak plasma with fuel by using collective acceleration of plasma rings confined by a toroidal magnetic field (compact tori). Compact tori can be produced, e.g., by means of magnetized Marshall guns. The plasma density and the average flow velocity in such guns reach 7×10^{21} m^{-3} and 220 km/s, respectively. The current density in these sources is very high, which causes the contamination of the injected plasma with the erosion products of the electrode material. Since this plasma is confined by a magnetic field, its density is limited and, in order to increase the mass of the accelerated material, it is necessary to increase the plasma volume.

The maximal plasma density (5×10^{26} m^{-3}) was achieved in experiments with capillary discharges [5]. Unfortunately, this plasma is strongly contaminated with impurities and thus cannot be used to fuel fusion devices.

A fairly high plasma density ($\sim 10^{23}$ m^{-3}) was reached at the outlet of a coaxial accelerator in plasma focus experiments [6]. However, the directed plasma velocity in this region was too low.
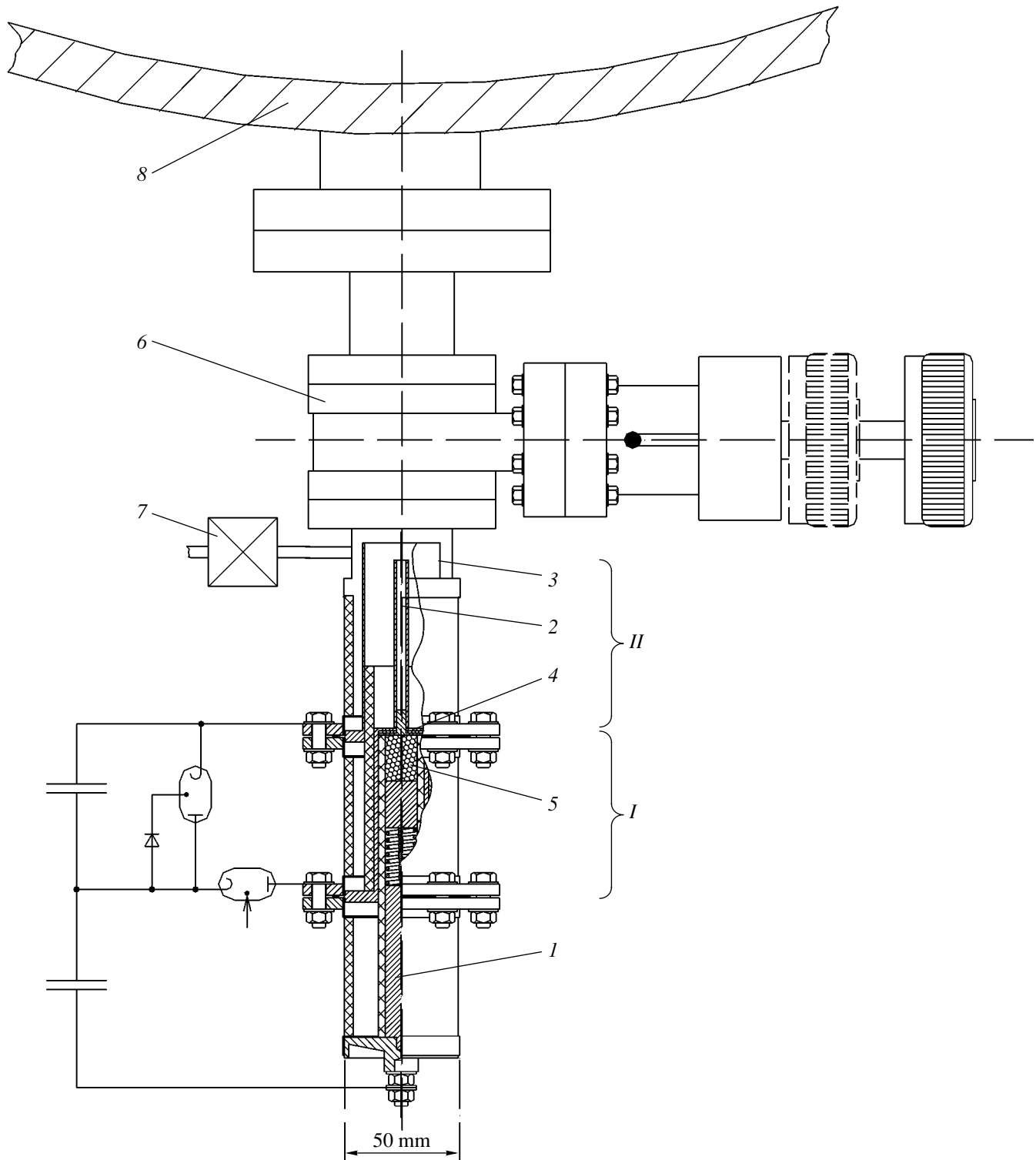
Fig. 1. Two-stage source for plasma injection into the Globus-M tokamak: (*I*) gas-generating stage, (*II*) plasma-generating stage, (*1*) central electrode, (*2*) intermediate electrode, (*3*) outer electrode, (*4*) grid filter, (*5*) granules, (*6*) sliding shutter, (*7*) vacuum valve, and (*8*) tokamak vacuum chamber.

It is also necessary to mention the injection of high-energy neutral beams. Such beams (with a neutral velocity of ~15 000 km/s and density of ~10^{16} m^{-3}) are primarily intended for plasma heating, but they can also be used to increase the plasma density in the tokamak plasma core. The use of neutral beam injection as the

main method for refueling the reactor is problematic because of the very high cost of MeV ion sources [7].

In [8], a plasma jet source (a modified Bostick source) with titanium-hydride electrodes was investigated. This source was successfully used to ionize gas in the Extrap T2 Reversed Field Pinch (Alfvén Laboratory, Stockholm) and to inject plasma into the Tornado-X device with a magnetic field of 0.2 T and plasma density of 10^{17}–10^{19} m^{-3} (Ioffe Physicotechnical Institute, Russian Academy of Sciences, St. Petersburg). A further increase in the plasma density in this source substantially increased the amount of impurities due to the erosion of the electrodes.

It may therefore be concluded that there are sources capable of accelerating high-density plasma to relatively low velocities and others capable of accelerating low-density plasma to high velocities. However, none of the known sources is able to produce high-purity plasma jets with both high density and high velocity. A substantial improvement of the plasma source parameters was achieved in a two-stage source [9] and its modification that will be considered below. In this paper, we present results from experiments on the injection of dense hydrogen plasma into the Globus-M tokamak by means of a two-stage source. The injection is used to increase the plasma density during a discharge, as well as to preionize the working gas and initiate the main discharge.

2. TWO-STAGE SOURCE FOR PLASMA INJECTION INTO THE GLOBUS-M TOKAMAK

A two-stage high-density gas/plasma source been designed, created, and investigated at the Ioffe Physicotechnical Institute, Russian Academy of Sciences (see [9]). The source uses condensed granules capable of accumulating gas and releasing it under the action of an electric discharge. The electric current passing through the granules produces a high-density gas cloud. The gas is separated from nongaseous impurities using a fine-mesh grid filter placed between granules and the coaxial plasma accelerator. The electric discharge excited between the coaxial electrodes ionizes the gas and accelerates the produced plasma jet.

A schematic of such a two-stage source for injecting plasma into the Globus-M tokamak is shown in Fig. 1. The first (gas-generating) stage contains titanium hydride granules (5). The granules are placed between the central (1) and intermediate (2) electrodes. The second (plasma-generating) stage is a version of a conventional pulsed coaxial plasma accelerator consisting of the outer (3) and intermediate (2) electrodes. The stages are separated from one another by a fine-mesh grid (4), which prevents nongaseous impurities from penetrating into the second stage. Both stages are connected to a low-inductance capacitive energy storage through an ignitron. Special means were used to optimize the inductance of the power source. The parameters of the
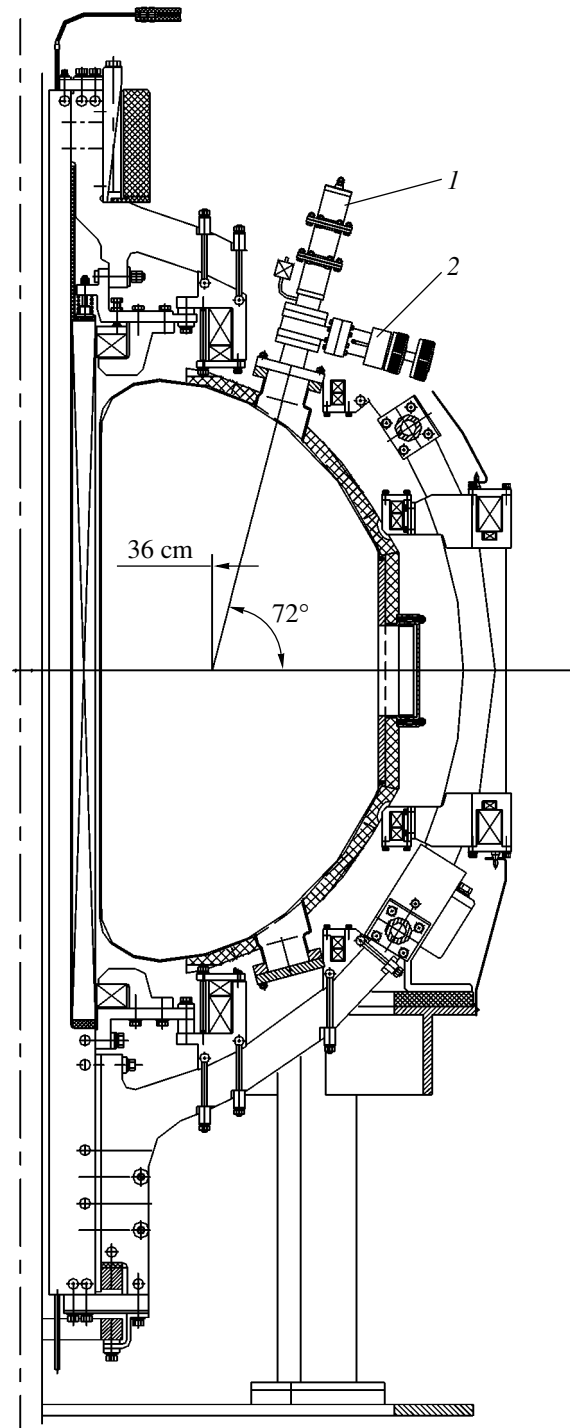

Fig. 2. Position of the plasma source in the Globus-M spherical tokamak: (*1*) plasma source and (*2*) sliding shutter.

generated plasma were preliminarily studied at a test bench. The source generated a plasma jet with a duration of 50 μs, density of 10^{22} m^{-3}, particle number of 5×10^{18}–10^{19}, degree of ionization of 90%, and velocity of 15–70 km/s.
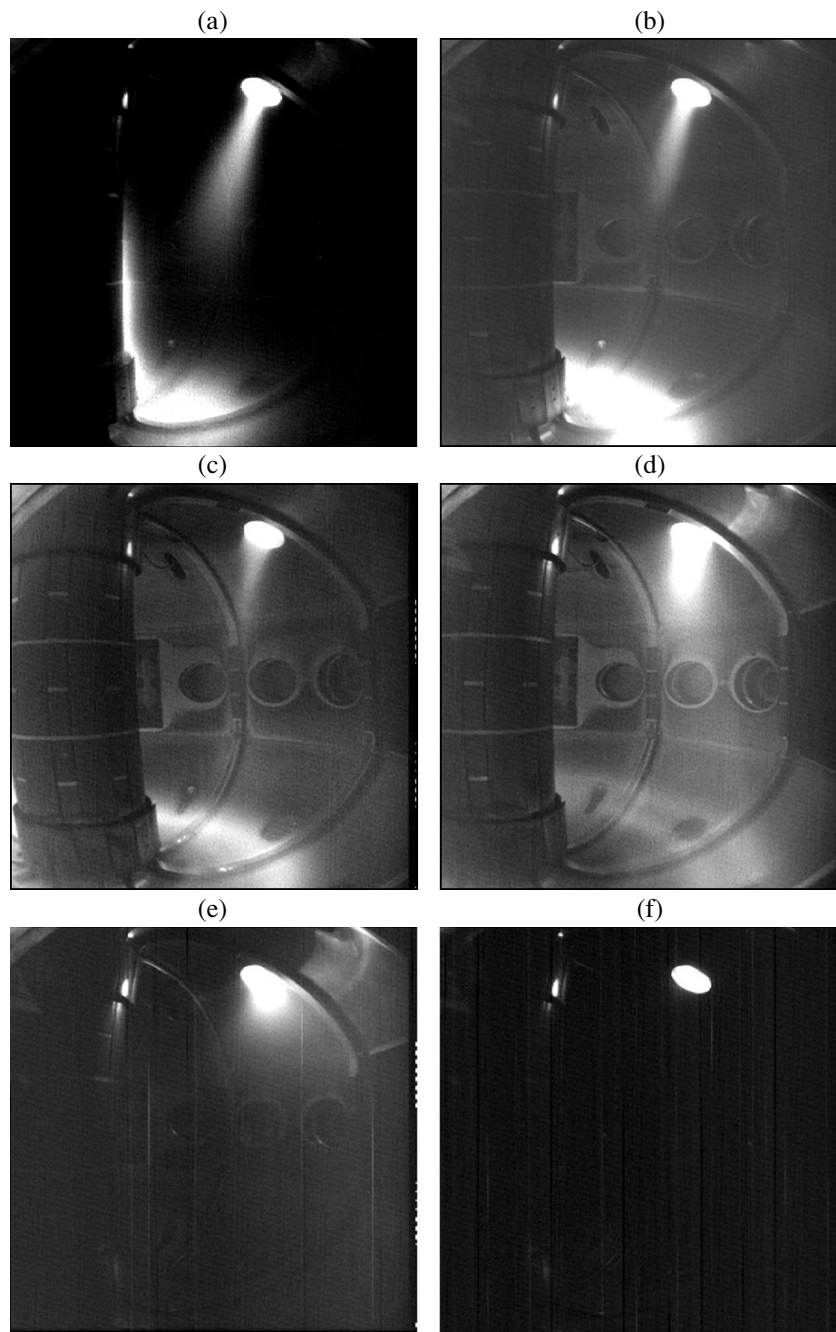
Fig. 3. Emission from a plasma jet injected into the vacuum chamber at different toroidal magnetic fields: (a) 0, (b) 0.005, (c) 0.05, (d) 0.07, (e) 0.12, and (f) 0.25 T.

Source *1* was attached to the vacuum chamber of the Globus-M tokamak through an inclined flange and a sliding shutter (*2*) (see Fig. 2). The jet was injected along a chord inclined at an angle 18° to the vertical axis. Up to 50 pulses could be produced without refilling the source with a fresh portion of titanium hydride granules.

The source was equipped with replaceable electrodes of the plasma-generating stage of length 0.06,

0.3, 0.6, and 1.2 m. This allowed us to vary the plasma jet velocity from 15 to 70 km/s.

We carried out three types of experiments on the injection of high-density hydrogen plasma jet into the Globus-M tokamak [10]: (i) the jet was injected into the vacuum toroidal magnetic field without switching on the eddy field, (ii) the jet was injected into the magnetic field before a discharge (instead of gas puffing with RF
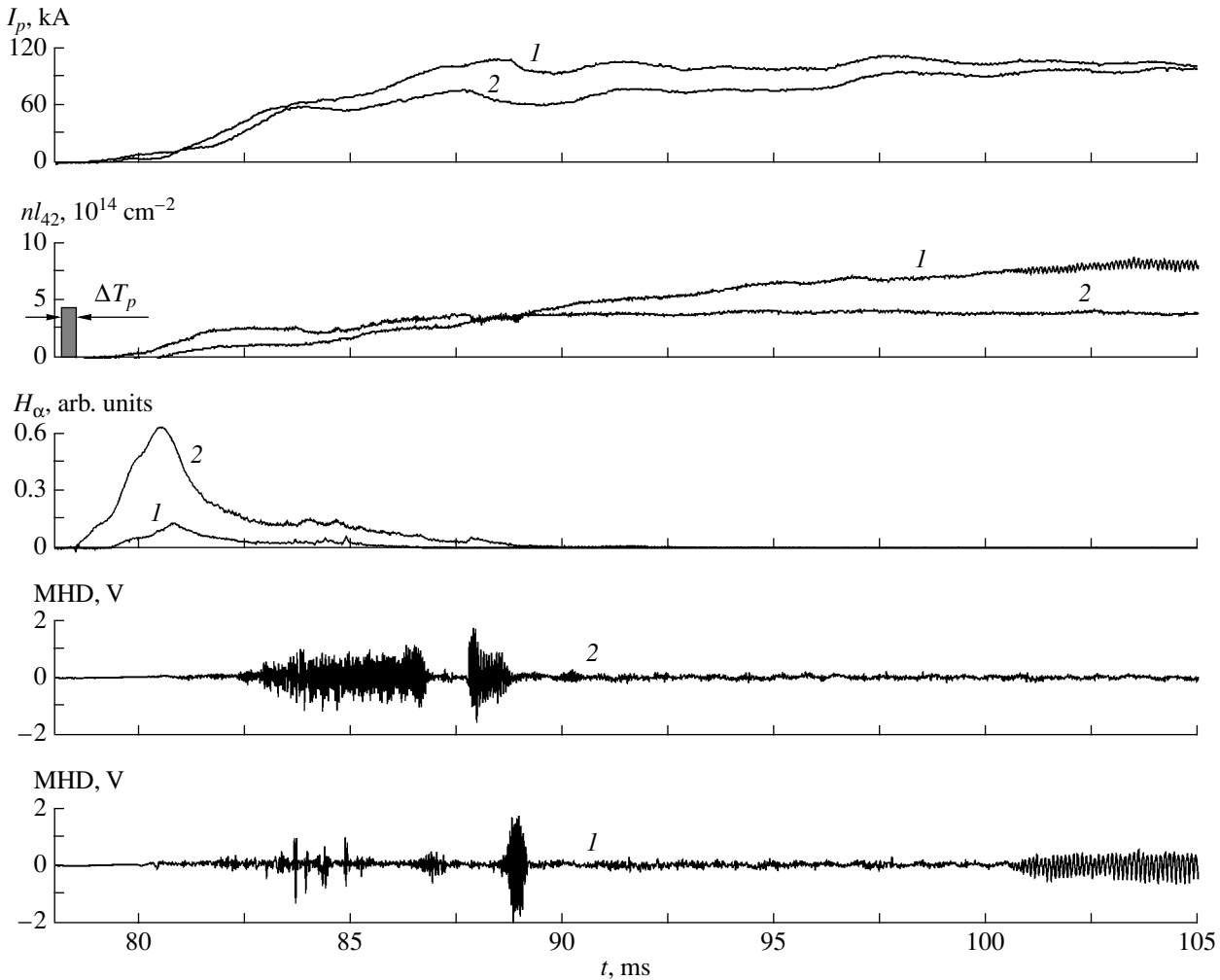
Fig. 4. Initiation of a toroidal discharge (*1*) by the plasma source (shot no. 3386) and (*2*) by gas puffing with RF preionization (shot no. 3397): I_p is the toroidal current, nl_{42} is the plasma density integrated along a vertical chord at a distance of 42 cm from the axis, H_α is the hydrogen line intensity, MHD is the Mirnov coil signal, and ΔT_p is the duration of plasma injection (~50 μs).

preionization), and (iii) the jet was injected into deuterium plasma in the steady-state phase of a discharge.

The parameters of the Globus-M tokamak are as follows: the aspect ratio is $A = R/a = 1.5$, the major radius is $R = 0.36$ m, the minor radius is $a = 0.24$ m, the toroidal field on the axis is $B_T \leq 0.62$ T, the plasma current is $I_p \leq 0.5$ MA, and the current pulse duration is $\tau_{pulse} \leq 0.3$ s.

In all the experiments, we measured the plasma parameters. The plasma density integrated along vertical chords at distances of $R = 24, 42,$ and 50 cm from the axis was measured by an interferometer at a wavelength of 1 mm. The radiation from the injected plasma inside the vacuum chamber was recorded with the help of a video camera. The time evolution of the hydrogen concentration in the deuterium plasma was measured by an ACORD-12 charge-exchange neutral particle analyzer [11]. The time evolution of the density profile

was measured by a multichannel radar reflectometer in the frequency range 19.6–60.5 GHz [12].

3. STUDY OF THE POSSIBILITY OF CONTROLLING THE PARAMETERS OF THE TOKAMAK PLASMA WITH THE HELP OF AN EXTERNAL SOURCE OF A HIGH-DENSITY PLASMA JET

3.1. Penetration of the Jet through the Toroidal Magnetic Field

A dense (10^{22} m^{-3}), highly ionized (90%) hydrogen plasma jet with a total particle number of 5×10^{18}–10^{19} and velocity of 30 km/s was injected into the toroidal magnetic field during 50 μs. Measurements of the radiation from the injected plasma allowed us to estimate the depth to which the jet penetrated into the tokamak plasma (Fig. 3). The lower the magnetic field, the deeper the jet penetrates into the tokamak plasma at the
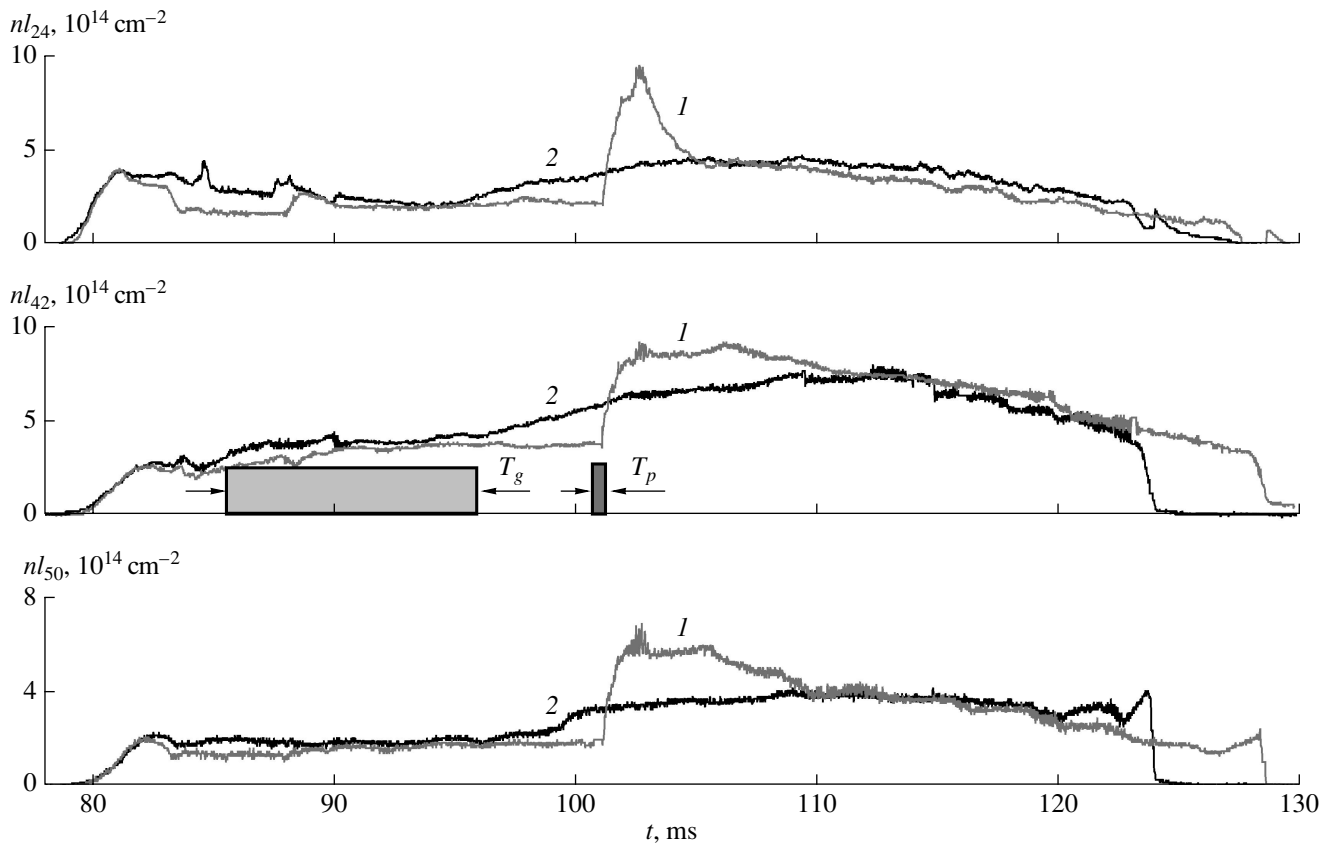
Fig. 5. Time evolution of the plasma density the steady-state phase of a discharge with (*1*) plasma jet injection (shot no. 3381) and (*2*) additional gas puffing (shot no. 3389): nl_{24}, nl_{42}, and nl_{50} are the plasma densities integrated along vertical chords at distances of 24, 42, and 50 cm from the axis, respectively; ΔT_p is the duration of plasma injection (~50 μs); and ΔT_g is the gas-puffing duration (~10 ms).

same initial velocity. It might be expected that a magnetic field of ~0.2 T would be sufficient to stop the jet just near the source nozzle (in this case, the field in the central region of the chamber is 0.25 T). When the field was lower than 0.15 T, the jet reached the opposite wall of the chamber. We note, however, that, in all of the experiments described below, the magnetic field in central region was higher than 0.25 T.

3.2. Plasma Injection before a Discharge

The plasma jet with a duration of ~50 μs was injected just before the eddy field was switched on at a steady-state toroidal magnetic field of ~0.3 T. These experiments were performed without both preliminary gas puffing and RF ionization at the electron-cyclotron resonance frequency. The jet parameters were chosen such that the total number of particles in the jet was nearly the same as that during gas puffing (~10^{19}). Figure 4 compares the parameters of the tokamak plasma obtained using jet injection before a discharge (without gas puffing and RF preionization) and those obtained under standard operating conditions with gas puffing and RF preionization. It can be seen that, in a discharge

with jet injection, the toroidal current increases more rapidly and reaches a higher value at the same loop voltage, the MHD activity is suppressed, the plasma density is higher, and the H_α intensity decreases in comparison to those in a discharge with gas puffing and RF preionization.

3.3. Control over the Plasma Density during the Steady-State Phase of a Discharge

The duration of the jet injected in the steady-state phase of a discharge was also as short as ~50 μs. The injection of a hydrogen plasma jet into deuterium plasma in this phase did not increase signals from Mirnov coils, but increased the electron density integrated along vertical chords (Fig. 5). The plasma density increased over ~1 ms just after injection. This led to a more rapid growth of the density in comparison to that during gas puffing, when the density grew over ~15 ms. A slower plasma decay was observed along the central chord ($R = 42$ cm) in comparison to that measured along peripheral chords at radii of $R = 24$ and 50 cm; this means that the peakedness of the density profile increased over time. It should be noted that the
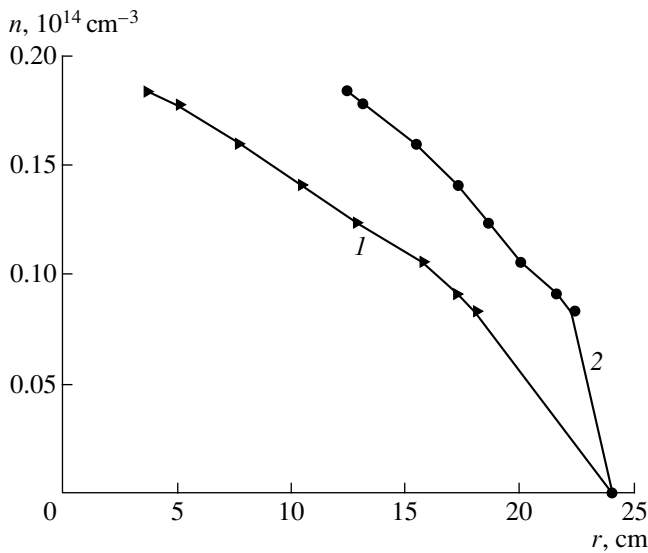
Fig. 6. Radial profiles of the plasma density n measured by a reflectometer in shot no. 5276 (*1*) 19 and (*2*) 32 ms after the beginning of the discharge (r is the minor plasma radius).
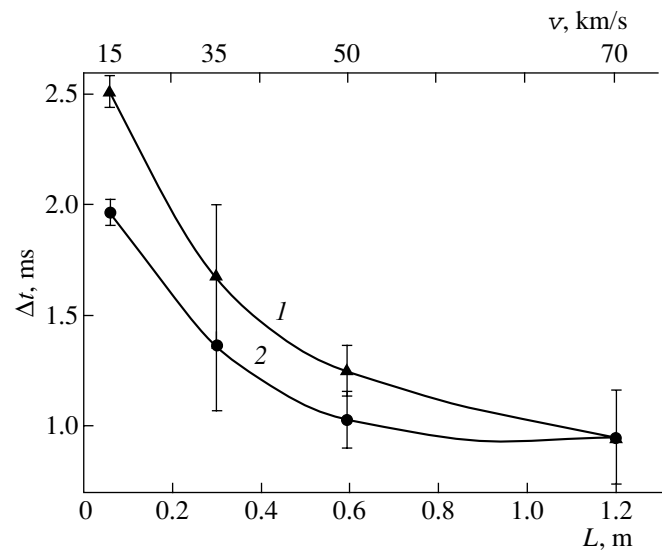

Fig. 7. Growth time Δt of the plasma density integrated along the (*1*) central and (*2*) peripheral chords as a function of the accelerator length L (v is the plasma velocity at the exit from the accelerator).

intensity of the CIII carbon line (which is not shown in the figure) varied only slightly during injection. This indicates that the impurity influx in the discharge was insignificant.

Measurements of the plasma density profile with the help of a radar reflectometer confirmed that the density gradient increased not only at the edge, but also in the plasma core (Fig. 6). It can be seen that, 32 ms after injection, the density profile became steeper.

The experiments showed that the plasma jet velocity increased with increasing accelerator length (the lengths of the central and intermediate electrodes of the second stage). The growth time of the plasma densities integrated along the central and peripheral chords was measured for different accelerator lengths (Fig. 7). It can be seen that the time during which the jet penetrates into the tokamak plasma decreases with increasing accelerator length. The density growth time was found to be equal to 2.5 and 0.95 ms for accelerator lengths of 0.06 and 1.2 m, respectively. Note that the gas jet injected by the first (gas-generating) stage penetrated into the tokamak plasma for 4.5 ms. The plasma jet with the maximum (70 km/s) velocity efficiently penetrated into the core of the tokamak plasma.

The time evolution of the hydrogen concentration in the deuterium plasma was measured by a charge-exchange neutral particle analyzer (Fig. 8). It can be seen that the hydrogen flux increases as the plasma density increases for 1–2 ms after jet injection. The hydrogen flux was maximum at an energy of 470 eV. The hydrogen concentration in the deuterium plasma in this experiment increased to 25%. This indicates that the plasma injected with a velocity of 30 km/s penetrates

into the high-temperature region of the tokamak plasma.

4. DISCUSSION OF THE RESULTS

Our experiments have shown that the source generates a high-density plasma jet, whose velocity (15–70 km/s) depends on the accelerator length. The injected jet does not produce significant perturbations in the confined plasma; i.e., it does not introduce impurities and does not promote MHD activity. The reason for this is probably related to the high purity of the injected plasma jet. The absence of impurities may be explained by the very high gas pressure in the source; the short pulse duration; and the low density of the accelerator current, which does not cause electrode erosion.

Our experiments on the injection of a high-density plasma jet into the spherical tokamak have revealed a discrepancy between theory and experiment. In the spherical tokamak, there is a gradient of the toroidal magnetic field along the injection direction. For the given position of the source with respect to the toroidal magnetic field, the magnetic field varied from 0.32 T at the outer boundary to 1.2 T at the inner boundary of the plasma column along the injection direction. Based on the classical considerations of the interaction of a high-density unmagnetized plasma with a magnetic field, it can be assumed that the plasma jet should be stopped by the magnetic field at the point where the density of the jet kinetic energy (the plasma jet pressure) becomes equal to the magnetic field pressure [13]. Let us consider the equilibrium conditions for the pressures of the plasma jet and the magnetic field in the Globus-M toka-
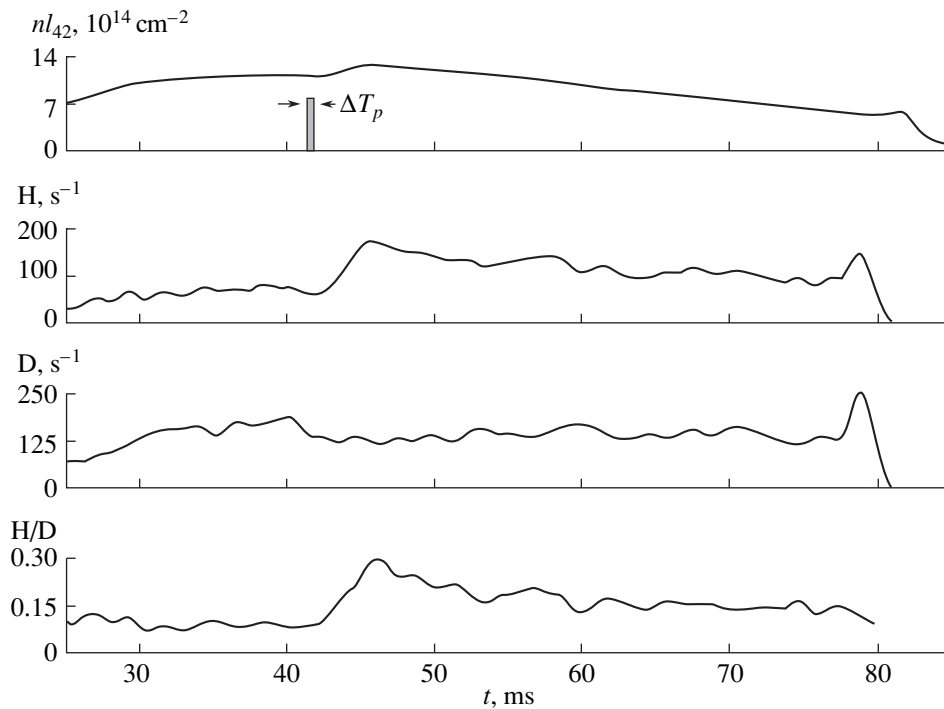
Fig. 8. Time evolution of the hydrogen concentration in a deuterium plasma measured by charge-exchange neutrals with energies of 470 eV (shot no. 6068): H and D are the hydrogen and deuterium neutral fluxes, respectively; H/D is the ratio between hydrogen and deuterium fluxes; nl_{42} is the plasma density integrated along a vertical chord at a distance of 42 cm from the axis; and ΔT_p is the duration of plasma injection.

mak. For example, a field of 0.32 T is sufficient to stop a plasma jet with a density of 10^{22} m^{-3} and velocity of 15–70 km/s. So, it might be expected that the jet would be stopped at the plasma periphery. However, the jet substantially affects the plasma parameters in the central region of the plasma column. Figure 6 demonstrates that the growth time of the tokamak plasma density decreases with increasing jet velocity, and Fig. 8 shows that the hydrogen flux increases as the plasma density increases over 1–2 ms after jet injection. Probably, there is a certain mechanism (other than the classical one) for the interaction of a high-density plasma jet with a plasma confined by a magnetic field that is still to be studied. It may be supposed that the injected plasma jet recombines into the fast neutral flux. In this case, the flux of neutrals with energies of several tens of electronvolts can easily penetrate through the magnetic field of the Globus-M tokamak. This is confirmed by Fig. 3a. It is seen that the jet consists of a glowing and a dark region. Probably, the injected jet initially consists of ionized particles and then, due to recombination, receives neutrals that collide with the chamber wall and knock out excited atoms and ions from it.

plasma jet with a high degree of ionization was successfully injected into the Globus-M low-aspect-ratio tokamak. The experiments have confirmed the efficiency of using plasma jets to control the plasma density in tokamaks. It is demonstrated that the plasma jet does penetrate into the plasma core. The higher the jet velocity, the more rapidly it penetrates into the plasma. We have shown that the injected plasma does not disturb the stability of the confined plasma, the intensity of carbon impurity lines changes only slightly during injection, and the plasma density increases by 20–30% over the initial density ($\sim 2 \times 10^{19}$ m^{-3}). The experiments have shown that the plasma jet can be efficiently used to initiate a discharge (instead of gas puffing with RF preionization). It is found that, when the plasma jet is injected before a discharge, more favorable conditions (as compared to those during gas puffing) are created for the current ramp-up at a lower MHD activity in the plasma column. Plasma injection in the steady-state phase of a discharge leads to a more rapid growth of the tokamak plasma density, a longer decay time of the plasma core, and a steeper density profile in comparison to those during conventional gas puffing.

5. CONCLUSIONS

We have investigated the possibility of using a new type of high-density high-velocity plasma source to fuel magnetic confinement systems. A high-density

ACKNOWLEDGMENTS

We thank the Globus-M team for assistance in performing experiments. We are also grateful to V.B. Mineev for fruitful discussions. This work was

REFERENCES

1. S. K. Combs, Rev. Sci. Instrum. **64**, 1979 (1993).

2. E. M. Drobyshevsky, B. G. Zhukov, and V. A. Sakharov, IEEE Trans. Magn. **31**, 299 (1995).

3. S. D. Grishin, L. V. Leskov, and N. P. Kozlov, *Plasma Accelerators* (Mashinostroenie, Moscow, 1983) [in Russian].

4. R. Raman, F. Martin, B. Quirion, *et al.*, Phys. Rev. Lett. **73**, 3101 (1994).

5. V. K. Semenov and L. A. Spektorov, Zh. Tekh. Fiz. **34**, 853 (1964) [Sov. Phys. Tech. Phys. **9**, 651 (1964)].

6. R. P. Vasiljeva, M. I. Pergament, and A. I. Yaroslavsky, in *Proceedings of the 3rd International Conference on Plasma Physics and Controlled Nuclear Fusion Research, Novosibirsk, 1968* (IAEA, Vienna, 1969), Vol. II, p. 39.

7. ITER Physics Basis Editors, Nucl. Fusion **39**, 2416 (1999).

8. A. V. Voronin and K. G. Hellblom, Plasma Phys. Controlled Fusion **41**, 293 (1999).

9. A. V. Voronin and K. G. Hellblom, Plasma Phys. Controlled Fusion **43**, 1543 (2001).

10. V. K. Gusev, V. M. Amoskov, A. S. Ananiev, *et al.*, in *Proceedings of the 19th IAEA Fusion Energy Conference, Lyon, 2002*, Paper EX/P3-10.

11. A. V. Izvozchikov, M. P. Petrov, S. Ya. Petrov, *et al.*, Zh. Tekh. Fiz. **62** (1), 157 (1992) [Sov. Phys. Tech. Phys. **37**, 201 (1992)].

12. V. G. Petrov, A. A. Petrov, A. Yu. Malyshev, *et al.*, Prib. Tekh. Éksp., No. 4, 91 (2003).

13. L. J. Perkins, S. K. Ho, and J. H. Hammer, Nucl. Fusion **28**, 1365 (1988).

Translated by N.F. Larionova

=========== **PLASMA OSCILLATIONS** ===========
AND WAVES

Slow Nonlinear Waves in Magnetic Flux Tubes

Yu. D. Zhugzhda

Institute of Terrestrial Magnetism, Ionosphere, and Radio-Wave Propagation, Russian Academy of Sciences,
Troitsk, Moscow oblast, 142090 Russia

Kiepenheuer Institut für Sonnenphysik, Freiburg, Germany

Received February 11, 2004; in final form, December 2, 2004

Abstract—A theory of weakly nonlinear slow waves in magnetic flux tubes is developed in the ideal MHD approximation. Fairly simple approximate dispersion relations are derived that are valid for waves of arbitrary wavelength. These dispersion relations make it possible to obtain a number of new model evolutionary equations for body and surface slow waves in magnetic flux tubes. It is established that there are two families of exact analytic solutions to the equations for weakly nonlinear slow waves. It is found that both the body and surface solitary waves can be in the form of either contractions or bulges running along the tube. A model Korteweg–de Vries–Burgers equation is derived and generalized to waves of arbitrary wavelength. It is shown that exact analytic solutions to these equations correspond to shock waves and hydraulic jumps (or bores) with nonoscillating fronts. © 2005 Pleiades Publishing, Inc.

1. INTRODUCTION

The magnetic flux tube approximation [1], together with the magnetic slab approximation, is widely used in astrophysics and geophysics as the simplest model for studying waves in inhomogeneous plasmas. Recent progress in space observations has made it possible to reveal fast, slow, and bending oscillations and waves in coronal arcs [2–6], which gave a new impetus to the exploration of waves in magnetic flux tubes. In the present paper, the analysis is restricted to a simple magnetic flux tube in the form of an infinite cylinder filled with a homogeneous isotropic plasma in a uniform longitudinal magnetic field. The external plasma and magnetic field are also assumed to be uniform. An important simplifying assumption is that of an infinitely thin interface between the internal and external plasma; this makes it possible to exclude from consideration the resonant effects occurring across the transition boundary layer. Of course, it is also necessary to assume that the total (gas-kinetic plus magnetic) pressure is the same on both sides of the tube boundary; this imposes restrictions on the ratios between the plasma densities and plasma temperatures on both sides and also between the strengths of the internal and external magnetic fields. It should be noted that, according to high-resolution observations of the solar atmosphere, the magnetic fields usually manifest themselves in the form of an ensemble of magnetic flux tubes, the most illustrative example being the sunspot penumbra, which consists entirely of long thin flux tubes.

The linear theory of MHD waves in magnetic flux tubes was developed through the efforts of many scientists [7–11]. It was found that, for certain parameters of the plasma and magnetic field inside and outside a magnetic flux tube, the waves within the tube are com-

pletely reflected from its boundary; i.e., the tube becomes a waveguide. The tube may be subject to four kinds of oscillations, namely, it can guide fast and slow magnetosonic waves and also can undergo bending and twisting oscillations. The aim of the present paper is to consider slow waves in a magnetic flux tube with a fixed axis.

The theory of nonlinear waves in thin magnetic flux tubes [8, 11, 12] began to be developed simultaneously with the linear theory of waves in magnetic flux tubes. The thin-tube approximation is an analogue of the shallow water approximation in hydrodynamics. Nonlinear equations were derived that describe the propagation of slow and bending nonlinear waves along thin tubes. The thin-tube approximation for slow waves [12], which was obtained by expanding the dependent variables in power series in the radius of the tube, is valid in the limit $kR_0 \longrightarrow 0$, where R_0 is the tube radius and k is the longitudinal wave vector. In this limit, slow waves become so-called tube modes, which propagate along the tube with the tube velocity $C_T = C_A C_S/(C_A^2 + C_S^2)^{0.5}$. Accounting for the next-order terms in the series expansions of the dependent variables in the tube radius yielded a two-mode approximation for fast and slow waves [13, 14], which is valid for waves of arbitrary wavelength in a sufficiently cold plasma. The two-mode approximation, however, does not take into account dispersion due to the response of the external medium—an effect predominating in the long-wavelength approximation [14].

In most cases, the theory of weakly nonlinear dispersive waves is based on the model equations whose linear part is determined by converting the dispersion relation into a linear differential (or an integrodifferen-

tial) wave equation and whose nonlinear term is found by expanding the nonlinear equations to second (or third) order in the wave amplitude. For waves in magnetic flux tubes, the dispersion relation contains Bessel functions and thus cannot generally be converted into a wave equation. The conversion to a wave equation is possible in the long-wavelength approximation, in which the dispersion relation is substantially simplified. It is this circumstance that enabled Roberts [15–17] to derive an equation for weakly nonlinear dispersive surface waves in magnetic flux tubes surrounded by a plasma with no external magnetic field present. Roberts deduced the nonlinear term in the thin tube approximation, in which the set of three-dimensional MHD equations can be reduced to a set of one-dimensional equations for long slow waves running along a tube (these waves are often called tube waves). The equation derived by Roberts for surface waves in magnetic flux tubes turned out to be identical to the Leibovich equation [18] for vortex filaments in fluids, and it is now commonly referred to as the Leibovich–Roberts (LR) equation. In [19, 20], the LR equation was generalized to the case of a magnetized surrounding plasma. Another equation for this case was obtained by Molotovshchikov and Ruderman [21]. The Molotovshchikov–Ruderman (MR) equation and the LR equation differ from one another because they were derived for different approximate dispersion relations. Pritchard [22], who simplified the dispersion relation used by Leibovich, obtained one more equation for the vortex filaments by replacing the modified Bessel function in dispersion relation with its asymptotic expansion. The Pritchard equation is also valid for waves on the surfaces of magnetic flux tubes. These three equations are asymptotically equivalent because, in the long-wavelength limit, the difference between the wave dispersions determined by the corresponding dispersion relations asymptotically approaches zero. Nevertheless, the nonlinear waves described by these equations possess different properties. For instance, an exploration of the LR equation [23, 24] revealed that the solitary waves described by it occur for amplitudes smaller than a certain critical amplitude. On the other hand, Molotovshchikov and Ruderman [21] showed that their equation has solutions describing solitary waves of arbitrary amplitude. Moreover, they asserted that the solitary waves are solitons. That the solutions to the asymptotically equivalent equations have different properties stems from the difference between the corresponding dispersion relations beyond the long-wavelength limit. The linearized LR equation implies that, as the wavenumber increases, the phase velocity decreases to a certain minimum value and then increases to its initial value; thus, the phase velocities in the long- and short-wavelength limits are the same. In accordance with the linearized MR equation, the wave phase velocity decreases monotonically as the wavenumber increases; moreover, for short waves, the dependence of the phase velocity on the wavenumber is linear. The linearized

Pritchard equation in turn implies that, as the wavenumber increases, the wave phase velocity decreases to its minimum value and then increases without bound, because it is proportional to the logarithm of the dimensionless wavenumber. None of the three behaviors agrees with the actual dependence of the phase velocity of the surface waves on the wavenumber, specifically, the phase velocity, which is initially equal to the tube velocity, decreases monotonically with increasing wavenumber and, in the short-wavelength limit, approaches the phase velocity of the surface waves propagating along the boundary of a very thick tube (see Fig. 2a). Accordingly, special care must be taken when using the above three equations. In particular, none of them helps to answer the question of whether the amplitudes of the solitary waves can be arbitrary. Therefore, there was no point to debating this issue in [21, 23, 24]. It should be noted that, in the case of vortex filaments, the LR equation correctly describes the phase velocity of the linear vortex waves in the short-wavelength limit and thus can be used to analyze waves of arbitrary wavelength. In the present paper, new approximate dispersion relations for surface waves are proposed that correctly describe both the long- and short-wavelength limits. These dispersion relations made it possible to derive new nonlinear wave equations. It is these equations that should serve as a basis for the exploration of the properties of nonlinear waves in magnetic flux tubes.

A history of the study of nonlinear body waves began with a confusion: Molotovshchikov and Ruderman [21] obtained an equation for the body waves according to which weakly nonlinear dispersive body waves cannot exist. Later, when the Korteweg–de Vries (KdV) equation for body waves was derived in [25] from a very rough dispersion relation, the question arose of whether the conclusions of Molotovshchikov and Ruderman were correct. More recently, in [19, 20], it was proved that the LR equation, as well as two other versions of the equation for the surface waves, is valid for body waves too, and it became apparent that the conclusions of Molotovshchikov and Ruderman were erroneous. A more detailed examination showed that Molotovshchikov and Ruderman [21] considered an isolated magnetic flux tube that is not affected by the presence of a plasma around it, whereas all three versions of the LR equation were derived for waves in a tube affected by the external plasma. The waves in a magnetic flux tube that is affected by the external medium have properties very different from those of waves in an isolated tube. All of the presently known equations for body waves were derived from approximate dispersion relations that contradict the exact dispersion relation beyond the long-wavelength limit. Hence, in solving the problem for body waves, the task is the same as in the case of surface waves, namely, to obtain approximate dispersion relations for waves of arbitrary wavelength. This is the purpose of the present paper.
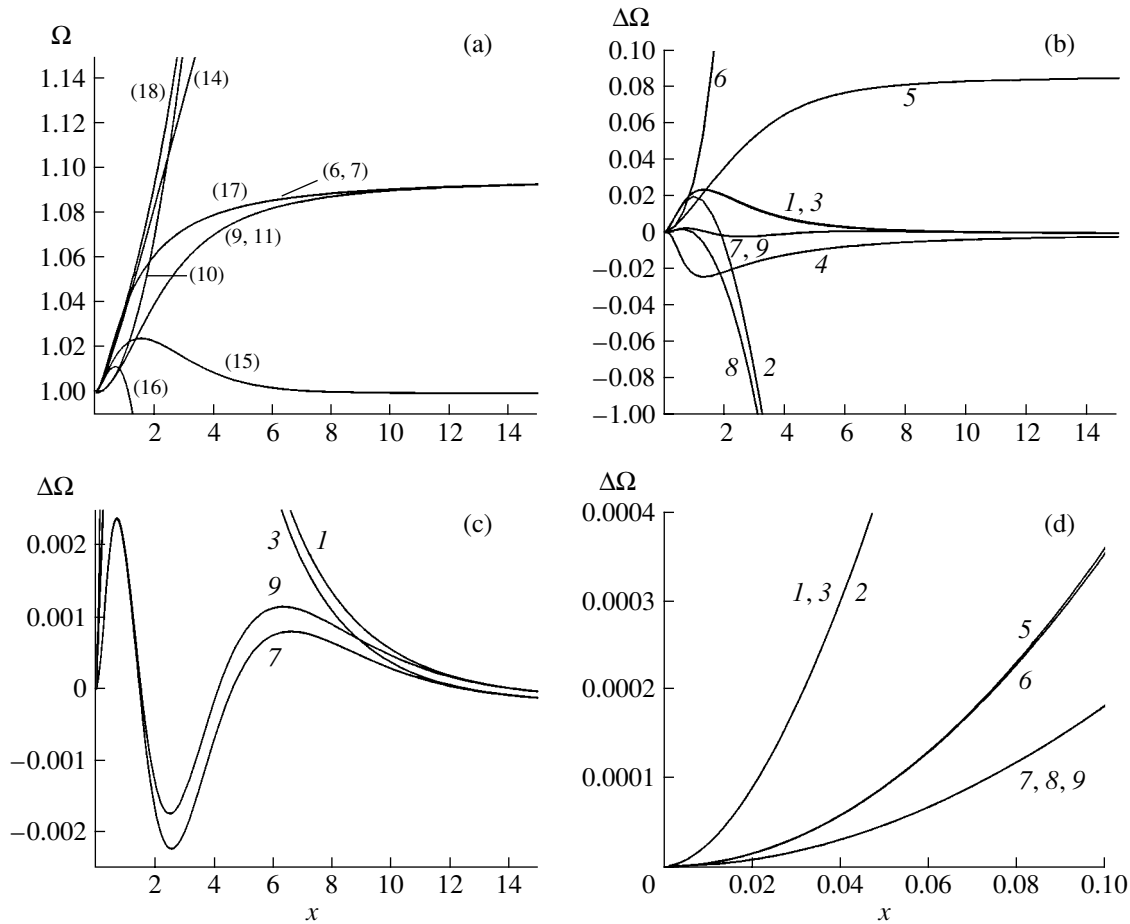
Fig. 1. (a) Exact dimensionless phase velocity of the body waves, $\Omega = V_{\mathrm{ph}}/C_T$, calculated from Eq. (6) and expression (7), and approximate phase velocities of the body waves, calculated from expressions (10), (11), and (15)–(18), as functions of the dimensionless wavenumber $x = kR_0$ for $\beta = 0.2$, $\beta_e = 0.01$, and $C_{Se}^2/C_S^2 = 2$. (b–d) Relative accuracy $\Delta\Omega = 1 - V_{\mathrm{ph}}^{\mathrm{aprx}}/V_{\mathrm{ph}}^{\mathrm{exact}} = 1 - \Omega^{\mathrm{aprx}}/\Omega^{\mathrm{exact}}$ of the approximate dispersion relations (i.e., their accuracy relative to exact dispersion relation (6)) as a function of $x = kR_0$. Curves *1–8* correspond, respectively, to approximate dispersion relations (9)–(11), (13), and (15)–(18). Curve *9* corresponds to dispersion relation (17), in which approximation (11) is replaced with solution (9) to the dispersion relation in the two-mode approximation.

Waves in magnetic flux tubes and slabs were explored in the ideal MHD approximation under the assumption that the plasma is isotropic, and it is only recently that the first papers on waves in an anisotropic plasma [26, 27] have appeared.

The first step in developing the theory of weakly nonlinear slow waves of arbitrary wavelength in magnetic flux tubes was made in my recent paper [28]. The present work is a continuation of that study.

In what follows, an analysis will be made of nonlinear slow waves beyond the long-wavelength limit. At first glance, it might seem impossible to find approximate dispersion relations for waves of arbitrary wavelength in magnetic flux tubes, because the exact dispersion relation, which contains Bessel functions, appears to be very complicated. Up to now, only asymptotic forms of the exact dispersion relation in the long-wave-

length limit have been used. We succeeded in finding fairly exact and, at the same time, quite simple approximate dispersion relations for body and surface waves. These dispersion relations made it possible to derive a new type of nonlinear evolutionary equations and even to obtain exact analytic solutions to some of them.

The next step in developing the theory of nonlinear waves will to be to study the breaking of nonlinear dispersive waves and the onset of shock waves. Until recently, all that was hitherto known about shock waves in magnetic flux tubes is the Hugoniot relations at the shock front, which were obtained in the thin-tube approximation [29, 30]. In what follows, an equation will be obtained that generalizes the Korteweg–de Vries–Burgers (KdVB) equation to waves of arbitrary wavelength. Exact analytic solutions to this equation
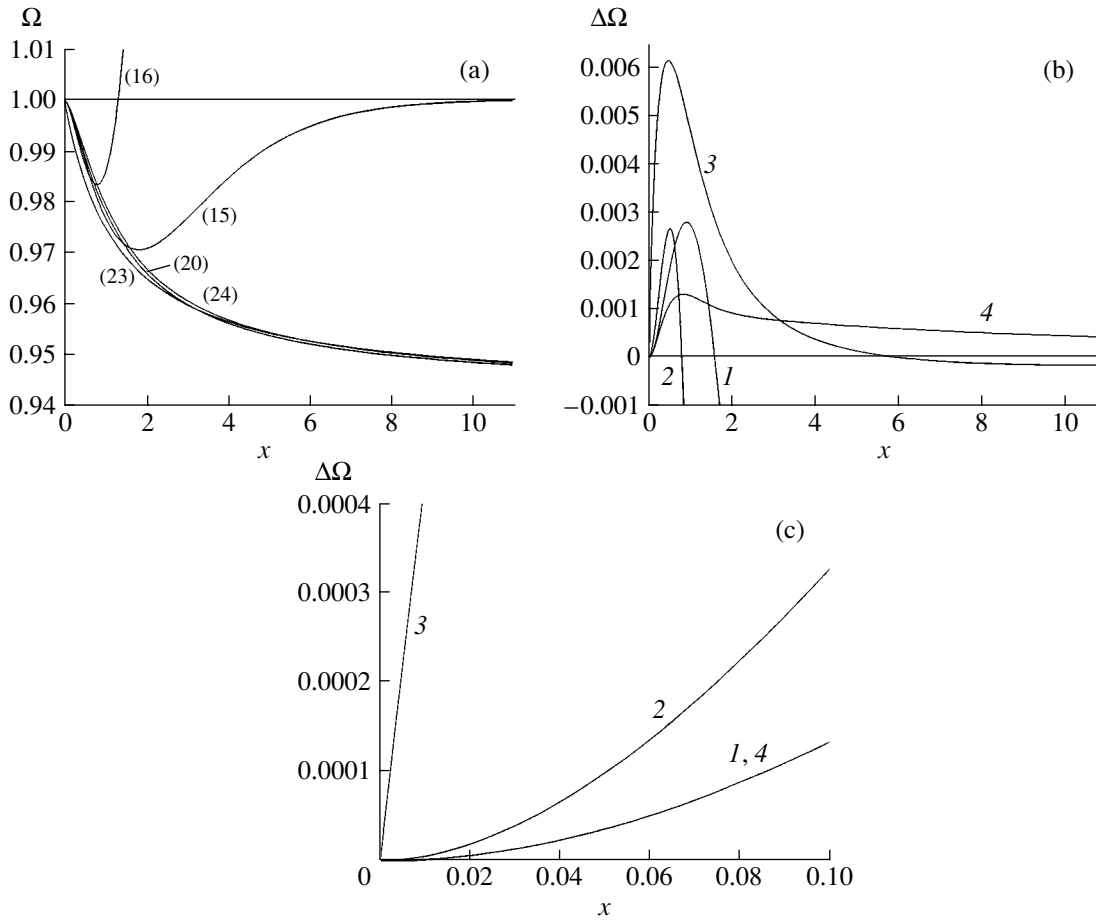
Fig. 2. (a) Exact dimensionless phase velocity of the surface waves, $\Omega = V_{ph}/C_T$, calculated from Eq. (20), and approximate phase velocities of the surface waves, calculated from expressions (15), (16), (23), and (24), as functions of the dimensionless wavenumber $x = kR_0$ for $\beta = 1.5$, $\beta_e = 15$, and $C_{Se}^2/C_S^2 = 2$. On the scale adopted in the figure, the dispersion curve calculated from approximate expression (24) is virtually indistinguishable from that calculated from exact equation (20). (b, c) Relative accuracy $\Delta\Omega = 1 - V_{ph}^{aprx}/V_{ph}^{exact} = 1 - \Omega^{aprx}/\Omega^{exact}$ of approximate dispersion relations (i.e., their accuracy relative to exact dispersion relation (6)) as a function of $x = kR_0$. Curves *1–4* correspond, respectively, to approximate dispersion relations (15), (16), (23), and (24).

show that not only shock waves but also nonlinear waves of the bore type can exist in magnetic flux tubes.

The purpose of this study is to elaborate approximate dispersion relations for waves of arbitrary wavelength. Here, use will be made of the same nonlinear term as in the entire theory of nonlinear waves in magnetic flux tubes. This term is evaluated in the long-wavelength approximation and therefore is incapable of taking into account nonlinear processes in the surrounding plasma. The latter circumstance may be a cause for concern, but it should be noted that the search for an approximate dispersion relation for nonlinear waves of arbitrary wavelength, as well as the allowance for the effect of the surrounding plasma on the dispersion properties of nonlinear waves in the tube, is the subject of a separate study.

2. DISPERSION OF SLOW WAVES IN MAGNETIC FLUX TUBES

The basic equation for axisymmetric waves in magnetic flux tubes is usually written in the form proposed by Edwin and Roberts [10]:

$$\frac{k^2 C_A^2 - \omega^2}{k^2 C_{Ae}^2 - \omega^2} m_e K_1(m_e R_0) \begin{pmatrix} J_0(n_0 R_0) \\ I_0(m_0 R_0) \end{pmatrix}$$

$$\mp n_0 \Delta K_0(m_e R_0) \begin{pmatrix} J_1(n_0 R_0) \\ I_1(m_0 R_0) \end{pmatrix} = 0,$$

$$m_0^2 = -n_0^2 = \frac{(\omega^2 - k^2 C_S^2)(\omega^2 - k^2 C_A^2)}{(C_S^2 + C_A^2)(k^2 C_T^2 - \omega^2)} > 0,$$

(1)

$$m_e^2 = \frac{(\omega^2 - k^2 C_{Se}^2)(\omega^2 - k^2 C_{Ae}^2)}{(C_{Se}^2 + C_{Ae}^2)(k^2 C_{Te}^2 - \omega^2)} > 0.$$

Here, J are Bessel functions, I and K are modified Bessel functions, R_0 is the tube radius, and the subscript e refers to the parameters of the external plasma. The condition for the total (gas-kinetic plus magnetic) pressure to be continuous at the tube boundary determines the ratio Δ of the plasma densities in the regions outside and inside the tube for given speeds of sound in these regions, C_S and C_{Se}, and given Alfvén speeds, C_A and C_{Ae}:

$$\Delta = \frac{\rho_{0e}}{\rho_0} = \frac{2C_S^2 + \gamma C_A^2}{2C_{Se}^2 + \gamma C_{Ae}^2}, \tag{2}$$

where $\gamma = c_p/c_v$. With the choice of the minus sign and the Bessel function J_0, Eq. (1) is the dispersion relation for body waves, and, with the choice of the plus sign and the modified Bessel function I_0, it is the dispersion relation for surface waves.

Equation (1) is so cumbersome that it cannot be converted into a wave equation and thereby cannot be directly incorporated into the theory of nonlinear waves. Up to now, use was made only of approximate expansions of Eq. (1) in the long-wavelength limit. The objective of this section is to describe a method for deriving such approximate dispersion relations for waves of arbitrary wavelength that can be transformed to a wave equation. This method was used to search for approximate dispersion relations for slow waves in magnetic flux tubes.

2.1. Body Waves

When the effect of the external medium is ignored and, accordingly, zero boundary conditions are imposed, Eq. (1) simplifies to

$$J_1(j) = 0, \quad j^2 = n_0^2 R_0^2. \tag{3}$$

The second of Eqs. (3) is a biquadratic equation for the frequency. Its solutions determine the frequencies of the fast and slow body waves in terms of the plasma parameters and the roots of the first of Eqs. (3). The frequency of the slow body waves can be expressed as

$$\omega_b^2 = 2k^2 C_T^2 \left(1 + \sqrt{1 - \frac{4C_T^2 k^2 R_0^2}{(C_A^2 + C_S^2)(k^2 R_0^2 + j^2)}}\right)^{-1}, \tag{4}$$

In searching for the asymptotic expressions for the frequency, this representation turned out to be the most convenient. The frequencies of the slow waves are found by substituting the roots $j = j_{1,n}$ of the Bessel function into formula (4), which then reads

$$\omega_{b,n} \approx C_T k \left(1 + \frac{C_T^2 k^2 R_0^2}{2(C_A^2 + C_S^2) j_{1,n}^2}\right). \tag{5}$$

In [19, 20], a method was proposed for reducing general equation (1) to equations of the form (3). To do this, it is sufficient to eliminate the frequency in Eq. (1) with the help of formula (4). It turns out that substituting different solutions to biquadratic equation (3) into Eq. (1) splits the latter into two separate equations for the slow and for the fast waves. This procedure yields the following equation for the slow body waves in a magnetic flux tube embedded in a magnetized plasma:

$$\frac{jJ_1(j)}{J_0(j)} = \frac{m_b x}{\Delta} \frac{C_A^2 - C_b^2}{C_{Ae}^2 - C_b^2} \frac{K_1(m_b x)}{K_0(m_b x)},$$

$$m_b^2 = \frac{(C_{Se}^2 - C_b^2)(C_{Ae}^2 - C_b^2)}{(C_{Se}^2 + C_{Ae}^2)(C_{Te}^2 - C_b^2)}, \quad x = kR_0, \tag{6}$$

$$C_b^2 = 2C_T^2 \left(1 + \sqrt{1 - \frac{4C_T^2 x^2}{(C_A^2 + C_S^2)(x^2 + j^2)}}\right)^{-1}. \tag{7}$$

Expression (7) for the phase velocity C_b of the body waves has been obtained from formula (4). It is this expression for the phase velocity that was found to be most optimal for numerical solution of Eq. (6). Substituting the roots of Eq. (6) into expressions (4) and (7) gives, respectively, the frequencies and phase velocities of the slow body waves. In contrast to the roots of Eqs. (3), the roots of Eq. (6) are functions of $x = kR_0$ and of the plasma parameters outside and inside the tube, $j = j(x, \beta_i, \beta_e, \delta)$, where $\beta_{i,e} = C_{S,Se}^2/C_{A,Ae}^2$, and $\delta = C_{Se}^2/C_S^2$. The roots of Eq. (6) exhibit very different behavior in the following two cases:

(i) If $\min(C_{Se}, C_{Ae}) < C_b < \max(C_{Se}, C_{Ae})$ and $0 \le kR_0 \le \infty$, then the roots of Eq. (6) vary within the range $j_{0,n} < j_n < j_{1,n}$.

(ii) If $C_b < C_{Te}$ and $0 \le kR_0 \le \infty$, then the minimum root of Eq. (6), which determines the frequency of the first ($n = 1$) mode, varies within the range $0 < j_1 < j_{0;1}$, whereas the roots of Eq. (6) that correspond to higher ($n > 1$) modes vary within the ranges $j_{1;n-1} < j_n < j_{0;n+1}$, where $j_{1,0;n}$ are the roots of the equation $J_{1,0}(j) = 0$.

In the short-wavelength limit $kR_0 \longrightarrow \infty$, the phase velocities of all the modes of the slow body waves approach the speed of sound, $C_b \longrightarrow C_S$. In this case, the second of Eqs. (3) reduces the equation $(V_{ph}^2 - C_S^2)(V_{ph}^2 - C_A^2) = 0$. The second solution to this equation, namely, $V_{ph} = C_A$, refers to the fast waves. In the long-wavelength limit $x = kR_0 \longrightarrow 0$, the phase velocity (7) of the body waves is approximately equal to

$$C_b \approx C_T \left(1 + \frac{C_T^2 x^2}{2(C_A^2 + C_S^2) j^2}\right). \tag{8}$$

Consequently, as the wavenumber increases from zero to infinity, $0 \leq x = kR_0 \leq \infty$, the phase velocities of all the modes of the slow body waves increase monotonically from the tube velocity C_T to the speed of sound C_S.

In contrast to surface waves, the main distinguishing feature of body waves is often considered to be the occurrence of the nodes of the radial wave function for the longitudinal velocity inside the magnetic flux tube. The presence of the nodes indicates, in particular, that the waves do not propagate exactly along the tube but instead undergo total internal reflection from the tube boundary, as, for example, in waveguides with perfectly reflecting walls. There is one exception to this, however. It turns out that, in the second of the above cases of the existence of real roots to Eq. (6), namely, for $V_{ph} < C_{Te}$, the first mode of the body waves does not have nodes within the tube, because the wave function for the longitudinal velocity is proportional to $J_0(jr/R_0)$ and the root j to Eq. (6) is always less than the first root of the function J_1. It is this first mode of the body waves at $V_{ph} < C_{Te}$ that is the subject of exploration in nonlinear theory since only in this case are the equations of the problem dealing with a wave running along a magnetic flux tube, and thus they can be reduced to a one-dimensional wave equation. This mode can exist because the tube is an open waveguide, i.e., the field lines emerge from the tube. A detailed analysis of the first mode of the body waves is necessary in order to eliminate the confusion created because, on the one hand, this mode was not described in the fundamental paper by Edwin and Roberts [10] and, on the other hand, Molotovshchikov and Ruderman [21] asserted that body waves rapidly become shock waves since they run radially within a magnetic flux tube while undergoing reflections from its wall.

Dispersion relation (6) with expression (7) is too complicated to serve as the basis for deriving the corresponding one-dimensional wave equation for the first mode of the body waves in the case $C_b < C_{Te}$. It can, however, be simplified substantially by linearizing the two-mode approximation for body waves [14]. The resulting approximate dispersion relation

$$x^2\omega^4 - (4 + x^2)(C_S^2 + C_A^2)k^2\omega^2 + (4 + x^2)C_S^2 C_A^2 k^4 = 0$$

coincides with the second of Eqs. (3) with the substitution $j = 2$, and the approximate expression for the frequency of the slow body waves is found from formula (4), which, after the same substitution, reads

$$\omega_b = kC_T\left(2\left(1 + \sqrt{1 - \frac{4C_T^2 x^2}{(C_A^2 + C_S^2)(x^2 + 4)}}\right)^{-1}\right)^{\frac{1}{2}}. \quad (9)$$

This is typical geometric dispersion, which gives the dependence of the wave frequency on the plasma parameters within the tube and on $x = kR_0$ (i.e., on the ratio of the wavelength to the tube diameter). In the long-wavelength limit, dispersion relation (9) for the

frequency of the body waves can be significantly simplified:

$$\omega_b \approx kC_T(1 + \lambda x^2), \quad \lambda = \frac{C_T^2}{8(C_A^2 + C_S^2)}. \quad (10)$$

In [14], it was shown that the inaccuracy of this approximate dispersion relation arises as a result of ignoring the wave dispersion introduced by the external medium. The geometric dispersion of body waves is far greater than that due to the response of the external medium because the field of the body waves is concentrated mainly within the tube and is insignificant in the surrounding plasma. It is for this reason that the two-mode approximation is quite exact almost over the entire wavelength range. In [25], this simple approximate dispersion relation (10) made it possible to derive the KdV equation for body waves in the long-wavelength limit. Dispersion relation (9) for body waves of arbitrary wavelength was obtained in the two-mode approximation and thus cannot be transformed to a wave equation with which to obtain an evolutionary equation. A simple approximate dispersion relation for body waves of arbitrary wavelength was proposed in my recent paper [28]:

$$\omega_b \approx kC_T\left(1 + \frac{(C_S - C_T)\lambda x^2}{C_S - C_T + \lambda C_T x^2}\right), \quad (11)$$

In that paper, it was found that this approximate dispersion relation, which was not derived rigorously but was simply guessed intuitively, can easily be converted into a wave equation. It turns out, however, that this approximate dispersion relation for body waves, as well as more exact dispersion relations of the form

$$\omega_b \approx kC_T\left(1 + \frac{(C_S - C_T)\sum_{n=1}^{N}\lambda_n x^{2n}}{C_S - C_T + C_T\sum_{n=1}^{N}\bar{\lambda}_n x^{2n}}\right), \quad (12)$$

can be derived in a fairly simple way. It is sufficient to expand dispersion relation (9) and approximate dispersion relation (12) in powers of x and $1/x$ and to equate the coefficients of the same powers of x and of $1/x$ up to Nth power in the expansions. The resulting set of equations for the coefficients λ and $\bar{\lambda}$ turns out to be overdetermined, necessitating that the equation for $1/x^{2n}$ be discarded. A similar approximation can be obtained by omitting the equation for x^{2n}. Thus, the resulting approximate dispersion relation for $N = 1$ reads

$$\omega_b \approx kC_T\left(1 + \frac{(C_S - C_T)\bar{\lambda}x^2}{C_T + C_T\bar{\lambda}x^2}\right),$$

$$\bar{\lambda} = \frac{(C_A^2 - C_S^2)C_T}{2C_S^3}. \quad (13)$$

Dispersion relations (11) and (13) differ from one another in the accuracy with which they approximate dispersion relation (9) in the long- and short-wavelength ranges. Dispersion relation (11) approximates dispersion relation (9) to within terms on the order of x^4 in the long-wavelength range and to within terms on the order of $1/x^2$ in the short-wavelength range. In contrast, dispersion relation (13) yields a more accurate approximation, on the order of $1/x^4$, in the short-wavelength range and a less accurate approximation, on the order of x^2, in the long-wavelength range. In order to approximate dispersion relation (9) at least with fourth-order accuracy over the entire wavelength range, it is necessary to use one of the two possible approximate dispersion relations with $N = 2$.

The drawback of dispersion relation (11) is that it does not take into account the wave dispersion introduced by the external medium. An approximate relation for the dispersion of body waves due to the response of an external medium was obtained in [19, 20]:

$$\omega_{b,\,\mathrm{srf}} \approx k C_T \left(1 + \frac{A x K_0(mx)}{m K_1(mx)} \right), \tag{14}$$

$$A = \frac{\Delta}{4}\left(\frac{C_T}{C_A}\right)^4\left(\frac{C_{Ae}^2}{C_T^2} - 1\right), \quad m^2 = \frac{(C_{Se}^2 - C_T^2)(C_{Ae}^2 - C_T^2)}{(C_{Ae}^2 + C_{Se}^2)(C_{Te}^2 - C_T^2)}.$$

This dispersion relation is valid not only for body waves but also for the surface waves ($C_{Ae} < C_{\mathrm{srf}} < C_{Se}$), which will be discussed in the next section. A particular case of this dispersion relation for surface waves in a magnetic flux tube surrounded by an unmagnetized plasma was derived by Roberts [16] in his first paper on nonlinear waves in magnetic flux tubes, and Molotovshchikov and Ruderman [21] used dispersion relation (14) to obtain an equation for the surface waves in the case of a magnetized surrounding plasma. In [19, 20], as well as in [16], the LR equation was generalized to this latter case with the help of the approximate dispersion relation

$$\omega_{b,\,\mathrm{srf}} \approx k C_T (1 + A x^2 K_0(mx)), \tag{15}$$

which follows from relation (14) with allowance for the fact that $m x K_1(mx) \longrightarrow 1$ as $x \longrightarrow 0$. In accordance with Pritchard's idea [22], replacing the modified Bessel function with the leading-order logarithmic term of its asymptotic expansion reduces dispersion relation (15) to

$$\omega_{b,\,\mathrm{srf}} \approx k C_T \left(1 + 2\chi x^2 \left(\ln\frac{mx}{2} + E \right) \right),$$
$$\chi = \frac{\Delta C_T^2 (C_T^2 - C_{Ae}^2)}{8 m C_A^4}, \tag{16}$$

where E is Euler's constant. It is precisely these three dispersion relations (14)–(16) that underlie the above three asymptotically equivalent equations for the body and surface waves in magnetic flux tubes, as was discussed in the Introduction.

The question now arises of which of the three relations (14)–(16) correctly describes the dispersion of waves of arbitrary wavelength due to the response of the external medium. Approximate dispersion relations (14) and (16) imply that the wave phase velocity increases without bound with increasing tube thickness or, equivalently, with decreasing wavelength. This prediction contradicts the fact that the phase velocity of the body waves approaches the speed of sound as $x \longrightarrow \infty$. It has been pointed out above that, according to approximate dispersion relation (15), the phase velocity in the short-wavelength limit $x \longrightarrow \infty$ approaches the tube velocity C_T and, consequently, the external plasma has no effect in this limit, as it ought to be. This means that approximate dispersion relation (15) gives an adequate description of the effect of the external plasma on the body waves in magnetic flux tubes. Hence, we have relation (11) for the geometric dispersion of waves of arbitrary wavelength, which dominates for $x \gg 1$, and relation (15) for the dispersion of waves of arbitrary wavelength, which arises as a result of the response of the external medium and dominates for $x \ll 1$. Since the total dispersion is a superposition of these two dispersions, it is natural to combine the two dispersion relations as follows:

$$\omega_b \approx k C_T \left(1 + \frac{(C_S - C_T)\lambda x^2}{C_S - C_T + C_T \lambda x^2} + A x^2 K_0(mx) \right). \tag{17}$$

This approximate dispersion relation turns out to be the best of all known relations, in particular, in the long-wavelength limit (see Fig. 1). In the long-wavelength range, dispersion relation (17) can be simplified to the relation

$$\omega_b \approx k C_T (1 + \lambda x^2 + A x^2 K_0(mx)), \tag{18}$$

which yields even greater accuracy in this limit but is disadvantageous in that the phase velocity increases without bound for large kR_0 values. It is important to note that approximate dispersion relation (18) can be immediately derived from Eq. (6) and expression (7) in the long-wavelength limit. This is an independent confirmation of the validity of summing the two dispersions, as is done in relation (17). The approximate dispersion relations for all other body modes in the long-wavelength limit are also obtained from exact dispersion relation (6) and expression (7):

$$\omega_{b,\,n} \approx k C_T (1 + \lambda_n x^2 + A_n x^2 K_0(mx)),$$
$$\lambda_n = \frac{4\lambda}{(j_{1,\,n-1} + \sqrt{2})^2}, \quad A_n = \frac{4 j_{1,\,n-1} A}{j_{1,\,n-1} + \sqrt{2}}, \tag{19}$$
$$\text{for} \quad n > 1.$$

Hence, the dispersion of all the modes of body waves can be described as the sum of the dispersion due to the response of an external medium and the conventional geometric dispersion, the former dominating in the long-wavelength range and the latter dominating in the remaining wavelength range. For modes higher than the first one, approximate dispersion relations similar to relations (11) and (17) can be obtained through the replacements $\lambda \longrightarrow \lambda_n$ and $A \longrightarrow A_n$.

A comparison of dispersion relations (18) and (19) to dispersion relation (5) for waves in an isolated magnetic flux tube shows that the wave dispersions differ not only because of the response of the external medium but also because of the differences in the geometric dispersion properties of the body waves. This explains why, as has already been pointed out in the Introduction, the conclusion of Molotovshchikov and Ruderman [21] that dispersive body waves do not exist is valid only for an isolated magnetic flux tube. In fact, they derived their equation with allowance for only geometric dispersion relation (5), which refers exclusively to this case.

In order to compare different approximate dispersion relations, Fig. 1a presents the results of calculating the wave dispersion from exact equation (6) and from approximate relations (9)–(11), (13), and (15)–(18) for plasma parameters characteristic of the solar corona. From Fig. 1b we can see that approximate dispersion relation (11) is fairly exact over the entire wavelength range, although, in the long-wavelength range, it is less accurate than the known relations (15) and (16). As for approximate dispersion relation (17), which takes into account the geometric dispersion and the dispersion due to the response of an external medium, it is seen to be more accurate than all other known approximate relations over the entire wavelength range. From Fig. 1c we see that dispersion relation (11) and the two-mode approximation provide essentially the same accuracy. In the long-wavelength range, which is illustrated in Fig. 1d, all of the approximate dispersion relations can be divided into three groups. First, in this range, the accuracy of approximate dispersion relation (11), and, accordingly, of its long-wavelength asymptotic (10), is lowest. Second, high accuracy is provided by the known approximate dispersion relations (15) and (16), which essentially coincide in the long-wavelength range. Finally, the accuracy of the newly proposed approximate dispersion relation (17) and its asymptotic (18) is greatest. An unexpected result is that, in the short-wavelength range, the second of the possible approximate dispersion relations (12), namely, relation (13) with $N = 1$, which is shown by curve *4* in Fig. 1b, turns out to be less accurate than relation (11).

All of the above approximate dispersion relations (11), (17), and (18) for body waves are simple enough to be used to derive new nonlinear evolutionary equations.

2.2. Surface Waves

Similar to body waves, dispersion relation (1) for surface waves in magnetic flux tubes is rewritten as

$$\frac{C_A^2 - C_{\mathrm{srf}}^2}{C_{Ae}^2 - C_{\mathrm{srf}}^2} m_s x \frac{K_1(m_s x)}{K_0(m_s x)} + j\Delta \frac{I_1(j)}{I_0(j)} = 0,$$

$$j = m_0 R_0, \quad m_s^2 = \frac{(C_{Se}^2 - C_{\mathrm{srf}}^2)(C_{Ae}^2 - C_{\mathrm{srf}}^2)}{(C_{Se}^2 + C_{Ae}^2)(C_{Te}^2 - C_{\mathrm{srf}}^2)}, \quad (20)$$

$$C_{\mathrm{srf}}^2 = 2C_T^2 \left(1 + \sqrt{1 - \frac{4C_T^2 x^2}{(C_A^2 + C_S^2)(x^2 - j^2)}}\right)^{-1},$$

where C_{srf} is the phase velocity of the surface waves, which is a function of j, x, and of the plasma parameters. Dispersion relation (20) has a solution only under the condition $C_{Ae} < V_{\mathrm{ph}} < C_{Se}$. The only root of this dispersion relation increases from zero to infinity, $0 \le j \le \infty$ as the dimensionless wavenumber changes in the range $0 \le kR_0 \le \infty$. The frequency of the surface waves is expressed through the root of dispersion relation (20) and through the plasma parameters as

$$\omega_{\mathrm{srf}}^2 = 2k^2 C_T^2 \left(1 + \sqrt{1 - \frac{4C_T^2 x^2}{(C_A^2 + C_S^2)(x^2 - j^2)}}\right)^{-1}. \quad (21)$$

As the wavenumber increases, the phase velocity of the surface waves decreases monotonically from the tube velocity C_T to the phase velocity at the discontinuity, C_{intf}, satisfying the equation

$$\frac{V_A^2 - C_{\mathrm{intf}}^2}{V_{Ae}^2 - C_{\mathrm{intf}}^2} \frac{m_1}{m_2} + \Delta = 0,$$

$$m_{1,2}^2 = \frac{(C_{Se,S}^2 - C_{\mathrm{intf}}^2)(V_{Ae,A}^2 - C_{\mathrm{intf}}^2)}{(C_{Se,S}^2 + V_{Ae,A}^2)(C_{Te,T}^2 - C_{\mathrm{intf}}^2)}, \quad (22)$$

which is the limiting case of dispersion relation (20) in the short-wavelength range because

$$\frac{K_1(m_e x)I_0(m_0 x)}{K_0(m_e x)I_1(m_0 x)} \longrightarrow 1 \quad \text{at} \quad x \longrightarrow \infty.$$

As was mentioned above, the three dispersion relations (14)–(16) for long-wavelength body waves are also valid for long-wavelength surface waves. For surface waves of arbitrary wavelength, however, there exists no approximation similar to the above two-mode approximation, which helped to find the approximate dispersion relation for body waves of arbitrary wavelength. Nonetheless, we succeeded in finding a fairly simple and, at the same time, quite exact approximate dispersion relation for the surface waves:

$$\omega_{\mathrm{srf}} \approx kC_T \left(1 + \frac{(C_T - C_{\mathrm{intf}})A|x|}{(C_T - C_{\mathrm{intf}}) - AC_T|x|}\right). \quad (23)$$

This relation yields a correct phase velocity for the surface waves in the long-wavelength limit: $V_{ph} \longrightarrow C_T$ as $x \longrightarrow 0$ (Fig. 2a). Although, in the long-wavelength range, approximate dispersion relation (23) is far less accurate than relations (14)–(16), it is valid for surface waves of arbitrary wavelength and thereby makes it possible to correctly handle the long-wavelength limit, in contrast to approximate dispersion relations (14)–(16), which yield incorrect phase velocities of the surface waves in short-wavelength limit. According to relations (14)–(16), the phase velocity of the surface waves in the short-wavelength limit $x \longrightarrow \infty$ approaches either infinity or the tube velocity, rather than the phase velocity at the discontinuity, C_{intf}, as it ought to be.

The idea of approximate dispersion relation (23) stems from the properties of approximate dispersion relation (14) for short-wavelength body waves. The point is that the second term in parentheses in relation (14) is approximately proportional to the dimensionless wavenumber, $AxK_0(mx)/(mK_1(mx)) \approx A|x|$. It is not surprising that the accuracy of approximate dispersion relation (23) in the long-wavelength range is low, since it is based on approximate dispersion relation (14) for short-wavelength waves. In order to increase the accuracy in the long- and intermediate-wavelength ranges, it is natural to switch from relation (23) to the approximate dispersion relation

$$\omega_{srf} \approx kC_T\left(1 + \frac{(C_T - C_{intf})AxK_0(mx)}{(C_T - C_{intf})mK_1(mx) - C_TAxK_0(mx)}\right), \quad (24)$$

which, for long-wavelength waves, coincides with dispersion relation (14). In the long-wavelength limit $x \leq 0.1$, all four approximate dispersion relations (14)–(16) and (24) are asymptotically equivalent, but only relation (24) yields a correct short-wavelength limit.

All of the approximate dispersion relations that were discussed above take into account only the wave dispersion due to the response of an external medium. This does not imply, however, that the surface waves are not subject to geometric dispersion. It turns out that asymptotic (18) of the dispersion relation in the long-wavelength limit is valid not only for body but also for surface waves, because it can be immediately derived from exact dispersion relation (20). In contrast to the case of body waves, the total dispersion of surface waves is dominated by the response of the external medium not merely in the long-wavelength limit but over the entire wavelength range. In the short-wavelength limit, the geometric dispersion is generally unimportant because a short-wavelength surface wave is a wave at a curved boundary between the internal and the external plasma.

In order to compare different approximate dispersion relations, Fig. 2a shows the results of calculating the wave dispersion from exact relation (20) and from approximate relations (15), (16), (23), and (24) for plasma parameters characteristic of the solar corona. From Fig. 2b we can see that, in the long-wavelength range, dispersion relation (23) for waves of arbitrary wavelength is far less accurate than approximate dispersion relations (15), (16), and (24). The accuracy of more complicated approximate dispersion relation (24) for waves of arbitrary wavelength is high over the entire wavelength range, but it is somewhat lower than that of approximate dispersion relation (23) in the short-wavelength limit. From Fig. 2c we see that, in the long-wavelength range, dispersion relation (16) is far less accurate than dispersion relations (24) and (15). This indicates that replacing the modified Bessel function with its asymptotic expansion results in a serious loss of accuracy. The dispersion of surface waves is almost completely dominated by the response of the external medium, which is reflected in the dependence of the parameter A in relation (15) on the parameters of the surrounding plasma. For body waves, the parameter λ in relation (10) is independent of the parameters of the external medium, so, in order for the external response to be taken into account, it was necessary to add dispersion relation (15) to dispersion relation (11). For surface waves, the simple approximate dispersion relation (23) ought to be made more complicated. Nevertheless, as will be clear later, both approximate dispersion relations (23) and (24) can be used in nonlinear theory.

3. NONLINEAR SLOW WAVES

All of the presently known nonlinear evolutionary equations for slow waves in magnetic flux tubes were obtained in the different long-wavelength approximations that have been mentioned above. The nonlinear terms in these equations are the same. The objective of this paper is to obtain evolutionary equations for waves of arbitrary wavelength from the above approximate dispersion relations (11), (17), (18), and (23), which are valid over the entire wavelength range.

3.1. Body Waves

The nonlinear evolutionary equation contains dispersion terms and a nonlinear term. The nonlinear term for the surface waves was obtained by Roberts [16] in the thin-tube approximation [12]. In [14], it was shown that the thin-tube approximation is valid not only for an unmagnetized surrounding plasma (the case considered by Roberts) but also for a magnetized surrounding plasma. Consequently, the nonlinear term for the body waves coincides with the nonlinear term obtained by Roberts for the surface waves. The nonlinear term evaluated in [25] in the two-mode approximation [13, 14] also coincides with Roberts's nonlinear term. In what follows, the expression for the nonlinear term that was obtained in [25] will be used for both body and surface waves.

The wave equation can be obtained from dispersion relation (11) for the body waves through the replacements $\frac{\partial}{\partial t} \longleftrightarrow i\omega$ and $\frac{\partial}{\partial z} \longleftrightarrow ik$ (see [31], p. 367). In this case, dispersion relation (11) should be rewritten as

$$\omega_D\left(1 + \frac{\hat{\lambda}C_T k^2}{C_S - C_T}\right) - \hat{\lambda}C_T k^3 = 0, \quad (25)$$

$$\omega_D = \omega - kC_T, \quad \hat{\lambda} = \lambda R_0^2,$$

where ω_D is the frequency in a frame of reference moving with the velocity C_T (this reference frame is usually used to derive nonlinear evolutionary equations for waves in magnetic flux tubes). Dispersion relation (25) leads to the evolutionary equation

$$\frac{\partial B}{\partial \tau} - \frac{\hat{\lambda}C_T}{C_S - C_T}\frac{\partial^3 B}{\partial \tau \partial z^2} - \hat{\lambda}C_T\frac{\partial^3 B}{\partial z^3} - \epsilon B\frac{\partial B}{\partial z} = 0, \quad (26)$$

where λ is to be found from dispersion relation (11) and the coefficient ϵ in front of the nonlinear term,

$$\epsilon = \frac{C_A^2}{B_0}\frac{(3C_S^2 + (\gamma + 1)C_A^2)C_T}{2C_S^2(C_S^2 + C_A^2)}, \quad (27)$$

coincides exactly with the corresponding term in the KdV equation derived in [25] for the surface waves. In Eq. (26), as well as in the KdV equation [25], the dependent variable is the longitudinal magnetic field perturbation B. In the long-wavelength limit, the second term in Eq. (26) should be omitted and, hence, Eq. (26) is reduced to the KdV equation. This correspondence makes it possible to uniquely choose the nonlinear term in Eq. (26). The nonlinear term that was obtained for the KdV equation [14, 25] was used to derive Eq. (26), which was thus obtained without using the long-wavelength approximation for the wave dispersion.

Evolutionary equation (26) has two distinct exact solutions for a solitary wave, which look like typical soliton solutions. At first glance, the solution of the first kind is similar to the solution to the KdV equation,

$$B = B_a \mathrm{sech}^2((z + V\tau)/L), \quad B_a > 0, \quad (28)$$

$$V = \frac{\epsilon B_a}{3}, \quad L = 2\sqrt{\frac{\hat{\lambda}C_T(3(C_S - C_T) + \epsilon B_a)}{\epsilon B_a(C_S - C_T)}}. \quad (29)$$

The condition $B_a > 0$ implies that the solitary wave is a contraction of a magnetic flux tube because, under the magnetic flux conservation condition, an increase in the longitudinal magnetic field, $B_0 + B$, is possible only for a smaller tube cross section. A wave of this kind is a contraction running along a magnetic flux tube. For sufficiently small wave amplitudes such that $B_a \ll 3(C_S - C_T)/\epsilon$, solution (28) is reduced to the solution to the KdV equation derived in [25]. A distinctive feature of

solution (28) (as compared to the solution to the KdV equation) is that the width L approaches a finite limiting value $L = 2\sqrt{\hat{\lambda}C_T/(C_S - C_T)}$ as the amplitude B_a of the solitary wave increases. In the laboratory frame of reference, the wave velocity is equal to $C_T - V$; i.e., it is always lower than the tube velocity.

The second exact solution to Eq. (26), namely,

$$B = -B_a \mathrm{sech}^2((z - V\tau)/L), \quad B_a > 0, \quad (30)$$

$$V = \frac{\epsilon B_a}{3}, \quad L = 2\sqrt{\frac{C_T\hat{\lambda}(\epsilon B_a - 3(C_S - C_T))}{\epsilon B_a(C_S - C_T)}}, \quad (31)$$

also looks like a typical soliton solution but, in contrast to solution (28), it corresponds to a bulge running along the tube with the velocity $C_T + V$ in the laboratory frame of reference. This solution is possible only for sufficiently large wave amplitudes B_a, greater than the critical amplitude $B_a^{(\mathrm{cr})}$,

$$\frac{B_a^{(\mathrm{cr})}}{B_0} = \frac{3(C_S - C_T)}{\epsilon B_0} \overset{\beta \ll 1}{\approx} \frac{3\beta^2}{\gamma + 1}, \quad (32)$$

where $\beta = C_S^2/C_A^2$. The characteristic width L of a solitary wave equals zero for the critical wave amplitudes $B_a = B_a^{(\mathrm{cr})}$. For wave amplitudes smaller than the critical amplitude $B_a^{(\mathrm{cr})}$, this solution is singular because $L^2 < 0$. For $B_a = B_a^{(\mathrm{cr})}$, the nonlinear correction to the wave velocity is equal to $C_S - C_T$. Consequently, in the laboratory frame, the velocity of a nonlinear solitary bulge wave is always higher than the speed of sound. Hence, for wave amplitudes greater than the critical amplitude $B_a^{(\mathrm{cr})}$, two types of nonlinear body waves can exist, namely, contractions and bulges, both of which run along the magnetic flux tube.

3.1.1. Canonical equation. To explore the general properties of nonlinear equations that appear in different physical problems, we reduce them by means of the coordinate transformations to what is usually called the canonical form—the simplest form with the smallest possible number of parameters [32]. Equation (26) is an evolutionary equation for waves described by the dispersion relation

$$\omega = kC_1 \pm \frac{C_1\tilde{\lambda}k^3}{1 \pm \tilde{\lambda}k^2 C_1/(C_2 - C_1)}, \quad (33)$$

$$\tilde{\lambda} > 0, \quad C_2 \gtrless C_1,$$

where C_1 and C_2 are the wave phase velocities at $k \longrightarrow 0$ and $k \longrightarrow \infty$, respectively. By an appropriate coordinate transformation, the evolutionary equation corresponding to dispersion relation (33) can be brought to the canonical form

$$u_t - au_{txx} \pm u_{xxx} - 6uu_x = 0, \qquad (34)$$

where $a = C_1/|C_2 - C_1|$. To the best of my knowledge, evolutionary equations like Eq. (34) have not yet appeared in the theory of nonlinear waves [32]. Equation (34) has two distinct nonsingular soliton solutions for waves with a normal and an anomalous dispersion, respectively,

$$u = \pm 2B^2 \operatorname{sech}^2 \frac{Bx \pm 4B^3 t}{\sqrt{4aB^2 \mp 1}}, \qquad (35)$$

$$u = \mp 2B^2 \operatorname{sech}^2 \frac{Bx \mp 4B^3 t}{\sqrt{4aB^2 \pm 1}}. \qquad (36)$$

One of the solutions (35) and (36) becomes singular at $4aB^2 \leq 1$.

Along with the solutions corresponding to solitary waves, Eq. (34) has two distinct periodic solutions for the so-called cnoidal waves. These solutions are expressed in terms of Jacobi's elliptic functions,

$$u = \pm 2B^2 \operatorname{cn}[K(m)/\pi(kx + \omega t)|m],$$

$$V_{\mathrm{ph}} = \pm \frac{4B^2(2m^2 - 1)}{m}, \qquad (37)$$

$$\frac{k^2 K(m)^2}{\pi^2} = \frac{B^2}{4aB^2(2m^2 - 1) - m^2},$$

$$u = \mp 2B^2 \operatorname{cn}[K(m)/\pi(kx + \omega t)|m],$$

$$V_{\mathrm{ph}} = \mp \frac{4B^2(2m^2 - 1)}{m}, \qquad (38)$$

$$\frac{k^2 K(m)^2}{\pi^2} = \frac{B^2}{4aB^2(2m^2 - 1) + m^2},$$

where $K(m)$ is the complete elliptic integral of the first kind. In the limit $m \longrightarrow 1$, these solutions pass over to solutions (35) and (36) because $kK(m)/\pi \longrightarrow B/\sqrt{4aB^2 \pm 1}$. The cnoidal waves are running waves in the form of alternating contractions and bulges. The difference between two periodic solutions (37) and (38) lies in the relationship between the lengths of the contractions and bulges. In one of the two possible kinds of cnoidal waves, the contractions are longer than the bulges, and vice versa in the other type.

Equation (34) cannot be reduced to any of the known evolutionary equations but it includes two widely used evolutionary equations as particular cases.

For sufficiently small amplitudes ($a \longrightarrow 0$) such that $4aB^2 \ll 1$, Eq. (34) is reduced to the KdV equation; hence, only one of solutions (35) and (36) is nonsingular in this case. Equation (34) in which the term with the third derivative is omitted and it is assumed that $a = 1$ becomes the so-called long-wavelength equation, arising in the theory of waves on the surfaces of liquids [33]. This long-wavelength equation, which is also known as the Benjamin–Bona–Mahony (BBM) equation, corresponds to the dispersion relation $\omega = k/(1 + k^2)$. Of course, the solutions to the KdV equation differ from those to the BBM equation. This is due to the fact that the KdV and BBM equations are particular cases of Eq. (34), which has two different kinds of solutions for both solitary waves and cnoidal waves. This is a good ground to assert that Eq. (34) belongs to a special class of evolutionary equations.

Solutions (35) and (36) to Eq. (34) look like the well-known solutions to the KdV equation and differ from them only in the width of the solitons. The difference $(1 - \sqrt{1 - 4aB^2})/B \approx 2aB$ between one of solutions (35) and (36) and the solution to the KdV equation tends to zero as $aB^2 \longrightarrow 0$, which nothing but the long-wavelength limit. The same property holds for the solutions to the KdV and BBM equations. The BBM equation does not belong to the class of completely integrable equations [34]. The solitary waves described by this equation change their amplitudes after the interaction and acquire an oscillating tail. There is no doubt that Eq. (34), too, does not belong to the class of completely integrable equations, because it includes the BBM equation as a particular case. Thus, solutions (35) and (36) to Eq. (34) are not soliton solutions. However, in order to analyze the question of whether the solution is a soliton or not, it is first of all necessary to determine what is the purpose of the analysis: to establish whether the equation belongs to the class of completely integrable equations or whether the properties of a solitary wave that is actually observed in nature are well described by the equation. There are reasons to argue that, in contrast to the commonly accepted view, a solitary wave discovered in 1834 by J.S. Russell [35] is not, strictly speaking, a soliton, because the KdV equation that has an exact soliton solution and is traditionally mentioned in connection with the solitary wave discovered by Russell is a model equation based on an approximate dispersion relation. The model BBM equation [33], which is based on a more exact dispersion relation than that underlying the KdV equation, has a solution differing from the exact soliton solution, as was mentioned above [34]. It is also known that the Boussinesq equation (see [31], Section 13.11) is based on an even more exact dispersion relation for waves on the surfaces of liquids. Moreover, an equation is known that is based on the exact dispersion relation (see [31], Section 13.14). The solutions to the last two equations are not solitons, although, in the long-wavelength limit, they differ insignificantly from the soliton solution to

the KdV equation. Consequently, J.S. Russell observed not a soliton but rather a solitary wave with parameters very close to those of a soliton. It is not always possible to notice a slight difference between the widths of the solitary wave observed by Russell and of the soliton described by the exact solution to the KdV equation. This is why, in each specific case, the task is to find out whether or not the observed wave is a soliton within the accuracy of observations, measurements, or numerical experiments. A comparison between the solutions to, e.g., the KdV, BBM, and Boussinesq equations is aimed, in particular, at determining how much the parameters of a solitary wave differ from those of an ideal soliton in order to estimate the experimental accuracy required to reveal this difference. Based on what was said above, it can be stated that solutions (35) and (36) to Eq. (34) are very similar to solitons. Moreover, in the long-wavelength limit, one of these solutions approaches the solution to the KdV equation. In order to determine the extent to which solutions (35) and (36) differ from the soliton solutions, it is necessary to carry out explorations similar to those done for the BBM equation [34].

3.1.2. Generalized equation. Equation (26) does not take into account the effect of the external plasma on the dispersion of body waves. This disadvantage was overcome by using approximate dispersion relation (17). In this case, the evolutionary equation contains additional integral dispersion terms inherent in the LR equation:

$$\frac{\partial B}{\partial \tau} + \frac{\hat{\lambda} C_T}{C_S - C_T}\frac{\partial^3 B}{\partial \tau \partial z^2} - \hat{\lambda} C_T \frac{\partial^3 B}{\partial z^3} - \epsilon B \frac{\partial B}{\partial z}$$
$$+ \Delta_T \left(\frac{\partial^3}{\partial z^3} + \frac{\hat{\lambda} C_T}{C_S - C_T}\frac{\partial^5}{\partial z^5} \right) \int_{-\infty}^{+\infty} \frac{B(z', t)dz'}{[\alpha^2 + (z' - z)^2]^{1/2}} = 0, \tag{39}$$

where

$$\Delta_T = \frac{1}{8}\left(\frac{C_T}{C_A}\right)^4 \left(1 - \frac{C_{Ae}^2}{C_T^2}\right)\frac{\rho_{0e}}{\rho_0}k^2 C_T R_0^2, \tag{40}$$

$$\alpha^2 = m^2 R_0^2 = \frac{(C_{Se}^2 - C_T^2)(C_{Ae}^2 - C_T^2)}{(C_{Ae}^2 - C_{Se}^2)(C_{Te} - C_T^2)}R_0^2. \tag{41}$$

Equation (39) is the most general of the presently known nonlinear evolutionary equations for slow body waves in magnetic flux tubes. This equation, which includes the LR equation [16, 19, 20], the KdV equation [25], and Eq. (26) as particular cases, has no exact analytic solution (like the LR equation, which contains similar integral terms). This is why the most interesting question, in my opinion, is whether Eq. (39) has two types of solutions, as does Eq. (26), which is a particular case of Eq. (39). As may be seen from the numerical

results presented in Fig. 1d, the difference between Eqs. (39) and (26) that arises from different dispersion terms in them is largest in the long-wavelength limit. In the long-wavelength range, Eq. (39) simplifies to

$$\frac{\partial B}{\partial \tau} - \hat{\lambda} C_T \frac{\partial^3 B}{\partial z^3} - \epsilon B \frac{\partial B}{\partial z}$$
$$+ \Delta_T \frac{\partial^3}{\partial z^3} \int_{-\infty}^{+\infty} \frac{B(z', t)dz'}{[\alpha^2 + (z' - z)^2]^{1/2}} = 0. \tag{42}$$

Equation (42) is based on approximate dispersion relation (18), which is the most accurate of all approximate dispersion relations for long-wavelength body waves that have been obtained so far because it takes into account both types of dispersion of the body waves (see Fig. 1d). To the best of my knowledge, Eq. (42) has not yet appeared in the theory of nonlinear waves [32]. The KdV equation that was derived in [25] for slow waves follows from Eq. (42) in which the integral term describing the dispersion due to the response of the external medium is ignored. The LR equation that was obtained in [20] for body waves follows from Eq. (42) in which the second term, describing the geometric dispersion, is discarded. The KdV equation has an exact soliton solution corresponding to a solitary wave in the form of a contraction running along a magnetic flux tube [25]. The classical LR equation [16] for vortex filaments and for surface waves in a magnetic flux tube has a solution corresponding to a solitary wave [36] in the form of a bulge running along the tube. The LR equation for body waves [20] differs from the classical LR equation in the sign of the dispersion term. Since the dispersion terms have opposite signs, a solitary body wave is a running contraction rather than a running bulge, as is the case with surface waves. Thus, when two dispersion terms from Eq. (42)—the geometric dispersion and the dispersion due to the response of the external medium—are considered separately in the KdV and LR equations, they both lead to solutions in the form of running contractions. Consequently, it may be stated that Eq. (42), as well as more general Eq. (39), has wave solutions in the form of solitary contractions. In the short-wavelength limit, the difference between Eqs. (26) and (39) is insignificant because the wave dispersion in this limit is essentially insensitive to the response of the external medium (Figs. 1a, 1b, 1c). It might then be supposed that Eq. (39), as well as Eq. (26), has a second kind of solution in the form of solitary bulges running along a magnetic flux tube. Hence, it is possible to state that Eq. (39), like Eq. (26), has two solutions, corresponding to solitary waves in the form of contractions and bulges running along the tube.

In the long-wavelength limit, Eqs. (39) and (42) can be used to determine the extent to which solitary body waves are close in properties to solitons.

3.2. Surface Waves

The sought-for evolutionary equation is derived by rewriting dispersion relation (23) as

$$\omega_D\left(1 + \frac{\lambda_s C_T |k|}{C_T - C_{\text{intf}}}\right) + \lambda_s C_T k |k| = 0, \tag{43}$$

$$\omega_D = \omega - kC_{\text{intf}}, \quad \lambda_s = -AR_0,$$

where the notation λ_s has been introduced for convenience because, for surface waves, we have $A < 0$. This dispersion relation yields the evolutionary equation

$$\frac{\partial B}{\partial \tau} - \lambda_s C_T\left(\frac{1}{C_T - C_{\text{intf}}}\frac{\partial^2}{\partial \tau \partial z} + \frac{\partial^2}{\partial z^2}\right) H(B(z, \tau)) \tag{44}$$

$$-\epsilon B \frac{\partial B}{\partial z} = 0,$$

where $H(B)$ is the Hilbert transform operator,

$$H(B(z, \tau)) = \frac{1}{\pi}\int_{-\infty}^{\infty} \frac{B(z', \tau)dz'}{z' - z}.$$

The Hilbert transform method for deriving evolutionary wave equations from dispersion relations was developed earlier in connection with the Benjamin–Ono (BO) equation (see, e.g., [15]). The nonlinear term added in Eq. (44) coincides with the nonlinear term in the LR equation, in which, as well as in Eq. (44), the dependent variable is the longitudinal velocity. Unfortunately, this nonlinear term does not take into account nonlinear effects occurring outside the tube, although it seems that they should be important in the case of surface waves. This problem requires separate consideration, which, however, goes beyond the scope of the present study.

Equation (44) has two families of soliton solutions. The solutions of one of the families describe solitary waves in the form of bulges running along a magnetic flux tube,

$$B = \frac{B_a}{1 + (z - V\tau)^2/L^2}, \quad B_a < 0, \tag{45}$$

$$V = -\frac{\epsilon B_a}{4}, \quad L = -\frac{\lambda_s C_T(4 - \epsilon B_a/(C_T - C_{\text{intf}}))}{\epsilon B_a}, \tag{46}$$

whose velocity in the laboratory frame of reference, $C_T + V$, is higher than the tube velocity. These solutions are nonsingular for any amplitude, and the characteristic length of the bulge approaches the limiting value $L \longrightarrow \lambda_s C_T/(C_T - C_{\text{intf}})$ with increasing amplitude, although the amplitude is restricted by the natural constraint $B_0 + B_a > 0$. In the long-wavelength limit, Eq. (44) is reduced to the BO equation, This is somewhat surprising in view of the fact that the BO equation arises in the theory of slow surface waves in magnetic slabs [15], while the surface waves in magnetic flux tubes are described by the LR equation. The reason for

this is that Eq. (44) was obtained from approximate dispersion relation (23), which, in the long-wavelength limit, is less accurate than relation (15). The solutions to the LR equation and to Eq. (44), however, do not qualitatively contradict each other in the long-wavelength range because, in both cases, they describe solitary waves in the form of bulges running along a magnetic flux tube with a velocity higher than the tube velocity. The solutions differ somewhat only in the velocity of the bulges and in their characteristic widths and shapes. Beyond the long-wavelength range, however, the discrepancy remains large. Hence, the LR equation has a soliton solution only for wave amplitudes smaller than a certain critical amplitude, whereas Eq. (44) has a soliton solution for arbitrary wave amplitudes. That the LR equation has no soliton solutions in the form of solitary wave with sufficiently large amplitudes [23, 24] follows directly from the fact that, beyond the long-wavelength range, the corresponding dispersion relation (15) certainly contradicts the exact dispersion relation (Fig. 2a). Thus, we had to sacrifice some accuracy in the approximate dispersion relation in the long-wavelength limit in order to obtain the evolutionary equation that has an exact analytic solution over the entire wavelength range.

The second family of solutions to Eq. (44) describes solitary waves in the form of contractions running along a magnetic flux tube,

$$B = \frac{B_a}{1 + (z - V\tau)^2/L^2}, \quad B_a > 0, \tag{47}$$

$$V = -\frac{\epsilon B_a}{4}, \quad L = \frac{\lambda_s C_T(\epsilon B_a/(C_T - C_{\text{intf}})) - 4)}{\epsilon B_a}, \tag{48}$$

whose velocity in the laboratory frame of reference, $C_T + V$, is always less than the tube velocity. In contrast to the case with body waves, the second family of solutions exists for any values of the wave amplitude, except for a special situation in which the characteristic wavelength approaches zero at $B_a^{(\text{cr})} = 4(C_T - C_{\text{intf}})/\epsilon$. The length of the contraction L, which is given by the second of expressions (48), tends to zero as the amplitude increases from zero to the critical amplitude $B_a^{(\text{cr})}$, and, for amplitudes greater than the critical amplitude, it increases and approaches the limiting value $\lambda_s C_T/(C_T - C_{\text{intf}})$. In actuality, however, because of the pressure catastrophe, which will be considered in the next section, the length of the contraction cannot be less than a certain critical length at which the shock fronts begin to develop within the contraction.

3.2.1. Canonical equation. Equation (44) is an example of an evolutionary equation based on the dispersion relation

$$\omega = kC_1 \pm \frac{C_1\tilde{\lambda}k|k|}{1 \pm \tilde{\lambda}|k|C_1/(C_2 - C_1)}, \tag{49}$$

$$\tilde{\lambda} > 0, \quad C_2 \gtrless C_1,$$

where C_1 and C_2 are the wave phase velocities at $k \longrightarrow 0$ and $k \longrightarrow \infty$, respectively. By an appropriate coordinate transformation, the evolutionary equation corresponding to dispersion relation (49) can be brought to the canonical form

$$u_t - aHu_{tx} \pm Hu_{xx} + 2uu_x = 0,$$

$$(Hf)(x) = \int\limits_{-\infty}^{\infty} \frac{f(y)}{y - x} dy, \tag{50}$$

where $a = C_1/|C_2 - C_1|$. To the best of my knowledge, evolutionary equations like Eq. (50) have not yet appeared in the theory of nonlinear waves [32]. With $a = 0$, Eq. (50) is the classical BO equation.

Equation (50) has two distinct nonsingular soliton solutions for waves with a normal and an anomalous dispersion, respectively:

$$u = \frac{2C}{1 + C^2(x - Ct)^2/(aC \pm 1)^2}, \tag{51}$$

$$u = -\frac{2C}{1 + C^2(x + Ct)^2/(aC \mp 1)^2}. \tag{52}$$

Regardless of the type of dispersion, Eq. (50) has two families of solutions, which correspond to waves in the form of bulges or contractions running along a magnetic flux tube. Moreover, the length of the waves of one type decreases monotonically with increasing amplitude and approaches the limiting value $L = a$, whereas the characteristic length of the waves of the other type decreases to become zero (at $C = 1/a$) with increasing amplitude and, at large amplitudes, it increases and approaches the same limiting value.

Equation (50) also has simple solutions for periodic nonlinear waves,

$$u = \frac{C\tanh\phi_0}{1 + \text{sech}\,\phi_0 \cos[C(x - Ct)/(aC \pm 1) + \psi_0]}, \tag{53}$$

$$u = -\frac{C\tanh\phi_0}{1 + \text{sech}\,\phi_0 \cos[C(x + Ct)/(aC \mp 1) + \psi_0]}, \tag{54}$$

where ϕ_0 and ψ_0 are constants. With $a = 0$, solution (53) is the known periodic solution to the BO equation [37].

3.2.2. Generalized equation. Recall that, in the long-wavelength range, Eq. (44) is less accurate than the LR equation. Dispersion relation (24) makes it possible to derive an evolutionary equation that is valid for waves of arbitrary wavelength and is free of this drawback. The desired partial differential wave equation is obtained from the dispersion relation by the method developed by Whitham [31], who showed that the dispersion relation $V_{\text{ph}} = C(k)$ leads to the wave equation

$$\frac{\partial y(t, z)}{\partial t} + \frac{\partial}{\partial t} \int\limits_{-\infty}^{\infty} y(t, z') K(z' - z) dz' = 0, \tag{55}$$

$$K(z) = \frac{1}{2\pi} \int\limits_{-\infty}^{\infty} C(k) e^{-ikz} dk. \tag{56}$$

The sought-for wave equation is derived by rewriting dispersion relation (24) as

$$\omega_D \left(mK_1(mx) - \frac{AC_T}{C_T - C_{\text{intf}}} xK_0(mx) \right)$$
$$- AkC_T xK_0(mx) = 0. \tag{57}$$

The wave equation that is based on approximate dispersion relation (57) for surface waves can be reduced to

$$\frac{\partial}{\partial\tau} \int\limits_{-\infty}^{+\infty} \frac{m^2 v(z', t) dz'}{[\lambda^2 + (z' - z)^2]^{3/2}} + bv\frac{\partial v}{\partial z}$$
$$- \frac{AR_0 C_T}{2} \left(\frac{\partial^3}{\partial z^3} + \frac{1}{C_T - C_{\text{intf}}} \frac{\partial^3}{\partial\tau\partial z^2} \right)$$
$$\times \int\limits_{-\infty}^{+\infty} \frac{v(z', t) dz'}{[\lambda^2 + (z' - z)^2]^{1/2}} = 0, \tag{58}$$

$$b = \frac{C_A^2 [3C_S^2 + (\gamma + 1)C_A^2]}{2(C_S^2 + C_A^2)^2}, \quad \lambda^2 = m^2 R_0^2,$$

where v is the longitudinal velocity. This is a generalization of the LR equation [19, 20]. Like the LR equation, Eq. (58) has no exact analytic solutions. As for numerical solutions to this equation, they can help to refine the analytic solutions to Eq. (44). In the long-wavelength limit, Eq. (58) is reduced to the LR equation. To the best of my knowledge, Eq. (58) has not yet been appeared in the theory of nonlinear waves [32]. This equation, like Eq. (50), has two different families of solutions, which describe waves in the form of contractions or bulges running along a magnetic flux tube. It is obvious that, in contrast to Eq. (50), the solutions of one of the families should be singular for sufficiently small wave amplitudes because, in the long-wavelength limit, all the three asymptotically equivalent equations have only one solution, which describes waves in the form of bulges. In other words, the existence of two solutions to Eq. (50) over the entire range of possible wave amplitudes is attributed to the fact that approximate dispersion relation (23) is not accurate enough in the long-wavelength range.

In the long-wavelength approximation, surface waves seem to have much in common with solitons. In the Introduction, it was pointed out that, based on the results of numerical explorations of the MR equation [21], Molotovshchikov [38] arrived at the conclusion that nonlinear surface waves are solitons. In actuality, however, the surface wave is not a perfect soliton and the above conclusion is erroneous, because the MR equation, as well as all the other known evolutionary

wave equations, is based on an approximate dispersion relation and thereby is nothing more than a model one. In addition, it should not be thought that the numerical solution carried out by Molotovshchikov [38] cannot be said to furnish conclusive proof of the complete integrability of the MR equation. What can give rise to some doubt is the fact that, for sufficiently large wave amplitudes or, equivalently, for sufficiently short wavelengths, the MR equation is reduced to the completely integrable BO equation because, in this limit, the dispersion relation used by Molotovshchikov and Ruderman is reduced to a relation of the form $\omega \sim k|k|$. Consequently, if the wave amplitudes chosen for numerical simulations are not small enough for the solutions to the MR equation to differ substantially from the solutions to the BO equation, the deviation of the solution from being solitonic may pass unnoticed. Numerical treatment of Eq. (58) can provide a more reliable answer to the question about the extent to which nonlinear surface waves are close to solitons.

4. WEAKLY NONLINEAR WAVES AND SHOCK FRONTS

Model equations for dispersive waves do not describe the breaking of waves and the formation of shock fronts when the wave amplitudes are sufficiently large. An analysis of many nonlinear physical problems, such as those about a hydraulic jump (or bore) [31, 39], the flow of viscous liquid in an elastic tube [40], the flow of bubbled liquid [41], and collisionless shock waves, leads to the KdVB equation, which takes into account not only dispersion and nonlinearities but the damping as well. Since the KdV equation is a particular case of Eq. (26), it is natural to supplement it with a dissipative term that, in the case of space plasma, describes the damping by viscosity and heat conduction. The generalized KdVB equation for body waves of arbitrary wavelength that are described by dispersion relation (11) reads

$$
\frac{\partial B}{\partial \tau} - \frac{\hat{\lambda} C_T}{C_S - C_T} \frac{\partial^3 B}{\partial \tau \partial z^2} - \hat{\lambda} C_T \frac{\partial^3 B}{\partial z^3}
$$
$$
- \epsilon B \frac{\partial B}{\partial z} + \Lambda \frac{\partial^2 B}{\partial z^2} = 0,
$$
(59)

where the coefficient Λ depends on the viscosity and thermal conductivity of the plasma. This equation has two exact analytic solutions:

$$
B = B_a \mathrm{sech}^2((z - V\tau)/L)
$$
$$
- 2B_a(\tanh((z - V\tau)/L) + 1),
$$
(60)

$$
B_a = \frac{(C_S - C_T)(2\hat{\lambda} C_T + \Lambda L)}{((C_S - C_T)L^2 + 4\hat{\lambda} C_T)\epsilon},
$$
$$
V = \frac{2(C_S - C_T)(2\hat{\lambda} C_T + \Lambda L)}{(C_S - C_T)L^2 + 4\hat{\lambda} C_T},
$$
(61)

$$
L = \frac{5\hat{\lambda} C_T \pm \sqrt{\hat{\lambda} C_T(25\hat{\lambda} C_T + 24\Lambda^2/(C_S - C_T))}}{\Lambda}. \quad (62)
$$

Solutions (60)–(62) are a generalization of the exact analytic solution to the KdVB equation that was obtained quite recently as a result of the joint efforts of a group of mathematicians (see [43] and the references cited therein). For slow body waves in magnetic flux tubes, the KdVB equation, which is a particular case of Eq. (59) in the long-wavelength limit, reads

$$
\frac{\partial B}{\partial \tau} - \hat{\lambda} C_T \frac{\partial^3 B}{\partial z^3} - \epsilon B \frac{\partial B}{\partial z} + \Lambda \frac{\partial^2 B}{\partial z^2} = 0, \quad (63)
$$

and its unique solution, which coincides in structure with solutions (60), depends on the parameters of the equation as

$$
B_a = \frac{3\Lambda^2}{25\hat{\lambda} C_T \epsilon}, \quad V = \frac{6\Lambda^2}{25\hat{\lambda} C_T}, \quad L = \frac{10\hat{\lambda} C_T}{\Lambda}. \quad (64)
$$

Solutions (60) and (64) describe a smooth jump, which differs from the function $\tanh(x) + 1$ in a somewhat larger width of the transition region.

Numerous studies of the KdVB equation by means of its phase diagrams [42, 44, 45] showed that it has two types of solutions that correspond to a shock wave and to a hydraulic jump, which is also called a bore [39]. To the best of my knowledge, there has been no discussion of the physical meaning of the above exact solution to Eq. (63), obtained by a combined effort of mathematicians, although it was mentioned that, in the limit of small Λ values, the solution to Eq. (63) is not reduced to the solution to the Burgers equation, which describes shock waves. In fact, solution (64) implies that the characteristic width of the shock front, L, should increase as Λ decreases—a situation diametrically opposite to that with a shock wave, whose front should become narrower as Λ decreases. All this indicates that solution (64) to Eq. (63) describes a bore whose front, in contrast to the shock front, has a finite width for any parameter values [39].

In order to compare solution (64) to Eq. (63) with two solutions (60) to Eq. (59), we take the limit of small Λ values for these solutions:

$$
\text{Hydraulic jump (bore)} \Rightarrow B_a \approx \frac{3\Lambda^2}{25\hat{\lambda} C_T \epsilon},
$$
$$
V \approx \frac{6\Lambda^2}{25\hat{\lambda} C_T}, \quad L \approx \frac{10\hat{\lambda} C_T}{\Lambda},
$$
(65)

$$\text{Shock wave} \Rightarrow B_a \approx \frac{C_S - C_T}{2\epsilon},$$

$$V \approx C_S - C_T, \quad L \approx -\frac{12\Lambda}{5(C_S - C_T)}. \tag{66}$$

It turns out that, in this limit, the first of two solutions (66) coincides exactly with solution (64) to Eq. (63) and, therefore, describes a bore. The second of solutions (66) is allied in properties with a shock wave because, as $\Lambda \longrightarrow 0$, the front width approaches zero, $L \longrightarrow 0$, while the magnetic field jump B_a and the wave velocity remain constant. In the limit at hand, both of the waves in the laboratory frame propagate with the speed of sound. Hence, a shock wave is described by generalized KdVB equation (59), which is valid for waves of arbitrary wavelength. This result is not surprising because it is only in an approximation valid for all wavelengths that the narrow shock front can be described by taking into account high-frequency modes. The higher the dissipation, the less the difference between the shock wave and the bore. In the limit of strong dissipation, the two solutions (66) coincide,

$$B_a = \pm\frac{\Lambda}{14\epsilon}\sqrt{\frac{6(C_S - C_T)}{\hat{\lambda}C_T}}, \quad V = \pm\frac{\Lambda}{7}\sqrt{\frac{6(C_S - C_T)}{\hat{\lambda}C_T}},$$

$$L = \pm 2\sqrt{6\hat{\lambda}C_T/(C_S - C_T)}, \tag{67}$$

and, moreover, the front width of both of the waves is independent of the dissipation rate. In the limit of small Λ values, however, the shock wave leads not to an increase in the diameter of the tube, as implied by the Hugoniot conditions [29, 30] for shock waves in magnetic flux tubes, but rather to a decrease in the tube diameter, which should be accompanied by a decrease in entropy. This indicates that the shock wave is non-evolutionary and thereby should break into several discontinuities. For large Λ values, the shock wave is evolutionary only under the condition $\Lambda > \lambda C_T(C_S - C_T)$, i.e., when its velocity in the laboratory frame is positive, $C_T + V > 0$. The exact condition for the wave to be evolutionary can readily be found from expressions (61) and (62). Hence, the shock wave is evolutionary only when the dissipation is sufficiently strong, which agrees completely with the theory of waves in dispersive media [42, 44, 45].

Solutions (60) and (64), which occupy a special position among all possible steady solutions to Eqs. (59) and (63), have two unusual properties. The first is that they do not contain a free parameter and, thus, the wave amplitude is not arbitrary but is determined by the parameters of the equation. This property distinguishes solutions (60) and (64) from all of the above solutions for solitary waves, into which the wave amplitude enters as a free parameter. The second property is that there are no oscillations behind the wave front, although their presence in the limit of small Λ values is implied by all of the above-mentioned studies

on nonlinear waves in dispersive media [42, 44, 45]. These two properties indicate that such waves can occur only under some specific initial conditions. In fact, it is known [39] that, under certain conditions, oscillations behind the front of a bore can be very small. Hence, exact analytic solutions to the KdVB equation and to its analogue for waves of arbitrary wavelength made it possible to determine the profiles of a shock wave and a bore with nonoscillating fronts.

It should be emphasized, however, that special care must be taken when analyzing surface waves by means of Eq. (59) because, in the limit of small Λ values, in which the shock front becomes progressively narrower, it turns out that the longitudinal magnetic field and, accordingly, the diameter of the magnetic flux tube should change in a jumplike manner. The same assumption was made in deriving the Hugoniot conditions [29, 30] for shock waves in magnetic flux tubes. In my earlier paper [28], this problem was analyzed under the assumption that a narrow shock front can occur in the tube at a place where the derivative of the tube diameter, $\dfrac{\partial R(z)}{\partial z}$, is discontinuous, i.e., where a cusp arises at the tube surface. This is in direct analogy to the sharpening of the crests of waves on the surface of a liquid, but there is one essential difference. The waves in magnetic flux tubes appear as bulges or contractions; hence, the cusp can point outward from the tube or toward its axis, respectively. In the latter case, the classical wave-breaking mechanism associated with the gradient catastrophe does not come into play; hence, the waves are broken by the pressure catastrophe, occurring at the necks of the contractions in accordance with Bernoulli's law, which implies that the temperature and density increase and the plasma is accelerated as the magnetic flux tube narrows. This effect was first pointed out in [46], where it was revealed in analyzing the properties of solutions to the KdV equations for the body waves. The nonlinear wavebreaking mechanism associated with the pressure catastrophe is possible solely in a magnetic flux tube. The only mechanism that always operates in a homogeneous plasma is the classical mechanism associated with the gradient catastrophe. On the other hand, the conditions for MHD waves to be evolutionary cannot be reduced to the principle of increase in entropy alone [47].

Of particular interest is the possible onset of a bore in a magnetic flux tube. Solutions (60) and (64)–(67) imply that a pronounced hydraulic jump in the bore can occur only when the dissipation is sufficiently strong. In the well-studied cases of a hydraulic jump [39] and of collisionless shock waves [42], strong damping is associated with the turbulence driven by the instability of a multistream sheared flow within the wave front. Turbulence can be generated in the event of the gradient catastrophe in waves in the form of bulges and pressure catastrophe in waves in the form of contractions.

5. CONCLUSIONS

Approximate dispersion relations for body and surface waves of arbitrary wavelength made it possible to derive a number of new evolutionary equations, in particular, those having exact analytic solutions. These equations exhibit unique properties because they have two kinds of solutions corresponding to solitary waves. To the best of my knowledge, such equations have not yet been appeared in nonlinear physics. It was found that the body and surface solitary waves can be in the form of contractions or bulges of the magnetic flux tube. Accordingly, the equations have two kinds of periodic solutions. Some progress has also been achieved in developing the theory of shock waves in magnetic flux tubes, which is still in its infancy because all that was hitherto known about this subject is the Hugoniot conditions [29, 30]. Two analytic solutions to the generalized KdVB equation have been obtained that describe the properties not only of shock waves but also of nonlinear waves of the bore kind, which therefore can exist in magnetic flux tubes too.

The main drawback of the present paper is like that of the modern theory of slow waves in magnetic flux tubes, specifically, the use of the same nonlinear coefficient that was evaluated in the thin-tube approximation. In particular, the same coefficient is used to describe both surface and body waves. But doing so is hardly justified because the nonlinear coefficient for the surface waves should depend on the parameters of the surrounding plasma, while the coefficient used depends only on the parameters of the plasma within the tube. The nonlinear coefficient for waves of arbitrary wavelength should also depend on the wavenumber; however, this is a subject of separate examination. In this context, it should be stressed that the theory of nonlinear slow waves of arbitrary wavelength in magnetic flux tubes has reached nearly the same point of development as the theory of waves of arbitrary wavelength on the surfaces of liquids. The BBM and Boussinesq equations are valid for waves of arbitrary wavelength because they are based on the approximations to the exact dispersion relation

$$\omega^2 = gk\tanh(kh_0). \qquad (68)$$

These equations, however, contain the nonlinear term that was obtained in the long-wavelength limit, as is the case with the equations derived above for slow waves of arbitrary wavelength in magnetic flux tubes. The advantage of dispersion relation (68) over exact dispersion relations (6) and (20) is that the frequency in it depends explicitly on the wavenumber. This made it possible to derive an equation for waves of arbitrary wavelength from the exact dispersion relation (see [31], Section 13.14). The equation derived, however, is very complicated and therefore was not explored in sufficient detail. Moreover, all explorations dealt with the equation containing the nonlinear term obtained in the long-wavelength limit (see [31], Section 13.14).

REFERENCES

1. *Physics of Magnetic Flux Ropes,* Ed. by C. T. Russell, E. R. Priest, and L. C. Lee (Am. Geophys. Union, Washington, 1990).
2. J. B. Gurman and D. E. DeForest, Astrophys. J. Lett. **501**, L217 (1998).
3. L. Ofman, V. M. Nakariakov, and D. E. DeForest, Astrophys. J. **514**, 441 (1999).
4. D. Berghmans and F. Clette, Sol. Phys. **186**, 207 (1999).
5. I. De Moortell, J. Ireland, R. W. Walsh, and A. W. Hood, Sol. Phys. **209**, 61 (2002).
6. I. De Moortel, A. W. Hood, J. Ireland, and R. W. Walsh, Sol. Phys. **209**, 89 (2002).
7. V. V. Zaĭtsev and A. V. Stepanov, Issled. Geomagn. Aéron. Fiz. Solntsa **37**, 3 (1975).
8. D. D. Ryutov and M. P. Ryutova, Zh. Éksp. Teor. Fiz. **43**, 943 (1976) [Sov. Phys. JETP **16**, 491 (1976)].
9. B. I. Meerson, P. V. Sasorov, and A. V. Stepanov, Sol. Phys. **58**, 165 (1978).
10. P. M. Edwin and B. Roberts, Sol. Phys. **88**, 179 (1983).
11. H. C. Spruit, Sol. Phys. **75**, 3 (1982).
12. B. Roberts and A. R. Webb, Sol. Phys. **56**, 5 (1978).
13. Y. D. Zhugzhda, Phys. Plasmas **3**, 10 (1996).
14. Y. D. Zhugzhda, Phys. Plasmas **9**, 971 (2002).
15. B. Roberts and A. Mangeney, Mon. Not. R. Astron. Soc. **198**, 7 (1982).
16. B. Roberts, Phys. Fluids **28**, 3280 (1985).
17. B. Roberts, Astrophys. J. **318**, 590 (1987).
18. S. Leibovich, J. Fluid Mech. **42**, 803 (1970).
19. Y. D. Zhugzhda, Phys. Scr. **T84**, 159 (2000).
20. Y. D. Zhugzhda and M. Goossens, Astron. Astrophys. **377**, 330 (2001).
21. A. L. Molotovshchikov and M. S. Ruderman, Sol. Phys. **109**, 247 (1987).
22. W. G. Pritchard, J. Fluid Mech. **42**, 61 (1970).
23. T. J. Bogdan and I. Lerche, Quart. Appl. Math. **46**, 365 (1988).
24. E. Weisshaar, Phys. Fluids A **1**, 1406 (1989).
25. Y. D. Zhugzhda and V. M. Nakariakov, Phys. Lett. A **233**, 413 (1997).
26. I. Ballai, R. Erdelyi, Y. Voitenko, and M. Goossens, Phys. Plasmas **9**, 4280 (2002).
27. I. Ballai and Y. D. Zhugzhda, Phys. Plasmas **9**, 2593 (2002).
28. Y. D. Zhugzhda, Phys. Plasmas **11**, 2256 (2004).
29. G. Herbold, P. Ulmschneider, H. C. Spruit, and R. Rosner, Astron. Astrophys. **145**, 157 (1985).
30. Y. D. Zhugzhda and V. Bromm, Astron. Astrophys. **300**, 302 (1995).

31. G. B. Whitham, *Linear and Nonlinear Waves* (Wiley, New York, 1974; Mir, Moscow, 1977).

32. M. J. Ablowitz and P. A. Clarkson, *Solitons, Nonlinear Evolutionary Equations, and Inverse Scattering* (Cambridge Univ. Press, Cambridge, 1991).

33. T. B. Benjamin, J. L. Bona, and J. J. Mahony, Philos. Trans. R. Soc. London, Ser. A **272**, 47 (1972).

34. J. L. Bona, W. G. Pritchard, and L. R. Scott, Phys. Fluids **23**, 438 (1980).

35. J. S. Russell, in *Proceedings of the 14th Meeting of the British Association for Advancement of Sciences, York, 1884*, Part 1, p. 311.

36. S. Leibovich and J. D. Randall, J. Fluid Mech. **51**, 625 (1972).

37. J. Satsuma and Y. Ishimori, J. Phys. Soc. Jpn. **46**, 681 (1979).

38. A. L. Molotovshchikov, Mekh. Zhidk. Gaza, No. 2, 183 (1989).

39. J. Lighthill, *Waves in Fluids* (Cambridge Univ. Press, Cambridge, 2002).

40. R. S. Johnson, J. Fluid Mech. **42**, 49 (1970).

41. L. van Wijngaarden, Annu. Rev. Fluid Mech. **4**, 369 (1972).

42. R. Z. Sagdeev, D. A. Usikov, and G. M. Zaslavsky, *Nonlinear Physics: from the Pendulum to Turbulence and Chaos* (Nauka, Moscow, 1988; Harwood, Chur, 1988).

43. Feng Zaoheng, Phys. Lett. A **293**, 57 (2002).

44. M. I. Rabinovich and D. I. Trubetskov, *Oscillations and Waves in Linear and Nonlinear Systems* (Nauka, Moscow, 1984; Kluwer, Dordrecht, 1989).

45. V. I. Karpman, *Nonlinear Waves in Dispersive Media* (Nauka, Moscow, 1973; Pergamon, Oxford, 1975).

46. Y. D. Zhugzhda and V. M. Nakariakov, Sol. Phys. **175**, 107 (1997).

47. L. D. Landau and E. M. Lifshitz, *Electrodynamics of Continuous Media* (Fizmatgiz, Moscow, 1959; Pergamon, Oxford, 1960).

Translated by O.E. Khadin

PLASMA OSCILLATIONS
AND WAVES

Interaction of Microwave Radiation Undergoing Stochastic Phase Jumps with Plasmas or Gases

V. I. Karas'[1], Ya. B. Faĭnberg[1, †], A. F. Alisov[1], A. M. Artamoshkin[1],
R. Bingham[2], I. V. Gavrilenko[1], V. D. Levchenko[3], M. Lontano[4],
V. I. Mirny[1], I. F. Potapenko[3], and A. N. Starostin[5]

[1]*National Science Center Kharkov Institute of Physics and Technology, ul. Akademicheskaya 1, Kharkov, 61108 Ukraine*
[2]*Rutherford Appleton Laboratory, Chilton, Didcot, Oxfordshire, OX11 OQX, UK*
[3]*Keldysh Institute of Applied Mathematics, Russian Academy of Sciences, Miusskaya pl. 4, Moscow, 125047 Russia*
[4]*"Piero Caldirola" Istituto di Fisica del Plasma, Associazione Euratom–ENEA per la Fusione–CNR, Milano, Italy*
[5]*Troitsk Institute for Innovation and Fusion Research, Troitsk, Moscow oblast, 142092 Russia*

Abstract—New types of beam–plasma devices generating intense stochastic microwave radiation in the interaction of electron beams with hybrid plasma waveguides were developed and put into operation at the National Science Center Kharkov Institute of Physics and Technology (Ukraine). The objective of the paper is to discuss the results of theoretical and experimental studies and numerical simulations of the normal and oblique incidence of linearly polarized electromagnetic waves on an interface between a vacuum and an overcritical plasma. The main results of the reported investigations are as follows: (i) for the parameter values under analysis, the transmission coefficient for microwaves with a stochastically jumping phase is one order of magnitude greater than that for a broadband regular electromagnetic wave with the same spectral density; (ii) the electrons are heated most efficiently by obliquely incident waves with a stochastically jumping phase and, in addition, the electron distribution function has a high-energy tail; and (iii) necessary conditions for gas breakdown and for the initiation of a microwave discharge in stochastic fields in a light source are determined. The anomalously large transmission coefficient for microwaves, the anomalous character of the breakdown conditions, the anomalous behavior of microwave gas discharges, and the anomalous nature of collisionless electron heating, are attributed to stochastic jumps in the phase of microwave radiation. © 2005 Pleiades Publishing, Inc.

INTRODUCTION

Litvak and Tokman [1] demonstrated that, because of the classical analogue of the effect of electromagnetically induced transparency in quantum systems, electromagnetic waves in a plasma can pass through the region where they should be absorbed. Faĭnberg *et al.* [2] showed that stochastic electric fields with a finite phase correlation time can efficiently heat particles in a collisionless plasma, so physically the inverse correlation time in the interaction between a particle and an electromagnetic wave has in fact the meaning of an effective collision frequency [2, 3].

The objective of the present paper is to determine the conditions for the effective penetration of microwaves with a stochastically jumping phase into a high-density plasma, to study the collisionless electron heating by it, and to utilize microwaves to initiate microwave discharges in light sources. In Section 1, we discuss the results of theoretical investigations of the normal and oblique incidence of linearly polarized electromagnetic waves on an interface between a vacuum and an overcritical plasma. The electron dynamics

is described by the relativistic Vlasov equation for the electron distribution function together with Maxwell's equations for self-consistent electromagnetic fields under the assumption that the ions are immobile. We use the method [4] that not only provides a complete nonlinear kinetic description of the electron dynamics for a plasma of arbitrary density and for electromagnetic waves of arbitrary intensity but also makes it possible to carry out numerical simulations by taking short time steps in comparison to the electron plasma period. We consider how an overcritical plasma is penetrated by three types of waves, namely, a microwave with a stochastically jumping phase, a broadband regular wave with the same spectral density, and a monochromatic wave.

The possible mechanisms whereby electromagnetic waves penetrate through a wave barrier in a plasma are as follows:

(i) linear and nonlinear conversion between different types of waves,

(ii) linear and nonlinear echoes involving van Kampen waves,

(iii) the linear induced transparency of a wave barrier ("beam antennas"),
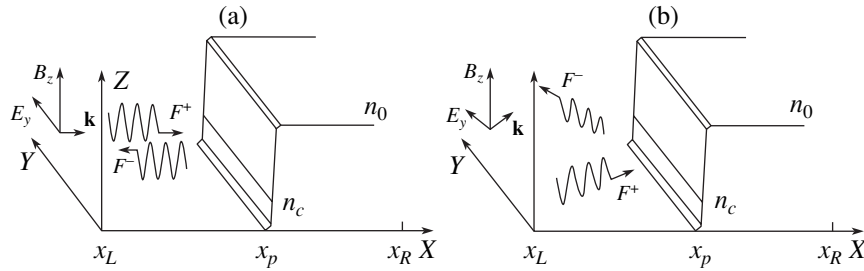
---

† Deceased.

Fig. 1. Schematic representation of the computation region for the cases of (a) a normally and (b) an obliquely incident microwave.

(iv) collisional penetration of a wave into a wave barrier, and

(v) penetration of a wave into a wave barrier due to the jumps in its phase (this penetration mechanism is associated with the fact that the transmission coefficient is proportional to the time derivative of the wave phase, which in turn is determined by the derivative of the electric field)—an effect that is the subject of the present study.

The known mechanisms whereby electromagnetic waves can heat plasma particles are as follows:

(i) resonant absorption due to the synchronism between a wave and a particle (the particle always oscillates in phase with the wave),

(ii) collisional absorption due to the loss of synchronism between a wave and a particle in collisions (as a result, the absorption efficiency is proportional to the ratio of the collision frequency to the wave frequency),

(iii) linear and nonlinear absorption in a nonuniform wave, and

(iv) wave absorption due to the jumps in the phase of the wave when it loses its synchronism with the particle—an effect that was investigated in [2] and is the subject of the present study.

1. THEORETICAL STUDY OF THE NORMAL AND OBLIQUE INCIDENCE OF ELECTROMAGNETIC WAVES ON AN INTERFACE BETWEEN A VACUUM AND A HIGH-DENSITY PLASMA

1.1. Physical Model

Here, we describe the results of investigations of the incidence of three types of electromagnetic waves, namely, a monochromatic wave, a stochastic wave with a finite phase correlation time, and a broadband wave with the same spectral density, from vacuum on a plasma half-space. Numerical simulations were carried out by means of two techniques: a particle-in-cell (PIC) method for solving the Vlasov equation and a method based on a grid splitting scheme (the SUR code). A study of the transmission coefficients for different types of waves showed that a monochromatic wave is reflected from the plasma almost totally (except for its front), whereas a stochastic wave is reflected only

slightly, due mainly to the penetration of the wave pulses associated with stochastic jumps in the wave phase. In turn, the transmission coefficient for a broadband regular wave having the same spectral density as the wave with a stochastically jumping phase is much less; the reason is that, in this case, the plasma slab simply acts as a filter that transmits waves with the frequencies $\omega > \omega_p$ (where $\omega_p = (4\pi e^2 n_0/m)^{1/2}$ is the electron Langmuir frequency, n_0 is the plasma density, e is an elementary charge, and m is the mass of an electron) and reflects others.

1.2. Formulation of the Problem

Numerical simulations were carried out for a computation region $x_L < x < x_R$ that is shown schematically in Fig. 1. Initially, a uniform electron plasma ($n = n_0$) with a Maxwellian electron velocity distribution occupies the half-space to the right of the point $x = x_p$. The background plasma ions are assumed to be immobile. The electron plasma density n_0 is above the critical density ($\omega_p > \omega_0$).

Let a plane-polarized electromagnetic wave with the wave vector $\mathbf{k} = (k_x, 0, 0)$ and with the field components $\mathbf{E} = (0, E_y, 0)$ and $\mathbf{B} = (0, 0, B_z)$ be normally incident on the plasma from the left. In vacuum, in a cross section $x = x_L$ that is sufficiently far from the plasma boundary, the field components of a microwave with a stochastically jumping phase are given by the expressions

$$E_y^{\mathrm{sp}}(x, t) = B_z^{\mathrm{sp}}(x, t)$$
$$= F_0 \cos(\omega_0 t - k_x x + \widehat{\varphi}(t)). \tag{1.1}$$

We consider a stationary Poisson process with the frequency $1/\tau$; specifically, we assume that, over a sufficiently long time interval T, the phase $\widetilde{\varphi}$ undergoes, on the average, T/τ jumps. In each jump, the phase randomly takes a value within the interval $[-\pi, \pi)$ with equal probability. The correlation coefficient for such a stochastic process has the form (see, e.g., [3])

$$R(t) = \exp\left(-\frac{|t|}{\tau}\right)\cos\omega_0 t,$$

the spectral density being

$$G(\omega) = \frac{1}{(1/\tau)^2 + (\omega - \omega_0)^2}.$$

We also consider a broadband wave with the same spectral density but with time-independent phases φ^{lr} and time-independent amplitudes F^{lr}:

$$E_y^r(x, t) = B_z^r(x, t)$$
$$= \sum_l F_0^{lr} \cos(\omega_l t - k_l x + \varphi^{lr}). \qquad (1.2)$$

Together with a wave undergoing stochastic phase jumps and a broadband wave, we consider a regular monochromatic wave with the electromagnetic field components

$$E_y^{mf}(x, t) = B_z^{mf}(x, t)$$
$$= F_0 \cos(\omega_0 t - k_x x + \varphi_0). \qquad (1.3)$$

1.3. Basic Equations and Numerical Methods

The electron dynamics is described by the Vlasov equation for the electron distribution function $f(t, x, p_x, p_y)$:

$$\frac{\partial f}{\partial t} + V_x \frac{\partial f}{\partial x} - e\left[E_x + \frac{V_y}{c} B_z\right] \frac{\partial f}{\partial p_x}$$
$$- e\left[E_y - \frac{V_x}{c} B_z\right] \frac{\partial f}{\partial p_y} = 0. \qquad (1.4)$$

In one-dimensional geometry, the longitudinal electric field E_x can be determined from the Gauss formula,

$$E_x = E_x\big|_{x = x_L} + 4\pi \int_{x_L}^{x} \rho(\xi) d\xi. \qquad (1.5)$$

In planar geometry, Maxwell's equations for the electromagnetic field,

$$\frac{1}{c}\frac{\partial E_y}{\partial t} + \frac{\partial B_z}{\partial x} = -\frac{4\pi}{c} j_y,$$

$$\frac{1}{c}\frac{\partial B_z}{\partial t} + \frac{\partial E_y}{\partial x} = 0,$$

can be decoupled by introducing the auxiliary fields $F^{\pm} = E_y \pm B_z$:

$$\left(\frac{1}{c}\frac{\partial}{\partial t} \pm \frac{\partial}{\partial x}\right) F^{\pm} = -\frac{4\pi}{c} j_y, \qquad (1.6)$$

where the charge density and the transverse current density are given by the expressions

$$\rho = e\left(n_0 - \int f(x, \mathbf{p}) d\mathbf{p}\right),$$
$$j_y = -e\int V_y(x) f(x, \mathbf{p}) d\mathbf{p}. \qquad (1.7)$$

The boundary conditions for the longitudinal electric field and the transverse auxiliary fields have the form

$$E_x\big|_{x = x_L} = 0, \quad F^+\big|_{x = x_L} = F(t),$$
$$-F^-\big|_{x = x_R} = 0, \qquad (1.8)$$

where the function $F(t)$ is given by expression (1.1), (1.2), or (1.3).

The above equations were solved numerically using the SUR code [4–6].

1.4. Simulation Results

Numerical simulations of a normally incident electromagnetic wave were carried out for the following parameter values: $V_y^{\mathrm{osc}} = 3V_T$, $\omega_0 = 0.5\omega_p$, $\tau = 40/\omega_p$, and $x_R - x_L \geq 2000\lambda_D$ (here, V_T is the electron thermal velocity and λ_D is the Debye length). The total run time of the code is $T = 5000/\omega_p$. The numerical results are illustrated in Figs. 2–4. The transmission coefficient for a wave is defined as the ratio of the electromagnetic wave energy at the point $x = x_R$ (i.e., the energy that has passed through the plasma) to the energy of the incident wave at the point $x = x_L$ (with allowance for the corresponding time shift).

The incident electromagnetic wave is mostly reflected from the plasma slab, without having any significant effect on the plasma electrons. The longitudinal fields in the plasma are weak (two to four orders of magnitude weaker than the transverse fields). During the run time of the code ($5000/\omega_p$), the longitudinal energy of the electrons (as well as their temperature) changes by no more than 1%. The electron distribution function remains nearly Maxwellian, but a small fraction of the electrons (about 10^{-4}) are accelerated in both directions from the plasma boundary.

A monochromatic wave is reflected from the plasma almost totally (except for its front). A stochastic wave is reflected to a lesser extent due mainly to the penetration of the wave pulses associated with stochastic jumps in the wave phase. The transmission coefficient for a broadband wave with the same spectral density as that of a wave undergoing stochastic phase jumps is one order of magnitude less because, in this case, the plasma slab simply acts as a filter that transmits waves with the frequencies $\omega > \omega_p$ and reflects others.

The oblique incidence of an electromagnetic wave was simulated for the same parameter values as those for the normal incidence, the only difference being in the length of the time interval, $T = 2500/\omega_p$. In this case, the electromagnetic wave incident on the plasma has a strong impact on the electron dynamics, especially at large angles of incidence. The longitudinal electric fields in the plasma are close in strength to the transverse fields. The longitudinal energy of the electrons and their temperature increase severalfold. The electron
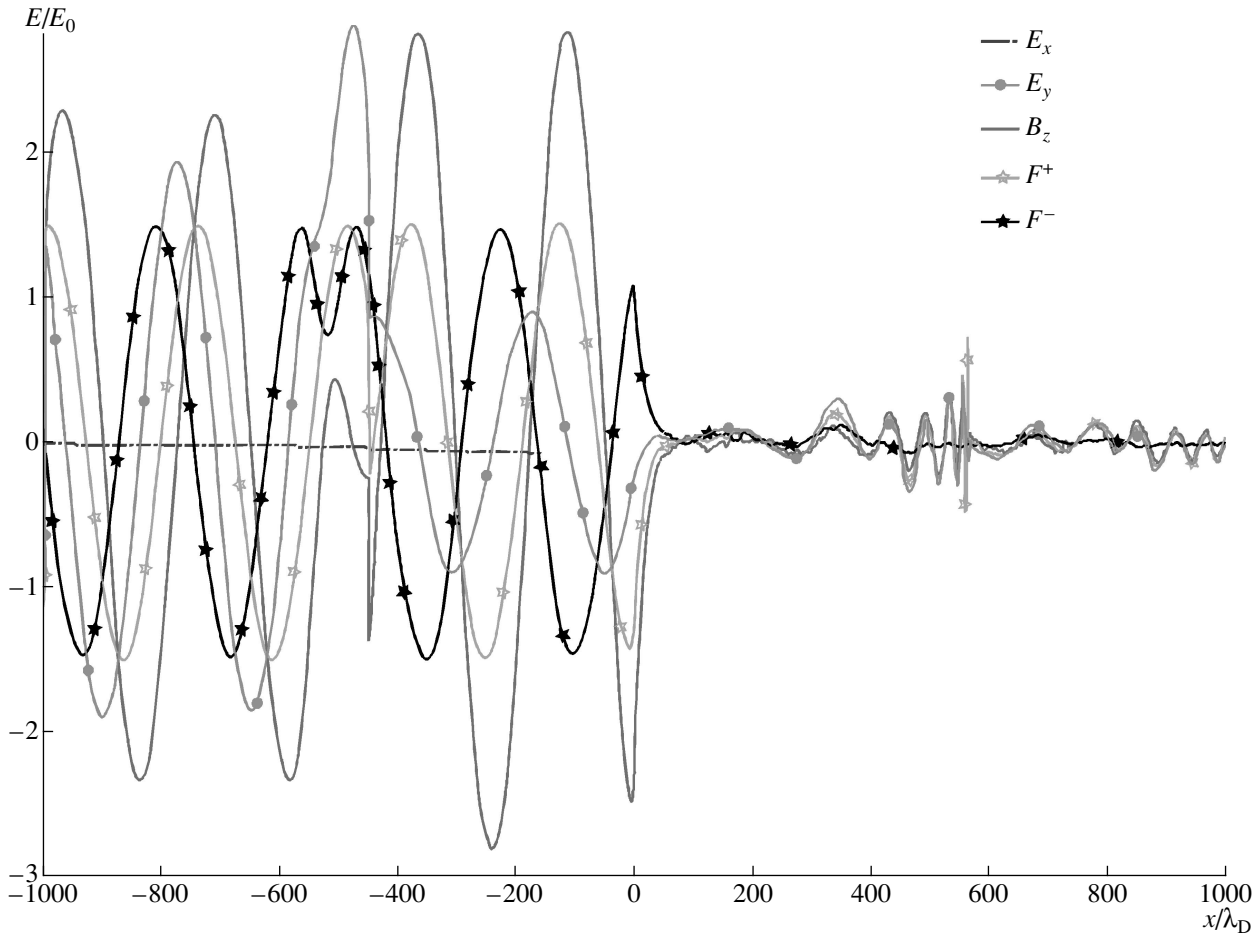
Fig. 2. Spatial profiles of the amplitudes of the incident (F^+) and reflected (F^-) waves and of the components of the transmitted wave (E_x, E_y, B_z) for the case of a microwave with a stochastically jumping phase. The plasma boundary is at $x = 0$.

distribution function becomes non-Maxwellian: it has a tail of accelerated electrons. The energy of the incident transverse wave is partially converted into the energy of the longitudinal wave and partially into the electron energy.

In order to illustrate the practical importance of the situation under examination, we present characteristic waveforms of stochastic signals in actual beam–plasma generators [7–9].

From Fig. 5 we can see that stochastic jumps in the phase of the signal occur very frequently (after each two to three periods or even more often).

2. EXPERIMENTAL INVESTIGATION OF THE PASSAGE OF STOCHASTIC ELECTROMAGNETIC RADIATION THROUGH A HIGH-DENSITY PLASMA

The passage of stochastic electromagnetic radiation from a broadband generator [10] through a plasma was investigated experimentally on the device [11] whose block diagram is illustrated in Fig. 6. The plasma in

cavity *2* was created by M-571 magnetron *1* with a controlled output power ($W \leq 2.5$ kW), operating at a frequency of $f = 2.475$ GHz.

The working gas (deuterium) was puffed into and pumped out of cavity *2* through pipes *3* and *4*. The mirror magnetic field (whose longitudinal profile is shown in Fig. 6a) was produced by solenoids *5*, positioned at the ends of cavity *2*.

It should be noted that, although the experimental investigations were carried out under conditions different from those analyzed theoretically in Section 1 (the experiments were performed with a short plasma cavity, rather than with a semi-infinite plasma, and with a nonzero external magnetic field), an important point, as will be clear later, is that they justified the main conclusion of Section 1 that microwaves with a stochastically jumping phase can penetrate far deeper into the plasma than a broadband wave with the same spectral density. Preliminary experimental results were reported in [12].

A signal from G4-76A generator *6* of regular waves or from broadband generator *7* of microwaves with a stochastically jumping phase was fed through coaxial
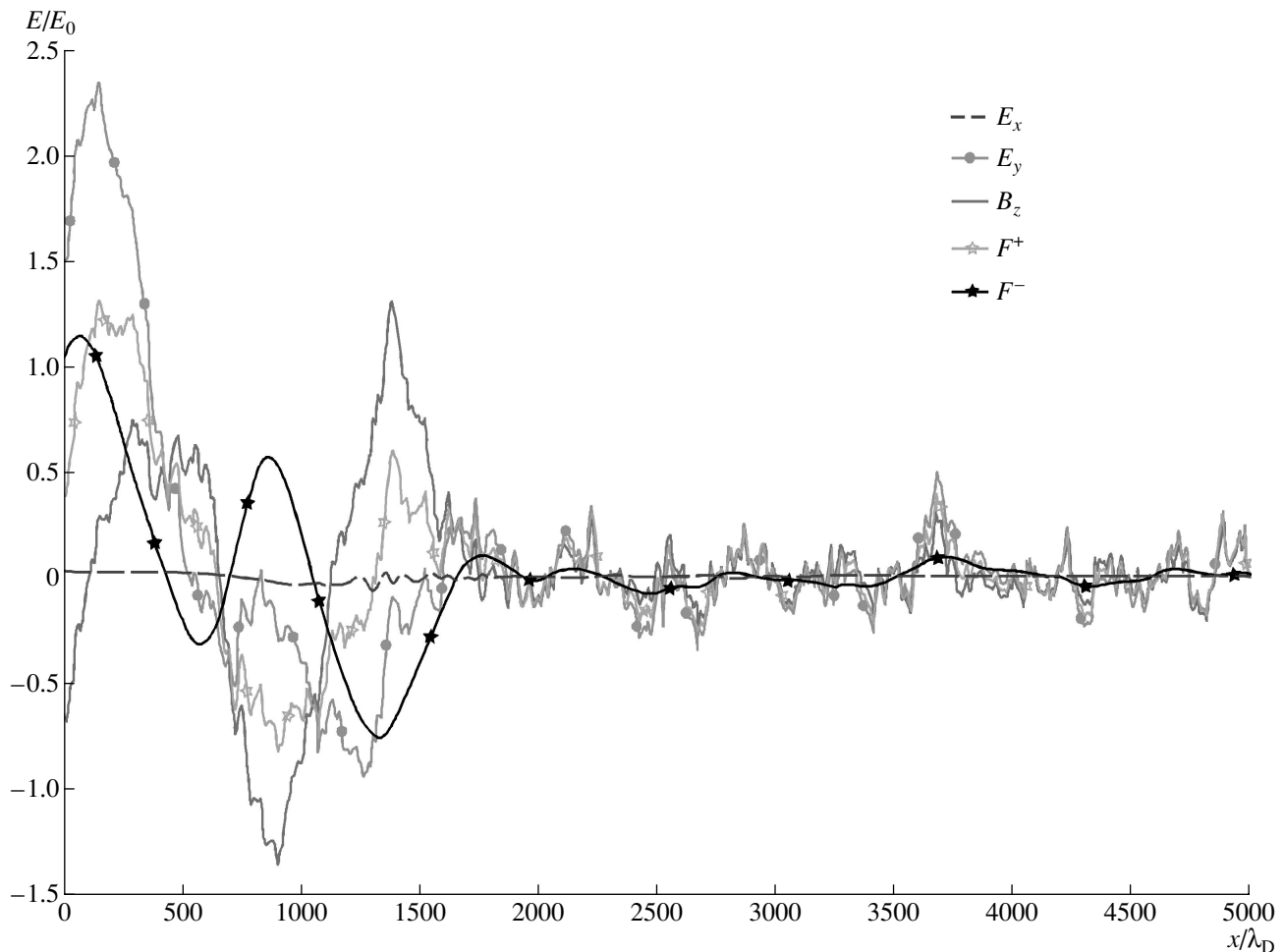
Fig. 3. Spatial profiles of the intensities of the incident (F^+) and reflected (F^-) waves and of the electromagnetic field components of the transmitted wave (E_x, E_y, B_z). The plasma boundary is at $x/\lambda_D = 1500$. The wave phase undergoes regular jumps after each time interval of length $\tau = 40/\omega_p$.

T-connector *8* and É6-32 ferrite isolator *9* and then through coaxial line *10* to emitting probe *11*, placed at the device axis. The signal that had passed through plasma-filled cavity *2* was received by probe *12* and was fed through É6-32 ferrite isolator *13* and coaxial T-connector *14* to S4-60 spectrum analyzer *15* or to S7-19 oscilloscope *16*. Ferrite isolators *9* and *13* served to suppress the signal from magnetron *1*. The emitting and receiving probes of length $l = 100$ mm and diameter $d = 1$ mm were the end portions of the central conductors of an RK-2 coaxial cable. They were protected from contact with the plasma by ceramic tubes with an outer diameter of 4 mm. In experiments, the position of the emitting probe was fixed, the distance between its end and the end of the cavity being 45 mm. The cavity was a stainless-steel cylindrical chamber with a diameter of $D = 50$ cm and length of $L = 50$ cm. At both ends, the main cavity was equipped with beyond-cutoff (for the electromagnetic waves under investigation) auxiliary cavities.

The density of the plasma created in the cavity by the magnetron could be varied from 10^9 to 10^{10} cm^{-3} by varying the magnetron power. The dependence of the plasma density on the magnetron current at a working gas pressure of $p = 5 \times 10^{-5}$ torr is shown in Fig. 7.

We also investigated how the plasma density depends on the working gas pressure and found that this dependence was far weaker than that on the magnetron current. This is why we varied the plasma density in the cavity at a constant gas pressure only by varying the magnetron current.

The signals from a G4-76A generator or from a generator of stochastic radiation (the amplitude–frequency characteristics of these signals are shown in Figs. 8–12) were fed to the cavity through an emitting probe *11* installed in a fixed position. The signal that had passed through the plasma was received by probe *12*, which could be installed in one of the four fixed positions within the cavity, and then was fed to the spectrum analyzer. Since there was a small number of eigenmodes of
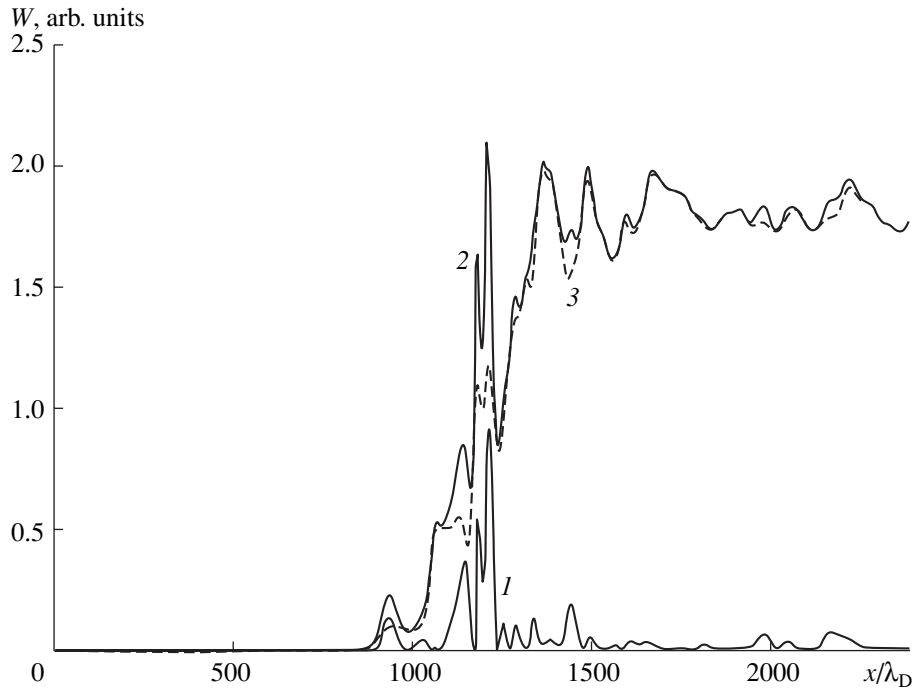
Fig. 4. Spatial profiles of the energy of the longitudinal field of the regular radiation (W, curve *1*), stochastic radiation (W_s, curve *2*), and radiation whose phase undergoes regular jumps after each time interval of length τ (W_τ, curve *3*).
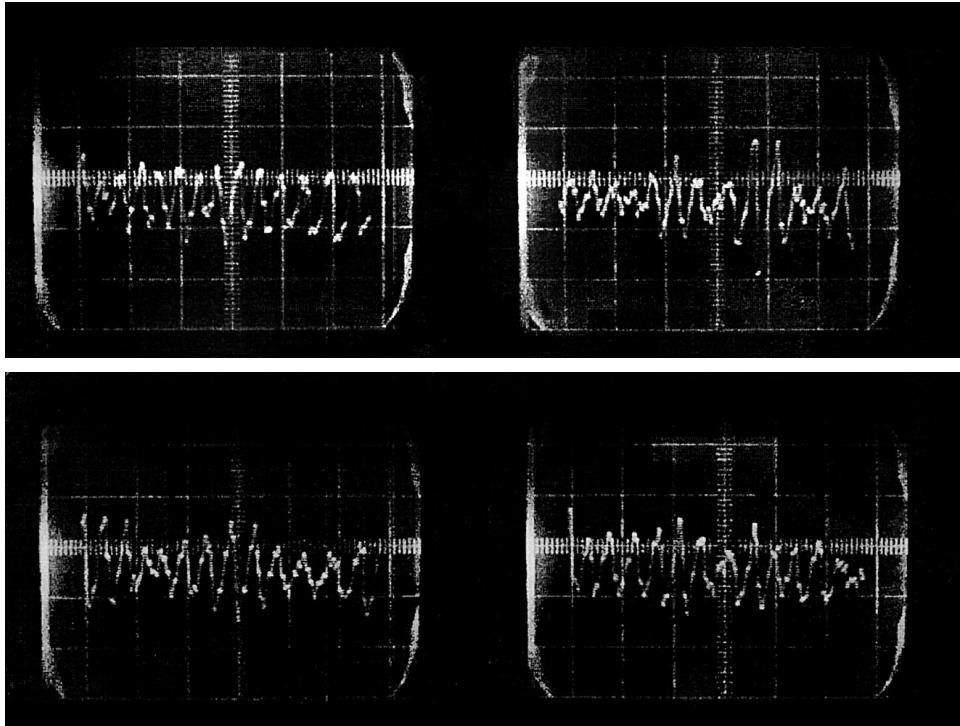

Fig. 5. Microwave signal with a stochastically jumping phase from a beam–plasma generator.

the plasma waveguide with frequencies below 1 GHz, it was expedient to identify them by choosing four such positions of the probe that corresponded to the nodes or antinodes of these eigenmodes.
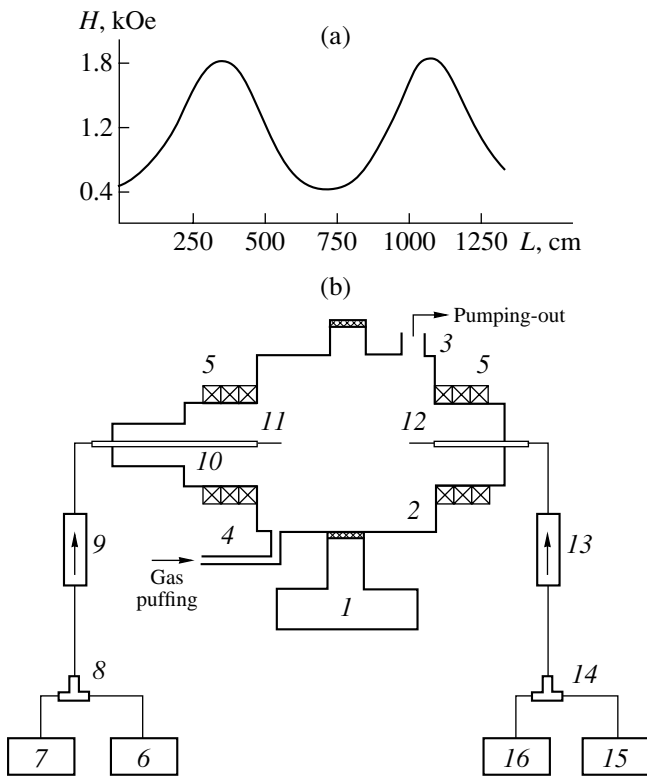
Fig. 6. (a) Longitudinal magnetic field profile in the experimental setup for investigating the passage of stochastic electromagnetic radiation through a plasma and (b) block diagram of the experimental setup: (*1*) magnetron, (*2*) cavity, (*3*) pumping-out, (*4*) gas puffing, (*5*) solenoids, (*6*) G4-76A generator, (*7*) generator of broadband stochastic radiation, (*8, 14*) T-connectors, (*9, 13*) ferrite isolators, (*10*) coaxial line, (*11*) emitting probe, (*12*) receiving probe, (*15*) S4-60 spectrum analyzer, and (*16*) S7-19 oscilloscope.
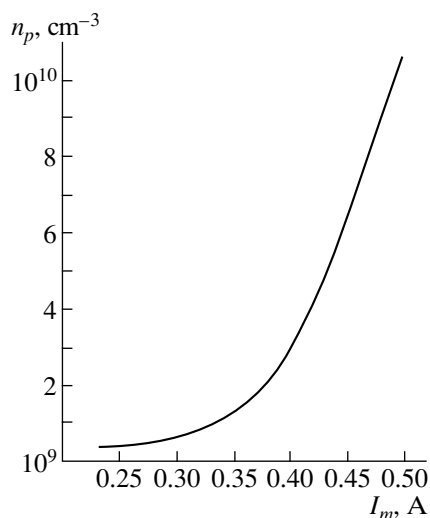
Fig. 7. Plasma density vs. magnetron current.

2.1. Results and Discussion

Let us analyze the structure of a stochastic signal from a broadband generator after it has passed through the plasma. The corresponding results obtained for a low-density plasma ($n_p \approx 5 \times 10^9$ cm^{-3}) and a high-density plasma ($n_p \approx 10^{10}$ cm^{-3}) are presented in Figs. 9–11. It can be seen that the signals that arrive at the receiving probe at different positions have different amplitude–frequency characteristics. Note that the conditions of our experiments correspond to a magnetized plasma, because the electron gyrofrequency ω_{He} exceeds the electron Langmuir frequency, $\omega_{He}^2 \gg \omega_p^2$.

It is known that, in this case, the eigenmodes of the system under discussion exist in two different frequency ranges. These are the ranges of working frequencies ω above the cutoff frequency $\omega_{cut} = \sqrt{\omega_p^2 + c^2 k_\perp^2}$ (where $k_\perp = 2.4/R$, with R being the cavity radius) and below the electron Langmuir frequency ω_p. The range of frequencies of up to 1 GHz, which was investigated in our experiments, overlaps with both of them. In this frequency range, the number of eigenmodes of the plasma cavity is small. However, the waveforms of the signals show the presence of many unnatural waves that are attributed to the small cavity length and the short distance between probes *11* and *12* (the amplitude of the waves excited by probe *11* cannot decrease substantially over such a short distance). The maximum in the amplitude of the transmitted stochastic signal in the high-frequency range at a frequency of $f_{1a} = 800$ MHz (Fig. 10a) corresponds to the first radial harmonic with a longitudinal field structure such that there are two minima at the cavity ends and one maximum at the center of the cavity. Note that, in Fig. 10, the signal amplitude at this frequency is somewhat lower than its maximum value, because the receiving probe is displaced from the center of the cavity (the case in which the receiving probe is placed just at the center of the cavity is presented in Fig. 11). The maxima in the amplitude of the stochastic signal in the high-frequency range at a frequency of $f_{2a} = 950$ MHz (Figs. 9a, 9c) correspond to the first radial harmonic with a longitudinal field structure such that the longitudinal wavelength is equal to the cavity length, i.e., the field has a maximum and a minimum within the cavity and vanishes at the center of the cavity and at its ends. We can see from Fig. 11 that the signal amplitude at this frequency is minimum at the center of the cavity (that it is minimum rather than zero stems from the fact that the probe is extended rather than pointlike) because the amplitude of the mode in question is maximum at distances from the cavity ends that are equal to one-quarter of the cavity length. The next eigenmode of the cavity corresponds to the first radial harmonic with a longitudinal field structure such that the cavity length is equal to 1.5 longitudinal wavelengths, i.e., the field has three extremes within the cavity and is zero at the cavity ends
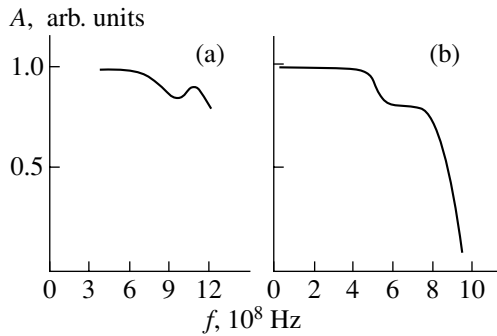
A, arb. units

Fig. 8. Amplitude–frequency characteristics of the signals from (a) the G4-76A generator and (b) the generator of stochastic radiation.

and between the extreme points. However, even in the absence of plasma, the frequency of this eigenmode is higher than 1 GHz, i.e., is beyond the frequency range under investigation. A further increase in the magnetron current results in a corresponding increase in the plasma density and, accordingly, in the frequencies f_1 and f_2, which thus turn out to be above the working range of frequencies. Recall that, first, in the low-frequency range, the eigenmodes of the cavity can propagate within it only when it is filled by a plasma of corresponding density, and, second, the existence of unnatural waves is a consequence of the small geometric dimensions of the cavity and the short distance between the probes. These two remarks refer in full measure to both stochastic and regular signals.

Let us analyze the passage of a regular signal through the cavity, compare the results obtained with those for microwaves with a stochastically jumping phase, and examine the degree to which they agree with the theoretical results presented in the first part of this paper (see also [6]). Figure 12 shows the amplitude–frequency characteristic of a regular signal that has passed through the cavity (a) without a plasma, (b) with a low-density plasma ($n_p \approx 5 \times 10^9$ cm^{-3}), and (c) with a high-density plasma ($n_p \approx 10^{10}$ cm^{-3}). From Fig. 12a we can see that, in the absence of plasma, regular signals at frequencies higher than 400 MHz pass through the cavity; in this case, the cutoff frequency is equal to 478 MHz, which corresponds to the critical wavelength ($\lambda_{cr} = 2.62R$) for the E_{01} mode. It is also seen that the peaks corresponding to the eigenmodes of the cavity are pronounced only slightly. In order for the transmitted signals from an incident regular wave and from an incident wave with a stochastically jumping phase to have the same amplitude, the amplitude of the former should be one to two orders of magnitude larger than that of the latter. This provides evidence for a low efficiency of the excitation of waves in the cavity by a regular signal, on the one hand, and for a lack of selectivity between eigenmodes and unnatural waves during the passage of a regular signal, on the other hand.

2.2. Conclusions

Our experimental investigations of the excitation of regular and stochastic electromagnetic waves in plasmas of different densities and their passage through a cavity allow us to draw the following conclusions:

(i) A regular wave excites a cavity less efficiently than does a wave with a stochastically jumping phase (in order for the transmitted signals from an incident
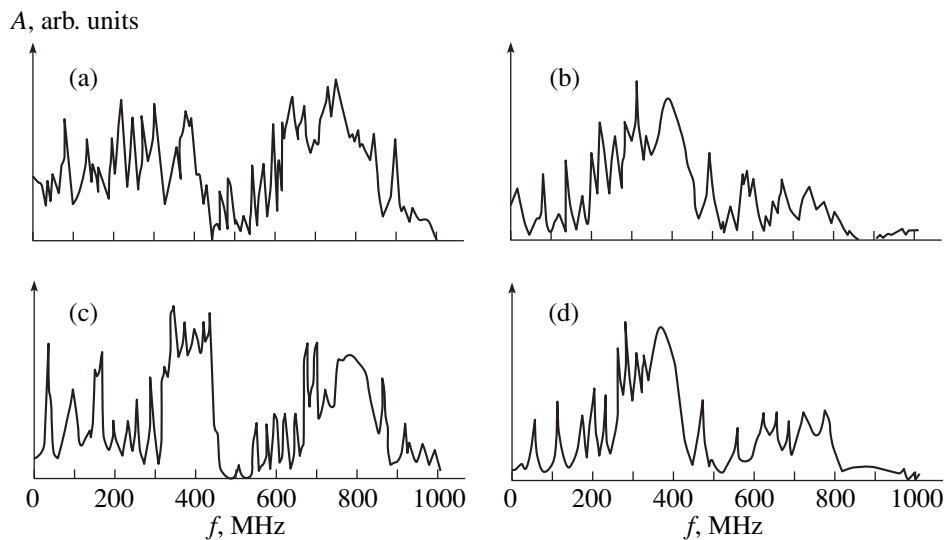
A, arb. units

Fig. 9. Frequency spectrum of a stochastic signal that has passed through a plasma of density $n_p \approx$ (a, c) 5×10^9 and (b, d) 10^{10} cm^{-3}. The distance between the emitting and receiving probes is (a, b) 14.0 and (c, d) 33.5 cm.
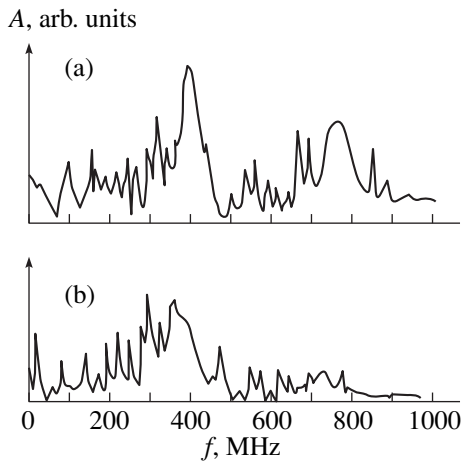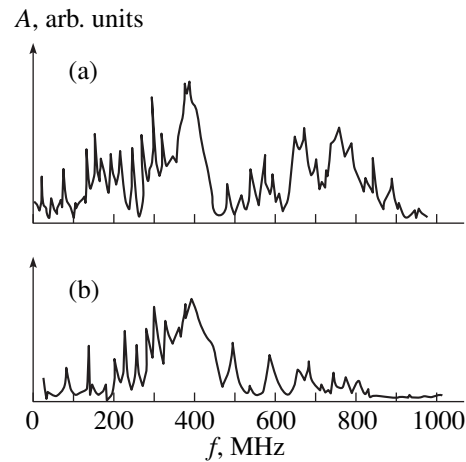
A, arb. units

(a)

(b)

0   200   400   600   800   1000
f, MHz

Fig. 10. Frequency spectrum of a stochastic signal that has passed through a plasma of density $n_p \approx$ (a) 5×10^9 and (b) 10^{10} cm^{-3}. The distance between the emitting and receiving probes is 27.0 cm.

A, arb. units

(a)

(b)

0   200   400   600   800   1000
f, MHz

Fig. 11. Frequency spectrum of a stochastic signal that has passed through a plasma of density $n_p \approx$ (a) 5×10^9 and (b) 10^{10} cm^{-3}. The distance between the emitting and receiving probes is 20.6 cm.

regular wave and from an incident wave with a stochastically jumping phase to have the same amplitude, the amplitude of the former should be one to two orders of magnitude larger than that of the latter).

(ii) As a regular monochromatic signal excites a cavity and passes through it, selectivity between eigenmodes and unnatural waves is lacking.

The results of our experimental investigations are in satisfactory qualitative agreement with the theoretical predictions.

3. MICROWAVE DISCHARGE INITIATED BY WAVES WITH A STOCHASTICALLY JUMPING PHASE AND ITS APPLICATION

In 1992, specialists from the Fusion System Corporation (Maryland) designed a highly efficient light source operating in the quasi-solar spectral region and based on an electrodeless microwave gas discharge in a sulfur-containing tube [13]. The continuous (molecular) spectrum of high-power optical radiation from a sulfur-containing lamp resembles that of the Sun, but with depressed levels of IR and UV radiation. In October 1994, the Fusion Lighting Company, Inc. (Washington, DC) demonstrated two efficient light systems, which attracted the attention of experts and potential consumers to new light sources, the development of which was perceived as a very important technological breakthrough immediately before the 21st century. The first light sources based on a sulfur-containing tube were pumped by two 1.7-kW magnetrons operating in the frequency range from 915 to 2450 MHz. The best results were achieved in 1996: the light flux from a lamp was 480 klm, and the light-output efficiency was 95 lm/W.

The physical mechanism underlying the operation of sulfur-based lamps is the emission of photons in quantum transitions between the energy states of evaporated sulfur molecules that are excited or ionized by a
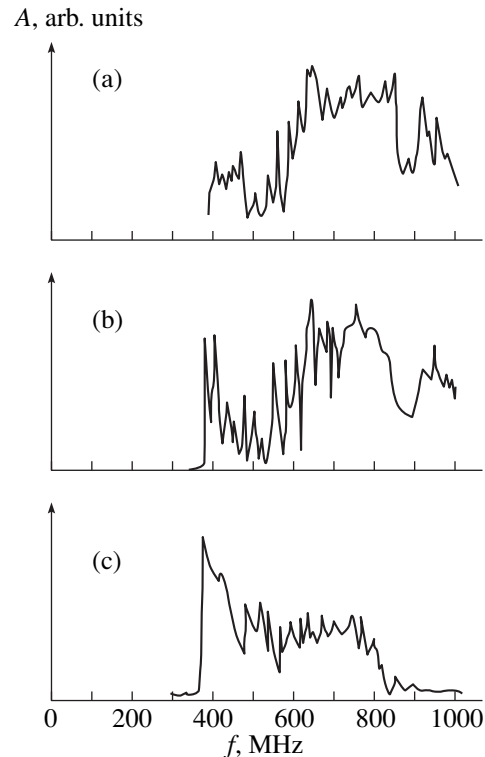
A, arb. units

(a)

(b)

(c)

0   200   400   600   800   1000
f, MHz

Fig. 12. Frequency spectrum of a regular signal that has passed through a cavity (a) without a plasma ($n_p = 0$) and with a plasma of density $n_p \approx$ (b) 5×10^9 and (c) 10^{10} cm^{-3}. The distance between the emitting and receiving probes is 33.5 cm.

microwave discharge within a small volume bounded by a spherical quartz shell.

The conversion of the microwave (pump) energy is into optical radiation proceeds as follows: Just after the amplitude of the electric component of the microwave field in the cavity (in the region where the sulfur lamp is placed) increases to a breakdown value, a microwave discharge is initiated in a buffer gas (argon) saturated with sulfur vapor (initially, sulfur is in a solid state). In this stage, the lamp radiates not a continuous spectrum but rather individual spectral lines corresponding to typical energy transitions in argon and sulfur atoms, including pronounced IR and UV lines. As the microwave energy is absorbed by a low-pressure discharge and as the number of ionization events increases, the plasma density increases and the bombardment of the inner shell surface (which has been coated with sulfur in the course of previous discharges) by the charge particles (primarily, by the electrons, which are the most mobile charge carriers) intensifies. During the bombardment by the charge particles (which move mainly along the microwave electric field), the shell is rapidly heated, the sulfur is partially evaporated, and the pressure increases. This process consists of two steps: the melting of different polymorphic forms of sulfur (the melting points being 112.8 and 119.3°C) and their complete evaporation (the boiling point being $T_{boil} = 444.6$°C); as a result, the concentration of sulfur molecules within the shell becomes fairly high. In a stable plasma operating mode (a high-power discharge), the spectrum of the resulting optical light has a molecular character: it reflects transitions between numerous energy levels, including the rotational and vibrational degrees of freedom of the molecules, and thereby is quasi-continuous. The emission spectrum possesses this property at different microwave powers and different initial amounts of sulfur in a lamp of a given size.

The main problems associated with microwave pumping are as follows (see, e.g., [14]):

(i) To choose the power of a microwave signal and its shape (continuous or amplitude-modulated).

(ii) To design a microwave transmission line from a microwave source (generator) to a load (electrodeless lamp), to construct a transmitter (whose operating regime should depend on the mode of microwave radiation), and to provide an appropriate topography of the microwave field in the region where it interacts with the working substance of the lamp (just after the generator is switched on and in the plasma operating mode).

(iii) To maintain the stable operation of the microwave generator loaded by the lamp, whose parameters change substantially during the development of a microwave discharge (from the switching on of the generator up to the beginning of the steady-state plasma operating mode).

(iv) To prevent undesirable microwave emission at the pump frequency f_w and its harmonics ($2f_w$, ..., $5f_w$, ..., nf_w) into the surrounding space (if only the optical
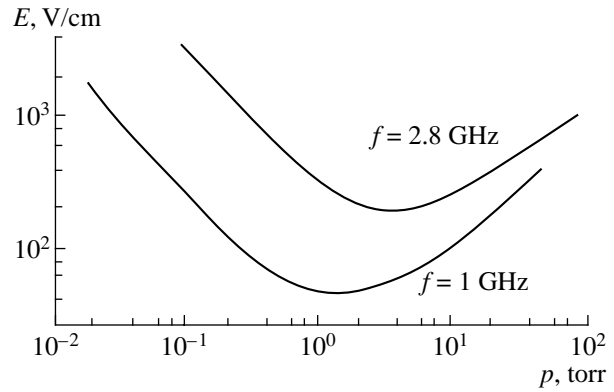

Fig. 13. Thresholds for microwave breakdown of argon (borrowed from [15]).

light is intended for use) and to ensure environmental safety and electromagnetic compatibility, a closely related task being to find compromise between the optical transparency of the wall of the microwave cavity (in which microwave fields interact with the plasma) and undesirable microwave emission.

The underlying problem is that of choosing the microwave field frequency so as to satisfy the requirement that the input microwave power be minimum. In order to determine the working microwave frequency, it is necessary to compare three parameters: the diameter of the shell Λ ($\Lambda \approx 1$–2 cm), the electron mean free path l, and the electron oscillation amplitude A. Discharges in argon that evaporate sulfur (which is an electronegative element) can be initiated only when the electrons oscillate within a quartz shell, i.e., when $A < \Lambda/2$. The capture of electrons by sulfur molecules can only be balanced by intense ionization. The amplitude of the electron oscillations in a microwave field is equal to

$$A = \frac{eE_0}{m\omega\sqrt{\omega^2 + \nu_c^2}}, \qquad (3.1)$$

where ν_c is the collision frequency, E_0 is the microwave field amplitude, and ω is the oscillation frequency. For $\nu_c \gg \omega$, the desired inequality is satisfied when $2eE_0/(m\nu_c\omega\Lambda) < 1$. This indicates that the boundary frequency depends on the diameter of the quartz shell, the pressure within it, and the microwave (or RF) field intensity. It is known (see, e.g., [15]) that, for all gases, the dependence of the threshold field for gas breakdown on the pressure has a minimum that separates two branches (Fig. 13). Along the left branch, the threshold field decreases with increasing pressure and the situation is as follows: the higher the field frequency and the smaller the discharge chamber, the stronger the threshold field. Along the right branch, the threshold field increases with increasing pressure and its dependence on the size of the discharge chamber and on the microwave field frequency becomes increasingly less pronounced; in the limit of high pressures, this dependence

is negligibly weak and the right branches at any size of the discharge chamber and any microwave field frequency asymptotically approach a single branch.

All these results can be qualitatively explained by reference to an elementary analysis of the rate at which an electron gains energy in an alternating electric field and by using the criterion for breakdown. The ionization rate is primarily determined by the time during which the energy of an electron increases to a level slightly above the ionization energy of a gas (hereafter, we are interested in argon), $I_{Ar} = 15.76$ eV. In order to estimate the threshold for breakdown, we first consider discharges in argon at low pressures. In this case, the electron diffusion is very rapid and the diffusive electron losses are large. To balance them, it is necessary that the ionization rate be high, i.e., the electromagnetic field be strong. In strong fields, however, elastic collisions play an insignificant role in electron energy losses. The electron energy does not exceed I_{Ar} because an electron with such a high energy immediately loses it in ionization events. Consequently, only a limited fraction of energy is transferred from an electron to an atom per elastic collision, $(\Delta\varepsilon_{el})_{max} \approx (2m/M)I_{Ar}$. As for the amount of energy $\Delta\varepsilon_E$ gained by an electron in collisions in an alternating electric field, it is proportional to E_0^2; so, for the sufficiently strong fields required to balance large diffusive losses, we have $\Delta\varepsilon_E \gg (\Delta\varepsilon_{el})_{max}$. Ignoring the energy losses in elastic collisions and assuming that the elastic collision frequency is much lower than the electromagnetic field frequency ($\nu_c \ll \omega$), we find that, in the limit of low pressures, the ionization rate in argon is approximately equal to

$$\nu_i(E_0) = \left(\frac{d\varepsilon}{dt}\right)_E \frac{1}{I_{Ar}} = \frac{e^2 E_0^2 \nu_p}{m\omega^2 I_{Ar}}, \tag{3.2}$$

where ν_p is the transport collision frequency. In accordance with the criterion for steady breakdown, we have $\nu_i(E_0) = \nu_D = D/\Lambda^2$ (where ν_D is the collision frequency corresponding to the diffusion of electrons from a region with a characteristic size Λ and D is the diffusion coefficient). Consequently, for low pressures, the rms threshold field is equal to

$$E_{tr} = \left(\frac{Dm\omega^2 I_{Ar}}{e^2 \Lambda^2 \nu_p}\right)^{1/2}. \tag{3.3}$$

For regular microwave radiation, the threshold field just obtained is directly proportional to the frequency and is inversely proportional to the gas density (pressure) and the size of the discharge region, in complete agreement with the known experimental data (see, e.g., [15]). For a field frequency of $f = 1$ GHz, the minimum threshold field for breakdown, $E_0 = 60$ V/cm, corresponds to an argon pressure of nearly 133 Pa. It should be noted that the microwave range is preferable from the standpoint of minimizing the breakdown field. It is, however, inexpedient to further increase the field fre-

quency because the electron mean free path satisfies the relationship $A\omega$. Indeed, for low pressures, we have $A \propto 1/\omega^2$, so the electron mean free path decreases with frequency. It is clear that the discharge should be initiated over the entire volume within the shell. This can be done when the penetration depth δ of the microwave field into the plasma is comparable to the shell radius Λ. The depth to which microwaves penetrate into a conducting plasma is equal to $\delta = c/\sqrt{2\pi\sigma\omega} \geq \Lambda$, where σ is the plasma conductivity.

An important task is to determine the power of a microwave generator that is required to initiate a discharge in a buffer gas and then to maintain it in a plasma after the evaporation and ionization of sulfur.

Recall that, for microwave discharges in regular electromagnetic fields, the threshold field is minimum when the collision frequency is equal to the electromagnetic field frequency (see, e.g., [15]). Thus, at a frequency of $f \approx 3.0$ GHz, the minimum threshold field for breakdown of Ar at a pressure of about 650 Pa is 500 V/cm. Such field strengths can be achieved in a cavity in which one of the walls is transparent to light. In the situation under analysis, the electric field amplitude E_Q is proportional to $\sqrt{100P(W)Q}$, where $P(W)$ is the generator power in watts and Q is the quality factor of the cavity. It follows from this that, for $Q = 100$, the microwave power should be 25 W. The effective amplitude of the alternating electric field, E_{eff}, which should exceed the threshold field E_{th}, is smaller than E_0:

$$E_{eff} = \frac{E_0}{\sqrt{2}} \frac{\nu_c}{\sqrt{\nu_c^2 + \omega^2}}. \tag{3.4}$$

Hence, in order to excite a plasma by regular microwaves, the power of the generator should be about 100 W.

In the present paper, we propose to initiate microwave discharges in argon containing sulfur vapor by microwaves with a stochastically jumping phase. The advantages of this method are as follows:

(i) such microwaves are capable of initiating discharges at lower gas pressures because the jumping phase slows electron diffusion,

(ii) the jumps in the phase ensure that the collisionless electron heating is not accompanied by energy losses in elastic and inelastic collisions, and

(iii) a uniform microwave discharge is easy to initiate because microwaves with a stochastically jumping phase can deeper penetrate into an overcritical plasma.

A discharge excited in argon heats the quartz shell, leading to the evaporation of sulfur and producing a sulfur-containing argon plasma. The luminescence of argon is then followed by light emissions from the polymorphous sulfur, whose spectral properties have much in common with those of solar radiation. The pressure of sulfur vapor is determined by the amount of

sulfur within the quartz shell. Usually, sulfur concentrations of about 2–5 mg/cm^3 are sufficient.

The field required to maintain a discharge in a plasma is far weaker than that needed for gas breakdown. The amplitude E_d of the maintaining field is related to the plasma electron temperature by the relationships [15]

$$\sqrt{\frac{k_B T_e}{I_{Ar}}}\exp\left(\frac{I_{Ar}}{k_B T_e}\right) = \text{const}(pR)^2$$
$$= 1.27 \times 10^7 c_T^2 (pR)^2, \qquad (3.5)$$
$$E_d = \frac{m}{e}\sqrt{\frac{3k_B T_e}{M}(\omega^2 + \nu_c^2)},$$

where R is the radius of the discharge channel and M is the atomic mass of the gas. The value of the constant c_T depends on the sort of gas; for instance, for argon, we have $c_T = 4 \times 10^2$. The channel radius is $R \sim 1$ cm; therefore, for a pressure of nearly 100 Pa, the electron temperature (which decreases with increasing pressure) is equal to $T_e = 3 \times 10^4$ K. Let us substitute this value of T_e into the expression for E_d.

For $\nu_c \ll \omega$, the maintaining field amplitude E_d is equal to

$$E_d = \frac{m\omega}{e}\sqrt{\frac{3k_B T_e}{M}} = \frac{2\pi mc^2}{e\lambda}\sqrt{\frac{3k_B T_e}{Mc^2}}. \qquad (3.6)$$

For molecular sulfur ($Mc^2 = 50$ GeV), we have $E_d \sim 0.4$ V/cm. The field E_d increases with ν_c and reaches a level of 1–2 V/cm when ν_c becomes higher than ω. It should be taken into account, however, that the electron temperature T_e decreases with increasing ν_c. Note also that formula (3.6) is valid only for elastic collisions. To maintain a discharge in a plasma in which inelastic collisions play an important role, the field E_d should be raised by approximately one order of magnitude.

Let us now consider the conditions for breakdown in argon by microwave radiation from the generator described in [9]. The working frequency of this generator is 400 MHz, the mean rate of the phase jumps being $\nu_{jp} = 2 \times 10^8$ s^{-1}. It is important to keep in mind that, when the electron energy increases from zero to the ionization energy I_{Ar}, the cross section for elastic collisions of electrons with argon atoms varies greatly (by a factor of about 30), being at its maximum several times larger than the ionization cross section corresponding to electron energies of 15–20 eV. This makes it possible to initiate discharges in argon by microwaves with a stochastically jumping phase at pressures as low as 4 Pa. In this case, the mean rate of phase jumps is equal to the maximum elastic collision frequency, which corresponds to electron energies close to the ionization energy. Operation under such conditions is advantageous in that, first, no energy is lost in elastic collisions, and, second, due to the jumps in the phase,
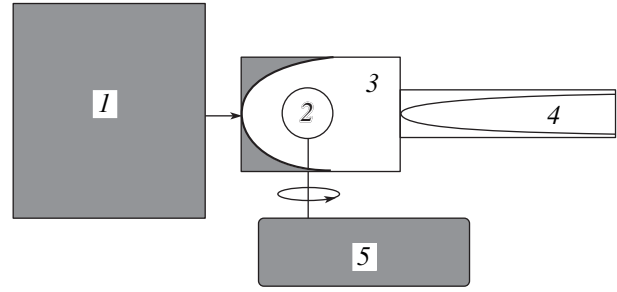

Fig. 14. Block diagram of a microwave-discharge-based light source: (*1*) power supply unit, high-power microwave generator, and matching system; (*2*) quartz shell filled with an Ar–S gas mixture; (*3*) microwave cavity and light output system; (*4*) lightguides; and (*5*) system for rotation and forced cooling of the quartz shell.

the electron diffusion remains insignificant and the electromagnetic energy is efficiently transferred to electrons. Considering the effective rate of the phase jumps as the transport collision frequency ν_p and substituting it into expression (3.3), we find that, in the case at hand, the required threshold field does not exceed 50 V/cm, which agrees well with the results of preliminary experiments on determining the threshold electric field of microwave radiation with a stochastically jumping phase.

We thus have estimated the electric field required to initiate and maintain a discharge in a shell containing an Ar–S mixture.

Our numerical simulations and preliminary experiments show that, in order to initiate a microwave discharge at a frequency of 450 MHz in argon at a pressure of 4 Pa, the microwave electric field strength should be about 50 V/cm, whereas sulfur vapor can be excited by an electric field of 25 V/cm, which can easily be achieved with an input power of several hundred watts, even without using discharge chambers equipped with microwave cavities. With the use of such chambers, it is possible to substantially reduce the generator power. The block diagram of a microwave-discharge-based source of visible light is shown in Fig. 14 (which is borrowed from [16]).

In a sulfur-based light system (SLS) demonstrated by the Fusion Lighting Company, Inc., the shell is placed within a chamber that is opaque to microwaves but is transparent to visible light. The working microwave frequency of this system, 450 ± 50 MHz, is consistent with standards adopted for industrial, scientific, and medical applications. With the version of the light system proposed by the company, it becomes possible to design compact low-power SLSs, in addition to the already existing traditional SLSs with output powers in the kilowatts range [13, 14, 16], which are usually based on 2450 ± 50-MHz magnetrons. The systems for rotation and forced cooling of the shell ensure a thermal regime that does not destroy the quartz shell filled with an Ar–S gas mixture. Inside the microwave chamber,

the shell rotates at a rate of 600 rpm. Technologically, the engineering design of the device in question should ensure maximum light yields from a cavity utilizing harmless microwave radiation consistent with the adopted standards. Experts from the Fusion Lighting Company, Inc., propose to fabricate cavities from grids and additional mesh screens. An important role in the system proposed by the company is played by a parabolic reflector and a prism lightguide. The practical role of the parabolic reflector is to ensure that light is emitted into a hollow prismatic lightguide. The shell is inserted into the cavity positioned at the focus of the parabolic reflector. A specially devised array of lightguides serves as an efficient means to transmit light to consumers. This technology makes it possible to use lightguides whose surfaces partially reflect light and partially transmit it to form a required distribution of the output light intensity. The parameters of the lightguides are as follows: they are acrylic, and their walls are as thick as 3 mm, the outer diameter and length being 250 mm and 28 m, respectively.

Such light sources make it possible to obtain considerable (multifold) energy saving, while simultaneously increasing the level of illumination. They are demonstrated in the American Museum of Astronautics.

4. CONCLUSIONS

New types of beam–plasma generators of intense stochastic microwave radiation were developed and put into operation at the National Science Center Kharkov Institute of Physics and Technology (Ukraine). In the present paper, we have discussed the results of theoretical and experimental studies and numerical simulations of the normal and oblique incidence of linearly polarized electromagnetic waves on an interface between a vacuum and an overcritical plasma. The main results of our investigations are as follows: (i) for the parameter values under consideration, the transmission coefficient for microwaves with a stochastically jumping phase is found to be one order of magnitude greater than that for a broadband wave with the same spectral density; (ii) the electrons are shown to be heated most efficiently by obliquely incident waves with a stochastically jumping phase and, in addition, the electron distribution function has a high-energy tail; and (iii) necessary conditions for gas breakdown and for the maintenance of a microwave discharge in stochastic fields in a light source have been determined. The anomalously large transmission coefficient for microwaves, the anomalous character of the breakdown conditions, the anomalous behavior of microwave gas discharges, and the anomalous nature of collisionless electron heating have been attributed to stochastic jumps in the phase of microwave radiation.

REFERENCES

1. A. G. Litvak and M. D. Tokman, Phys. Rev. Lett. **88**, 095003 (2002).

2. Ya. B. Faĭnberg, F. G. Bass, and V. D. Shapiro, Zh. Éksp. Teor. Fiz. **49**, 329 (1965) [Sov. Phys. JETP **22**, 230 (1965)].

3. S. A. Akhmanov, Yu. E. D'yakov, and A. S. Chirkin, *Introduction to Statistical Radiophysics and Optics* (Nauka, Moscow, 1981) [in Russian].

4. V. D. Levchenko and Yu. S. Sigov, in *Dynamics of Transport in Fluids, Plasmas, and Charged Beams*, Ed. by G. Maino and A. Provenzale (World Scientific, Singapore, 1995), p. 121.

5. L. V. In'kov and V. D. Levchenko, Preprint No. 133 (Keldysh Institute of Applied Mathematics, Russ. Acad. Sci., Moscow, 1995).

6. V. I. Karas' and V. D. Levshenko, in *Proceedings of V International Workshop on Strong Microwaves in Plasmas, Nizhni Novgorod, 2002*, Ed. by A. G. Litvak (Institute of Applied Physics, Russ. Acad. Sci., Nizhni Novgorod, 2003), Vol. 2, p. 550; V. I. Karas' and V. D. Levshenko, Vopr. At. Nauki Tekh., Ser.: Plasm. Elektron. Nov. Metody Uskoreniya, No. 4, 133 (2003).

7. A. N. Antonov, Yu. P. Bliokh, Yu. A. Degtyar', *et al.*, Fiz. Plazmy **20**, 777 (1994) [Plasma Phys. Rep. **20**, 699 (1994)].

8. A. K. Berezin, Ya. B. Faĭnberg, A. M. Artamoshkin, *et al.*, Fiz. Plazmy **20**, 782 (1994) [Plasma Phys. Rep. **20**, 703 (1994)].

9. A. K. Berezin, Ya. B. Faĭnberg, Yu. M. Lyapkalo, *et al.*, Fiz. Plazmy **20**, 790 (1994) [Plasma Phys. Rep. **20**, 710 (1994)].

10. A. Alisov, V. Antipov, A. Artamoshkin, *et al.*, *International School and Conference on Plasma Physics and Controlled Fusion, Alushta, 2002*, Book of Abstracts, p. 140.

11. S. I. Solodovchenko, A. F. Shtan', and N. I. Nazarov, in *Proceedings of III Interregional Meeting on Thin Films in Electronics, Moscow–Ioshkar-Ola, 1992*, p. 13 [in Russian].

12. A. F. Alisov, A. M. Artamoshkin, I. A. Zagrebel'nyĭ, *et al.*, Vopr. At. Nauki Tekh., Ser.: Plasm. Elektron. Nov. Metody Uskoreniya, No. 4, 69 (2003).

13. J. T. Dolan, M. G. Ury, and D. A. MacLeean, in *Proceedings of VI International Symposium on Science and Technology of Light Sources, Budapest, 1992*, p. 301.

14. A. Kozlov, V. Perevodchikov, R. Umarhodzhaev, and E. Shlifer, in *Proceedings of IV International Workshop on Microwave Discharges: Fundamentals and Applications, Zvenigorod, 2000*, Ed. by Yu. A. Lebedev (Yanus-K, Moscow, 2001), p. 235.

15. Yu. P. Raĭzer, *Fundamentals of Modern Gas-Discharge Physics* (Nauka, Moscow, 1980) [in Russian].

16. A. Didenko, B. Zverev, A. Koljashkin, and A. Prokopenko, in *Proceedings of IV International Workshop on Microwave Discharges: Fundamentals and Applications, Zvenigorod, 2000*, Ed. by Yu. A. Lebedev (Yanus-K, Moscow, 2001), p. 205.

Translated by G.V. Shepekina

Nonlinear Dynamics of the Interaction
of a Modulated Electron Beam with a Plasma

V. A. Balakirev, A. V. Borodkin, and I. N. Onishchenko

National Science Center Kharkov Institute of Physics and Technology,
ul. Akademicheskaya 1, Kharkov, 61108 Ukraine
Received August 26, 2004; in final form, December 9, 2004

Abstract—The excitation of plasma waves during the injection of an unmodulated and a density-modulated electron beam into a semi-infinite cold plasma is investigated. It is shown that the Langmuir oscillation energy accumulated in the plasma increases substantially near the plasma boundary and that the dimension of the region where the Langmuir oscillation energy is localized decreases with time. © *2005 Pleiades Publishing, Inc.*

1. INTRODUCTION

Modulated relativistic electron beams provide an effective tool for the excitation of regular waves in a plasma. Intense Langmuir waves can be used to accelerate charged particles [1, 2] and can serve as pump waves in free-electron plasma lasers [3, 4].

The dynamics of the excitation of wake plasma waves by a train of a finite number of relativistic electron bunches was investigated in [5]. In this case, the wake fields generated by individual bunches add together coherently, thereby substantially increasing the amplitude of the resulting wake plasma wave behind the train of bunches. The nonlinear excitation of a regular plasma wave by a modulated electron beam injected steadily into a semi-infinite plasma was considered in [6, 7]. In such a system, the steady state is ensured by the finite value of the wave group velocity with which the field energy is carried into the plasma, so the maximum wave amplitude turns out to be limited. Note that the relaxation of an unmodulated beam interacting with a plasma waveguide to a steady state was studied in [8].

In the present paper, we investigate the nonlinear dynamics of the excitation of plasma oscillations by a monoenergetic electron beam injected into a cold plasma (with a zero electron temperature, $T_e = 0$) in the absence of an external magnetic field. We consider a situation in which the group velocity of the excited plasma oscillations is zero, so the effects of accumulation of plasma oscillations in the beam injection region play an important role in the beam relaxation. The influence of the accumulation effects on the quasilinear relaxation of a beam in a plasma was studied in [9], and the influence of the accumulation of plasma oscillations in a semi-infinite plasma on the relaxation of an unmodulated beam in the linear stage of the beam–plasma instability and dissipative instability was considered in [10] (in which the maximum energy density of the excited oscillations was also estimated). In what follows, we will investigate the effect of accumulation of the plasma oscillation energy by numerically analyzing a set of nonlinear equations describing the interaction of a monoenergetic electron beam with a semi-infinite plasma. The influence of the finite transverse plasma dimension on the nonlinear dynamics of the beam–plasma interaction was studied in [11, 12].

2. FORMULATION OF THE PROBLEM
AND BASIC EQUATIONS

We consider a semi-infinite ($z > 0$) homogeneous cold plasma into which a one-dimensional monoenergetic electron beam, generally with a modulated density, is continuously injected. Since we will be interested in the excitation of the electron Langmuir plasma oscillations, we assume that the ions are immobile. The beam electron density in the injection plane ($z = 0$) changes periodically according to the law

$$n_b = n_{b0}[1 + h\cos(\omega_m t)], \tag{1}$$

where h is the modulation depth of the beam density and ω_m is the modulation frequency.

The set of dimensionless equations describing the dynamics of the excitation of a plasma wave by a modulated electron beam contains the equation for the complex wave amplitude and the equation of motion of the beam electrons:

$$\frac{\partial C}{\partial \tau} = -\frac{1}{2\pi}\int_{-\pi}^{\pi} e^{-i\varphi}(1 + h\cos\varphi_0)d\varphi_0, \tag{2}$$

$$\frac{d^2\varphi}{d\xi^2} = \mathrm{Re}(Ce^{i\varphi}), \tag{3}$$

where $C = \dfrac{ekE}{m v_0^2} \dfrac{1}{\delta^2}$ is the dimensionless wave amplitude, $\delta = (\omega_{p0}^2 \omega_b)^{1/3} / v_0$, $k = \omega_m / v_0$, v_0 is the initial velocity of the beam electrons, $\omega_{p0} = \left(\dfrac{4\pi n_{p0} e^2}{m} \right)^{1/2}$ is the Langmuir frequency of the plasma electrons, n_{p0} is the plasma density, e and m are the charge and mass of an electron, $\omega_b = \left(\dfrac{4\pi n_{b0} e^2}{m \gamma_0^3} \right)^{1/2}$ is the Langmuir frequency of the beam electrons, γ_0 is the initial relativistic factor of the beam electrons, $\xi = \delta z$, $\varphi = \delta(v_0 t_l - z)$, t_l is the time at which a beam electron arrives at the point z, and $\tau = \delta(v_0 t - z)$. In Eq. (2), the integration is carried out over the phases of the beam electrons in the injection plane. Equations (2) and (3) have been obtained under the resonance condition $\omega_m = \omega_{p0}$, which implies that the electron beam density is modulated at the frequency of plasma oscillations.

The set of Eqs. (2) and (3) was solved numerically for the following boundary and initial conditions:

$$\varphi(\xi = 0) = \varphi_0, \quad \frac{d\varphi(\xi = 0)}{d\xi} = 0, \tag{4a}$$

$$C(\tau = 0) = \begin{cases} 10^{-2}, & h = 0 \\ 0, & h \neq 0. \end{cases} \tag{4b}$$

In the case of a modulated beam, initially there are no Langmuir oscillations within the plasma volume.

3. LINEAR THEORY OF THE EXCITATION OF LANGMUIR OSCILLATIONS

For small amplitudes of the excited wave, we can linearize the set of Eqs. (2) and (3) to obtain the following linear equation for the wave amplitude:

$$\frac{\partial C}{\partial \tau} = \frac{i}{2} \int_0^\xi d\xi' \int_0^{\xi'} d\xi'' C(\xi'', \tau) - h/2. \tag{5}$$

The solution to Eq. (5) can be found by the Laplace-transform method:

$$C = \frac{1}{2\pi i} \int_{\sigma - i\infty}^{\sigma + i\infty} \frac{dp}{p} e^{\lambda p} \left(C_0 - \frac{h\tau}{2\lambda p} \right) \cos\left(2\lambda \sqrt{\frac{i}{p}} \right), \tag{6}$$

where $\lambda = \dfrac{1}{2}(\tau \xi^2)^{1/3}$. For large λ values, the integral in solution (6) can be estimated by the saddle point method:

$$C \approx \frac{1}{4\pi i} \sqrt{\frac{\pi}{\lambda}} e^{-i\frac{\pi}{6}} \left(C_0 - \frac{h\tau e^{-i\frac{\pi}{6}}}{2\lambda} \right) e^{3\lambda e^{i\frac{\pi}{6}}}. \tag{7}$$

Estimate (7) shows that, in the case of a modulated beam, the plasma wave is excited even at a zero initial amplitude. In terms of the variables ξ and $\bar{t}$, where $\bar{t} = \delta v_0 t$ is the dimensionless time ($\tau = \bar{t} - \xi$), the absolute value of the plasma wave amplitude is equal in order of magnitude to [13]

$$|C| \propto \exp\left(\frac{3^{\frac{3}{2}}}{4} [(\bar{t} - \xi)\xi^2] \right)^{\frac{1}{3}}.$$

At the point $\xi_{max} = \dfrac{2}{3}\bar{t}$, the absolute value of the plasma wave amplitude reaches its maximum value

$$|C|_{max} \approx \exp\left(\frac{\sqrt{3}}{2^{4/3}} \bar{t} \right).$$

Hence, in the initial stage of instability, a nonuniform field distribution forms such that its maximum amplitude $|C|_{max}$ is at the point ξ_{max}. The position of the maximum is then displaced into the plasma with a velocity equal to $2/3 v_0$, and the maximum field amplitude increases at a rate equal to the growth rate of the beam–plasma instability. In the region $\bar{t} \gg \xi$, the field grows at a far slower rate,

$$|C| \approx \exp\left(\frac{3^{\frac{3}{2}}}{4} \bar{t}^{\frac{1}{3}} \xi^{\frac{2}{3}} \right). \tag{8}$$

For a modulated beam ($h \neq 0$), the plasma wave is excited even at a zero initial amplitude. This follows immediately from formula (7). The electron beam entering the plasma has the shape of a train of already formed bunches. In the initial stage of the excitation of a plasma wave, its amplitude is small, so the displacement of the bunches and their deformation can be ignored. In this approximation, the beam can be regarded as a given current modulated so as to be in resonance with plasma waves. The amplitude of the plasma wave grows according to the law

$$|C| = \begin{cases} \dfrac{h}{2}(\bar{t} - \xi), & \bar{t} \geq \xi \\ 0, & \bar{t} \leq \xi. \end{cases} \tag{9}$$

We see that the wave amplitude equals zero at the leading edge of the beam ($\xi = \bar{t}$) and increases linearly from the beam's leading edge toward the plasma boundary. The linear increase in the amplitude is due to the coherent addition of the wake fields generated by individual bunches, as in the case of a train of a finite number of bunches [5, 14].

4. RESULTS OF NUMERICAL CALCULATIONS

4.1. The Case of an Unmodulated Beam

The nonlinear stage of instability was investigated by numerically solving the set of Eqs. (2) and (3) with initial conditions (4). We begin by analyzing the results obtained for an unmodulated beam. Figure 1 shows the spatial profiles of the plasma wave amplitudes at different times. We see that, in the initial stage of instability, a nonuniform plasma wave is excited. The amplitude of the wave field has one maximum, in agreement with the predictions of linear theory. The maximum propagates into the plasma with a velocity equal to $2/3 v_0$, and then it stops propagating and starts moving in the opposite direction, i.e., toward the plasma boundary. After the first maximum, new maxima in the profile of the wave field amplitude are produced, each being lower than the previous one. The Langmuir wave amplitude at the first maximum increases continuously and, by the time $\bar{t} = 30$, it becomes greater than the maximum field amplitude in a spatially periodic problem [15] by a factor of 5.

The spatial field structure propagates toward the plasma boundary at a progressively decreasing rate. The maximum field amplitude, too, increases at a progressively slower rate. No steady state is established, however. An analysis of the phase plane ($v = \dfrac{d\varphi}{d\xi}$, φ) in Fig. 2 shows that a compact electron bunch forms in the region of the first maximum of the wave field amplitude, which is followed by a partial demodulation of the beam. At the point $\xi = 5.2$, where the field amplitude is minimum, the dimension of the bunch in the phase plane is largest. As the field amplitude increases further in space, the bunch is compressed once again. In this case, however, the total number of electrons in the bunch decreases because of a partial phase mixing of the electrons in the beam. This is why the second maximum in the wave field amplitude is lower than the first one, and so on.

4.2. Nonlinear Dynamics of the Excitation of a Plasma Wave by a Modulated Beam

Let us now consider the nonlinear dynamics of the excitation of a Langmuir wave by a density-modulated electron beam in a homogeneous plasma. Numerical calculations were carried out for a beam with a modulation depth equal to $h = 0.5$ and 1. Figures 3 and 4
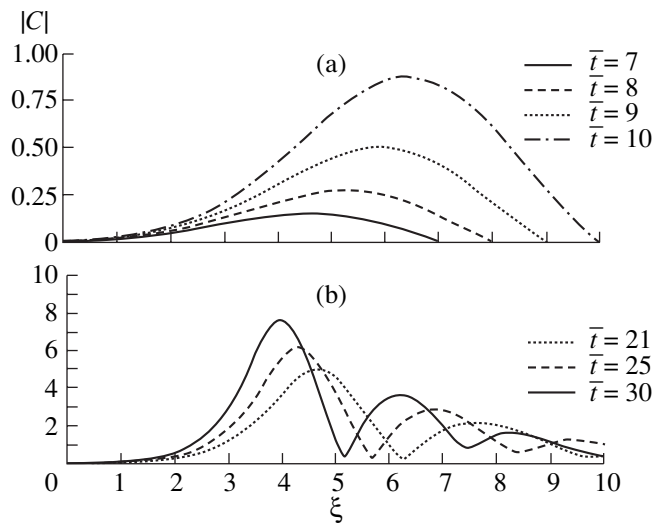

Fig. 1. Field amplitude $|C|$ vs. ξ at different times $\bar{t}$ for $h = 0$.
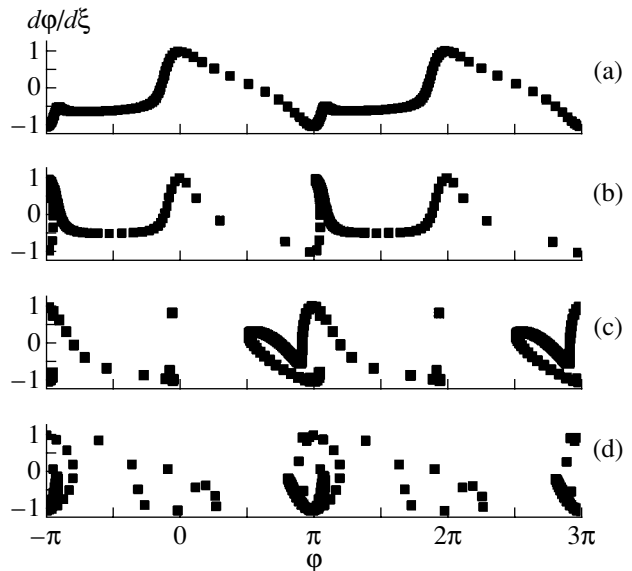

Fig. 2. Phase planes of an electron beam at the time $\bar{t} = 30$ for $\xi = $ (a) 3.5, (b) 5.2, and (c) = 6.0.

show that, in the initial stage of the process (when the beam current can be treated as given), the wave amplitude increases linearly from the leading edge of the electron beam toward the plasma boundary. At the plasma boundary ($\xi = 0$), through which a given beam current is continuously injected, the amplitude always increases according to a linear law, $|C| = \dfrac{h\bar{t}}{2}$. As the plasma wave amplitude increases, the approximation in which the beam current can be treated as given is violated. For $h = 0.5$ (Fig. 3), the inverse effect of the field on the beam leads to compression of the bunches (i.e.,
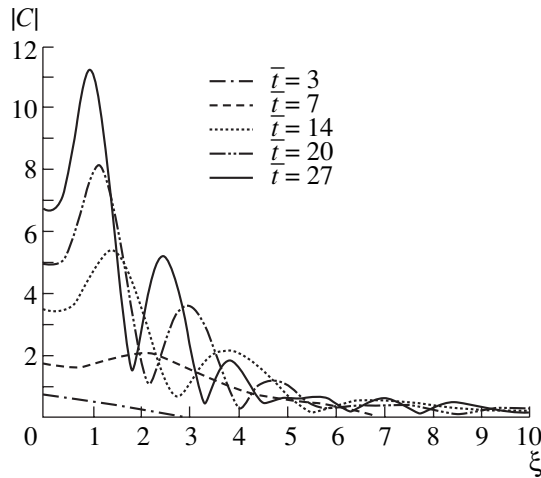
Fig. 3. Field amplitude |C| vs. ξ at different times $\bar{t}$ for $h =$ 0.5.
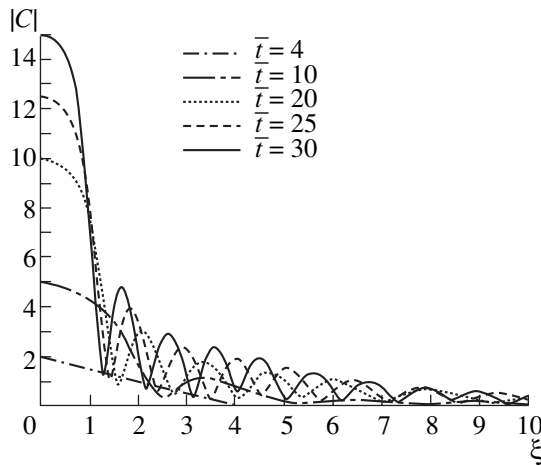

Fig. 4. Field amplitude |C| vs. ξ at different times $\bar{t}$ for $h =$ 1.0.

to an increase in the modulation depth). Accordingly, at the point where the modulation depth is maximum, the field grows faster than at the plasma boundary (at which the modulated beam current can always be treated as given). As a result, a maximum in the profile of the field amplitude forms near the boundary. The maximum wave amplitude increases continuously, and the position of the maximum is displaced toward the plasma boundary. As time progresses, new maxima in the profile of the field amplitude are produced after the first maximum, each being lower than the previous one. The spatial scales of the field maxima are shorter than those in the case of an unmodulated beam, whereas the field amplitude at the first maximum is larger (by the time $\bar{t}$ = 27, it becomes as large as 11).

In the case of a deeply modulated electron beam ($h = 1.0$, which corresponds to a train of bunches), the spatial field distribution is radically different. From Fig. 4 we can see that the field amplitude at the plasma boundary always increases to the greatest extent. The reason is that, in this case, the bunches are not subject to the phase focusing.

5. CONCLUSIONS

The main feature of the excitation of waves by a monoenergetic electron beam in a cold ($T_e = 0$) plasma is that no steady state is established. The wave energy is accumulated in a plasma layer whose dimension decreases with time. In the case of an unmodulated electron beam, a spatially localized maximum appears in the profile of the field amplitude of plasma waves; in the nonlinear stage, it is displaced toward the injection plane. After this first maximum, new maxima in the profile of the field amplitude are produced, each being lower than the previous one.

The process of the excitation of plasma waves by a density-modulated electron beam depends substantially on the beam modulation depth. For a slightly modulated beam, the maximum amplitude of the plasma wave inside the plasma increases faster than at its boundary, at which the modulated beam current can always be treated as given and the plasma wave grows linearly. The spatial scale of the region where the energy of the plasma waves is localized is shorter than that in the case of an unmodulated beam, and the spatial period of the wave field structure is shorter. In the case of a deeply modulated beam ($h = 1.0$), the phase focusing effect is absent, and the amplitude increases to the greatest extent at the plasma boundary.

There are a number of factors that limit the increase in the amplitude of the plasma waves. In the case of an unmodulated beam, these are the electron thermal motion and, accordingly, the finite value of the group velocity [8]. In this case, the steady state is established on a time scale of about $t_* \sim L_w/v_g = L_w v_0/v_{TE}^2$, where L_e is the dimension of the field localization region and v_{TE} is the electron thermal velocity. When the beam pulse duration t_p is less than t_*, no steady state is established. In the case of a density-modulated beam, the increase in the wave amplitude can also be limited when the resonance condition $\omega_m \approx \omega_{pe}$ fails to hold due to the relativistic frequency shift [12].

REFERENCES

1. Ya. B. Faĭnberg, Fiz. Plazmy **26**, 362 (2000) [Plasma Phys. Rep. **26**, 335 (2000)].
2. P. Chen, J. M. Dawson, R. W. Huff, and T. Katsouleas, Phys. Rev. Lett. **54**, 693 (1985).
3. V. A. Balakirev, V. I. Miroshnichenko, and Ya. B. Faĭnberg, Fiz. Plazmy **12**, 983 (1986) [Sov. J. Plasma Phys. **12**, 563 (1986)].

4. C. Joshi, T. Katsouleas, and J. M. Dawson, IEEE J. Quantum Electron. **23**, 1477 (1987).

5. V. A. Balakirev, Yu. P. Bliokh, I. N. Onishchenko, and Ya. B. Faĭnberg, Fiz. Plazmy **14**, 218 (1988) [Sov. J. Plasma Phys. **14**, 123 (1988)].

6. V. A. Balakirev, I. N. Onishchenko, and A. P. Tolstoluzhskiĭ, Ukr. Fiz. Zh. **26**, 1036 (1981).

7. V. A. Balakirev, I. N. Onishchenko, and G. V. Sotnikov, Izv. Vyssh. Uchebn. Zaved., Radiofiz. **32**, 1351 (1989).

8. N. S. Erokhin, M. V. Kuzelev, S. S. Moiseev, *et al.*, *Nonequilibrium and Nonresonance Processes in Plasma Radiophysics* (Nauka, Moscow, 1982) [in Russian].

9. Ya. B. Faĭnberg and V. D. Shapiro, Zh. Éksp. Teor. Fiz. **47**, 1389 (1964) [Sov. Phys. JETP **20**, 937 (1964)].

10. B. A. Al'terkop, S. G. Arutyunyan, and A. A. Rukhadze, Zh. Tekh. Fiz. **49**, 2511 (1979) [Sov. Phys. Tech. Phys. **24**, 1422 (1979)].

11. B. A. Al'terkop, A. S. Volokitin, V. E. Rosinskiĭ, *et al.*, Fiz. Plazmy **3**, 173 (1977) [Sov. J. Plasma Phys. **3**, 100 (1977)].

12. B. A. Al'terkop, A. S. Volokitin, V. E. Rosinskiĭ, *et al.*, Zh. Tekh. Fiz. **50**, 226 (1980) [Sov. Phys. Tech. Phys. **25**, 140 (1980)].

13. S. S. Kalmykova, Ukr. Fiz. Zh. **25**, 1268 (1980).

14. Ya. B. Faĭnberg, V. A. Balakirev, I. N. Onishchenko, *et al.*, Fiz. Plazmy **20**, 674 (1994) [Plasma Phys. Rep. **20**, 606 (1994)].

15. I. N. Onishchenko, A. R. Linetskiĭ, N. G. Matsiborko, *et al.*, Pis'ma Zh. Éksp. Teor. Fiz. **12**, 407 (1970) [JETP Lett. **12**, 281 (1970)].

Translated by I.A. Kalabalyk

PLASMA
DYNAMICS

Plasma Flows in Crossed Magnetic and Electric Fields

A. G. Belikov

National Science Center Kharkov Institute for Physics and Technology,
Akademicheskaya ul. 1, Kharkov, 61108 Ukraine
Received January 22, 2004; in final form, September 20, 2004

Abstract—The effect of the magnitude and direction of an external electric field on the plasma flowing through a magnetic barrier is studied by numerically solving two-fluid MHD equations. The drift velocity of the plasma flow and the distribution of the flow electrons over transverse velocities are found to depend on the magnitude and direction of the electric field. It is shown that the direction of the induced longitudinal electric field is determined by the direction of the external field and that the electric current generated by the plasma flow significantly disturbs the barrier field. © 2005 Pleiades Publishing, Inc.

1. Transverse (with respect to the magnetic field) plasma flows caused by the polarization electric field and $\mathbf{E} \times \mathbf{H}$ drift were studied theoretically in [1–3] and those caused by an external electric field were studied in [4]. The problem of the plasma flowing through a magnetic barrier in an external electric field was studied experimentally in [5, 6]. To solve this problem analytically, one has to introduce some simplifications. Thus, in [4], it was assumed that perturbations caused by the flow were small and, therefore, the constant electric (E_0) and magnetic (H_0) fields were considered to be given. Conditions were also defined under which these assumptions were valid. The electric field caused by the transverse polarization of the plasma flow was ignored, and only the longitudinal polarization of the flow was taken into account. In [6], an attempt was made to balance the transverse polarization field (or at least to partially neutralize it) by applying an external electric field. The experiments showed that, in this case, the plasma flow filling the magnetic trap was quieter and the plasma was better confined in the trap.

The aim of the present study was to theoretically investigate plasma flows propagating across a magnetic field in the presence of both the polarization electric field and a constant external electric field perpendicular to the plasma flow under conditions such that the field perturbations caused by the flow are not small. The propagation of a plasma jet across a magnetic field is accompanied by the shift of the plasma flow electrons with respect to the ions; this leads to the generation of charged polarization layers on the jet surface. The polarization field E_{pol}, together with the barrier magnetic field H_0, causes the plasma between these layers to drift with the velocity $v_d = c \dfrac{E_{\mathrm{pol}}}{H}$. By properly choosing the parameters of the problem, one can provide conditions under which the plasma flow velocity v_d in the barrier is close to the velocity v_0 of the incident flow. The main parameters determining the polar-

ization electric field are the incident flow velocity v_0 and the barrier magnetic field H_0. By shorting the drift gap through an external resistance, one can partially discharge the polarization layers and reduce the polarization field, thereby affecting the jet propagation [7]. However, this field is bounded from above by the value $\dfrac{v_0 B_0}{c}$. The external electric field can be arbitrarily varied both in magnitude and direction, thus providing an efficient means for controlling the plasma flow. This effect can play an important role in various high-voltage magnetic devices: in plasma accelerators operating in a quasi-steady regime [8], in magnetically insulated ion diodes [9], and during the injection of plasma into magneto-electrostatic traps [10]. In this study, we consider a plasma jet that, while moving through a magnetic barrier, passes a region with a constant external electric field that can considerably exceed the polarization field. Before entering this region, the flow velocity is $v = v_d$. However, within this region, the flow velocity changes because the plasma moves in both the polarization and external electric fields: $E_y = E_0 + E_{\mathrm{pol}}$. Note that, when considering the change in the flow velocity, it should be taken into account that the external electric field also affects the polarization field and that the induced electric current can disturb the barrier magnetic field.

2. In the present paper, plasma motion is studied by numerically solving two-fluid MHD equations [11]. In our calculations, we use the model developed in [1, 2, 7]. The MHD equations are solved together with the equations for electric and magnetic fields. We do not use the quasineutrality condition $n_e = n_i$ and assume that the electron and ion densities vary independently of one another.

It is assumed that all the quantities depend only on the longitudinal coordinate x (in the direction of the plasma flow). Since the flow is bounded in the direction perpendicular to the magnetic field, the uniformity

breaks down at the flow boundaries. This can be taken into account by imposing proper boundary conditions. In what follows, a plasma consisting of electrons and hydrogen ions is considered.

The final set of equations can be written as

$$\frac{d}{dx}(n_e v_e) = 0, \quad \frac{d}{dx}(n_i v_i) = 0,$$

$$mn_e v_e \frac{d v_{xe}}{dx} = -en_e\left(E_x + \frac{v_{ye}B}{c}\right)$$

$$-\frac{dp_e}{dx} - \alpha_\perp u_x - \alpha_\wedge u_y - \beta_\perp^{uT}\frac{dT_e}{dx},$$

$$Mn_i v_i \frac{d v_{xi}}{dx} = en_i\left(E_x + \frac{v_{yi}B}{c}\right)$$

$$-\frac{dp_i}{dx} + \alpha_\perp u_x + \alpha_\wedge u_y + \beta_\perp^{uT}\frac{dT_e}{dx},$$

$$mn_e v_{xe} \frac{d v_{ye}}{dx} = -en_e\left(E_y - \frac{v_{xe}B}{c}\right)$$

$$-\alpha_\perp u_y + \alpha_\wedge u_x - \beta_\wedge^{uT}\frac{dT_e}{dx},$$

$$Mn_i v_{xi} \frac{d v_{yi}}{dx} = en\left(E_y - \frac{v_{xi}B}{c}\right) \quad (1)$$

$$+\alpha_\perp u_y - \alpha_\wedge u_x + \beta_\wedge^{uT}\frac{dT_e}{dx},$$

$$3/2 n_e v_{xe}\frac{dT_e}{dx} + n_e T_e \frac{d v_{xe}}{dx}$$

$$= -\frac{d}{dx}(\beta_\perp^{uT} u_x) - \frac{d}{dx}(\beta_\wedge^{Tu} u_y) - \frac{d}{dx}\left(k_\perp^e \frac{dT_e}{dx}\right)$$

$$-(R_x u_x + R_y u_y) - 3\frac{m}{M}\frac{n_e}{\tau_e}(T_e - T_i),$$

$$3/2 n_i v_{xi}\frac{dT_i}{dx} + n_i T_i \frac{d v_{xi}}{dx}$$

$$= -\frac{d}{dx}\left(k_\perp^i \frac{dT_i}{dx}\right) + 3\frac{m}{M}\frac{n_e}{\tau_e}(T_e - T_i),$$

$$\frac{d^2\varphi}{dx^2} = -4\pi e(n_i - n_e), \quad \frac{dB}{dx} = \frac{4\pi}{c}e(n_i v_i - n_e v_e).$$

Here, $u_x = v_{xe} - v_{xi}$ and $u_y = v_{ye} - v_{yi}$ are the components of the relative velocity and $R_x = -\alpha_\perp u_x - \alpha_\wedge u_y - \beta_\perp^{uT}\frac{dT}{dx}$, $R_y = -\alpha_\perp u_y + \alpha_\wedge u_x - \beta_\wedge^{uT}\frac{dT_e}{dx}$ are the components of the friction force. At $x = 0$, we set $v_{xe} = v_{xi} = $

v_0, $v_{ye} = v_{yi} = 0$, $T_e = T_i = T_0$, $\frac{dT_e}{dx} = \frac{dT_i}{dx} = 0$, $\varphi = 0$, and $B = 0$.

In the equations of motion, we took into account both the ion and electron inertia. Besides the electromagnetic forces, the pressure gradient and the friction force caused by collisions between the plasma particles were also taken into account. The energy balance equations for electrons and ions incorporated the electron and ion thermal conductivities. In our case, it was sufficient to take into account only the transverse (with respect to the magnetic field) components of the friction force and the heat flux. The coefficients $\alpha_\perp$, $\alpha_\wedge$, $\beta_\perp^{uT}$, $\beta_\wedge^{uT}$, $\beta_\wedge^{Tu}$, $k_\perp^e$, and $k_\perp^i$, which determine the friction force and the heat flux and are functions of the parameter $\omega\tau_e$, were taken from [11].

Set of Eqs. (1) was reduced to a dimensionless form. The spatial coordinates were normalized to $L = c/\omega_p$ (where $\omega_p = \sqrt{\frac{4\pi e^2 n_0}{m}}$, n_0 is the unperturbed plasma density, and m is the electron mass), the temperatures were normalized to the initial plasma temperature T_0, and the electric potential was normalized to $\varphi_0 = \frac{Mv_0^2}{2e}$.

The dimensionless parameters of the problem are as follows: $\alpha_1 = \sqrt{\frac{M}{m}}\frac{v_A}{v_0}$ is a quantity proportional to the ratio of the Alfvén velocity $v_A = \frac{B_0}{\sqrt{4\pi Mn_0}}$ to the velocity of the incident flow v_0; $\alpha_2 = \frac{T_0}{Mv_0^2}$ is the squared ratio of the ion thermal velocity to the plasma flow velocity; $\alpha_3 = \frac{c}{\omega_p \tau_0 v_0}$ (where $\tau_0 = \frac{c_k T_0^{\frac{3}{2}}}{n_0}$, with c_k being a constant) is a quantity inversely proportional to the magnetic Reynolds number R_m; the parameter $k = \frac{2mc^2}{Mv_0^2}$ characterizes the plasma quasineutrality; $\omega\tau_e$ is the Hall parameter; and the coefficients $\alpha_4 = \frac{n_0 v_0 L}{k_\perp^e}$ and $\alpha_5 = \frac{n_0 v_0 L}{k_\perp^i}$ characterize the electron and ion thermal conductivities, respectively.

Thus, we consider a plasma flow of density n_0 moving along the x axis with a velocity v_0. The magnetic field is directed along the z axis. The flow is bounded in the y direction: $0 < y < d$. It is assumed that the flow size along the magnetic field is sufficiently large, so the
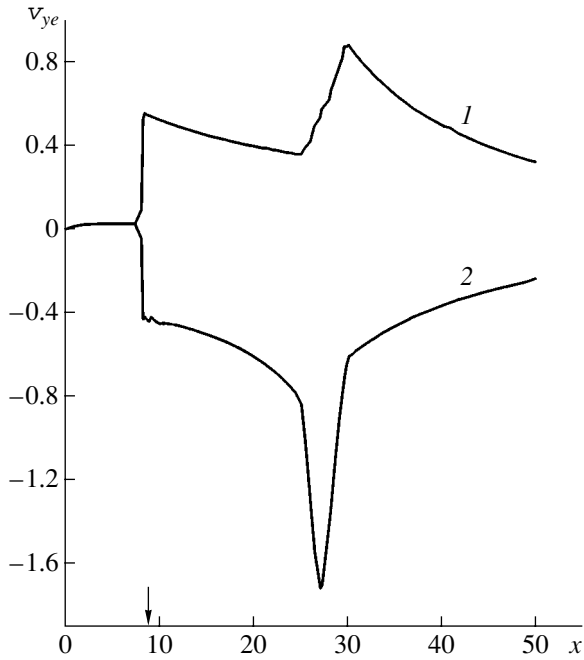
Fig. 1. Profiles of the transverse electron velocity at $\alpha_2 = 2.5 \times 10^{-5}$, $\alpha_3 = 15$, and $\omega\tau_e = 1.4$ for different directions of the external electric field: $E_0 = (1)$ –8 and (2) 8. The vertical arrow shows the front boundary of the region to which the external electric field is applied.

boundary effects can be ignored. The plasma flow passes through a region occupied by the magnetic field, whose profile is described by the formula

$$
B = \begin{cases} 0, & x < 0 \\ \dfrac{Bx}{b}, & 0 < x \le b \\ B_0, & b < x < b + a \\ \dfrac{B}{b}[(a + 2b) - x], & a + b < x \le a + 2b \\ 0, & x > a + 2b, \end{cases} \quad (2)
$$

where a and b are the sizes of the regions with a constant and linearly varying magnetic field, respectively. In our calculations, these parameters were varied in the ranges $b \simeq (1–5)\dfrac{c}{\omega_p}$ and $a \simeq (10–20)\dfrac{c}{\omega_p}$, provided that the condition $(a + 2b) < R_i$ was satisfied. The presence of the polarization layer was taken into account by specifying the normal component of the electric field E_y at the flow boundary. The field E_y can be defined as the product of the charge density n_e in the polarization layer by the layer width Δy (see [1]), which is determined by the difference between the positions of the electrons

and ions: $\Delta y = y_e - y_i \cong \int \dfrac{V_{ye} - V_{yi}}{V_i} dx$. Since the electron and ion velocities perpendicular to the flow are calculated while solving the above equations, the quantity Δy can be calculated at any cross section of the magnetic barrier. There is also an alternative way of calculating E_y. Experiments show that, even while moving in a uniform magnetic field, the flow velocity decreases because of a decrease in the polarization field due to the loss of a fraction of the polarization charge [3]. In the problem as formulated, it is rather difficult to take into account all the channels for charge losses. For this reason, we assume that the flow motion is accompanied by the generation of a low current that is closed, e.g., through the cold ambient plasma. Here, such a situation is modeled by introducing the equivalent circuit with an external resistance R, whose value determines this current [1, 7]. The generated current is generally low; hence, the resistance should be taken sufficiently high. The electric field E_y can be found using Ohm's law, which, in our case, takes the form

$$
j_y = \frac{\sigma(E_y + \omega_{ce}\tau_{ei}E_x)}{1 + (\omega_{ce}\tau_{ei})^2}, \quad (3)
$$

or, in the dimensionless form, $E_y = \alpha_3[1 + (\omega\tau)^2]j_y + \dfrac{B\tau E_x}{1836\alpha_3}$.

3. We performed calculations under conditions such that, in the absence of an external electric field, the plasma flow velocity changed only slightly after passing through the barrier. When the flow approached the region to which the external electric field was applied, the polarization electric field E_y had already been established and the flow moved with the drift velocity v_d. Within this region (the maximum field value $E_y = E_0$ was reached at $\sim 0.2\dfrac{c}{\omega_p}$), the transverse electron velocity v_{ye} significantly increased. Figure 1 shows the profiles of the transverse components of the electron velocity in the magnetic barrier for different directions of the external electric field. It can be seen that the change in the electric field direction is accompanied the change in the velocity direction. For ions, the increase in the transverse velocity is much less pronounced than for electrons; thus, the current is mainly determined by the electron component. The increase in the current and, accordingly, in the magnetic field generated by it can significantly affect the magnetic barrier field. Figure 2 shows the profiles of the unperturbed barrier field and the magnetic field perturbed by the plasma flow for different directions of the external electric field. It can be seen that the magnetic field appreciably changes and even reverses its direction within a certain region of the barrier. The external electric field also affects the polarization electric field. In this case, the flow motion is
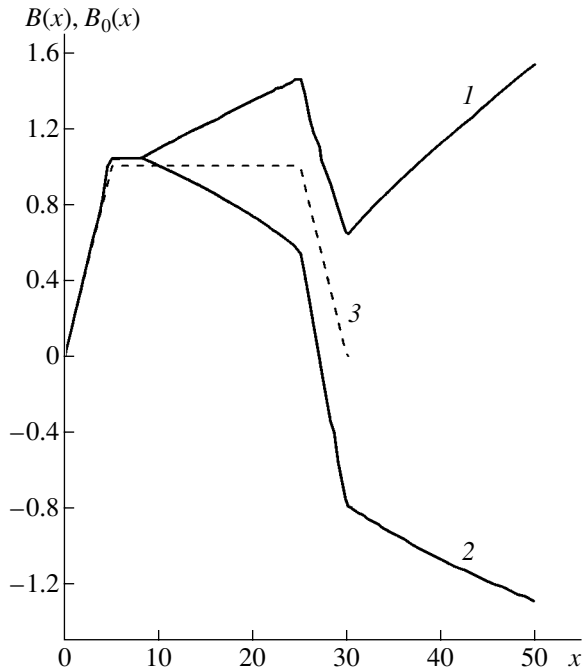
$B(x), B_0(x)$

Fig. 2. Magnetic field profiles in the plasma flow for different external electric fields: $E_0 = $ (*1*) –8, (*2*) 8, and (*3*) 0 (an unperturbed barrier).
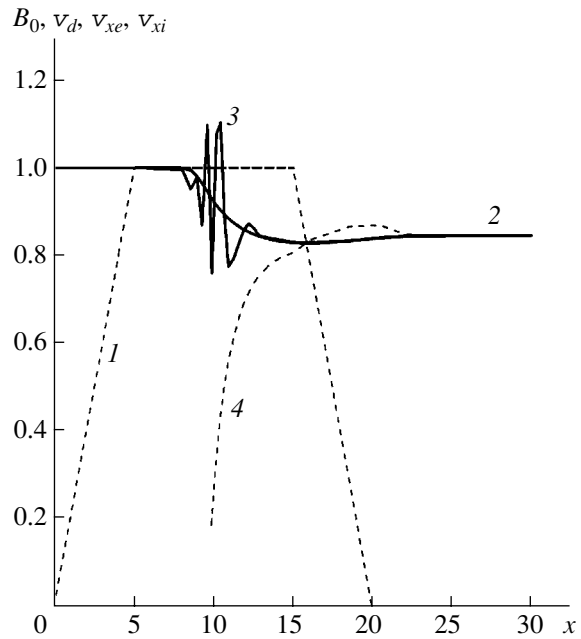
B_0, v_d, v_{xe}, v_{xi}

Fig. 3. Relaxation of the flow drift velocity after applying an external electric field for $\alpha_3 = 3$, $\omega\tau_e = 1.4$, $E_0 = 20$, $a = 10$, and $b = 5$: (*1*) unperturbed barrier field B_0, (*2*) longitudinal ion velocity v_{xi}, (*3*) longitudinal electron velocity v_{xe}, and (*4*) drift velocity v_d.

governed by the combined action of the resulting barrier magnetic field and the total electric field $E_{pol} + E_0$. As a result, after passing the magnetic barrier, the flow velocity is established that is equal to the drift velocity in this region. The current density in this region greatly decreases. The profiles of the flow velocity after passing the barrier region to which the external electric field is applied are shown in Figs. 3 and 4. When the direction of the external electric field coincides with the direction of the polarization field, this velocity is somewhat higher than the velocity of the incident flow (see Fig. 4). Such an increase in the velocity takes place up to the end of the magnetic barrier. Within the region with the external electric field, the electric potential decreased along the plasma flow. In our calculations, the maximum drop in the electric potential was (0.1–0.2)φ_0. The direction of the longitudinal electric field in the flow was such that the ion component was accelerated. The larger the potential drop, the larger the increase in the flow velocity. When the direction of the external electric field was opposite to the direction of the polarization field ($E_0 < 0$), the plasma flow usually slowed down to the thermal velocity. In this case, the electric potential sharply increased along the flow. The potential drop was positive and was on the order of the ion energy in the flow. Figure 5 shows the relevant profiles of the electron velocity. It can be seen that the longitudinal flow velocity decreases significantly, whereas the transverse electron velocity increases. The electron component is somewhat decelerated only when enter-

ing the region to which the external electric field is applied. Further on, the flow velocity decreases, while the plasma is almost quasineutral. The effect of the external electric field E_0 is reduced to the generation of the electric potential that decelerates the flow. The mag-
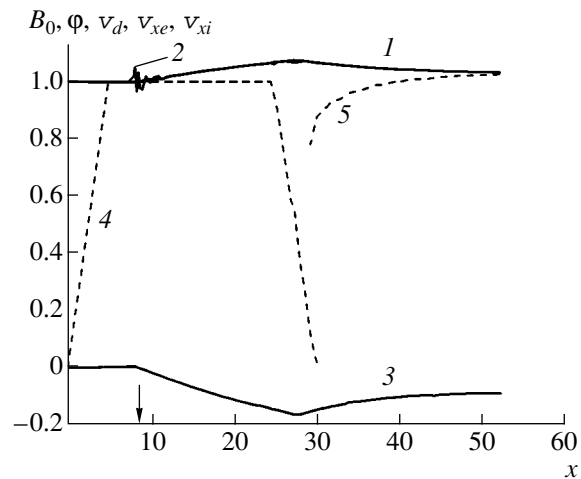
$B_0, \varphi, v_d, v_{xe}, v_{xi}$

Fig. 4. Relaxation of the flow drift velocity after applying an external electric field for ($\alpha_3 = 15$, $\omega\tau_e = 1.4$, and $E_0 = 8$: (*1*) longitudinal ion velocity v_{xi}, (*2*) longitudinal electron velocity v_{xe}, (*3*) electric potential φ, (*4*) unperturbed barrier field B_0, and (*5*) drift velocity v_d. The vertical arrow shows the front boundary of the region to which the external field is applied.
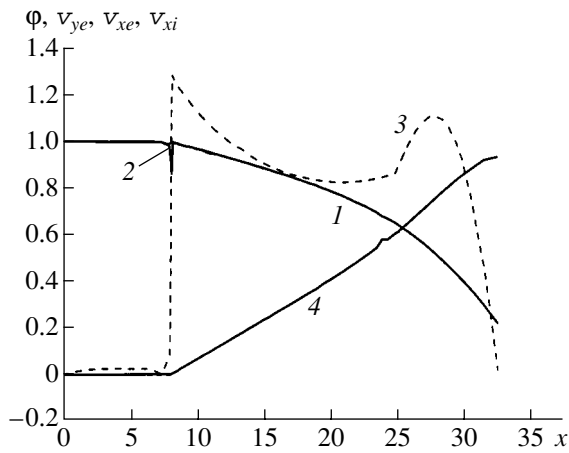
Fig. 5. Profiles of the (*1*) longitudinal ion velocity v_{xi}, (*2*) longitudinal electron velocity v_{xe}, (*3*) transverse electron velocity v_{ye}, and (*4*) electric potential φ in the plasma flow for $\alpha_3 = 15$, $\omega\tau_e = 1.4$, and $E_0 = -20$.
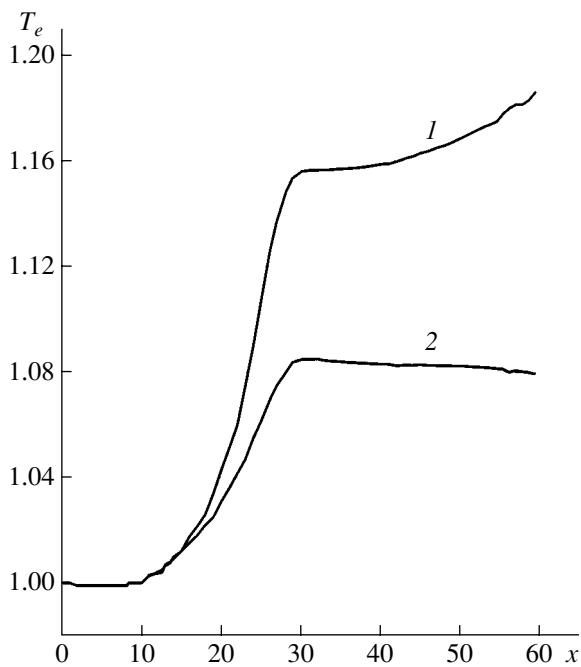

Fig. 6. Profiles of the electron temperature T_e in the plasma flow for different Reynolds numbers: $\alpha_3 = $ (*1*) 5 and (*2*) 10.

nitude and profile of this potential depend on both the magnitude of the external electric field and the flow parameters. Within our model, calculations can be performed only up to the instant at which the flow comes to a stop. To calculate the further evolution of the flow, it is necessary to solve a two-dimension problem.

In the absence of an external electric field, both the electron and ion temperatures decrease as the plasma flow propagates across the magnetic field. The decrease in the temperature depends on the electron and ion thermal conductivities (in our calculations the parameters α_4 and α_5 were varied within the range 10^{-2}–10^{-3}). The electron component is heated while passing the barrier region to which the external electric field is applied; as a result, the plasma temperature in the flow increases significantly. The higher the magnetic Reynolds number and the Hall parameter, the larger the increase in the electron temperature. An increase in the Hall parameter leads to a decrease in the heat removal, whereas an increase in the magnetic Reynolds number results in higher current density and stronger heating (see Fig. 6). The electron temperature increases by one order of magnitude with respect to the initial level, whereas the ion temperature changes insignificantly.

An increase in the external electric field is accompanied by the generation of electron density pulsations (rarefaction and compression regions along the flow). An increase in the magnetic Reynolds number also leads to the onset of density perturbations. The pulsations of the electron velocity and density are initially small and become pronounced only when the flow enters the region to which the external electric field is applied. When the Hall parameter is $\omega\tau_e \sim 1$–2, the pulsations are smoothed as the flow propagates further (Fig. 3). The profiles of the other quantities that depend on the electron density (the current density and the electric field E_y) also display pulsations. However, as the Hall parameter increases to 4–5, the amplitude of the pulsations increases greatly. This can lead to the generation of discontinuities related to the passage through the characteristic velocity (the thermal electron velocity v_{Te}). In this study, we did not analyze such flows.

4. Within the parameter range under study, the effect of an external electric field on a plasma jet propagating across a magnetic field can be described as follows: The transverse plasma velocity (primarily, the electron velocity) increases significantly in the barrier region to which the electric field is applied; this leads to an increase in the electric current. The magnetic field of this current can considerably affect the barrier magnetic field. The external electric field changes the polarization electric field, so the further plasma motion is governed by the combined action of these fields. In the region with established electric and magnetic fields, the plasma moves with a velocity that differs from the drift velocity in that part of the barrier where the external electric field is absent. When the external electric field is directed oppositely to the polarization field ($E_0 < 0$), the plasma flow can be decelerated down to the thermal velocity. The reason is that the external electric field induces a retarding electric potential. The decrease in the flow velocity depends on the magnitude and profile of this potential: under certain conditions, the plasma flow is decelerated down to the thermal velocity. The external electric field leads to an increase in the electron temperature in the plasma flow and gives rise to the

electron density perturbations, which increase with increasing parameter $\omega\tau_e$.

REFERENCES

1. K. D. Sinel'nikov and B. N. Rutkevich, Zh. Tekh. Fiz. **37**, 56 (1967) [Sov. Phys. Tech. Phys. **12**, 37 (1967)].
2. W. Peter, A. Ron, and N. Rostoker, Phys. Fluids **25**, 730 (1982).
3. J. Borovsky, Phys. Fluids **30**, 2518 (1987).
4. N. A. Khizhnyak, I. I. Demidenko, and N. S. Lomino, in *Studies of Plasma Bunches*, Ed. by V. T. Tolok (Naukova Dumka, Kiev, 1969), Vol. 4, p. 56 [in Russian].
5. K. D. Sinel'nikov, A. G. Dikiĭ, B. N. Rutkevich, *et al.*, in *Studies of Plasma Bunches*, Ed. by V. T. Tolok (Naukova Dumka, Kiev, 1969), Vol. 4, p. 123 [in Russian].
6. A. G. Dikiĭ, A. Yu. Voloshko, G. A. Silenok-Bel'skiĭ, *et al.*, in *Plasma Physics and Controlled Fusion*, Ed. by V. T. Tolok (Naukova Dumka, Kiev, 1971), p. 240 [in Russian].
7. A. G. Belikov and N. A. Khizhnyak, Fiz. Plazmy **21**, 723 (1995) [Plasma Phys. Rep. **21**, 685 (1995)].
8. A. A. Kalmykov, in *Physics and Applications of Plasma Accelerators*, Ed. by A. I. Morozov (Nauka i Tekhnika, Minsk, 1974), p. 48 [in Russian].
9. V. M. Bystritskiĭ, S. V. Grigor'ev, and A. V. Kharlov, Zh. Tekh. Fiz. **62** (12), 163 (1992) [Sov. Phys. Tech. Phys. **37**, 1211 (1992)].
10. M. S. Ioffe, B. I. Kanaev, and V. P. Pastukhov, Itogi Nauki Tekh., Ser. Fiz. Plazmy **9**, 5 (1989).
11. S. I. Braginskii, in *Reviews of Plasma Physics*, Ed. by M. A. Leontovich (Gosatomizdat, Moscow, 1963; Consultants Bureau, New York, 1965), Vol. 1.

Translated by N.N. Ustinovskiĭ

Investigation of the Charge and Potential of a Dust Grain in a Low-Pressure Plasma with Allowance for Ionization in the Intergrain Space

V. I. Sysun, A. D. Khakhaev, O. V. Oleshchuk, and A. S. Shelestov

Petrozavodsk State University, pr. Lenina 33, Petrozavodsk, Karelia Republic, 185640 Russia
Received October 20, 2004; in final form, November 30, 2004

Abstract—The formation of the ion flow to a dust grain and the distribution of the electric potential in a low-pressure dusty plasma are investigated theoretically with allowance for ionization in the intergrain space. Poisson's equation similar to the Langmuir plasma–sheath equation is solved numerically with the use of partial analytic solutions at the boundary of the Seitz–Wigner cell and in thin layers in the intergrain space. The charge and potential of a dust grain are found as functions of the grain radius and cell size. The grain potential and the total cell potential energy as functions of the cell size display weak minima, whose positions correspond to the observed intergrain distance in dusty crystals. © 2005 Pleiades Publishing, Inc.

The formation of crystal structures in a dusty plasma is governed mainly by the charge of a dust grain and the potential distribution in its vicinity. The charge and potential of a dust grain in plasma are usually described by using the orbit motion limited (OML) model, radial drift (RD) model, and hydrodynamic diffusion limited (DL) model [1]. The OML model, which has been previously applied to the probe theory, assumes that the total energy and momentum of ions arriving from infinity are conserved (collisions are ignored) and that there are no potential barriers throughout the ion path:

$$\frac{mV^2}{2} + e\varphi = \text{const}, \quad rmV\sin\theta = \text{const}.$$

In this model, the electron and ion current densities are

$$j_e = \frac{en_{e\infty}}{4}\sqrt{\frac{8kT_e}{\pi m}}\exp\left(-\frac{e|\varphi_a|}{kT_e}\right), \tag{1}$$

$$j_i = \frac{en_{i\infty}}{4}\sqrt{\frac{8kT_i}{\pi M}}\exp\left(1 + \frac{e|\varphi_a|}{kT_i}\right). \tag{2}$$

Here, $n_{e\infty}$ and $n_{i\infty}$ are the electron and ion densities at infinity, T_e and T_i are the electron and ion temperatures, m and M are the electron and ion masses, φ_a is the grain potential, and θ is the angle between the radius-vector and velocity of an ion. In a steady state, the equality of these currents determines the grain charge and potential. Recently, the applicability of the OML model has been called in question. In [2], it was shown that, when the ion distribution at infinity is Maxwellian, there are always potential barriers for the ions, even if the grain radius is very small. In [3, 4], it was pointed out that even very rare ion–neutral collisions substantially disturb the ion orbital motion and, thus, significantly affect

the ion current. At low pressures, volume ionization also plays an important role because, in this case, the ion current to a grain is completely balanced by ionization in the intergrain space; as a result, the actual mean free path of the ions is shorter than one-half of the intergrain distance. When the OML model fails to hold (especially at low ion temperatures), the RD model can be employed [5]. In this model, the ion current to a grain forms at infinity and remains unchanged up to the grain surface. The ions move radially with velocities determined by the local potential and the energy conservation law ($Mv_r^2 = 2e\varphi(r)$). In this case, Poisson's equation takes the form

$$\varepsilon_0\nabla^2\varphi = en_{e\infty}\exp\left(\frac{e\varphi}{kT}\right) - \frac{j_i}{V_r}. \tag{3}$$

Note that the RD model, as applied to the ion velocity, is a particular case of the hydrodynamic approximation

$$MV\frac{\partial V}{\partial r} = -e\frac{\partial\varphi}{\partial r} - MV\nu_{im}, \tag{4}$$

in which the collisional term is ignored (here, ν_{im} is the frequency of the ion–neutral collisions). In the hydrodynamic approximation, the introduction of the ionization term in the continuity equation allows one to describe the formation of the ion flow: $\nabla(n_iv_i) = n_ez$, where z is the ionization frequency. At high pressures, it is also necessary to take into account recombination [6]. At low pressures, when the ionization frequency exceeds the ion–neutral collision frequency, the collisional frequency in Eq. (4) should be replaced by the ionization frequency, because the origin of new ions with a zero initial velocity also leads to the deceleration of the ion flow. In experiments [9] on low-pressure dis-

charges without dust, the ionization frequency was determined from the ion current to the wall and the plasma electron density was determined from the balance of charged particles in the positive column. For a discharge in helium at $p = 2 \times 10^{-2}$ torr, $R = 1$ cm, and a current of $I = 0.3$ A, the ionization frequency was found to be $z = 1.5 \times 10^6$ s^{-1}, whereas, according to [10], the ion–neutral collision frequency was $\nu_{im} \approx 6 \times 10^5$ s^{-1}. For a discharge in mercury vapor at $p = 2.2 \times 10^{-4}$ torr, $R = 1.6$ cm, and a current of $I = 3$ A, the ionization frequency and the ion–neutral collision frequency were $z = 8.4 \times 10^4$ s^{-1} and $\nu_{im} \approx 8.8 \times 10^3$ s^{-1}, respectively. Note that these frequencies are close to those calculated using the Langmuir theory [7, 9]. In [11], the ionization frequency was also introduced in Eq. (4) when describing the ion current to a probe at low and moderate pressures. In the presence of dust, the ionization frequency should be higher because of the loss of charged particles on dust grains.

In the present paper, we consider the formation of the ion flow to a dust grain due to the ionization in a low-pressure plasma in the intergrain space. The problem is solved using two models: free-flight and hydrodynamic ones. The spatial dust structure in plasma is assumed to be in a steady state. The plasma volume around a grain is inversely proportional to the dust grain density. The ion flow to the grain forms due to the electron-impact ionization of the working gas in such an elementary volume (cell). For $T_i \ll T_e$, the initial ion velocity can be ignored and the newly born ions can be assumed to move toward the grain along the electric field lines. Preliminary estimates show that, for $T_i/T_e \sim 0.01$–0.05, this is indeed the case. Exact solution of the equation of motion for the ions with nonzero initial velocities is rather complicated and requires separate consideration. We assume that no ions enter a given elementary cell from the outside because the cell is surrounded by other cells, in which the ions flow to their own dust grains. We also assume that there is no directed ion flow across the entire dust structure (such a flow can exist, e.g., in electrode sheaths) because the effect of such a flow on the inner plasma structure seems to be of minor importance. In contrast to the ion component, the electron component is common for all the cells because the electron thermal velocity is much higher than the electron drift velocity toward the grains. Since the grain's field is repulsive for electrons, we assume that they obey a Boltzmann distribution; hence, the electron current to a grain can be calculated by formula (1). The shape of an actual cell is determined by the spatial dust structure and is close to cubic. To simplify calculations, we will consider a one-dimensional problem in which the cell is assumed to be a sphere of radius $r_d = (4\pi n_d/3)^{-1/3}$. This is the so-called Seitz–Wigner cell that was used in [6] to calculate the potential distribution in a dust structure formed in a high-pressure plasma. For spherical grains and large ratios between the radii of the cell and the grain, such a model

is expected to adequately describe the charge of the grain and the potential distribution near it.

Let us consider the formation of the ion flow inside the cell. The flux density of the ions produced within the layer of radius r' and thickness dr' through a spherical surface of radius r is $r'^2 n_e(r')z\,dr'/r^2$, and the flow velocity of these ions is $\sqrt{2e(\varphi(r') - \varphi(r))/M}$. By dividing the ion flux density by the velocity, we obtain the density of these ions at the radius r:

$$dn_i = \frac{r'^2 z n_e r'\,dr'}{r^2 \sqrt{2e(\varphi(r') - \varphi(r))/M}}.$$

Integration of the contributions from all the layers from r to r_d yields the total ion density

$$n_i(r) = \frac{1}{r^2}\int_{r''}^{r_d} \frac{r'^2 n_e r' z\,dr'}{\sqrt{\dfrac{2e|\varphi(r') - \varphi(r)|}{M}}}. \tag{5}$$

The ion current to the sphere of radius r is the sum of the differential currents,

$$I_i(r) = e\int_r^{r_d} 4\pi r'^2 n_e(r')z\,dr'. \tag{6}$$

The electron density is assumed to obey a Boltzmann distribution,

$$n_e(r) = n_{ed}\exp\!\left(\frac{e\varphi(r)}{kT_e}\right), \tag{7}$$

where n_{ed} is the electron density at the cell boundary. In this case, Poisson's equation takes the form

$$\frac{1}{r^2}\frac{\partial}{\partial r}\!\left(r^2\frac{\partial\varphi}{\partial r}\right)$$
$$= \frac{en_{ed}}{\varepsilon_0}\left(\exp\!\left(\frac{e\varphi}{kT_e}\right) - \frac{z}{r^2}\int_r^{r_d} \frac{\exp\!\left(\dfrac{e\varphi'}{kT_e}\right)r'^2\,dr'}{\sqrt{\dfrac{2e}{M}|\varphi - \varphi'|}}\right). \tag{8}$$

Since the neighboring cells are similar to one another, we assume that both the electric potential and its gradient are zero at the cell boundary. We also assume that the electron density at the boundary is given and equal to n_{ed}. Since dust grains are charged negatively, the ion density must be higher than the electron density. The ion density is determined by the ionization frequency in accordance with expression (5) in its limiting form at $r \longrightarrow r_d$. Similar boundary conditions for the potential were used in [6]. The surface

potential of a dust grain is determined by choosing the ionization frequency z' at which the ion current to the grain (see Eq. (6)) is equal to the electron current defined by Eq. (1).

A similar plasma–sheath equation was derived by Langmuir [7] for a gas-discharge positive column. However, in that paper, the boundary conditions were opposite: the potential and its gradient were assumed to be zero at the plasma center, whereas the wall potential was established automatically. It is rather difficult to solve this equation numerically because of the uncertainty that arises on the right-hand side of the equation when the denominator is close to zero. The perturbed zone is often divided into two regions: the quasineutral plasma region, in which the left-hand side of the equation is zero, and the sheath region, in which the electron density can be ignored and the ion flux is assumed to be constant. In our case, the sheath length is comparable to the total size of the cell and, therefore, such an approximation is inapplicable. Let us introduce the dimensionless variables:

$$x = \frac{r}{\lambda_d} = \frac{r}{\sqrt{\varepsilon_0 kT_e/n_{ed}e^2}}, \quad U = \frac{e\varphi}{kT_e},$$

$$n'_{e,i} = \frac{n_{e,i}}{n_{ed}}, \quad V^I = \frac{V}{\sqrt{\frac{kT_e}{M}}}, \quad A = \frac{z\lambda_d}{\sqrt{kT_e/M}} = \frac{z}{\omega_i},$$

where ω_i is the ion plasma frequency. In these variables, Eq. (8) takes the form

$$\frac{\partial^2 U}{\partial x^2} + \frac{2}{x}\frac{\partial U}{\partial x} = n'_e - n'_i, \tag{8'}$$

where the electron and ion densities are

$$n'_e = \exp(U), \quad n'_i = \frac{A}{x^2}\int_x^{x_d} \frac{x'^2 \exp(U)dx'}{\sqrt{2|U(x) - U(x')|}}. \tag{9}$$

We begin to numerically solve the equation starting from the cell boundary, where the problem can be reduced to a one-dimensional problem for a thin plane layer ($\Delta x \ll x_d$) and where one can obtain a simple analytic solution. Let us assume that $n'_e = 1$ and $n'_i = $ const > 1. Integrating Eq. (8'), we obtain

$$\frac{\partial^2 U}{\partial x^2} = 1 - n'_i, \quad \frac{\partial U}{\partial x} = (1 - n'_i)x,$$

$$U(x) = (1 - n'_i)\frac{x^2}{2}, \tag{10}$$

where x is counted from the cell boundary. After substituting this solution into the formula for the ion density, we have

$$n'_i(x) = A\int_0^x \frac{dx'}{\sqrt{(1 - n_i)(x'^2 - x^2)}},$$

$$\text{or} \quad n'_i(n'_i - 1)^{\frac{1}{2}} = A\int_0^1 \frac{d(x'/x)}{\sqrt{1 - (x'/x)^2}} = \frac{A\pi}{2} = B^{1/2}.$$

The root of the cubic equation $n'^2_i(n'_i - 1) = B$ is equal to

$$n'_i = \frac{1}{3} + \sqrt[3]{\frac{1}{27} + \frac{B}{2} + \sqrt{\frac{B}{27} + \frac{B^2}{4}}}$$
$$+ \sqrt[3]{\frac{1}{27} + \frac{B}{2} - \sqrt{\frac{B}{27} + \frac{B^2}{4}}}. \tag{11}$$

Thus, by specifying the parameter A, we can calculate the initial ion density and the behavior of the potential near the cell boundary. To ensure the stability of the numerical scheme, we used a three-point parabolic interpolation of the potential:

$$U(x) = \frac{(h - x)(2h - x)}{2h^2}U_0 + \frac{x(2h - x)}{h^2}U_1$$
$$- \frac{x(h - x)}{2h^2}U_2,$$

where h is the spatial step and x is counted from the point x_0. We also used the following approximate analytic solution for the density at each step:

$$n_i(x_k) = \frac{A}{x_k^2}\sum_{j=k}^{j=N-1}\left(\frac{x_j + x_{j+1}}{2}\right)^2$$
$$\times \exp\left(\frac{U_j + U_{j+1}}{2}\right)\int_0^h \frac{dx}{\sqrt{a\frac{x^2}{h^2} + b\frac{x}{h} + c}}, \tag{12}$$

where $a = U_j - 2U_{j+1} + U_{j+2}$, $b = -3U_j + 4U_{j+1} - U_{j+2}$, and $c = 2U_j - 2U_k$, with

$$\int \frac{dx}{\sqrt{ax^2 + bx + c}} = \frac{-1}{\sqrt{-a}}\arcsin\frac{(2ax + b)}{(b^2 - 4ac)^{1/2}}.$$

This approximation matches well to analytic solution (10) for the external layer. The parameter A is proportional to the ionization frequency and is determined by the grain radius so that ion current (6) is equal to the electron current:

$$I_e = 4\pi a^2 \frac{n_{ed}}{4}\sqrt{\frac{8kT_e}{\pi m}}\exp\left(\frac{e\varphi_a}{kT_e}\right).$$
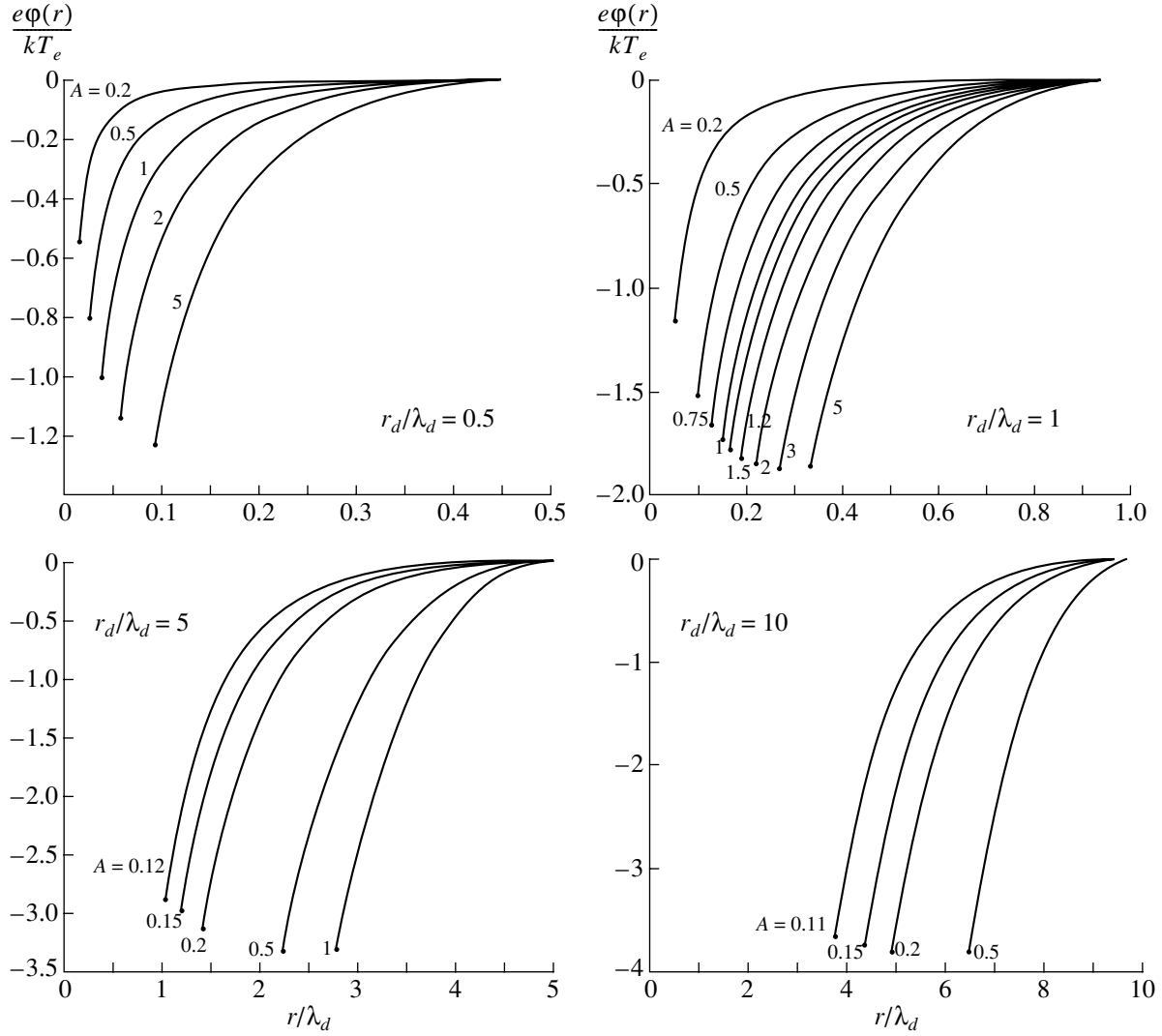
Fig. 1. Radial profiles of the electric potential in the cell.

In the dimensionless form, this condition looks like

$$A\int_0^{x_d} x^2 \exp(U)dx = x_a^2 \sqrt{\frac{M}{2\pi m}}\exp(U_a). \qquad (13)$$

The values of x_d and A were given, and the grain radius x_a was determined in the course of calculations, assuming that condition (13) is satisfied. Simultaneously, we calculated the total electron and ion charges in the cell (both reduced to the charge of the Debye sphere), the dust grain charge determined from the gradient of the potential on the grain surface, and the total electric field energy W^l in the cell:

$$Q_e^l = 3\int_{x_i}^{x_l} n_e^l(x)x^2\partial x = \frac{4\pi\int_a^{r_d} n_e(r)r^2 dr}{\frac{4}{3}\pi\lambda_d^3 n_{ed}}, \qquad (14)$$

$$Q_a^l = 3x_a^2 \frac{\partial U}{\partial x}\bigg|_{x=x_a} = \frac{Q_a}{\frac{4}{3}\pi\lambda_d^3 n_{ed}}, \qquad (15)$$

$$W^l = h\sum_k (U_k - U_{k+1})^2 k^2$$

$$= \int\left(\frac{\partial U}{\partial x}\right)^2 x^2 dx = \frac{\frac{\varepsilon_0}{2}\int_a^{r_d} E^2 4\pi r^2 dr}{\frac{3}{2}kT_e n_{ed}\frac{4}{3}\pi\lambda_d^3}. \qquad (16)$$

The electric field energy is normalized to the total thermal (kinetic) energy of electrons in the Debye sphere. The results of numerical simulations for neon are presented in Fig. 1 and Table 1. The points at the ends of the curves show the radius and potential of the dust

Table 1. Results from numerical calculations of the dust grain potential, the total electron and ion charge in the cell, and the ion density at the cell boundary in the free-flight approximation for ions

A	$a \times 10^3/\lambda_d$	U_a	n'_{id}	Q_e	Q_i
		$x_d/\lambda_d = 0.5$			
0.2	14	−0.59	1.084	0.129	0.156
0.5	25	−0.84	1.342	0.129	0.201
1	38	−1.03	1.779	0.126	0.267
2	57	−1.16	2.535	0.126	0.381
5	93	−1.25	4.314	0.120	0.633
		$x_d/\lambda_d = 1$			
0.2	52	−1.19	1.084	0.99	1.2
0.5	98	−1.54	1.342	0.96	1.53
1	151	−1.74	1.779	0.93	2.01
2	220	−1.86	2.535	0.87	2.79
5	333	−1.87	4.314	0.81	4.41
A	$a \times 10^2/\lambda_d$	U_a	n_{id}	Q_e	Q_i
		$x_d/\lambda_d = 5$			
0.12	103	−2.93	1.0333	110.4	127.8
0.15	119	−3.04	1.0503	106.8	128.4
0.2	141	−3.19	1.084	101.1	129.6
0.5	221	−3.36	1.342	80.1	140.4
1	277	−3.35	1.779	65.1	159.3
		$x_d/\lambda_d = 10$			
0.11	357	−3.69	1.0282	759	885
0.15	435	−3.77	1.0503	687	852
0.2	490	−3.82	1.084	621	822
0.5	644	−3.83	1.342	429	783

grain. In all the cases, the potential near the cell boundary behaves as $\left(\dfrac{r_d}{r} - 1\right)^2$.

For grains with a large size x_a, this dependence holds almost up to the grain surface. For $x_a \ll 1$ (small grains), the potential near the grain increases more gently, according to the law $U \sim 1/x_a$. The grain charge determined from the gradient of the electric potential at the grain surface is equal to the difference between the total ion and electron charges in the cell. This confirms the validity of the above procedure for solving Poisson's equation. At the same time, because of the significant contribution from the plasma ion component, the grain potential is less negative than the potential of an isolated grain with the same charge but without a surrounding plasma. Because of the nonuniformity and inequality of the electron and ion distributions within the cell, the difference between the electron and ion densities at the cell boundary is not equal to the density of the plasma particles multiplied by their charge.

Table 2 presents the results of numerical calculations of the potential and charge distributions in a Seitz–Wigner cell in a hydrodynamic approximation with allowance for volume ionization. In this approximation, the individual ion velocities are replaced with the velocities averaged over the ensemble. The equation of ion motion then takes the form

$$
\begin{aligned}
MV_i\frac{\partial V_i}{\partial r} &= -e\frac{\partial \varphi}{\partial r} - kT_i\frac{\partial n_i}{n_i\partial r} - MV_i\left(z\frac{n_e}{n_i} + \nu_{im}\right) \\
&\approx -e\frac{\partial \varphi}{\partial r} - MV_i z\frac{n_e}{n_i}.
\end{aligned}
\tag{17}
$$

Ignoring the pressure gradient and ion–neutral collisions, we obtain

$$
M\frac{V_i^2}{2} = e\varphi - \int_r^{r_d} MV_i z\frac{n_e}{n_i}dr.
$$

Table 2. Results from numerical calculations carried out in the hydrodynamic approximation

A	$a \times 10^3/\lambda_d$	U_a	n'_{id}	Q_e	Q_i
		$x_d/\lambda_d = 0.5$			
0.15	11	−0.55	1.041	0.126	0.144
0.5	24	−0.85	1.297	0.123	0.192
1	38	−0.99	1.696	0.123	0.255
2	56	−1.14	2.360	0.120	0.360
5	92	−1.21	4.05	0.117	0.600
		$x_d/\lambda_d = 1$			
0.2	52	−1.17	1.07	0.99	1.2
0.5	97	−1.5	1.297	0.96	1.53
1	149	−1.7	1.696	0.93	1.98
2	217	−1.82	2.36	0.9	2.73
5	330	−1.82	4.05	0.81	4.29
A	$a \times 10^2/\lambda_d$	U_a	n_{id}	Q_e	Q_i
		$x_d/\lambda_d = 5$			
0.15	118	−3	1.041	109.2	130.5
0.5	219	−3.28	1.297	83.1	142.8
1	275	−3.27	1.696	68.1	161.4
2	324	−3.1	2.36	55.5	190.5
10	407	−2.43	6.2	33.9	298.2
		$x_d/\lambda_d = 10$			
0.15	432	−3.7	1.041	708	870
1	729	−3.6	1.696	342	840
5	864	−2.9	4.05	189	1134

In the dimensionless variables, we have

$$n'_i = \frac{j'_i}{V'_i} = \frac{A}{x^2}\frac{\int_x^{x_d} e^{U(x')}x'^2\,dx'}{\sqrt{2}\sqrt{-U' - A\int_x^{x_d}\frac{V'_i}{n'_i}e^{U(x')}\,dx'}}. \quad (18)$$

Though n_i in formula (18) is determined via the same unknown quantity n_i on the right-hand side, the problem can be solved by iterations. Near the cell boundary, the analytic solution is applicable. Assuming that $n'_e = 1$ and $n'_i = \text{const} \geq 1$ and using a one-dimensional planar approximation, we have

$$U_x = (1 - n'_i)\frac{x^2}{2}, \quad V_i = \sqrt{\frac{n'_i - 1}{2}}x.$$

For the density n_i, we obtain the equation

$$n'^2_i(n'_i - 1) = 2A^2 = B,$$

where $B^{1/2} = \sqrt{2}A$, instead of the previous formula $B^{1/2} = A\pi/2$ for the free-flight approximation. Such a replacement, however, only slightly affects the ion density. A comparison between Tables 2 and 1 shows that the data obtained for these two cases are very similar to one another. This allows one to use the hydrodynamic approximation not only at high pressures but also at moderate and even low pressures.

Using the results of calculations performed in the free-flight approximation, we found the charge and potential of a dust grain and the potential energy of the electric field in a Seitz–Wigner cell as functions of the cell radius at a fixed grain size. The results obtained for neon (solid curves) and argon (dashed curves) plasmas are shown in Fig. 2. The grain charge depends slightly on the cell radius and rapidly increases with grain radius. For $r_d/\lambda_d \leq 1$, the grain potential decreases with decreasing cell radius. For $a/\lambda_d \leq 0.05$, both the grain potential and the cell potential energy display weak minima at normalized cell radii of $r_d/\lambda_d \sim 0.5$–0.8, which are close to one-half of the experimentally observed intergrain distance. In an actual crystal structure, these minima can be significantly deepened due to
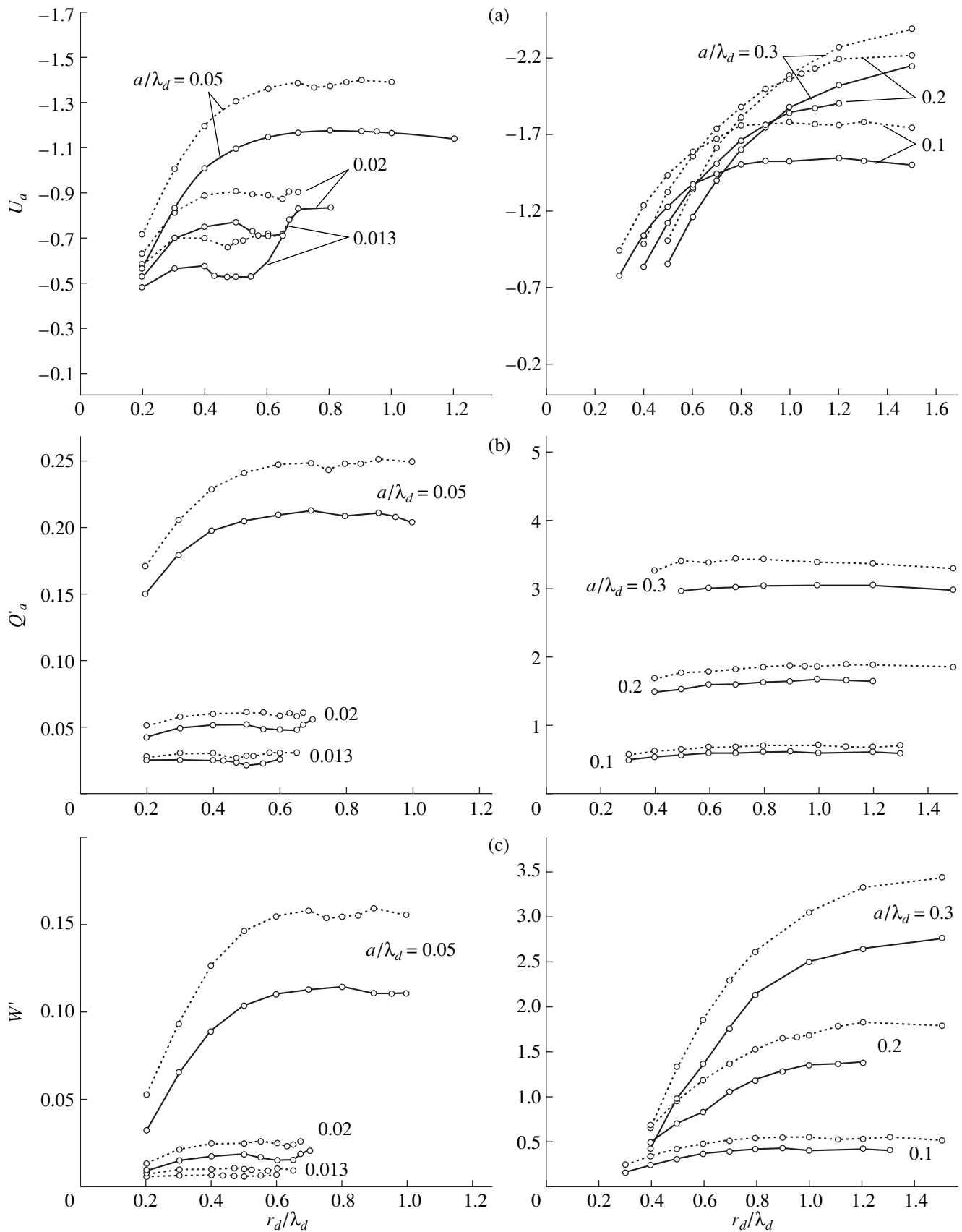
Fig. 2. (a) Potential of a dust grain of fixed size, (b) dust grain charge, and (c) electric field energy in the Seitz–Wigner cell as functions of the cell size.

the angular shift of charges of different polarities as the grains approach one another, i.e., due to the violation of the adopted spherical symmetry. This must be taken into account when estimating the intergrain distance in an actual crystal structure. Nevertheless, calculations performed with the use of a spherical Seitz–Wigner cell give quite correct estimates of the potential and charge of a dust grain and demonstrate the possibility of the formation of a plasma crystal due to the presence of minima in the electric potential and in the cell potential energy without invoking additional effects (the so-called shadow effects, collective interaction, etc. [8]).

ACKNOWLEDGMENTS

REFERENCES

1. V. N. Tsytovich, G. E. Morfill, and V. Kh. Tomas, Fiz. Plazmy **28**, 675 (2002) [Plasma Phys. Rep. **28**, 623 (2002)].

2. J. E. Allen and B. M. Annaratone, Plasma Phys. **63**, 299 (2000).

3. V. A. Shveĭgert, I. V. Shveĭgert, V. M. Bogdanov, *et al.*, Zh. Éksp. Teor. Fiz. **115**, 877 (1999) [JETP **88**, 482 (1999)].

4. A. V. Zobnin, A. P. Nefedov, V. A. Sinel'shchikov, and V. E. Fortov, Zh. Éksp. Teor. Fiz. **118**, 554 (2000) [JETP **91**, 483 (2000)].

5. C. M. C. Nairn, B. M. Annaratone, and J. E. Allen, Plasma Sources Sci. Technol. **7**, 478 (1998).

6. A. F. Pal', A. N. Starostin, and A. V. Filippov, Fiz. Plazmy **27**, 155 (2001) [Plasma Phys. Rep. **27**, 143 (2001)]; Fiz. Plazmy **28**, 32 (2002) [Plasma Phys. Rep. **28**, 28 (2002)].

7. L. Tonks and I. Langmnuir, Phys. Rev. **34**, 876 (1929).

8. V. E. Fortov, A. G. Khrapak, and S. A. Khrapak, Usp. Fiz. Nauk **174**, 495 (2004) [Phys. Usp. **47**, 447 (2004)].

9. V. L. Granovskiĭ, *Electric Current in a Gas* (Nauka, Moscow, 1971) [in Russian].

10. E. W. McDaniel and E. A. Mason, *The Mobility and Diffusion of Ions in Gases* (Wiley, New York, 1973; Mir, Moscow, 1976).

11. V. I. Sysun, Fiz. Plazmy **4**, 931 (1978) [Sov. J. Plasma Phys. **4**, 520 (1978)].

Translated by N.N. Ustinovskiĭ

NONLINEAR
PHENOMENA

Excitation of Langmuir Oscillations by a Laser Pulse in a Semi-Infinite Dense Plasma

V. A. Balakirev, I. V. Gavrilenko, V. I. Karas', Ya. B. Faĭnberg[†], and A. P. Tolstoluzhskiĭ

National Science Center Kharkov Institute of Physics and Technology,
ul. Akademicheskaya 1, Kharkov, 61108 Ukraine
Received October 23, 2004; in final form, December 20, 2004

Abstract—A study is made of the nonlinear mechanism for the excitation of Langmuir waves in a dense plasma by an intense laser pulse with the frequency $\omega = \omega_p/2$ (where ω_p is the electron plasma frequency). © 2005 Pleiades Publishing, Inc.

1. INTRODUCTION

The study of physical mechanisms for the excitation of Langmuir waves in plasma by laser radiation is of interest for a number of applications, first of all, for the acceleration of electrons and ions in plasma (the current state of this acceleration problem is reflected in papers [1–7] and the literature cited therein). In the present paper, we investigate the nonlinear mechanism for the excitation of a Langmuir wave by a laser pulse with a frequency equal to half the plasma frequency. On the one hand, such a pulse is subject to the skin effect in the plasma; on the other hand, the currents and charges induced in the plasma at the second harmonic of the laser frequency are in resonance with the Langmuir oscillations.

2. FORMULATION OF THE PROBLEM AND BASIC EQUATIONS

Let a laser pulse with a given intensity profile be normally incident from vacuum onto a semi-infinite homogeneous plasma. The laser pulse frequency ω is assumed to be half the plasma frequency, $\omega = \omega_p/2$, where ω_p is the electron plasma frequency. Such a pulse can penetrate into the plasma over a distance equal to the skin depth $\lambda_s = 2c/(\sqrt{3}\omega_p)$. The pulse with this frequency gives rise to a nonlinear plasma current at the plasma frequency; in turn, the current resonantly excites a Langmuir wave that propagates from the skin layer into the plasma.

The basic set of equations contains the equation of motion of the electron plasma component

$$m\left(\frac{\partial \mathbf{v}}{\partial t} + (\mathbf{v} \cdot \nabla)\mathbf{v}\right) = -e\mathbf{E} - \frac{e}{c}(\mathbf{v} \times \mathbf{H}) - v_{Te}^2 \frac{1}{n}\nabla n, \quad (1)$$

the continuity equation

$$\frac{\partial n}{\partial t} + \nabla \cdot (n\mathbf{v}) = 0, \qquad (2)$$

and Maxwell's equations for the electromagnetic field

$$\nabla \times \mathbf{E} = -\frac{1}{c}\frac{\partial \mathbf{H}}{\partial t}, \quad \nabla \times \mathbf{H} = -\frac{4\pi}{c}en\mathbf{v} + \frac{1}{c}\frac{\partial \mathbf{E}}{\partial t}, \quad (3)$$

$$\nabla \cdot \mathbf{E} = -4\pi e(n - n_0), \quad \nabla \cdot \mathbf{H} = 0, \qquad (4)$$

where n_0 is the ion background density and v_{Te} is the electron thermal velocity.

We seek the solution to Eqs. (1)–(4) in the form

$$\mathbf{E} = \mathbf{E}_l + \frac{1}{2}\mathbf{E}_t(z, t)e^{-i\omega t} + \text{c.c.},$$

$$\mathbf{H} = \frac{1}{2}\mathbf{H}_t(z, t)e^{-i\omega t} + \text{c.c.}, \qquad (5)$$

$$\mathbf{v} = \mathbf{v}_l + \frac{1}{2}\mathbf{v}_t(z, t)e^{-i\omega t} + \text{c.c.}, \quad n = n_0 + n_l, \qquad (6)$$

where the subscripts t and l refer, respectively, to the transverse laser wave and the longitudinal Langmuir wave. We substitute relationships (5) and (6) into Eqs. (1)–(4) and perform the corresponding averaging procedure to obtain the following set of coupled equations for the longitudinal and transverse perturbations:

$$m\frac{\partial \mathbf{v}_l}{\partial t} = -e\mathbf{E}_l - v_{Te}^2\frac{1}{n_0}\nabla n_l + \mathbf{F}_{NL}, \qquad (7)$$

$$\frac{\partial n_l}{\partial t} + n_0\nabla \cdot \mathbf{v}_l = 0, \qquad (8)$$

$$\nabla \cdot \mathbf{E}_l = -4\pi e n_l, \qquad (9)$$

$$\mathbf{F}_{NL} = -\frac{1}{4}\left\{m(\mathbf{v}_t \cdot \nabla)\mathbf{v}_t + \frac{e}{c}(\mathbf{v}_t \times \mathbf{H}_t)\right\}e^{-2i\omega t} + \text{c.c.}, \qquad (10)$$

[†] Deceased.

$$im\omega \mathbf{v}_t = e\mathbf{E}_t, \qquad (11)$$

$$\nabla \times \mathbf{H}_t = -\frac{4\pi}{c}en_0\mathbf{v}_t - i\frac{\omega}{c}\mathbf{E}_t, \qquad (12)$$

$$\nabla \times \mathbf{E}_t = i\frac{\omega}{c}\mathbf{H}_t, \qquad (13)$$

$$\nabla \cdot \mathbf{E}_t = 0. \qquad (14)$$

Using Eqs. (11) and (13) and keeping the terms of the second order in the field amplitude, we convert expression (10) for the nonlinear force into the form

$$\mathbf{F}_{NL} = \frac{e^2}{4m\omega^2}(\nabla E_t^2 e^{-2i\omega t} + \text{c.c.}).$$

Equations (7)–(9) for longitudinal perturbations are equivalent to the following equation for the longitudinal electric field of the Langmuir wave:

$$\frac{\partial^2 \mathbf{E}_l}{\partial t^2} + \omega_p^2 \mathbf{E}_l - v_{Te}^2 \Delta \mathbf{E}_l$$
$$= \frac{1}{4}\omega_p^2 \frac{mc^2}{e}(\nabla a^2 e^{-2i\omega t} + \text{c.c.}), \qquad (15)$$

where $a^2 = \dfrac{e^2 E_t^2}{m^2 c^2 \omega^2}$.

Under the conditions adopted here, laser radiation in the plasma is damped according to the law

$$a^2 = a_0^2 F(t/t_L)\exp(-2\kappa z), \qquad (16)$$

where $\kappa = \dfrac{\omega}{c}\sqrt{-\varepsilon(\omega)} = \dfrac{\sqrt{3}}{2}\dfrac{\omega_p}{c}$ and $\varepsilon = 1 - \dfrac{\omega_p^2}{\omega^2}$ is the plasma dielectric function. The function $F(t/t_L)$ describes the laser pulse profile, and t_L is the characteristic pulse duration. With allowance for relationship (16), Eq. (15) for the Langmuir wave field can be written in the form

$$\frac{\partial^2 E_l}{\partial t^2} + \omega_p^2 E_l - v_{Te}^2 \frac{\partial^2 E_l}{\partial z^2}$$
$$= -\omega_p^2 \frac{mc^2}{e}\kappa a_0^2 F(t/t_L)\cos(\omega_p t)e^{-2\kappa z}. \qquad (17)$$

For further analysis, it is convenient to switch to the dimensionless variables

$$\tau = \omega_p t, \quad \varsigma = z\omega_p/v_{Te}, \quad \psi = E_l/E_*,$$

$$E_* = \frac{\sqrt{3}}{2}E_m a_0^2, \quad E_m = \frac{mc\omega_p}{e}.$$

In these variables, Eq. (17) takes the form

$$\frac{\partial^2 \psi}{\partial \tau^2} + \psi - \frac{\partial^2 \psi}{\partial \varsigma^2} = -F(\tau/\tau_L)\cos\tau e^{-\alpha\varsigma}, \qquad (18)$$

where $\tau_L = \omega_p t_L$ and $\alpha = \sqrt{3}\,v_{Te}/c$.

Hence, the excitation of a Langmuir wave is described by the Klein–Gordon equation whose right-hand side contains the ponderomotive force at the second harmonic of laser radiation. The frequency of the second harmonic is equal to the plasma frequency.

Let us first consider the interaction of a laser pulse with a cold plasma ($v_{Te} = 0$). In this case, the excitation of Langmuir oscillations is described by the following inhomogeneous oscillator equation:

$$\frac{\partial^2 \psi}{\partial \tau^2} + \psi = -F(\tau/\tau_L)\cos\tau e^{-\xi},$$

where $\xi = \sqrt{3}\omega_p z/c$ is the dimensionless coordinate in units of the skin depth. The solution to this equation that satisfies the condition $\psi(t \longrightarrow -\infty) \longrightarrow 0$ has the form

$$\psi = \frac{1}{2}e^{-\xi}\left\{\cos\tau \int_{-\infty}^{\tau} F(\tau/\tau_L)\sin 2\tau d\tau \right.$$
$$\left. - \sin\tau \int_{-\infty}^{\tau} F(\tau/\tau_L)(1 + \cos 2\tau)d\tau \right\}.$$

We assume for simplicity that the laser pulse profile is symmetric, $F(\tau/\tau_L) = F(-\tau/\tau_L)$. After the pulse has interacted with the plasma ($\tau \longrightarrow \infty$), the field structure of the excited Langmuir oscillations has the form

$$\psi = -\frac{1}{2}e^{-\xi}A(\tau_L)\sin\tau,$$

where

$$A(\tau_L) = \int_{-\infty}^{\infty} F(\tau/\tau_L)(1 + \cos 2\tau)d\tau \qquad (19)$$

is the function of the laser pulse duration. From expression (19), we see that the plasma oscillations are concentrated within the skin layer. For a Gaussian laser pulse,

$$F(\tau/\tau_L) = \exp(-\tau^2/\tau_L^2);$$

the function $A(\tau_L)$ is given by the expression

$$A(\tau_L) = \sqrt{\pi}\tau_L(1 + e^{-\tau_L^2}).$$

For short ($\tau_L \ll 1$) and long ($\tau_L \gg 1$) laser pulses, the values of the function $A(\tau_L)$ differ by a factor of 2. In these limiting cases, the function $A(\tau_L)$ depends linearly

on the pulse duration. For a laser pulse with the model profile

$$F(\tau/\tau_L) = \cos\left(\frac{\pi}{2}\frac{\tau}{\tau_L}\right), \quad \tau_L \geq \tau \geq -\tau_L,$$

we have

$$A(\tau_L) = \frac{2\tau_L}{\pi}\left(2 + \frac{\cos 2\tau_L}{1 + 4\tau_L/\pi}\right). \tag{20}$$

The oscillating term on the right-hand side of expression (20) describes the interference between the Langmuir waves excited by the leading and trailing edges of the laser pulse.

Let us now take into account the thermal motion of the plasma electrons. In this case, the electrons carry the oscillation energy from a narrow skin layer into the plasma. The solution to the Klein–Gordon equation that describes this effect was derived using a Green's function approach. The Green's function $G(\varsigma - \varsigma', \tau - \tau')$ that satisfies the equation

$$\frac{\partial^2 G}{\partial \tau^2} + G - \frac{\partial^2 G}{\partial \varsigma^2} = \delta(\tau - \tau')\delta(\varsigma - \varsigma'),$$

and the boundary condition

$$G(\varsigma = 0, \varsigma', \tau - \tau') = 0 \tag{21}$$

has the form

$$G(\varsigma, \varsigma', \tau - \tau')$$
$$= G_1(\varsigma - \varsigma', \tau - \tau') - G_2(\varsigma + \varsigma', \tau - \tau'). \tag{22}$$

Here,

$$G_1(\varsigma - \varsigma', \tau - \tau')$$
$$= \frac{1}{2}\theta(\tau - \tau')\theta(\tau - \tau' - |\varsigma - \varsigma'|)J_0(\sqrt{(\tau - \tau')^2 - (\varsigma - \varsigma')^2}),$$

$$G_2(\varsigma + \varsigma', \tau - \tau')$$
$$= \frac{1}{2}\theta(\tau - \tau')\theta(\tau - \tau' - |\varsigma + \varsigma'|)J_0(\sqrt{(\tau - \tau')^2 - (\varsigma + \varsigma')^2}),$$

where $\theta(x)$ is the Heaviside step function of unit height and $J_0(x)$ is the Bessel function. Boundary condition (21) is obtained from the condition for the electron velocity to vanish at the plasma boundary. The first term on the right-hand side of expression (22) is the Green's function for a spatially infinite plasma, and the second term is the Green's function for the wave perturbation reflected from the plasma boundary. Accord-

ingly, the solution to the inhomogeneous Klein–Gordon equation can be written as

$$\psi(\tau, \varsigma) = -\frac{1}{2}\int_{-\infty}^{\tau} d\tau' \int_{0}^{\infty} d\varsigma' \theta(\tau - \tau' - |\varsigma - \varsigma'|)$$
$$\times J_0(\sqrt{(\tau - \tau')^2 - (\varsigma - \varsigma')^2})e^{-\alpha\varsigma'}F(\tau'/\tau_L)\cos\tau'$$
$$+ \frac{1}{2}\int_{-\infty}^{\tau} d\tau' \int_{0}^{\infty} d\varsigma' \theta(\tau - \tau' - |\varsigma + \varsigma'|)$$
$$\times J_0(\sqrt{(\tau - \tau')^2 - (\varsigma + \varsigma')^2})e^{-\alpha\varsigma'}F(\tau'/\tau_L)\cos\tau'. \tag{23}$$

In the first term on the right-hand side of expression (23) for the Langmuir wave field, it is convenient to switch to the new variables $\tau'_1 = \tau - \tau'$ and $\varsigma'_1 = \varsigma - \varsigma'$. The second term can be conveniently treated in terms of the variables $\tau'_1 = \tau - \tau'$. and $\varsigma'_1 = \varsigma + \varsigma'$. In these variables, we have

$$\psi(\tau, \varsigma) = -\frac{1}{2}\int_{0}^{\infty} d\tau' \int_{-\infty}^{\zeta} d\varsigma' \theta(\tau' - |\varsigma'|)$$
$$\times J_0(\sqrt{\tau'^2 - \varsigma'^2})e^{-\alpha(\varsigma - \varsigma')}F\left(\frac{\tau - \tau'}{\tau_L}\right)\cos(\tau - \tau')$$
$$+ \frac{1}{2}\int_{0}^{\infty} d\tau' \int_{\zeta}^{\infty} d\varsigma' \theta(\tau' - |\varsigma'|)$$
$$\times J_0(\sqrt{\tau'^2 - \varsigma'^2})e^{-\alpha(\varsigma' - \varsigma)}F\left(\frac{\tau - \tau'}{\tau_L}\right)\cos(\tau - \tau'). \tag{24}$$

For simplicity, we have dropped the subscript 1 from the integration variables in the integrands in this expression. With a specified explicit form of the function $F\left(\frac{\tau - \tau'}{\tau_L}\right)$, the field of the excited Langmuir wave can be calculated numerically from expression (24).

In the limit $\tau_L \gg 1$, Eq. (18) can be simplified as follows: We seek the solution to inhomogeneous Klein–Gordon equation (18) in the form

$$\psi(\varsigma, \tau) = \frac{1}{2}\Phi(\varsigma, \tau)e^{-i\tau} + \text{c.c.},$$

where $\Phi(\varsigma, \tau)$ is a time-dependent, slowly varying (over the interval from 0 to 2π) function representing the complex amplitude of the Langmuir oscillations. By averaging over time, we reduce Klein–Gordon equation (18) to the inhomogeneous parabolic equation

$$2i\frac{\partial \Phi}{\partial \tau} + \frac{\partial^2 \Phi}{\partial \varsigma^2} = e^{-\alpha\tau}F\left(\frac{\tau}{\tau_L}\right). \tag{25}$$
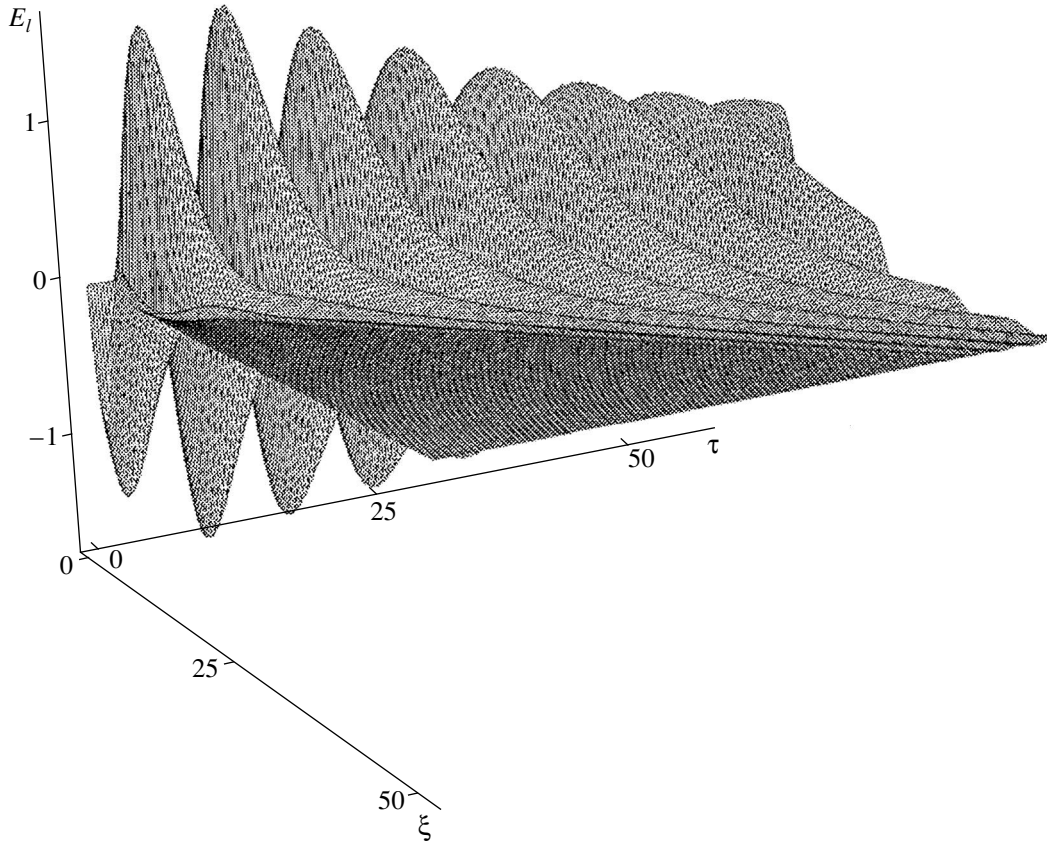
Fig. 1. Spatiotemporal distribution of the electric field of a Langmuir wave excited by a short laser pulse.

The Green's function of the parabolic equation

$$2i\frac{\partial G}{\partial \tau} + \frac{\partial^2 G}{\partial \varsigma^2} = \delta(\tau - \tau')\delta(\varsigma - \varsigma'),$$

that satisfies boundary condition (21) has the form

$$G(\varsigma - \varsigma', \tau - \tau') = -\frac{i}{2}\frac{\theta(\tau - \tau')}{\sqrt{2\pi(\tau - \tau')}}\exp\left[\frac{i(\varsigma - \varsigma')^2}{2(\tau - \tau')} - i\frac{\pi}{4}\right]$$

$$+ \frac{i}{2}\frac{\theta(\tau - \tau')}{\sqrt{2\pi(\tau - \tau')}}\exp\left[\frac{i(\varsigma + \varsigma')^2}{2(\tau - \tau')} - i\frac{\pi}{4}\right].$$

The solution to inhomogeneous parabolic equation (23) can be written as

$$\Phi(\varsigma, \tau) = -\frac{i}{\sqrt{8\pi}}e^{-i\pi/4}\int_{-\infty}^{\tau}d\tau'\frac{F(\tau'/\tau_L)}{\sqrt{\tau - \tau'}}$$

$$\times \int_0^{\infty}d\varsigma'\left\{\exp\left[\frac{i(\varsigma - \varsigma')^2}{2(\tau - \tau')} - \alpha\varsigma'\right] - \exp\left[\frac{i(\varsigma + \varsigma')^2}{2(\tau - \tau')} - \alpha\varsigma'\right]\right\}. \tag{26}$$

Let us consider the behavior of the Langmuir wave amplitude on time scales that are much longer than the pulse duration, $\tau \gg \tau'$. In this case, expression (26) for

the Langmuir wave amplitude can be substantially simplified to become

$$\Phi(\varsigma, \tau) = -\frac{i}{\sqrt{8\pi\tau}}e^{-i\pi/4}\tau_L U$$

$$\times \int_0^{\infty}d\varsigma'\left\{\exp\left[\frac{i(\varsigma - \varsigma')^2}{2\tau} - \alpha\varsigma'\right] - \exp\left[\frac{i(\varsigma + \varsigma')^2}{2\tau} - \alpha\varsigma'\right]\right\}, \tag{27}$$

where

$$U = \int_{-\infty}^{\infty}ds F(s).$$

For long time scales such that $\tau \gg (2\alpha^2)^{-1}$, ς/α, the integral in expression (27) can be evaluated approximately:

$$\Phi \simeq -\frac{\tau_L U \varsigma}{\sqrt{2\pi}\alpha^2\tau^{3/2}}\exp\left(-i\frac{\pi}{4} + i\frac{\varsigma^2}{2\tau}\right).$$

We see that the amplitude of plasma oscillations decreases as $\tau^{-3/2}$.
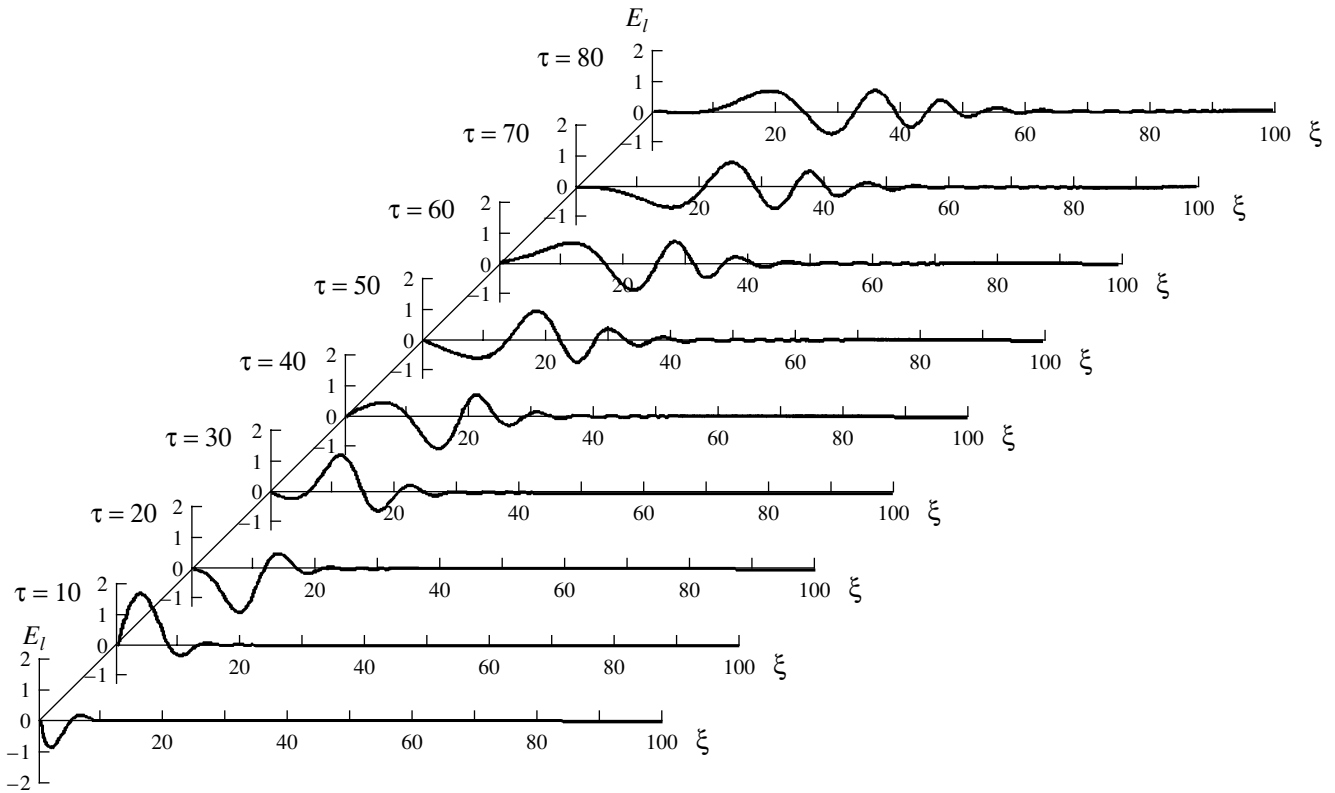
Fig. 2. Time evolution of the spatial profile of the electric field of a Langmuir wave excited by a short laser pulse for $\tau_L = 12$ and $\alpha = 0.433$.
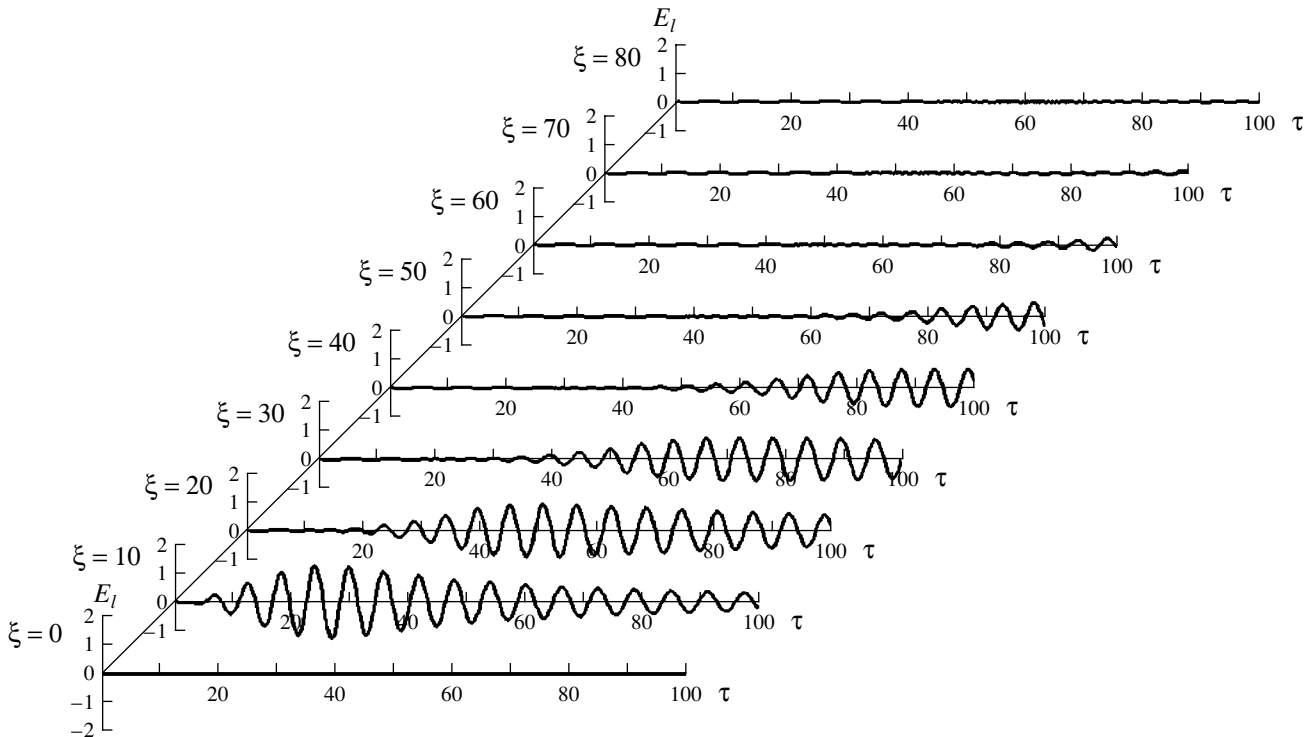

Fig. 3. Waveforms of the electric field of the excited Langmuir wave at different spatial points for $\tau_L = 12$ and $\alpha = 0.433$.

3. NUMERICAL RESULTS

In order to examine the nonlinear excitation of Langmuir waves by a laser pulse in a dense plasma in more detail, the electric field of the excited Langmuir wave was calculated numerically from expression (23) for the following dimensionless parameters: $\tau_L = 12$ and $\alpha = 0.433$. The laser pulse profile was modeled by the function

$$F(\tau/\tau_L) = \cos\left(\frac{\pi}{2}\frac{\tau}{\tau_L}\right).$$

For a laser pulse with the wavelength $\lambda = 1.05$ μm, the above dimensionless parameters correspond to the following values of the physical quantities: the plasma density is $n_0 = 4.5 \times 10^{21}$ cm^{-3}, the plasma frequency is $\omega_p = 3.77 \times 10^{15}$ s^{-1}, and the plasma electron temperature is $T_e = 32$ keV. The general pattern of the excitation of a Langmuir wave is illustrated in Fig. 1, and the details of this pattern are shown in Figs. 2 and 3. Figure 2 presents the spatial profiles of the electric field strength of the Langmuir wave in the plasma at different times. We can see that the Langmuir wave perturbation propagates into the plasma. The field in the plasma is oscillatory in character: in the direction from the leading edge of the wave perturbation toward the plasma boundary, the field amplitude first increases, reaching a maximum value, and then decreases to zero at the boundary. At each spatial point behind the leading edge of the propagating wave perturbation, the field oscillates at the plasma frequency (Fig. 3). Because of the dispersive spreading of the Langmuir wave packet, the maximum amplitude of the Langmuir wave perturbations decreases with time. In dimensional units, the strength of the longitudinal electric field is described by the expression

$$E_l\,[\text{V/Òm}] = \psi\frac{\sqrt{3}}{2}a_0^2\sqrt{n_0}. \tag{28}$$

4. CONCLUSIONS

We have investigated the nonlinear mechanism for the excitation of a Langmuir wave by an intense laser pulse in a dense plasma. The laser pulse has the frequency $\omega = \omega_p/2$ (where ω_p is the electron plasma frequency) and is normally incident from vacuum onto a semi-infinite plasma. Such a pulse penetrates into the plasma over a characteristic distance equal to $\lambda_s =$ $2c/(\sqrt{3}\omega_p)$. The pulse with the indicated frequency gives rise to a nonlinear plasma current at the plasma frequency, which resonantly excites a Langmuir wave in the skin layer. It is shown that this wave propagates from the skin layer into the plasma. The wave field in the plasma is oscillatory in character: in the direction from the leading edge of the wave perturbation toward the plasma boundary, the field amplitude first increases, reaching a maximum value, and then decreases to zero at the boundary. At each spatial point behind the leading edge of the propagating wave perturbation, the field oscillates at the plasma frequency. Because of the dispersive spreading of the Langmuir wave packet, the maximum amplitude of the Langmuir wave perturbations decreases with time. In dimensional units, the strength of the longitudinal electric field is given by expression (28).

It is important to note that, in a recent paper by Baton *et al.* [3], direct experimental evidence was found for the formation of accelerated electron bunches separated by the half-period of laser radiation during irradiation of a thick solid target by a relativistic laser beam.

ACKNOWLEDGMENTS

REFERENCES

1. V. A. Balakirev, V. I. Karas', I. V. Karas', *et al.*, Laser Part. Beams **19**, 597 (2001).
2. V. A. Balakirev, V. I. Karas', and I. V. Karas', Fiz. Plazmy **28**, 144 (2002) [Plasma Phys. Rep. **28**, 125 (2002)].
3. S. D. Baton, J. J. Santos, F. Amiranoff, *et al.*, Phys. Rev. Lett. **91**, 105 001 (2003).
4. M. J. Hogan, C. E. Clayton, C. Huang, *et al.*, Phys. Rev. Lett. **90**, 205 002 (2003).
5. Y. Kitagawa, T. Matsumoto, T. Minamihata, *et al.*, Phys. Rev. Lett. **68**, 48 (1992).
6. P. Sprangle, J. R. Penano, B. Hafizi, *et al.*, Phys. Plasmas **9**, 2364 (2002).
7. A. Maksimchuk, K. Flippo, H. Krause, *et al.*, Fiz. Plazmy **30**, 514 (2004) [Plasma Phys. Rep. **30**, 473 (2004)].

Translated by I.A. Kalabalyk

LOW-TEMPERATURE
PLASMA

Effect of the Vibrational Excitation of CO Molecules on the Parameters of an RF Discharge

A. A. Ionin*, D. V. Sinitsyn*, Yu. V. Terekhov*, I. V. Kochetov**, A. P. Napartovich**, and S. A. Starostin***

* *Lebedev Physical Institute, Russian Academy of Sciences, Leninskiĭ pr. 53, Moscow, 119991 Russia*
** *Troitsk Institute for Innovation and Fusion Research, Troitsk, Moscow oblast, 142190 Russia*
*** *Institute for Low-Temperature Plasma Physics, D-17489 Greifswald, Germany*
Received November 18, 2004; in final form, January 18, 2005

Abstract—A one-dimensional model of an RF discharge in CO-containing gas mixtures is developed. The model takes into account the effect of the degree of vibrational excitation of CO molecules on the structure of the discharge and on its parameters. Experimental data are presented from measurements of the voltage–power characteristics of RF discharges in gas mixtures with different CO contents in the pressure range of 10–100 torr. The model developed is used to calculate the dependence of the root-mean-square discharge voltage on the specific power deposition in an RF discharge under our experimental conditions. The experimental data are compared to the results of numerical simulations. For working gas pressures of about 100 torr, which are typical of the operation of slab CO lasers, the calculated voltage–power characteristics of an RF discharge agree satisfactorily with those obtained experimentally. The theoretical model predicts that the vibrational excitation of CO molecules leads to a redistribution of the RF field in the discharge gap and to an increase in the laser efficiency. © 2005 Pleiades Publishing, Inc.

1. INTRODUCTION

Considerable progress made in developing capillary and slab CO_2 and CO lasers during the past decade resulted from the proposal to excite laser media by capacitive transverse RF discharges in the frequency range of 1–200 MHz. The heat from the gas mixture is usually removed by cooling the electrodes (see, e.g., [1–3]). An RF discharge has a number of advantages over a dc glow discharge. The current in a glow discharge can be oriented across or along a narrow gap. In the first case, the cathode dark space—a region in which the excitation of molecular vibrations is very inefficient—occupies a fairly large part of the gap. In the second case, it is necessary to apply a high voltage. In addition, in both cases, the discharge current breaks into filaments as the gas pressure is increased. As for an RF discharge, its stability makes it possible to use low-voltage power sources; this simplifies the modulation of the RF pump power and makes the laser output power easier to control. In an RF discharge, each of the electrodes alternately operates as a cathode or an anode, and vice versa, depending on the phase of the RF field, and the conduction current near the electrode that is the cathode at a given time is closed by the displacement current. The electrode sheaths in an RF discharge are markedly smaller in size than those in a glow discharge, so the RF discharge is more efficient energetically. An RF discharge also makes it possible to excite fairly large volumes of active media (in planar geometry) without using external ionization sources.

There is little experimental information on the properties of RF discharges in slab CO lasers [4, 5], all the relevant data being obtained from discharge chambers devised to generate laser radiation. The boundary effects in such chambers, as well as plasma inhomogeneities along the optical axis, introduce errors in measurements; this may lead to disagreements between experiment and theory. Investigations of the properties of RF discharges in CO_2-containing mixtures on specially designed devices [6, 7] made it possible to measure the RF discharge parameters required to make comparisons with numerical results. In particular, the voltage–power (VP) characteristics of an RF discharge that were measured in [6, 7] agree satisfactorily with the results of numerical simulations [8].

The discharge plasmas in CO-containing mixtures and in mixtures typical of CO_2 lasers differ in properties because, in the first case, the degree of vibrational excitation is far greater than that in the second case. Thus, in the active medium of a CO laser, the distribution of CO molecules over the vibrational levels is characterized by the vibrational temperature of the low-lying levels of about 3000 K and also by an extended plateau at vibrational levels higher than the so-called Treanor vibrational level [9]. The vibrational excitation of molecules changes the electron energy distribution function (EEDF) and gives rise to new ionization mechanisms associated with the elementary processes at the high-lying vibrational levels. For a plasma of the positive column of glow discharges in CO-containing mixtures, such processes were discussed earlier in [10].

In the present paper, we develop a one-dimensional model of an RF discharge that takes into account the effect of the degree of vibrational excitation of CO molecules on the discharge properties. We present the data of measuring the VP characteristics of RF discharges in gas mixtures with different CO contents at different pressures in a specially designed device and compare the calculated results to the experimental data. We also theoretically investigate how the mechanisms whereby the ionization rate increases with the rate of vibrational excitation of CO molecules affects the spatial structure of the RF discharge and its parameters.

2. EXPERIMENTAL SETUP AND MEASUREMENT TECHNIQUE

In order to thoroughly investigate the properties of RF discharges in CO-containing gas mixtures, we designed a special RF discharge chamber (see Fig. 1) [11]. The electrode system of the discharge chamber (*1*) consisted of two diffusively cooled 10-mm-diameter cylindrical electrodes (*2*), placed coaxially at a distance of 1.9 mm from one another. The volume of the RF discharge region (*3*) was 0.15 cm^3. The voltage to the electrode system was supplied from an 81.36-MHz RF generator (*4*) through a detector of the ratio of the reflected to the transmitted RF power (*5*) and through a circuit (*6*) for matching the total load impedance to the output impedance (50 Ω) of the RF generator. The electrodes were cooled using containers (*8*) filled with room-temperature water (*7*).

The VP characteristics of the discharge were measured by a V3-53/1 RF voltmeter (*9*) and a thermocouple calorimeter. One junction (*10*) of a copper–constantan thermocouple was placed at one of the RF electrodes and the other junction (*11*) was kept at room temperature in one of the water containers (*8*). The thermal emf was measured by a microvoltmeter (*12*). The thermometric system was calibrated by measuring the temperatures of the electrodes heated by dc discharges with the known parameters. The measurement schemes and techniques, as well as the calibration procedure, were described in detail in [11].

3. THEORETICAL MODEL

In our model of an RF discharge, only one species of positive ions was taken into account and the concentration of negative ions was ignored because of the rapid decomposition of O$^-$ ions in collisions with CO molecules. The one-dimensional time-dependent continuity equations for the fluxes of electrons and positive ions were solved together with Poisson's equation. The continuity equations accounted for the drift of charged particles and their diffusion. The gas temperature was found from the time-averaged heat conduction equation.

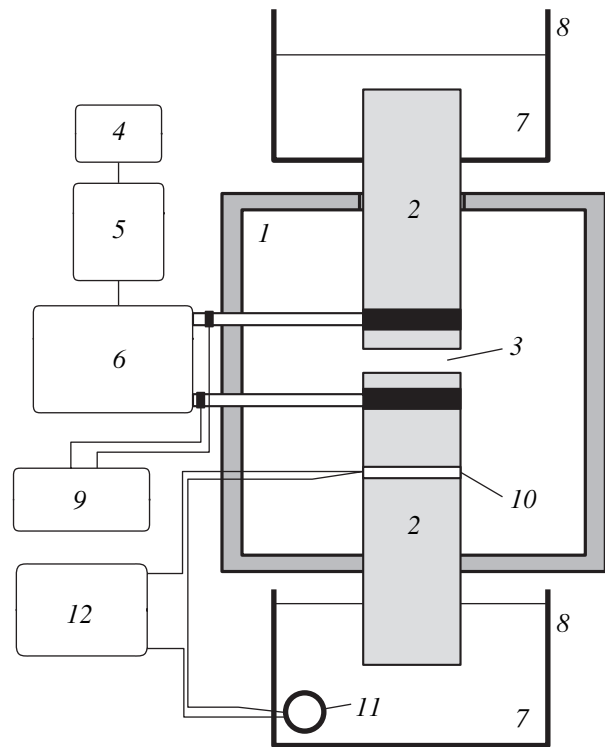The thermal conductivity of the gas mixture was determined from the thermal conductivities of the indi-

Fig. 1. Schematic of the experimental setup for measuring the VP characteristics of an RF discharge: (*1*) discharge chamber, (*2*) electrodes, (*3*) discharge region, (*4*) RF generator, (*5*) detector of the reflected RF power, (*6*) matching circuit, (*7*, *8*) cooling system, (*9*) RF voltmeter, (*10*, *11*) thermocouples, and (*12*) microvoltmeter.

vidual plasma components by means of the procedure described in [12]. The values of the thermal conductivities of the plasma components, as well as their dependence on temperature, were taken from [13].

In order to correctly take into account the effects responsible for the non-steady-state and nonlocal nature of the electron kinetic coefficients, it is necessary to solve the Boltzmann equation over space and time, which is a rather difficult task (for pure He, this problem was solved in [14]). Although the EEDF is non-Maxwellian, it is possible to introduce the mean electron energy as its main parameter and to assume that all the coefficients depend only on this mean energy (as was done in [15]). In this case, the mean electron energy is described by a time-dependent equation and can be found by solving it with allowance for electron heat conduction. In such an approach, the mean electron energy at each point within the interelectrode gap is a function of time. The transport coefficients in the equations for the mean energy and density of the electrons, as well as the ionization and attachment rate constants, were determined by numerically solving a homogeneous time-independent Boltzmann equation for the EEDF. In simulations, the mean electron energy was varied by varying the parameter *E*/*N*,
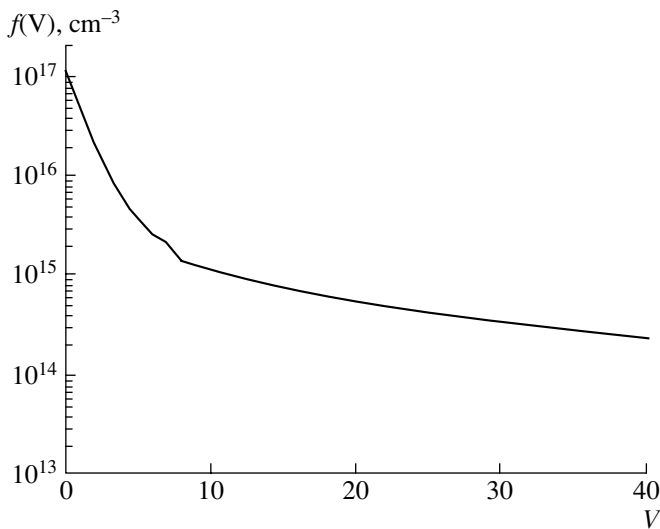
$f(V)$, cm^{-3}

Fig. 2. Typical form of the distribution function of CO molecules over vibrational levels, calculated from analytic formulas.

where E is the electric field strength and N is the gas density. The effect of vibrational excitation on the mean electron energy and transport coefficients was ignored. This assumption was proved by a special series of test calculations carried out for the typical discharge conditions under investigation.

In [16], it was shown that the rate constants of the processes with energy thresholds far above the mean electron energy are well approximated by the formula

$$\log\left[\frac{K(z)}{K(0)}\right] = \frac{Cz}{(E/N)^2}. \qquad (1)$$

Here, K is the rate constant of the corresponding process; $z = \exp(-\hbar\omega/T_V)$, with $\hbar\omega$ being a vibrational quantum energy; and T_V is the vibrational temperature. The constant C was found by processing the results of numerically solving the Boltzmann equation for the EEDF with allowance for collisions of electrons with vibrationally excited molecules. It was found that, for CO molecules, this constant has the same value for all high-threshold electronic processes [17]. In our work, the constant C in formula (1) was calculated numerically for each particular mixture. Hence, although the rate constants $K(0)$ are functions of the mean electron energy, their dependence on the vibrational temperature of the low-lying levels was calculated as a function of the local value of the reduced electric field E/N.

For each spatial cell of the numerical mesh, the vibrational temperature T_V of the low-lying levels of a CO molecule was calculated by matching the molecular distribution function over the vibrational levels in the Treanor region and the function $f_V = \dfrac{c}{V+1}$ (see, e.g., [9]). Here, V is the number of the vibrational level,

the parameter in the numerator is given by the expression $c = (w/\nu)^{0.5}$, w is the excitation rate of the vibrational levels $\left(w = \dfrac{W_V}{N_{CO}\hbar\omega}\right)$, W_V is the averaged (over the RF field period) power expended on the excitation of the vibrational levels of CO molecules, and ν is the effective V–V exchange frequency (which depends on the temperature and gas pressure). The expression for the V–V exchange frequency was taken from [18]. The typical shape of the molecular distribution function over vibrational levels is shown in Fig. 2. The approximation just described makes it possible to account for the dependence of the vibrational temperature of the low-lying levels on the excitation power and the translational gas temperature. Since the V–V exchange frequency is much lower than the pump frequency, it was calculated from the excitation power W_V averaged over the RF field period.

In [10], it was shown that, under the conditions typical of electric-discharge CO lasers, an important role may be played by the associative ionization reaction in collisions between the vibrationally and electronically excited molecules:

$$CO(V \geq 15) + CO(I^1\Sigma^-) \longrightarrow C_2O_2^+ + e. \qquad (2)$$
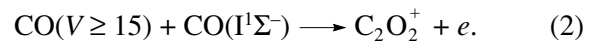
This ionization channel was taken into account by supplementing the RF discharge model with the equations describing the kinetics of excited molecules in the $CO(I^1\Sigma^-)$ state. The main mechanism for populating the $CO(I^1\Sigma^-)$ state is the electron-impact excitation of CO molecules from the ground state. As in [10], the cross section for this excitation process was taken from [19]. The rate of quenching of the $CO(I^1\Sigma^-)$ state is equal to the electron-impact excitation rate, on the one hand, and to the sum of the quenching rates in collisions with CO molecules in the ground states and in reaction (2), on the other hand. In [10], the ratio of the effective rate constant of reaction (2) to the quenching rate constant in collisions with CO molecules in the lowest vibrational state was estimated by comparing the results of model calculations to the experimental data and was found to be equal to 2 ± 0.5. This estimate was used in our kinetic model of an RF discharge. The scheme of the vibrational levels involved in the additional ionization channels is shown in Fig. 3, and the processes accounted for in the kinetic model are listed in the table. In calculating the rate constant for the excitation of the $CO(I^1\Sigma^-)$ state, as well as the rate constant for ionization from the ground state, the effect of the vibrational temperature was taken into account by means of formula (1). Under our experimental conditions, the quenching rate of the $CO(I^1\Sigma^-)$ level falls within the range 10^5–10^6 Hz, which is below the pump field frequency (81.36 MHz). This is why, in the balance equation for the $CO(I^1\Sigma^-)$ level, the rate of its excitation was averaged over the RF field period. The populations of high vibrational levels of a CO molecule ($V \geq 15$),

which are required to calculate the rates of associative ionization reaction (2), were determined from the above analytic formulas. The high rate of conversion of CO^+ ions into $C_2O_2^+$ ions (see table, reaction no. 7) allowed us to assume that the $C_2O_2^+$ ions are the dominant ion species.

The above equations were supplemented with the obvious boundary and initial conditions. The voltage across the discharge was determined from a given RF field power. The simulations were carried out using the finite-difference scheme proposed in [21, 22].

This difference scheme was implemented on a non-uniform spatial mesh that was made finer toward the electrodes. For a typical run of the code, the number of spatial steps was about 100. The scheme converged to a steady solution after several thousand periods of the RF field.

Fig. 3. Scheme of the levels of the CO molecules involved in the additional ionization channels.

4. RESULTS AND DISCUSSION

When modeling RF discharges, we assumed that the temperature of the discharge chamber wall and of the electrodes was independent of the power deposited in the discharge and was equal to 293 K (our measurements at the highest excitation powers showed that the wall temperature increased by no more than ~5–10 K). In [8], the VP characteristics of CO_2-containing gas mixtures were calculated numerically for the experimental conditions of [7]. A nonlocal model of RF discharges that was similar to the model developed here provided a good description of the experimental data from [7] at pressures above 40 torr.

In order to test our experimental method for determining the VP characteristic of the discharge, we carried out a series of measurements of this characteristic for discharges in the same CO_2-containing mixtures that were used in [7] and under nearly the same experimental conditions. Figure 4 shows the VP discharge characteristics measured in [7] (closed symbols) and in

the present paper (open symbols) and also presents the results of numerical simulations carried out for the conditions of these two experimental works (solid curves). In our experiments, the pump frequency (81.36 MHz) was somewhat lower than that in [7] (125 MHz), and the interelectrode distance (0.19 cm) was larger as compared to that in [7] (0.175 cm). For low excitation powers, the results obtained using our model agree well with the data from both experiments. The higher the excitation power, the worse the agreement between the model and our experiment; at the same time, the agreement with the experiment of [7] remains quite satisfactory. Presumably, this is because the pump frequency in the experiments of [7] is 1.5 times higher than that in our experiments. As was pointed out in [23], the normal current density in the α form of an RF discharge is comparable to that in a glow discharge. As the excitation power increases, the discharge extends over the entire gap surfaces of the electrodes and then begins to slip

Processes accounted for in the kinetic model

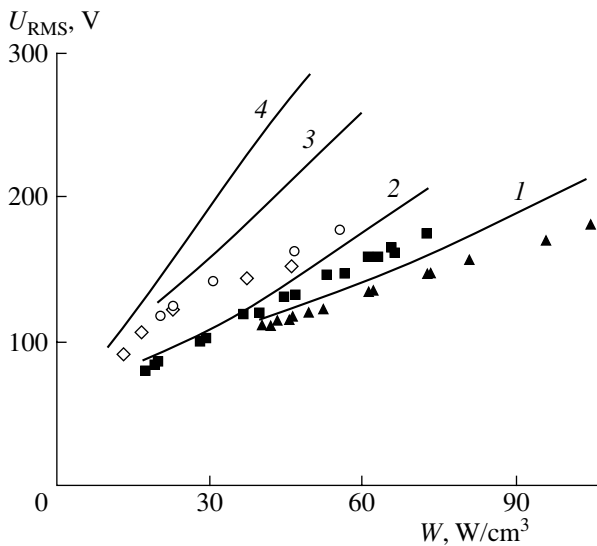| No.	Process	K, cm^3/s, cm^6/s	References
1	$CO(v) + e \rightleftharpoons CO(v') + e$	EEDF	
2	$CO + e \rightleftharpoons CO(I^1\Sigma^-) + e$	EEDF	
3	$CO + e \longrightarrow CO^+ + e + e$	EEDF	
4	$C_2O_2^+ + e \longrightarrow CO + CO$	EEDF	
5	$CO(v) + CO(v') \rightleftharpoons CO(v+1) + CO(v'-1)$	Analytic model	[9, 18]
6	$CO(v) + M \rightleftharpoons CO(v-1) + M$	Analytic model	[9]
7	$CO^+ + CO + M \longrightarrow C_2O_2^+ + M$	M = CO, He 1.4×10^{-28}	[20]
8	$CO(\geq 15) + CO(I^1\Sigma^-) \longrightarrow C_2O_2^+ + e$	$k_8/k_9 = 2.0 \pm 0.5$	[10]
9	$CO(I^1\Sigma^-) + CO \longrightarrow CO** + CO$	$k_8/k_9 = 2.0 \pm 0.5$	[10]

U_{RMS}, V

Fig. 4. Root-mean-square voltage across the discharge gap filled with a $CO_2 : N_2 : He : Xe = 19 : 19 : 57 : 5$ gas mixture vs. input power density. The solid curves and symbols show the numerical and experimental results, respectively, obtained at pressures of $P = (1, \blacktriangle)$ 70, $(2, \blacksquare)$ 40, $(3, \circ)$ 60, and $(4, \diamond)$ 30 torr. The closed symbols show the experimental results obtained in [7] for $f = 125$ MHz and $d = 0.175$ cm, and the open symbols show the results obtained in the present study for $f = 81.36$ MHz and $d = 0.19$ cm.

over their outer surfaces. The normal current density increases with the pump frequency; as a consequence, in our experiments, the discharge went out of the gap at excitation powers lower than those in the experiments of [7].

Figure 5 compares the calculated and experimental VP characteristics of RF discharges in CO : He mixtures with different contents of CO molecules at a pressure of 100 torr. We can see that, on the whole, the theory agrees satisfactorily with the experiment. The simulations reproduce the effect that was observed experimentally at low pressures, namely, the increase in the root-mean-square (rms) voltage across the discharge as the concentration of the molecular component in the gas mixture was increased (Fig. 5). As in the case of CO_2-containing mixtures, the agreement becomes somewhat worse at higher excitation powers.

Figure 6 illustrates the effect of the pressure on the rms voltage across the discharge gap filled with a CO : He = 1 : 10 gas mixture. In the experiment, the rms voltage at a fixed excitation power was found to be essentially independent of pressure, while the theoretical model predicts that, at an excitation power of 35 W/cm³, the rms voltage across the discharge should increase by a factor of more than 2 as the pressure of the working gas mixture decreases from 100 to 30 torr. The reasons for this discrepancy still remain unclear. In particular, as was mentioned above, it may well be that a low-pressure discharge in the interelectrode gap is difficult to initiate because of the low values of the parameter pd; in this case, breakdown can occur in the gas mixture within the ballast volume of the discharge chamber. Note that, according to [24], the optimal pressures in the gas mixture that provide the maximum radiation power from a CO laser lie in the range 80–100 torr.

The discharge power associated with the ion current is almost instantaneously converted into heat, so the
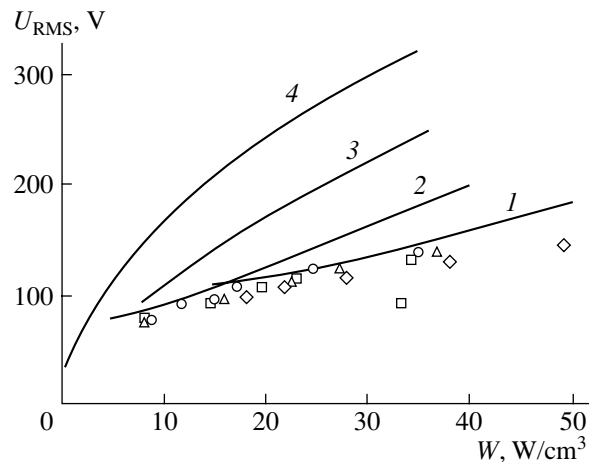
U_{RMS}, V

Fig. 5. Root-mean-square voltage across the discharge gap vs. input power density. The curves and symbols show the numerical and experimental results, respectively, for $P = 100$ torr, $f = 81.36$ MHz, $d = 0.19$ cm, and different gas-mixture compositions: CO : He = 1 : 5 (dashed-and-dotted curve, circles), CO : He = 1 : 10 (dashed curve, diamonds), and CO : He = 1 : 20 (solid curve, triangles).

U_{RMS}, V

Fig. 6. Root-mean-square voltage across the discharge gap filled with a CO : He = 1 : 10 gas mixture vs. input power density. The curves and symbols show the numerical and experimental results, respectively, for $f = 81.36$ MHz, $d = 0.19$ cm, and different gas pressures: $P = (1, \diamond) = 100$, $(2, \triangle)$ 60, $(3, \circ)$ 30, and $(4, \square)$ 10 torr.
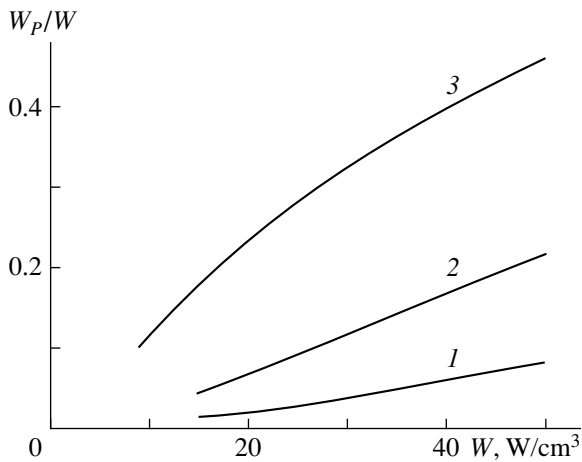
W_P/W

Fig. 7. Ratio of the power density W_P, associated with the positive ion current, to the total power density vs. total power density for $f = 81.36$ MHz, $d = 0.19$ cm, and a CO : He : Xe : $O_2 = 50 : 500 : 15 : 2$ gas mixture at different pressures: $P = (1)$ 100, (2) 60, and (3) 30 torr.

$(E/N)_{RMS}$, 10^{-16} V cm^2

Fig. 8. Calculated profiles of the root-mean-square reduced electric field $(E/N)_{RMS}$ along the discharge gap filled with a CO : He = 1 : 10 gas mixture. The solid curves were calculated from the complete model, and the dashed curves were obtained without allowance for the effect of the vibrational temperature of CO molecules. The calculations were carried out for $P = 100$ torr, $f = 81.36$ MHz, $d = 0.19$ cm, and $W = $ (a) 15 and (b) 50 W/cm^3.

laser efficiency decreases. Within the discharge volume, the ion current is, as a rule, low, but its contribution to the discharge current may be substantial near the electrodes. The effect of gas heating by the ion current is illustrated in Fig. 7, which shows how the ratio of the power density dissipated by the ions to the total power density depends on the latter at different pressures of the gas mixture. We can see that the relative value of the ion current increases with increasing excitation power and with decreasing gas pressure. It can be seen that, at a pressure of 30 torr and excitation powers of higher than 40 W/cm^3, about 40% of the RF discharge power goes directly into gas heating. In this case, efficient operation of the laser is impossible.

The mechanism for creating population inversion in a CO laser can come into play only when the degree of vibrational excitation is sufficiently high. In [25], the spectral and energy parameters of an RF-discharge-excited CO laser were calculated under the assumption that the vibrational excitation of CO molecules has no effect on the structure and characteristics of the discharge. This is why it is important to understand how this assumption manifests itself in the calculated parameters of an RF discharge and a CO laser. Figure 8 shows the profiles of the rms reduced electric field along the discharge gap that were calculated from the complete model and in the approximation in which the effect of the ionization of the vibrationally excited CO molecules on the processes under investigation was ignored. The profiles of the period-averaged rate constants γ of direct ionization (see table, reaction no. 1) and associative ionization (reaction no. 8) along the discharge gap are shown in Fig. 9. The central region of the discharge gap is dominated by associative ionization, whose intensity increases with increasing excitation power (Fig. 9, curves 2). The effect of the addi-
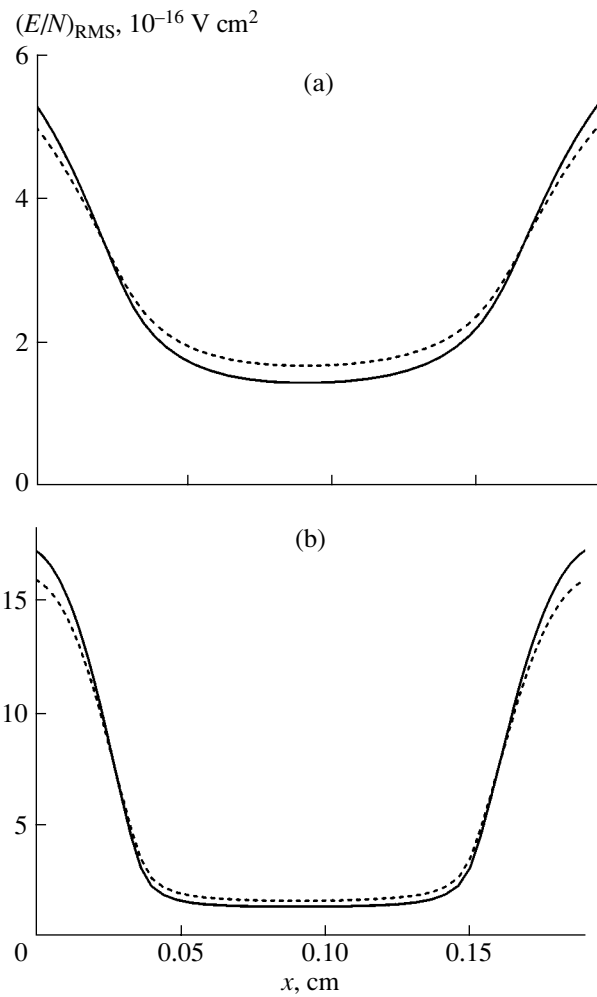
tional ionization channels associated with the vibrationally excited CO molecules weakens the reduced electric field $(E/N)_{RMS}$ at the center of the discharge gap by 10–20%. An analysis shows that associative ionization reaction (2) decreases the parameter $(E/N)_{RMS}$ to a greater extent than does the effect of the vibrational excitation on ionization rate constants (see formula (1)). At a fixed discharge power, a decrease in $(E/N)_{RMS}$ at the center of the discharge gap leads to an increase in $(E/N)_{RMS}$ near the electrodes. This occurs because the conduction current at the discharge center increases. In order for the conduction current to be closed near the cathode, the displacement current should grow at the expense of an increase in the field near the electrodes. Because of such behavior of the reduced electric field
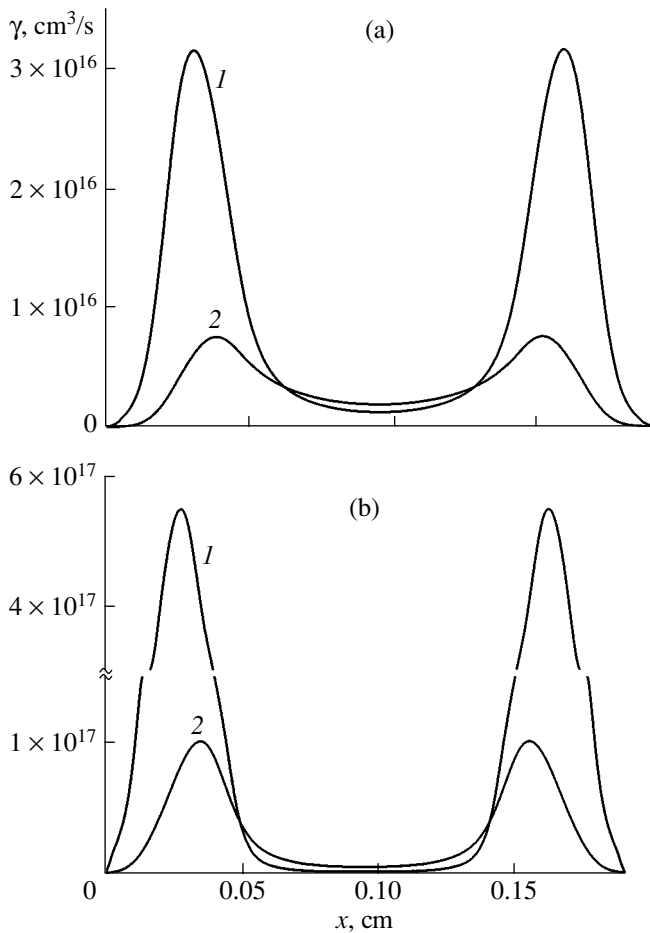
Fig. 9. Calculated profiles of the period-averaged rate constants of (*1*) direct ionization and (*2*) associative ionization along the discharge gap filled with a CO : He = 1 : 10 gas mixture. The calculations were carried out for $P = 100$ torr, $f = 81.36$ MHz, $d = 0.19$ cm, and $W =$ (a) 15 and (b) 50 W/cm^3.
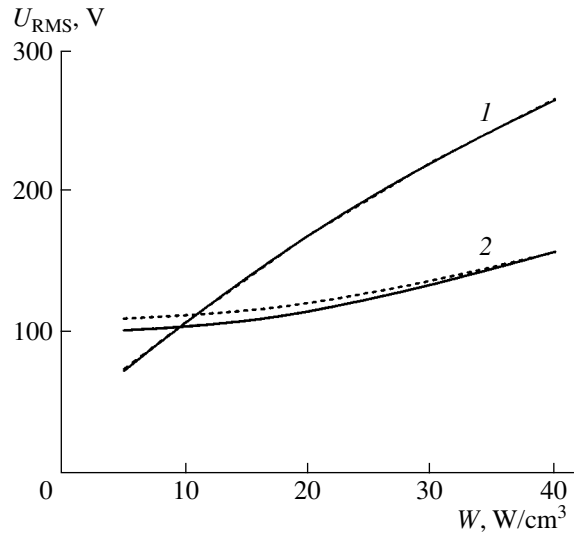
Fig. 10. Calculated dependence of the root-mean-square voltage across the discharge gap filled with a CO : He = 1 : 10 gas mixture on the total input power density. The solid curves were calculated from the complete model, and the dashed curves were obtained without allowance for the effect of the vibrational temperature of CO molecules. The calculations were carried out for $f = 81.36$ MHz, $d = 0.19$ cm, and $P =$ (a) 30 and (b) 100 torr.

$(E/N)_{\mathrm{RMS}}$ along the discharge gap, the vibrational excitation of the CO molecules has only a very minor influence on the VP characteristic of the discharge. This effect is demonstrated in Fig. 10, which shows the VP characteristics of discharges at different gas pressures. On the whole, the increase in the ionization rate due to the vibrational excitation of CO molecules lowers the voltage across the discharge gap. An analysis of the results of numerical simulations shows that the higher the pressure and the lower the excitation power, the larger the extent to which the discharge voltage decreases. At lower pressures, the voltage is not affected by the additional ionization mechanisms (see Fig. 10, in which two curves *1*, calculated for a pressure of 30 torr, are virtually indistinguishable from one another). For a self-sustaining discharge, the values of the reduced electric field E/N at which the discharge is sustained correspond to the range in which the fraction of power that is expended on the excitation of the vibra-

tional levels of CO molecules decreases with increasing reduced electric field. Since the additional ionization channels, namely, those related to the excitation of the high-lying vibrational levels of CO molecules, weaken the reduced electric field $(E/N)_{\mathrm{RMS}}$ in the discharge plasma, the fraction of power that is expended on the excitation of the vibrational levels increases (Fig. 11). From the standpoint of power generation, this is a positive effect because it increases the laser efficiency.

When being supplemented with the additional ionization mechanisms, the model predicts that the RF power density is somehow redistributed over the discharge gap. Estimates show that, in calculating the gas heating rate, one can ignore the energy transfer due to the diffusion of the excited molecules, i.e., the difference between the power density that goes into gas heating and the local discharge power density. In this case, for a fixed total power, the change in the gas temperature at the center of the discharge gap is determined by the power density profile. When the additional ionization mechanisms are taken into account, the model predicts a decrease in the parameter $(E/N)_{\mathrm{RMS}}$ and in the central power density and an increase in the power density in the electrode sheaths. This redistribution of the power density is accompanied by a decrease in the central temperature. An increase in the pressure leads to an insignificant decrease in the parameter $(E/N)_{\mathrm{RMS}}$ and to an increase in the temperature of the gas mixture at the center of the discharge. This last effect stems from the fact that the fraction of power dissipated within the sheaths decreases with increasing pressure (see Fig. 7).
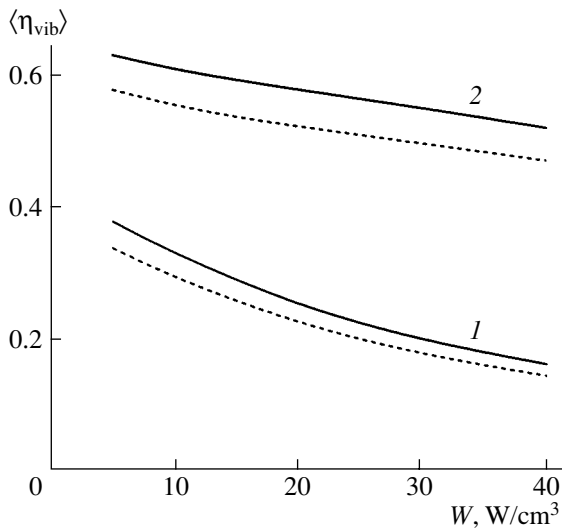
Fig. 11. Fraction of power that is expended on the excitation of the vibrational levels of CO molecules in a discharge gap filled with a CO : He = 1 : 10 gas mixture vs. input power density. The solid curves were calculated from the complete model, and the dashed curves were obtained without allowance for the effect of the vibrational temperature of CO molecules. The calculations were carried out for $f = 81.36$ MHz, $d = 0.19$ cm, and P = (a) 30 and (b) 100 torr.

5. CONCLUSIONS

With a special chamber designed to investigate the properties of RF discharges by measuring their VP characteristics, it became possible to experimentally determine how the root-mean-square voltage across the discharge gap depends on the power deposited in the discharges in different CO-containing gas mixtures at different pressures. This special chamber provided more exact measurements than can be done in a laser chamber [5]. The VP characteristics and other parameters of RF discharges in our experiments have been calculated numerically using a one-dimensional model. For working gas pressures of about 100 torr, which are optimal for the operation of slab CO lasers, the calculated VP characteristics of an RF discharge agree with those obtained experimentally. For a gas mixture at a pressure of 30 torr, the calculated root-mean-square voltage across the discharge gap was found to be markedly higher than the experimental one. In order to clarify the reasons for this discrepancy, additional investigations are required.

Numerical simulations performed with the use of our one-dimensional model have shown that, when the additional ionization mechanisms associated with the vibrational excitation of CO molecules are taken into account, the electric field turns out to be somewhat weaker at the center of the discharge gap and stronger near the electrodes. This leads to an increase in the power expended on the excitation of the vibrational levels of CO molecules and, accordingly, in the efficiency of a CO laser.

REFERENCES

1. A. D. Colley, F. Villarreal, A. A. Cameron, *et al.*, in *Gas Laser: Recent Developments and Future Prospects*, Ed. by W. J. Witteman and V. N. Ochkin; NATO ASI Series 3 **10**, 89 (1995).

2. Y. B. Udalov, S. N. Tskhai, P. J. M. Peters, *et al.*, in *Gas Laser: Recent Developments and Future Prospects*, Ed. by W. J. Witteman and V. N. Ochkin; NATO ASI Series 3 **10**, 73 (1995).

3. Xin Jianguo, Zhang Wang, and Jiao Wentao, Appl. Phys. Lett. **75**, 1369 (1999).

4. V. V. Kunn, V. G. Leont'ev, M. Z. Novgorodov, *et al.*, in *Proceedings of the 12th International Conference on Phenomena in Ionized Gases, Haboken, 1995*, Vol. 3, p. 67.

5. A. A. Ionin, Yu. M. Klimachev, I. V. Kochetov, *et al.*, Preprint No. 53 (Lebedev Physical Institute, Russ. Acad. Sci., Moscow, 2001).

6. P. P. Vitruk, H. J. Baker, and D. R. Hall, J. Phys. D **25**, 1767 (1992).

7. H. J. Baker, Meas. Sci. Technol. **7**, 1631 (1996).

8. S. A. Starostin, K. J. Boller, P. J. M. Peters, *et al.*, Fiz. Plazmy **28**, 68 (2002) [Plasma Phys. Rep. **28**, 63 (2002)].

9. B. Gordiets and S. Zhdanok, in *Nonequilibrium Oscillatory Kinetics*, Ed. by M. Capitelli (Springer-Verlag, New York, 1986; Mir, Moscow, 1989).

10. G. M. Grigor'yan, Y. Z. Ionikh, I. V. Kochetov, and V. G. Pevgov, J. Phys. D **25**, 1064 (1992).

11. A. A. Ionin, I. V. Kochetov, A. P. Napartovich, *et al.*, Preprint No. 34 (Lebedev Physical Institute, Russ. Acad. Sci., Moscow, 2002).

12. M. S. Wahid Syed and C. V. Madhusudana, Int. J. Heat Mass Transf. **43**, 4483 (2000).

13. *Handbook of Physical Quantities*, Ed. by I. S. Grigoriev and E. Z. Meilikhov (Énergoizdat, Moscow, 1991; CRC, Boca Raton, 1997).

14. V. A. Feoktistov, A. M. Popov, O. B. Popovicheva, *et al.*, IEEE Trans. Plasma Sci. **19**, 163 (1991).

15. J. P. Boeuf and Ph. Belenguer, in *Nonequilibrium Processes in Partially Ionized Gases*, Ed. by M. Capitelli and J. N. Bardsley (Plenum, New York, 1990), p. 155.

16. N. L. Aleksandrov and I. V. Kochetov, Teplofiz. Vys. Temp. **25**, 1062 (1987).

17. N. L. Aleksandrov and É. N. Son, in *Plasma Chemistry*, Ed. by B. M. Smirnov (Énergoatomizdat, Moscow, 1978), Vol. 7 [in Russian].

18. A. V. Dem'yanov, I. V. Kochetov, A. P. Napartovich, and A. N. Starostin, Teplofiz. Vys. Temp. **22**, 216 (1984).

19. W. C. Wells, W. L. Borst, and E. C. Zipf, Phys. Rev. A **8**, 2463 (1973).

20. L. I. Virin, G. V. Dzhagatspanyan, G. V. Karachevtsev, *et al.*, *Ion–Molecule Reactions in Gases* (Nauka, Moscow, 1979) [in Russian].

21. D. L. Sharfetter and H. K. Gummel, IEEE Trans. Electron Devices **16**, 64 (1969).

22. J.-B. Boeuf, Phys. Rev. A **36**, 2782 (1987).

23. Yu. P. Raizer, M. N. Shneider, and N. A. Yatsenko, *Radio-Frequency Capacitive Discharge* (Nauka, Moscow, 1995; CRC, London, 1995).

24. H. Zhao, H. J. Baker, and D. R. Hall, Appl. Phys. Lett. **59**, 1281 (1991).

25. I. V. Kochetov, A. P. Napartovich, and S. A. Starostin, Kvantovaya Élektron. **33**, 856 (2003).

Translated by G.V. Shepekina

Freely Localized Microwave Discharge in a Supersonic Gas Flow

**V. M. Shibkov, A. F. Aleksandrov, A. P. Ershov, I. B. Timofeev,
V. A. Chernikov, and L. V. Shibkova**

Moscow State University, Vorob'evy gory, Moscow, 119899 Russia
Received June 30, 2004; in final form, November 18, 2004

Abstract—A discharge produced by a focused microwave beam in a supersonic gas flow has been investigated experimentally. It is shown that the degree of ionization and the gas temperature in the discharge are fairly high and that the main properties of the discharge plasma are only slightly affected by the supersonic air flow. Discharges produced by focused microwave beams can find application in supersonic plasma aerodynamics. © 2005 Pleiades Publishing, Inc.

1. INTRODUCTION

In recent years, a new direction of plasma physics research—supersonic plasma aerodynamics—has been actively developed. It was proposed that the gas flow parameters near an aircraft be controlled and the aircraft aerodynamic characteristics be improved by producing plasma in front of the aircraft and at its planes. Various types of gas discharge (dc discharges, repetitive pulsed discharges, microwave discharges, etc.) can be used for this purpose (see [1–2]). It was suggested that low-temperature gas-discharge plasma can be utilized to ignite supersonic fuel flows in ramjet engines and to intensify the fuel combustion in them. Here, we propose that a freely localized (electrodeless) microwave discharge produced in a given spatial region by a focused high-power microwave beam be used for this purpose. This type of discharge in still air was previously studied in many laboratories (see, e.g., [3–12] and the literature cited therein).

It is well known that, if the electric field strength in the focal region of a focused microwave radiation exceeds a certain threshold value, gas breakdown occurs there. The plasma produced begins to efficiently absorb microwave energy. This leads to efficient ionization, dissociation, and excitation of the gas in this region. The absorbed energy is redistributed among different components and degrees of freedom of the molecular gas. A microwave discharge produced by a slightly converging microwave beam tends to propagate toward the microwave source, the propagation velocity being a function of the microwave intensity. Therefore, the propagation velocity and other characteristics of the discharge can be controlled by varying the microwave intensity [7]. Studies of the properties of a microwave discharge generated far from the walls of the discharge chamber and from the radiation source are important both for solving a number of fundamental problems of plasma physics and for implementing this

type of discharge. This method of delivering power is best suited, e.g., for producing plasma near an aircraft moving with a supersonic velocity in a dense atmosphere. The method allows one to control the air flow near the aircraft and to decrease its drag coefficient. A freely localized microwave discharge can also be used to initiate and optimize the combustion of the gaseous fuel in supersonic ramjet engines.

The aim of this study was to investigate the main properties of a freely localized discharge produced by a focused microwave beam in still air, as well as in supersonic air and air–propane flows.

2. EXPERIMENTAL SETUP

The experimental setup consists of a discharge chamber, a magnetron generator, a power supply system, a system for producing a supersonic gas flow, and a diagnostic facility (see Fig. 1).

The microwave source is a pulsed magnetron generator operating in the centimeter wavelength range. The parameters of the magnetron generator are as follows: the wavelength is $\lambda = 2.4$ cm, the pulsed microwave power is $W < 300$ kW, the pulse duration is $\tau = 1$–300 μs, and the period-to-pulse duration ratio is $Q = 1000$. The magnetron is powered from a pulsed modulator with a partial discharge of the capacitive storage. Microwave power was delivered to the discharge chamber through a 9.5×19-mm rectangular waveguide. The input microwave power was measured with the help of a directional coupler installed in the waveguide so that a fraction of microwave power was directed to the measuring arm containing an attenuator and a section with a crystal detector. The microwave pulse envelop at the detector output was recorded using a digital oscilloscope. The pulse envelop was nearly flat-top. The same signal was fed to a pulsed digital voltmeter measuring the pulse amplitude. The voltmeter was preliminarily
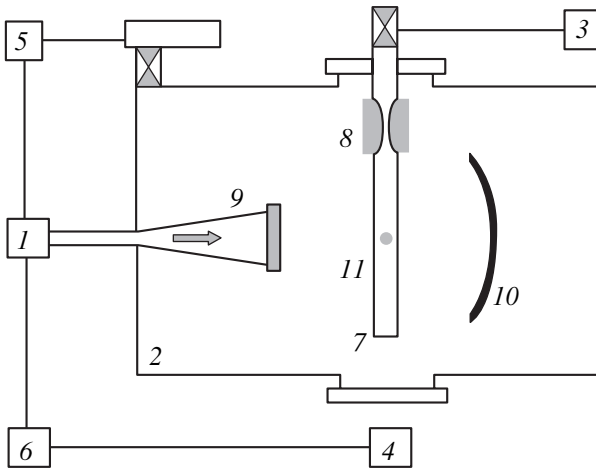
Fig. 1. A block diagram of the experimental setup: (*1*) magnetron, (*2*) discharge chamber, (*3*) system for producing supersonic flows, (*4*) diagnostic facility, (*5*) pump out, (*6*) synchronization unit, (*7*) aerodynamic channel, (*8*) Laval nozzle, (*9*) horn antenna, (*10*) metal mirror, and (*11*) microwave discharge.

calibrated with the help of a calorimetric power meter connected to the output of the main arm of the directional coupler. All the components of the microwave transmission line were sealed. To avoid electric breakdowns inside the waveguide, it was filled with an insulating gas (SF_6) at a pressure of 4 atm. The vacuum system allowed us to carry out experiments at air pressures of $p = 1–760$ torr.

We used two schemes for producing freely localized microwave discharges. In the first scheme, the microwave beam was focused by a 0.6-m-diameter dielectric lens with a focal length of 0.8 m. A freely localized microwave discharge was produced in the standing-wave operating mode. The focused microwave beam was directed onto a spherical metal mirror placed in front of the lens and was additionally focused by this mirror. However, to ignite fuels in actual engines, it seems more expedient to use another scheme for producing microwave discharges (Fig. 1). In this scheme, a horn antenna and a metal short-focus mirror are used instead of the lens. The microwave power is input into the discharge chamber through a rectangular waveguide, which is sealed in the chamber flange. The waveguide terminates with a rectangular horn inserted into the discharge chamber. The horn forms a microwave beam incident onto a spherical mirror with a focal length of 16 cm. This mirror is positioned in front of the horn at a distance of 30 cm from it. A microwave discharge in a supersonic flow is produced in a quartz cylindrical channel located between the horn and the mirror, in the focal plane of the mirror. In this series of experiments, we used a smooth 3-cm-diameter cylindrical aerodynamic channel without a stagnation zone.

The evacuated metal cylindrical discharge chamber is the basic component of the experimental setup. Its

functions are to provide the required pressure in experiments with freely localized microwave discharges in still gases and supersonic gas flows. It also serves as a reservoir for exhaust gases. The inner diameter of the discharge chamber is 1 m, and its length is 3 m. The chamber consists of a major and a minor section. The major section is mounted on a car and is equipped with a special lock unit; it can be detached from the minor section and be moved aside on rails. This allows us to easily access the chamber interior for the accommodation of the necessary experimental objects and for other purposes. The cylindrical wall of the chamber has more than twenty diagnostic windows of different diameter ($d = 10–50$ cm) and a number of sealed electric connectors, so it is possible to observe the processes occurring inside the chamber and to feed the required electric voltages and other control and auxiliary signals into the chamber without deteriorating vacuum in it.

A supersonic flow was produced by filling the discharge chamber with air through a specially profiled Laval nozzle mounted on the outlet tube of the electromechanical valve. In our experiments, we used a cylindrical nozzle designed for a Mach number of $M = 2$. The nozzle was made of a dielectric in order avoid its influence on the distribution of the electric field in the focal region of the microwave beam. The electromechanical valve was mounted on the chamber flange so as to produce a supersonic air flow along the vertical diameter of the chamber. To synchronize the operation of the electromechanical valve with the microwave discharge, we used a special circuit that provided the required time delay between the generation of the discharge and the opening of the valve. The electromechanical valve remained open over 2 s. A freely localized microwave discharge was produced within this time interval. The supersonic flow was perpendicular to the propagation direction of the microwave beam.

3. DIAGNOSTIC TECHNIQUES

In our experiments, we measured the integral emission spectrum from the discharge plasma, the time behavior of the intensities of various molecular bands and atomic lines at the outlet from the aerodynamic channel, and the translational and vibrational gas temperatures. The general view of a freely localized microwave discharge was recorded by a photographic camera and a digital video camera.

During the combustion of a supersonic air–propane flow in the aerodynamic channel, we observed the CH, CN, C_2, and OH molecular bands, as well as intense lines of atomic hydrogen and oxygen. For example, in a discharge excited in an air–propane mixture, the intensities of CN bands were three to five times higher than those in a discharge in air. However, even several centimeters downstream from the discharge, the intensities of CN bands dropped sharply, whereas the intensities of CH bands remained almost the same. Therefore, to confirm that the supersonic hydrocarbon fuel

flow in the aerodynamic channel was ignited by a freely localized discharge, we used, as an indicator, emission from the excited CH* radicals. The time behavior of the intensity of the 431.5-nm molecular band of the excited CH* radicals (the (0; 0) band of the $A^2\Delta \longrightarrow X^2\pi$ transition) was measured in different regions of the aerodynamic channel, at different distances downstream from the focal region of the microwave beam.

The translational gas temperature in a microwave discharge in air was determined by a spectroscopic method based on measuring the distribution of the line intensities in the rotational structure of the (0; 2) band of the second positive system of molecular nitrogen ($\lambda = 380.5$ nm) [7]. The vibrational temperature was determined from the relative intensities of the bands of the second positive system of molecular nitrogen [13] and molecular bands of cyanogen [14].

When determining the translational and vibrational gas temperatures, the emission spectra from a microwave discharge were recorded with the help of an STE-1 spectrograph (with a dispersion of 0.3–1.0 nm/mm) and a DFS-12 and an MDR-23 monochromator (with dispersions of 0.5 and 1.3 nm/mm, respectively). As a detector, we used either a photomultiplier or a CCD array (a photodiode unit consisting of a large number of light-sensitive elements arranged in a line) positioned behind the exit slit of the monochromator. The spatial resolution of the recording system depends on the size and number of light-sensitive elements. In our experiments, we used a CCD array consisting of 3650 elements, each 8×8 μm in size; this ensured spatial resolution of no worse than 0.4 mm. Video signals from the recording system, which were proportional to the emission intensity measured in the 300- to 900-nm spectral range, were encoded by an analog-to-digital converter and then stored in a PC. The discharge spectrum could then be displayed on a monitor or printed out with the use of a specially designed software.

4. RESULTS AND DISCUSSION

Microwave discharges in a focused microwave beam were produced both in still air and in supersonic gas flows with a Mach number of $M = 2$. When operating with gas flows, microwave discharges could be produced either in a free gas flow or upstream of a body flowed around by a supersonic flow.

4.1. Microwave Discharge in Still Air

The magnetron parameters allowed us to produce electrodeless discharges in a focused microwave beam at air pressures below 100 torr. When studying the spatiotemporal characteristics of microwave discharges at pressures higher than 100 torr, it was necessary to initiate the discharge externally because, in subcritical electric fields, the discharge cannot develop without a preliminary breakdown. It is known [5] that, after breakdown, the discharge can be maintained over a

long time by a subcritical field. The discharge can be initiated, e.g., by an intense laser pulse or by introducing an initiator (a metal needle or a special target) in the focal region of the microwave beam. In our experiments, we used a specially designed initiator consisting of two copper wires inserted in ceramic pipes. The initiator was placed in the focal region of the microwave beam, and its position was adjusted so that the wire ends lay at a distance of 5–20 mm from one another and were oriented along the electric field. A high voltage pulse ($\tau = 1$ μs) applied to the initiator resulted in gas breakdown across the initiator gap. The microwave pulse was switched on 40 μs after the initiating voltage pulse. The electrons surviving after the recombination of the preliminary plasma efficiently absorbed microwave energy, thereby stimulating the development of a microwave discharge. With such an initiator, discharges in focused microwave beams could be produced over a wide range of air pressures and microwave intensities.

Figure 2 shows the general view of a freely localized microwave discharge at different air pressures. It can be seen that, at low pressures, the freely localized microwave discharge looks like a chain of plasmoids separated by a distance of about 1 cm. The transverse size of the plasmoids is one to several centimeters. At the threshold input power, the total length of the discharge decreases with increasing pressure. At high pressures (by high pressures, we mean pressures at which the inequality $\nu_{eff} \gg \omega$ holds, where ν_{eff} is the effective electron–molecule collision frequency and ω is the microwave circular frequency), the microwave discharge is highly nonuniform and consists of several bright plasma channels, which are less that 1 mm in diameter and are extended along the microwave electric field.

We measured the translational and vibrational gas temperatures in microwave discharges produced in still air at different pressures and incident powers. Figure 3 shows the translational and vibrational gas temperatures as functions of the air pressure for the threshold incident power. It can be seen that the gas temperature increases monotonically from 500 K to 1800 K as the air pressure increases from 10 to 100 torr. The increase in the temperature can be explained as follows. At the threshold microwave power, the breakdown field increases in proportion to the air density n. In this case, as the pressure increases, the reduced electric field E/n remains constant, whereas the electron density increases [7]. This leads to an increase in the energy deposited in the gas and, accordingly, to an increase in the gas temperature. At the same time, the vibrational temperature varies nonmonotonically with pressure and passes through a minimum at $p \sim 30$ torr. This pressure corresponds to the minimum in the Paschen curve for the given microwave wavelength; i.e., the power required for initiating a freely localized microwave discharge is minimum at this pressure [7].

Figure 4 shows the translational and vibrational gas temperatures as functions of the incident power at an air
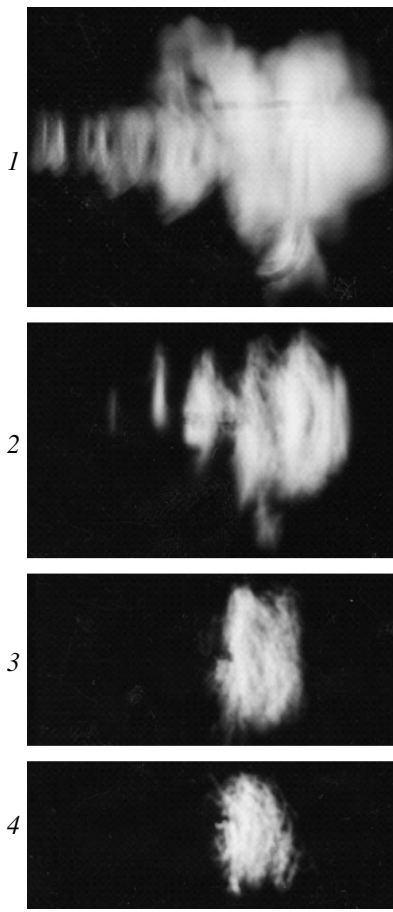
Fig. 2. General view of a freely localized microwave discharge produced in still air at a pulse duration of $\tau = 20$ μs; repetition rate of $f = 10$ Hz; and pressures of $p = (1)$ 40, (2) 80, (3) 300, and (4) 500 torr. The microwave beam propagates from left to right.

Fig. 3. Translational (1) and vibrational (2) gas temperatures in the plasma of a freely localized microwave discharge as functions of the air pressure at the threshold microwave power.

pressure of $p = 60$ torr. It can be seen that, as the microwave power increases, the gas temperature first increases and then decreases, whereas the vibrational temperature decreases monotonically. In a self-sustained discharge produced by a focused microwave beam, the electron density at low incident powers is close to the critical density [10]. The propagation velocity of the discharge front is low, the region occupied by the discharge plasma is no longer than 1–2 cm, and the microwave field penetrates freely into the plasma during the entire microwave pulse. In this case, the electronic states of molecules are efficiently excited, the gas is heated during the entire microwave pulse, and the gas temperature in the focal region increases with increasing microwave power. As the microwave power increases further, the propagation velocity of the discharge increases and the electron density reaches its critical value at the discharge front. As a result, the electric field in the focal region of the microwave beam decreases due to the skin effect and the gas heating rate decreases.
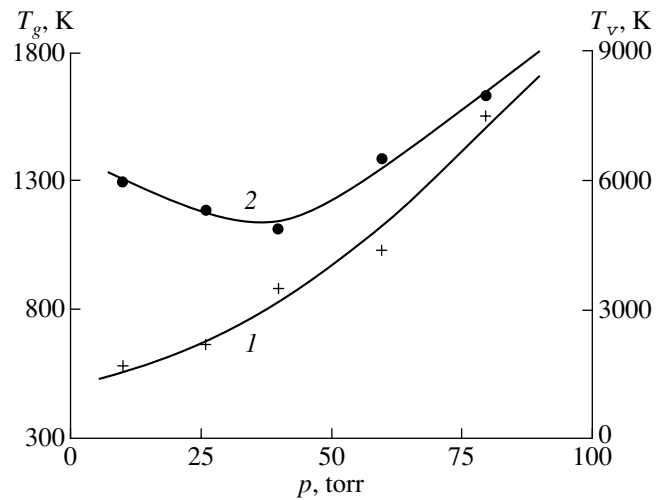
It was shown in [15] that the reduced electric field in the plasma produced by a focused microwave beam is fairly high. For this reason, in the initial phase of a discharge, excited and charged particles are efficiently produced and the gas temperature grows rapidly at a rate of 100 K/μs or more [16–18]. Rapid gas heating was also observed experimentally when studying discharges in air, nitrogen, and air–nitrogen mixtures [7, 11, 16–18]. It was shown that the gas was heated due to the deexitation of the electronic states of molecules, which were efficiently excited by electron impact at high values of the reduced electric field ($E/n \geq 10^{15}$ V cm^2).

4.2. Microwave Discharge in a Supersonic Flow

Most gas discharges are produced with the use of single- or multielectrode energy supply systems. From the practical standpoint, such systems are poorly suited to remotely control plasma production in a certain spatial region, e.g., ahead of a body moving with a supersonic velocity in the dense atmosphere (rather than at its surface). Electrodeless systems in which freely localized discharges are produced using focused microwave beams are best suited for this purpose.

In a freely localized discharge, the electric field is localized in the waist region of a focused microwave beam. Microwave beams can be focused in both still gases and gas flows. Gas breakdown in a microwave discharge occurs over a time that is shorter than the time during which the gas propagates through the discharge; therefore, the discharge is not blown off by the supersonic flow. In contrast, in a transverse electrode discharge, the current frozen in the moving plasma is carried away from the electrode gap and forms an unsteady current loop [19]. Hence, the plasma of a freely localized discharge can exist in a specified region

of space during the entire microwave pulse. It was demonstrated experimentally (see Fig. 5) that the discharge was not blown off by a supersonic flow from the focal region of a focused microwave beam. The experiments also showed that the power required for producing a microwave discharge depended only slightly of the flow velocity. Thus, there was almost no difference between the situation in which a freely localized microwave discharge was initially excited in still air and then a supersonic flow was switched on and the opposite situation in which a supersonic flow was initially switched on and then a microwave discharge was produced in the flow. Note that, under our experimental conditions, the gas flow velocity was much lower than the discharge propagation velocity and the supersonic air flow with a Mach number of $M = 2$ only slightly affected gas heating.

To confirm the hypothesis that plasma may be produced ahead of a body moving with a supersonic velocity in the dense atmosphere, we carried out experiments in which a microwave discharge was produced ahead of a model of the aircraft forepart flowed around by a supersonic air flow at pressures of $p = 50$–500 torr. Figure 6 shows the general view of microwave discharges at air pressures of 60 and 300 torr and a microwave pulse duration of $\tau = 30$ μs. It can be seen that the generation of a discharge in a focused microwave beam is a reliable method for remotely controlling the production of plasma in a specified spatial region ahead of an aircraft moving with a supersonic velocity in the dense atmosphere.

The possibility of controlling the ignition and combustion of the fuel in a hypersonic ramjet engine is an important condition for its practical use. When studying the combustion kinetics of hydrocarbon fuels in their mixtures with oxygen and air, attention has been mainly focused on the mechanisms for igniting gaseous fuels. For the most part, mechanisms determining the induction time of the mixture during its thermal self-ignition have been investigated. Only recently, publications appeared (see [1, 2]) in which the influence of a low-temperature gas-discharge plasma on the combustion kinetics was considered. In order to solve this problem, which largely determines progress in hypersonic aviation, it was proposed to use various types of plasma generators.

In our experiments, we studied the influence of a nonequilibrium plasma on the combustion kinetics of a gaseous hydrocarbon fuel using the ignition of a supersonic air–propane flow with a Mach number of $M = 2$ as an example. For ignition, we used a freely localized microwave discharge. A microwave discharge was excited in still air inside the aerodynamic channel; the plasma 1–2 cm in size was produced near the initiator (Fig. 7a). The discharge dimensions were found to increase with increasing power and duration of the microwave pulse. Figure 7b shows photographs of freely localized microwave discharges in supersonic air
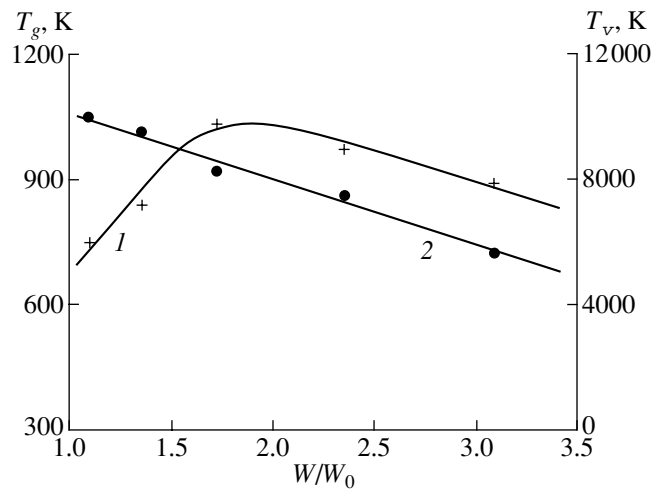
Fig. 4. (*1*) Translational and (*2*) vibrational gas temperatures in the plasma of a freely localized microwave discharge in air as functions of the microwave power (W_0 is the threshold power for gas breakdown at a pressure of $p = 60$ torr).

Fig. 5. The general view of a freely localized microwave discharge produced in a supersonic air flow ($M = 2$) at a pressure of $p = 350$ torr, pulse duration $\tau = 300$ μs, and repetition rate of $f = 10$ Hz. The microwave beam propagates from left to right. The arrow shows the direction of the supersonic flow. The arrow width is equal to the exit diameter of the Laval nozzle.

and air–propane flows in the aerodynamic channel. It turned out that the supersonic flow of a gaseous hydrocarbon fuel was easy to ignite by a microwave discharge. In our experiments, the combustion of a supersonic air–propane flow was successfully initiated by microwave beams with a duration as short as $\tau = 25$ μs. It should be noted that a repetitive transverse electrode discharge ensures the ignition of a supersonic air–propane flow only at pulse durations of no less than 100–150 μs, whereas the microwave pulse duration required for ignition is much shorter. This indicates that the number of active particles produced in a microwave
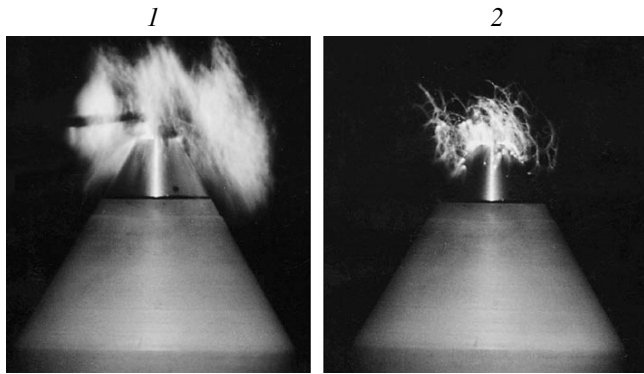
1   *2*

Fig. 6. The general view of a microwave discharge produced ahead of a body flowed around by a supersonic air flow at $M = 2$, $\tau = 30$ μs, $f = 100$ Hz, and a static air pressure in the chamber of $p = (1)$ 60 and (2) 300 torr. The microwave beam propagates from left to right, and the supersonic flow propagates from top to bottom.
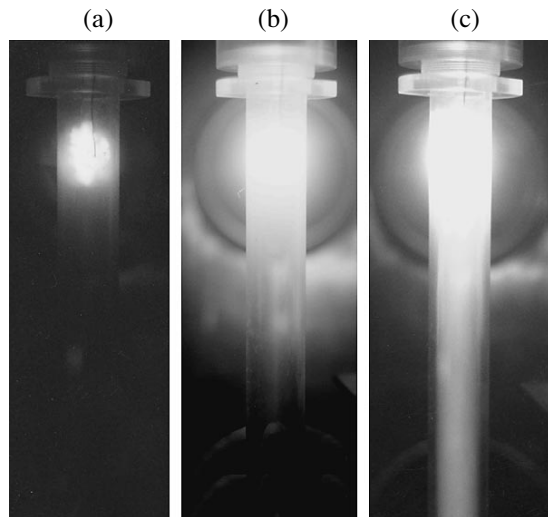
(a)   (b)   (c)

Fig. 7. The general view of a freely localized microwave discharge produced in still air at a microwave power of $W = 100$ kW (plot (a)) and in supersonic ($M = 2$) air and air–propane flows at $W = 200$ kW (plots (b) and (c), respectively). The static air pressure in the chamber is $p = 60$ torr, and the microwave pulse duration is $\tau = 100$ μs.

discharge is much larger than that in a dc electrode discharge.

Besides photographing the general view of a discharge in the aerodynamic channel, we recorded the emission spectra from the combustion products of an air–propane mixture in different regions of the aerodynamic channel. Thus, in the case of a microwave discharge in a supersonic air flow, the emission spectrum measured at a distance of $z = 7$ cm downstream from the beam focus did not contain any atomic lines and molecular bands. In contrast, in the emission spectrum from a

discharge in a supersonic air–propane flow, we observed intense radiation from the excited CH* radicals, the molecular bands of C_2 and CN, and the spectral lines of atomic oxygen and hydrogen. In this case, the radiation pulse lasted over ~1 ms, whereas the duration of the microwave pulse initiating combustion was $\tau = 100$ μs.

It was shown in [20] that, at high values of the reduced electric field ($E/n \geq 10^{15}$ V cm^2), a significant fraction (more than 50%) of the energy deposited in the discharge is spent on the excitation, dissociation, and ionization of molecules by electron impact with the subsequent generation of chemically active radicals. Since a self-sustained microwave discharge exists at high values of the reduced electric field [7], the number of active particles produced in such a discharge is larger than that in an electrode discharge. This should strongly affect the kinetics of the processes with the participation of active radicals and should result in a shorter induction time. Our experiments indicate that, at high values of the reduced electric field, the gas in a microwave discharge is rapidly heated ($dT_g/dt \sim 10^8$ K/s) and the degree of molecular dissociation is high (up to $\delta \sim 50\%$); this promotes rapid fuel ignition. It should be noted that, since the reduced electric field in a microwave discharge is high, the plasma is a source of intense UV radiation, which may substantially affect the production of active radicals via photoionization, photodissociation, and photoexcitation. This is also favorable for reducing the induction time. For this reason, we believe that it is necessary to more thoroughly examine the role of charged and active particles, which are very rapidly produced in a microwave discharge, and the influence of UV radiation on both the reduction of the induction time and the increase in the combustion efficiency of hydrocarbon mixtures.

5. CONCLUSIONS

The properties of freely localized microwave discharges in air and in supersonic air–propane flows have been investigated experimentally. It has been shown that the microwave discharge is a reliable and efficient tool for initiating the combustion of supersonic flows of hydrocarbon fuels. This method for initiating fuel combustion can find application in ramjet engines.

ACKNOWLEDGMENTS

REFERENCES

1. *1st–6th AIAA International Workshops on Weakly Ionized Gases, Colorado, 1997; Norfolk, 1998, 1999; Anaheim, 2001; Reno, 2003, 2004.*

2. *1st–5th International Workshops on Magneto- and Plasma Aerodynamics for Aerospace Applications, Moscow, 1999–2003.*

3. *High-Frequency Discharge in Wave Fields*, Ed. by A. G. Litvak (IPF AN SSSR, Gorki, 1988) [in Russian].

4. *International Workshops on Strong Microwaves in Plasmas, Nizhni Novgorod, 1991, 1994, 2003.*

5. G. M. Batanov, S. I. Gritsinin, I. A. Kossyǐ, *et al.*, Tr. Fiz. Inst. im. P.N. Lebedeva AN SSSR **160**, 174 (1985).

6. V. V. Gil'denburg and S. V. Golubev, Zh. Éksp. Teor. Fiz. **67**, 89 (1974) [Sov. Phys. JETP **40**, 46 (1975)].

7. A. S. Zarin, A. A. Kuzovnikov, and V. M. Shibkov, *Freely Localized Microwave Discharge in Air* (Neft' i Gaz, Moscow, 1996) [in Russian].

8. A. L. Vikharev, V. B. Gil'denburg, S. V. Golubev, *et al.*, Zh. Éksp. Teor. Fiz. **94** (4), 136 (1988) [Sov. Phys. JETP **67**, 724 (1988)].

9. G. I. Batskikh and Yu. I. Khvorostyanoǐ, Radiotekh. Élektron. (Moscow) **37**, 311 (1992).

10. A. A. Kuzovnikov, V. M. Shibkov, L. V. Shibkova, *et al.*, Zh. Tekh. Fiz. **67** (7), 19 (1997) [Tech. Phys. **42**, 733 (1997)].

11. V. M. Shibkov, Teplofiz. Vys. Temp. **35**, 693 (1997); **35**, 871 (1997).

12. V. G. Brovkin and Yu. F. Kolesnichenko, Pis'ma Zh. Tekh. Fiz. **17** (1), 58 (1991) [Sov. Tech. Phys. Lett. **17**, 22 (1991)].

13. V. N. Ochkin, Tr. Fiz. Inst. im. P.N. Lebedeva AN SSSR **78**, 3 (1974).

14. J. L. Spier and M. M. Smit-Miessen, Physica **9**, 422 (1942).

15. V. M. Shibkov, Teplofiz. Vys. Temp. **34**, 349 (1996); **34**, 525 (1996); **34**, 741 (1996).

16. A. M. Devyatov, A. A. Kuzovnikov, V. V. Lodinev, and V. M. Shibkov, Vestn. Mosk. Univ., Ser. 3: Fiz., Astron. **32** (2), 29 (1991).

17. A. V. Kalinin, V. M. Shibkov, and L. V. Shibkova, Vestn. Mosk. Univ., Ser. 3: Fiz., Astron., No. 1, 32 (1996).

18. V. V. Lodinev, V. M. Shibkov, and L. V. Shibkova, Vestn. Mosk. Univ., Ser. 3: Fiz., Astron., No. 1, 29 (1991).

19. A. P. Ershov, O. S. Surkont, I. B. Timofeev, *et al.*, Teplofiz. Vys. Temp. **42**, 516 (2004); **42**, 669 (2004).

20. Yu. P. Raizer, *Gas Discharge Physics* (Nauka, Moscow, 1987; Springer-Verlag, Berlin, 1991).

Translated by N.F. Larionova